

**Improving the process modelling capability
for manufacturing large composite
structures used on passenger aircraft**

by

Robert S. Pierce

BAeroEng (Hons)

A thesis submitted to Monash University
for the degree of Doctor of Philosophy

December 2014

Copyright notices

Notice 1:

Under the Copyright Act 1968, this thesis must be used only under the normal conditions of scholarly fair dealing. In particular no results or conclusions should be extracted from it, nor should it be copied or closely paraphrased in whole or in part without the written consent of the author. Proper written acknowledgement should be made for any assistance obtained from this thesis.

Notice 2:

I certify that I have made all reasonable efforts to secure copyright permissions for third-party content included in this thesis and have not knowingly added copyright content to my work without the owner's permission.

Statement of originality

This thesis contains no material that has been accepted for the award of a degree or diploma in this or any other university. To the best of the candidate's knowledge and belief, this thesis contains no material previously published or written by another person except where due reference is made in the text of this thesis.



Candidate: Robert S Pierce

December 2014

Abstract

As the aircraft manufacturing industry continues to transition from metals to composite materials for structural applications, it is becoming increasingly difficult and costly to manufacture components with traditional autoclave processes. The demand for large, complex and low-cost composite aerostructures is prompting advances in manufacturing with textile reinforcement materials and Liquid Composite Moulding (LCM) techniques. However, these methods continue to rely on operator skill and experience through empirical practices. In order to reduce production timescales and resources, this research focuses on the development of a Complete Process Model (CPM) that can simulate LCM, and emphasises the impact of dry fabric deformation on subsequent infusion.

First, the fabric deformation that results from draping was simulated using a hypoelastic continuum approach in the finite element package, Abaqus/Explicit. The strength of this model, which has been validated against existing simulated and experimental results, is attributed to the non-orthogonal tracking of fibre directions through the use of a user subroutine (VUMAT).

The tensile and shear properties of a carbon fibre, plain weave material were characterised experimentally in order to enhance the fidelity of fabric behaviour in the draping model. For improved shear measurements, an in-house Digital Image Correlation code was developed for use with a digital camera to monitor fabric deformation.

Radial permeability characterisation testing was also performed over a range of shear angles to capture the complete, deformation-dependent, anisotropic permeability behaviour of the aerospace-grade fabric. Video footage of the fluid flow was digitally captured and processed, using a statistical approach, in order to define permeability as a function of both shear angle and flow orientation.

The infusion stage of the simulation employed a Volume of Fluid method in ANSYS FLUENT to model transient, multiphase flow through an anisotropic porous medium. The approach was validated against experimental test results.

These components were combined to form the Complete Process Model. The material characterisation provided the necessary data for the draping model to produce a realistic prediction of the deformed fabric geometry and shear angle distribution. This information was then coupled with the results of the permeability characterisation experiments to create a complex permeability distribution, before being passed on to the infusion model. The CPM demonstrates the importance of linking draping deformation with infusion, shows significant improvement over traditional modelling, and serves as a solid foundation for further advances.

Acknowledgements

First and foremost, I would like to thank my supervisors: Prof. Brian Falzon, for the guidance during the early stages of the project at Monash, and ongoing support from Queen's University Belfast; and Prof. Mark Thompson, for the advice in the final stages of this research.

The resources, facilities and support provided by Monash University have been greatly appreciated, particularly from the Department of Mechanical and Aerospace Engineering and the Department of Materials Engineering.

I also wish to express my gratitude for the Australian Postgraduate Award – Industry (APAI) scholarship, in association with Boeing Research and Technology Australia (BR&TA), which have helped fund this work.

Furthermore, I would like to acknowledge the individual contributions of Romain Boman, who provided key advice in programming matters during his brief time at Monash in 2011, and Paul Evans for the support in conducting final experiments at BR&TA.

Finally, thank you to my family for putting up with my continued student lifestyle.

Nomenclature

A list of nomenclature used throughout this thesis is included here, followed by a summary of all the referenced acronyms.

Symbol	Description
∇	Vector gradient operator (grad)
$\sum_{i=a}^b$	Sum of arguments with i incrementally from a to b
$ i $	Absolute value of i
$\ i\ $	Norm of i
α, β	Angles
γ	Shear angle (shear strain)
δ	Sample extension
$d\boldsymbol{\varepsilon}$	Incremental strain tensor for the orthogonal basis
$d\boldsymbol{\varepsilon}^{f\alpha}$	Incremental strain tensor for the α fibre direction
ε_i	Strain in the i direction
ϵ	Porosity
η, ξ	Elemental, in-plane Cartesian coordinates
θ_α	Angle between orthogonal axes and fibre directions
μ	Fluid viscosity
ρ	Density
ρ_A	Fabric areal density
ρ_f	Fibre density
$\boldsymbol{\sigma}$	Cauchy stress tensor
$\boldsymbol{\sigma}^\nabla$	Objective derivative of the Cauchy stress tensor
$\boldsymbol{\sigma}_{New}$	Updated stress tensor for the current time increment
$\boldsymbol{\sigma}_{Old}$	Stress tensor from the previous time increment
$d\boldsymbol{\sigma}$	Incremental stress tensor for the orthogonal basis
$d\boldsymbol{\sigma}^{f\alpha}$	Incremental stress tensor for the α fibre direction
$\tau(\gamma)$	Shear stress as a function of shear angle

φ	Principal permeability direction
ϕ	Cell-centred variable
f	Face variable
\mathbf{C}	Constitutive tensor
$\mathbf{C}^{f\alpha}$	Constitutive tensor for the α fibre direction
d	Distance
\mathbf{d}_f	Displacement vector from an upstream cell centroid to a face
\mathbf{D}	Strain rate tensor
E_{11}	Tensile (Young's) modulus in the warp fibre direction
E_{22}	Tensile (Young's) modulus in the weft fibre direction
\mathbf{f}_α	Vector representing fibre direction α
\mathbf{f}_α^0	Initial state of the vector representing fibre direction α
\mathbf{F}	Deformation gradient tensor
F_i	Linear regression of the term N in the i direction over time
F_b	Normal bias force
$F_{sh}(\gamma)$	Normalised shear force as a function of shear angle
G_{12}	In-plane shear modulus
g	Gravitational constant
\mathbf{g}_α	Vector direction α from the orthogonal basis
\mathbf{g}_α^0	Initial state of vector direction α from the orthogonal basis
h	Cavity thickness
H	Sample gauge height
\mathbf{K}	Permeability tensor
K_1, K_2	Principal permeability values
K'_i	Quasi-isotropic permeability in the i direction
K_{eff}	Effective permeability
K_S	Streamwise permeability
K_T	Transverse permeability
N	Term relating flow front radius and inlet radius according to Adams et al. (1988)

$N_{S,i}$	Shape function equation for node i
p	Pressure
δr	Small increment in radius
r	Radius
r_0	Inlet radius
r_{ff}	Flow front radius
R^2	Coefficient of determination
\mathbf{R}	Rotation tensor
\mathbf{S}_K	Source term based on flow resistance in a porous material
δt	Small increment in time
t	Time
t_f	Final time
T_α	Transformation matrix from the orthogonal basis to fibre direction α
\mathbf{u}	Velocity vector
\mathbf{U}	Right stretch tensor
\mathbf{v}	Phase-averaged flow velocity
V_{fp}	Phase volume fraction
V_f	Fibre volume fraction
W	Sample gauge width
w_i	Inverse cubic distance weighting function
W_{Sum}	Sum of the weighting functions
x, y, z	Cartesian coordinates
x_i, y_i	Displacements associated with Cartesian coordinates
X_i, Y_i	Initial displacements associated with Cartesian coordinates

Acronym	Description
3K	Designation for tows made from 3000 fibres
API	Application Programming Interface
APS	Active Pixel Sensor
ASCII	American Standard Code for Information Interchange
BEM	Boundary Element Method
CCD	Charge-Coupled Device
CFD	Computational Fluid Dynamics
CFRP	Carbon Fibre Reinforced Plastic
CPM	Complete Process Model
CRE	Constant Rate of Extension
CVFE	Control Volume / Finite Element
DIC	Digital Image Correlation
FAN	Flow Analysis Network
FD	Finite Difference
FE	Finite Element
FEA	Finite Element Analysis
FINE	Floating Imaginary Nodes and Elements
FSI	Fluid-Structural Interaction
FV	Finite Volume
GN	Green-Naghdi
GUI	Graphical User Interface
LCM	Liquid Composite Moulding
LIMS	Liquid Injection Moulding Simulation
M3D4R	Designation for a three dimensional, four node, membrane element with reduced integration
MAC	Marker Cell
OCT	Optical Coherence Tomography
PRESTO	Pressure Staggering Option
RIFT	Resin Infusion under Flexible Tooling

RUC	Repeated Unit Cell
RVE	Representative Volume Element
S4R	Designation for a four node shell element with reduced integration
SCRIMP	Seeman Composites Resin Infusion Moulding Process
SDV	Solution Dependent state Variable
UDF	User-Defined Function
UDM	User-Defined Memory
UMAT	User material subroutine for Abaqus/Standard
VARI	Vacuum-Assisted Resin Infusion
VARTM	Vacuum-Assisted Resin Transfer Moulding
VFABRIC	User material subroutine for fabric behaviour in Abaqus/Explicit
VI	Vacuum Infusion
VOF	Volume of Fluid
VUMAT	User material subroutine for Abaqus/Explicit

Contents

Copyright notices	i
Statement of originality	iii
Abstract	v
Acknowledgements	vii
Nomenclature	ix
Contents	xv
1 Introduction	1
1.1 History of composite materials in commercial aircraft	1
1.2 Next generation airliners	1
1.3 Textile reinforcement materials	3
1.4 Out-of-autoclave manufacturing	4
1.5 Process modelling.....	5
1.6 Research objectives	5
1.7 Thesis outline.....	6
2 Review of LCM process modelling	8
2.1 Drape modelling	8
2.1.1 Geometric mapping and particle based methods.....	9
2.1.2 Continuum methods.....	10
2.1.3 Discrete and semi-discrete methods.....	11
2.2 Determination of mechanical properties	13
2.2.1 Experimental material characterisation	14
2.2.1.1 Tensile methods.....	14
2.2.1.2 Shear methods	15
2.2.1.3 Bending methods	16
2.2.2 Simulating fabric behaviour	17
2.3 Fabric permeability	17
2.3.1 Experimental permeability characterisation	18
2.3.2 Predictive modelling.....	20
2.3.3 Permeability and shear angle relationship.....	21
2.4 Infusion modelling	22
2.4.1 Control Volume / Finite Element (CVFE) methods.....	24
2.4.2 Volume of Fluid (VOF) methods	25

2.5	Process modelling.....	26
3	Draping simulation	27
3.1	Motivation	27
3.2	Continuum model.....	27
3.2.1	VFABRIC subroutine approach	28
3.2.2	VUMAT subroutine approach	29
3.3	Draping simulation validation	32
3.3.1	VFABRIC hemispherical punch simulation	32
3.3.2	VUMAT double dome punch simulation	36
3.3.3	VUMAT and VFABRIC comparison.....	39
3.4	Multiple ply modelling.....	40
3.5	Conclusions.....	41
4	Mechanical characterisation	42
4.1	Motivation	42
4.2	Tensile testing.....	42
4.2.1	Experimental approach	42
4.2.2	Tensile strip test results	44
4.3	Shear testing.....	47
4.3.1	Experimental approach	47
4.3.2	Narrow sample mechanical test results.....	49
4.3.3	Wide sample mechanical test results	50
4.3.4	Comparison of test results from different samples	52
4.4	Optical shear measurement	53
4.4.1	Method development	53
4.4.2	MATLAB Digital Image Correlation (DIC) code	53
4.4.3	Simplified cross correlation example.....	59
4.4.4	Evaluation of DIC results	60
4.5	Shear modulus determination.....	64
4.6	Material characterisation discussion and conclusions	68
5	Permeability characterisation	70
5.1	Motivation	70
5.2	Experimental approach	70
5.3	Flow front tracking and permeability calculation	72
5.3.1	Extended permeability theory	73
5.3.2	Development of MATLAB code	74
5.3.2.1	Raw directional permeability calculation	74
5.3.2.2	Data reduction for practical use	76

5.4	Single-ply test results.....	77
5.4.1	Observations	77
5.4.2	Raw results	78
5.4.3	Regression model validation	80
5.4.4	Data reduction and comparison with traditional methods.....	81
5.5	Discussion and conclusions.....	84
6	Infusion modelling	87
6.1	Motivation and software options.....	87
6.2	Modelling Theory.....	88
6.2.1	Multiphase modelling.....	88
6.2.2	Modelling porous media	89
6.2.3	Solution algorithm.....	89
6.2.4	Discretisation and interpolation.....	90
6.3	Model validation.....	91
6.3.1	Simulation of isotropic permeability tests	92
6.3.2	Simulation of anisotropic permeability tests	93
6.4	Comparison of CFX and FLUENT models	95
6.4.1	Mesh dependence.....	95
6.4.2	Time-step dependence.....	97
6.5	Further modelling capabilities	99
6.6	Discussion and conclusions.....	100
7	Complete Process Model (CPM)	102
7.1	Motivation	102
7.2	Extracting information from the draping model	103
7.3	Importing information into the infusion model	104
7.3.1	Recreating the deformed geometry.....	104
7.3.2	Referencing to the distributed properties	105
7.3.2.1	INIT macro function	105
7.3.2.2	PROFILE macro functions.....	106
7.4	Complete Process Model (CPM) demonstration	106
7.4.1	Experimental method.....	106
7.4.2	Simulation approach	108
7.5	Demonstration forming results	111
7.5.1	Material draw-in.....	112
7.5.2	Shear angles	114
7.6	Demonstration infusion results	115
7.6.1	Initial comparison with the Complete Process Model	116

7.6.2	Simulation calibration	117
7.6.3	Results from the calibrated Complete Process Model.....	120
7.7	Multiple ply modelling.....	124
7.7.1	Four ply simulation.....	124
7.7.2	Simulation results.....	125
7.7.3	Evaluation of alternative cases	126
7.8	Discussion	127
7.9	Process model enhancements.....	128
7.9.1	Software consolidation	128
7.9.2	Additional simulation components.....	129
7.9.3	Improved modelling detail and sophistication.....	130
8	Summary and Conclusions	132
8.1	Draping model	132
8.2	Material characterisation	132
8.3	Permeability characterisation	133
8.4	Infusion model.....	134
8.5	Complete Process Model.....	135
8.6	Conclusive remarks.....	135
	References	137
	Appendix A: VUMAT subroutine	145
	Appendix B: Python script	149
	Appendix C: UDF subroutine	152

1 Introduction

The commercial aerospace industry is highly motivated to develop lighter, high-strength structures that are easier to manufacture, machine, assemble and repair. Composite materials such as Carbon Fibre Reinforced Plastics (CFRP) have a specific strength and stiffness superior to the aluminium alloys traditionally used in commercial aircraft [1]. In addition to their high specific strength, carbon fibre composites also exhibit high structural damping, improved fatigue resistance, superior corrosion resistance and high energy absorption capabilities [2]. As such, these advanced materials have been of increasing interest to the aerospace industry for nearly half a century, since their initial development in 1964 at the Royal Aircraft Establishment in the United Kingdom [3].

1.1 History of composite materials in commercial aircraft

The implementation of composites in commercial aircraft has been a lengthy and conservative process. In the 1950s, aircraft such as the Boeing 707 and McDonnell Douglas DC-9 were early adopters, using fibreglass composites first for tertiary components (that had little influence on aircraft operation) and then later for secondary aircraft structures and control surfaces [4]. Until the end of the 1960s, composite parts were mainly manufactured and assembled using the same methodology as traditional metallic components. This proved to be costly and labour intensive, and thus detracted from the potential of carbon fibre reinforced plastics (CFRP) as a structural material. However, intelligent design and co-curing methods later proved that individual composite parts could be manufactured to replace multiple metallic components, and helped minimise the use of tedious fastening methods [3].

From the 1970s carbon fibre composites began replacing the fibreglass secondary structures [4] and other components to the point where, in the mid-1990s, airframes were nearly 15-20% composites by structural weight. Consequently, a critical limit had been reached with these materials, where the main room for advancement and further weight savings was in the development of composite structures for the wings and fuselage.

1.2 Next generation airliners

Today, the state of the art in wide-body commercial airliners, namely the Boeing 787 and Airbus A350, reveal some remarkable advances in composite aircraft structures. Both now include flight-critical fuselage and wing components made from CFRP, totalling more than 50% of the aircraft structural weight. Figure 1 compares the composite composition of these next generation airliners with similarly sized aircraft from the past 40 years and highlights the significance of this material advancement.

Looking at the commercial interest in these next generation airliners with unprecedented use of composite materials, the Boeing 787 and Airbus A350 have become the two fastest selling aircraft of their size [5, 6]. A comparison of the total number of aircraft orders is shown in Table 1, including the number of undelivered orders and the annual average since each aircraft was announced. Despite the immaturity of next generation aircraft, and the limited number of deliveries, their popularity is clear from this data: both the 787 and A350 have an adoption

rate 67% higher than the nearest competitor (the 777) with a comparable number of total orders.

Figure 2 shows the order history for similar wide-body aircraft over the past 40 years. Although there has been a steady increase in most aircraft orders over the years, initial demand for both the 787 and A350 was exceptional, with nearly 1400 combined orders before 2008. At the time, this figure represented nearly 30% of the total aircraft orders in this category, despite the fact that the 787 and A350 were still in development and had not even flown. However, economic difficulties and production uncertainty stalled interest in these aircraft from 2008 to 2012. As deliveries of the Boeing 787 have commenced in the last couple of years, interest has once again continued to grow rapidly. Data quantifying the rate of orders for these next generation aircraft is shown in Table 1, current to January 2014.

Due to the success of the the Boeing 787 and Airbus A350, many other aircraft manufacturers, such as Bombardier, COMAC, Embraer, Mitsubishi and Irkut (the United Aircraft Corporation), are beginning to follow suit, and are committing to similarly ambitious narrow-body aircraft with significant composite structural compositions (Figure 1).

As manufacturers now begin to approach another limit of composites application in aircraft structures, which appears to be the 50-60% mark, there still remains a strong motive to optimise the manufacturing and maintenance processes of composite materials. Many traditional fastening approaches are still used in conjunction with simplistic structural design, and thus the complexity and integration of multiple parts remains a clear priority for future improvements. Affordability, part performance, quality assurance and concurrent engineering are also key challenges to composites manufacturing. However, in recent years technological advances in textile composites and out-of-autoclave manufacturing processes have demonstrated the potential to overcome many of these issues [2].

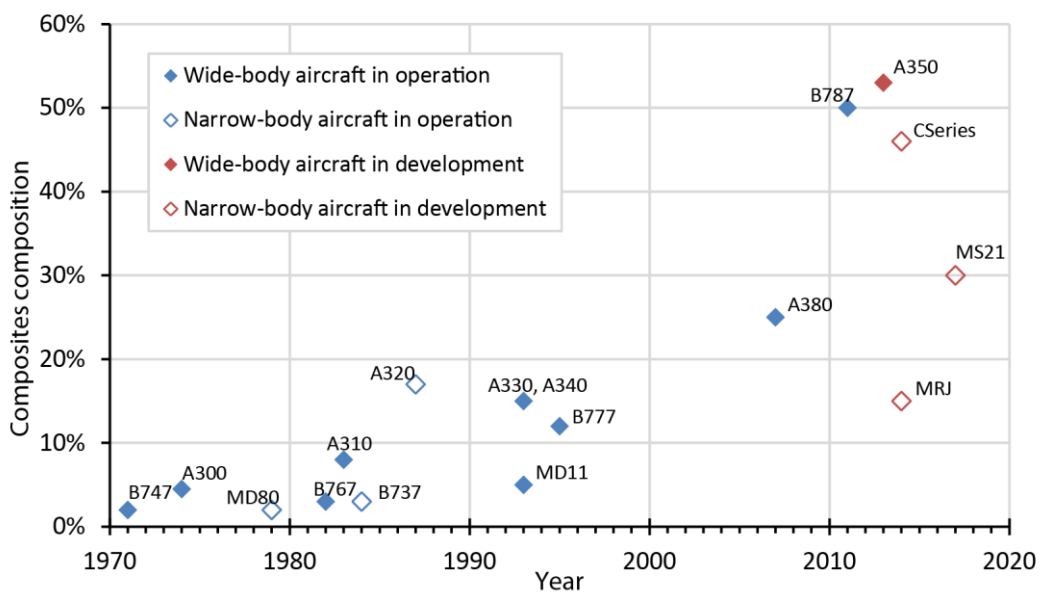


Figure 1: Commercial aircraft integration of composite materials by structural weight [2].

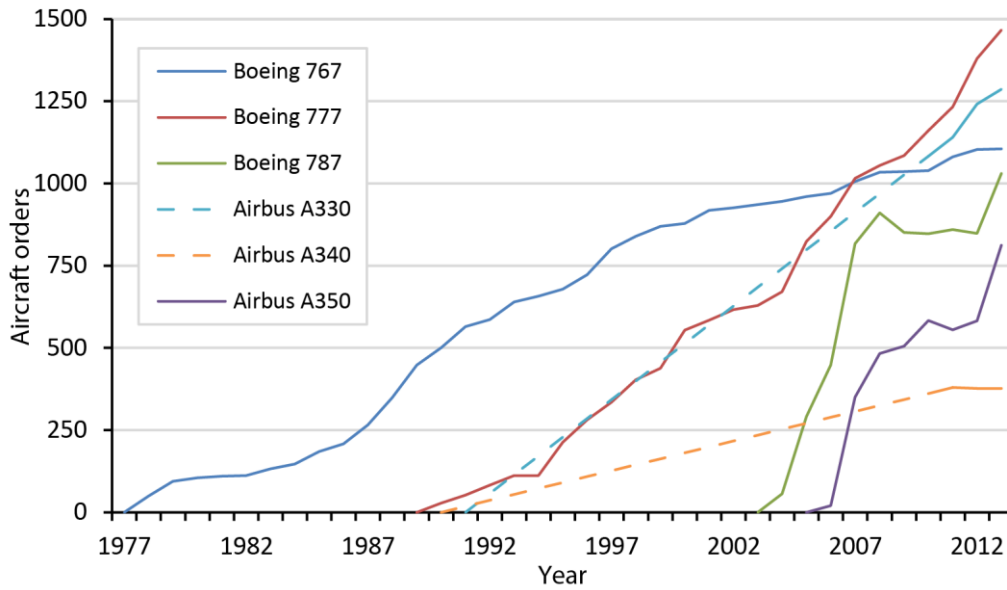


Figure 2: Cumulative orders for similarly sized wide-body aircraft from 1978 to July 2011 [5, 6].

Table 1: Ordered and undelivered wide-body aircraft to January 2014 [5, 6].

	Year announced	Total orders	Undelivered	Mean orders per year
Boeing 767	1978	1105	44	30.7
Boeing 777	1990	1467	303	61.1
Boeing 787	2004	1030	916	103.0
Airbus A330	1992	1286	240	51.4
Airbus A340	1991	377	0	15.1
Airbus A350	2006	812	812	101.5

1.3 Textile reinforcement materials

Currently, carbon fibre composite parts in the aerospace industry are often manufactured using stacked sheets of unidirectional (UD) carbon fibres that are pre-impregnated with resin (called 'prepreg' materials). However, textile reinforcement materials present numerous advantages over traditional UD laminates, despite some reduced stiffness and axial strength (estimated as 10-30% and 15-35% reductions respectively) [7]. Firstly, dry fabrics are easier to handle, and less likely to split or break during layup. Secondly, textile-reinforced composites are tougher: boasting improved impact resistance, damage tolerance and reduced notch sensitivity. Moreover, the out-of-plane mechanical properties are also improved, with greater peel strength and reduced delamination crack growth compared to UD prepregs. Dry fabrics also show superior forming capabilities over complex geometries, fitting double curvature geometries where UD prepregs and tapes fail [7].

The properties and behaviour of textile reinforcement materials are dependent on the mesoscopic fabric architecture, with a large variety of woven, knitted and non-crimp fabrics available. Several of the more common two dimensional woven fabrics are shown in Figure 3, with small 'Repeated Unit Cells' (RUCs) that can tile seamlessly to represent a larger section of material.

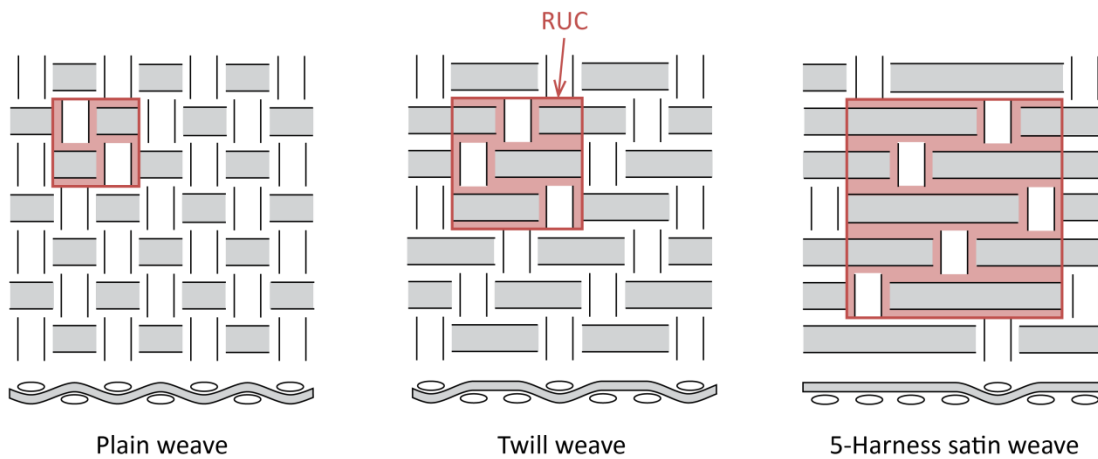


Figure 3: Plain, twill and 5-harness satin weave fabrics with Repeated Unit Cells (RUCs).

Plain weave fabrics are the most stable, with reduced yarn slippage, and are commonly more resistant to shear deformation. This stability and stiffness makes them preferable for flat laminates. Satin weaves, on the other hand, exhibit a high degree of drape and stretch in all directions, and though less stable than plain weaves, they can achieve a higher yarn density, and are thus more common for curved and complex parts in the aerospace industry. Lastly, twill weave fabrics offer a compromise between the properties of plain and satin weaves, draping reasonably well over complex tools and yet remaining quite stable when handled.

Overall, when using fabrics there are a greater variety of options in tailoring the material for its specific role [8]. In conjunction with Liquid Composite Moulding (LCM) techniques, the use of textile reinforcements also facilitates recycling, reduces waste and ensures a longer shelf life for the two separate components than that of the perishable prepregs [2].

1.4 Out-of-autoclave manufacturing

In addition to prepreg material limitations, prepreg processing relies on a costly autoclave to produce the high pressures and temperatures required for consolidation and curing. Subsequently, Liquid Composite Moulding (LCM) techniques are becoming a competitive alternative to the widely used prepreg methodology. They can be performed with a single rigid tool surface, without an autoclave, and are already capable of delivering high quality impregnation and fibre volume fractions near 60%, for a fraction of the capital cost [2]. The growing need for large and highly integrated composite aerostructures is pushing for advances in these out-of-autoclave LCM technologies.

Of the numerous LCM approaches, many of the more popular methods consist of forming dry materials into shape prior to resin infusion. Common names for such processes include: Resin Infusion under Flexible Tooling (RIFT), Vacuum Assisted Resin Transfer Moulding (VARTM), Vacuum Infusion (VI), Vacuum Assisted Resin Injection (VARI) and Seemann Composites Resin Infusion Moulding Process (SCRIMP). Typically, with these methods, dry plies of a fibrous reinforcement material are first formed over a rigid tool. Then a flexible vacuum bag is used to cover and seal the material, and a vacuum is drawn through the enclosed space such that the ambient pressure outside the bag imposes the necessary pressure to hold the shape of the part. Resin is then inlet, flowing slowly through the material before it is finally left to cure.

Such LCM methods originate from the Macro approach that was developed in the 1950s for boat hulls. More recently though, there has been significant interest in refining and applying the process for aerospace applications. Vacuum infusion is ideal for medium to large scale structures, and is capable of producing parts with lower void content than traditional methods, even without a debulking phase [9]. The emission of volatile organic chemicals from the manufacturing process can also be better controlled as all the curing reaction occurs within the sealed vacuum environment [10].

Despite the evident advantages, the reliability and repeatability of vacuum infusion manufacturing processes still pose some concerns when it comes to industrial application. They rely heavily on operator skill and experience in a trial-and-error process. Hence, an unnecessary amount of time, effort and material is wasted on failed attempts and flawed designs. However, this is a problem that process modelling aims to overcome in a cost effective manner.

1.5 Process modelling

In recent years, computer simulation has grown as a means of substituting costly experimental testing, particularly in fields like structural analysis. For manufacturing though, numerical modelling is still uncommon, and any flaws must be identified through experimentation. Predictive modelling also provides the opportunity for rapid prototyping and part optimisation prior to the need for any physical testing. However, the high degree of complexity and requisite expertise for such modelling efforts has precluded the use of sophisticated simulations in industry.

The simulation of textile reinforcements can be quite demanding since the material behaviour is characterised by phenomena at three different scales. Typically, these hierarchical levels are categorised as: macro, meso and micro pertaining to the levels of entire part geometry, internal textile architecture and individual fibres respectively. Purely macro-scale modelling is the simplest, and generally quickest, approach [11]. Meso-scale simulation attempts to recreate the complex yarn geometries and interactions, hence it is computationally expensive and limited to smaller parts. Lastly, micro-scale modelling focuses on the distribution and interaction of the fibres within yarns, thus it is the most ambitious of the three, and generally not feasible for a full scale simulation.

There has been considerable study in various modelling methods for composite materials manufacturing, although a comprehensive simulation of the draping and infusion process has not been demonstrated. Modelling approaches like Finite Element Analysis (FEA) and Computation Fluid Dynamics (CFD) can become quite complex, often requiring extensive knowledge of multiple software packages or programming languages. Subsequently, much of the work is currently limited to academia [12], underlining the need for relatively simple and accessible analytical tools for the transition to the aerospace industry to become possible.

1.6 Research objectives

In light of the weight saving transition to composite materials, and the evident advantages of fabric reinforcements, vacuum infusion methods, and process modelling; this research has been undertaken to enhance the manufacture of aircraft structures in the aerospace industry.

By replacing much of the tedious physical testing required for airframe development with comprehensive models, manufacturing can be performed at a reduced cost. However, the difficulty currently lies in simulating the draping process and its effect on resin infusion. Hence, this research was performed under the following objectives:

- To develop a realistic draping simulation for complex parts, incorporating yarn direction tracking and experimental material characterisation.
- To characterise permeability in relation to fabric shear deformation.
- To employ an infusion model using the results from draping and the distributed permeability to demonstrate the Complete Process Model (CPM).

In fulfilling these aims, the Complete Process Model has been devised from a number of components shown in Figure 4. Work is divided into three main areas: the draping model, material characterisation and the infusion model. Full details of the significance and development of each aspect are provided in the following chapters of this thesis.

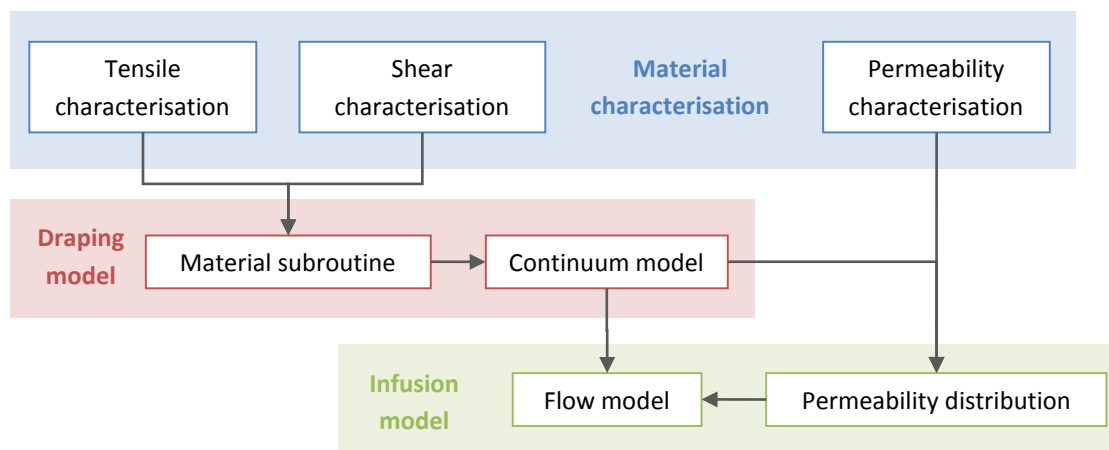


Figure 4: Complete Process Model (CPM) diagram.

1.7 Thesis outline

Following this introduction, Chapter 2 discusses each of the core concepts that serve as the foundation to this research. It is primarily a review of relevant literature and the current state-of-the-art for simulating fabric draping, material characterisation and infusion modelling.

Chapter 3 focuses on the development of a continuum-based Finite Element (FE) draping model as the first major component of the CPM. This chapter includes an evaluation of two different subroutines for replicating fabric behaviour that have been developed in house. There is also a comparison of the modelling results with previous simulations and experiments from literature for validation purposes.

The characterisation methods of mechanical material properties are outlined in Chapter 4, specifically tensile and shear fabric behaviour. Detailed properties are determined for the aerospace-grade carbon fibre plain weave fabric that is specific to this research. This chapter also contains a notable section on the development of a new Digital Image Correlation (DIC) approach for optical strain measurement that enhances the bias extension shear test.

Chapter 5 explores the relationship between permeability and shear deformation, starting with the experimental methods for permeability characterisation. A novel, low-cost, process for comprehensive permeability characterisation is also outlined in detail, along with experimental shear angle and permeability relationship results for the carbon fibre plain weave material.

The development and demonstration of a Computational Fluid Dynamics (CFD) approach for simulating infusion is shown in Chapter 6. Two different software packages are evaluated for the infusion modelling component of the CPM. Validation is achieved against the flow data from the permeability experiments discussed in the previous chapter.

The work in Chapter 7 illustrates the difficulties in combining all the individual elements from the previous chapters into a Complete Process Model for a novel and sophisticated simulation of vacuum infusion manufacturing to be possible. Emphasis is on linking the results of the draping model into the infusion model. The sophistication and capability of the model is demonstrated by comparison with traditional models and experimental infusion results. A discussion of the future potential of the model is also included in this chapter.

Lastly, Chapter 8 provides a summary of the whole thesis, highlighting the background, methods and findings from each chapter along with some conclusive remarks on the significance of this work.

2 Review of LCM process modelling

From an industrial perspective, there has been a particular effort to develop an ‘integrated design tool’ which combines manufacturing, infusion and performance aspects of a textile-reinforced composite component using several different software packages [12-14]. This chapter highlights and discusses the prominent literature in the field of LCM process modelling with textile reinforcements, by identifying the work from several distinct areas that each contribute to this vision.

The first stage of an LCM manufacturing process with textile reinforcements involves the physical forming of dry fabric material over a tool. This draping process can be modelled using a variety of methods that are documented in the following section of this chapter. In support of the draping simulation, to help replicate the true fabric behaviour, material characterisation is generally required. Ongoing research in this field is discussed in Section 2.2. Methods for determining fabric permeability are integral to infusion modelling and are outlined in Section 2.3, with emphasis on local permeability changes that result from the physical draping process. Finally, methods for simulating resin infusion into a dry reinforcement are outlined in Section 2.4.

2.1 Drape modelling

The physical draping of textile preform materials over complex tooling has long been studied, not only from a composites manufacturing perspective, but also by the apparel and, more recently, animation industries. The simulation of draping has proven to be quite difficult though, particularly from a purely mechanical perspective where the warp and weft yarn directions of a textile often exhibit a very high tensile stiffness but are susceptible to reorientation. This reorientation is made possible in textile reinforcement materials due to the relatively weak resistance to shear and bending modes. Hence, for a draping simulation to be successful, it is most important to capture this reorientation of yarns under shear loading [15].

The change in angle between fibre yarns, as a fabric deforms to fit a complex geometry, is commonly termed the shear angle, γ (Figure 5). Locally, it changes the material behaviour; as the shear angle increases, the two initially perpendicular yarns slowly begin to align and ‘lock’. As a result of shear locking there is a dramatic increase in shear stiffness that can induce lateral compaction under increased loading and result in out-of-plane buckling behaviour, or ‘wrinkling’. Generally, when modelled, this out-of-plane bending behaviour is neglected, as it is particularly difficult to emulate. Similarly, yarn slippage at higher strains is also problematic and not currently modelled, although in some cases it can be included merely as an inseparable behavioural component of the material characterisation.

Although the tensile properties tend to perform a secondary role to the shear behaviour in draping, highly detailed models that try to capture the tensile crimp interchange (the influence of tensile forces in one yarn direction on those of the other yarn direction) need to be biaxial and require more complex characterisation and implementation.

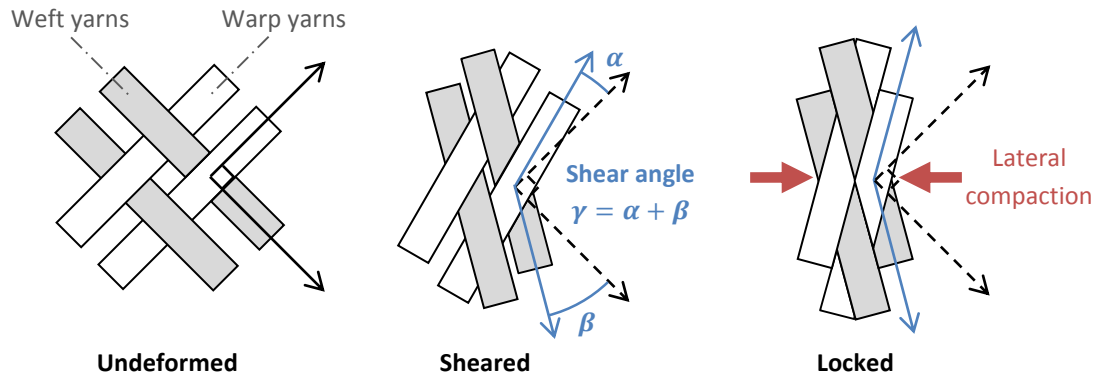


Figure 5: Plain weave Representative Unit Cell (RUC) illustrating different states of shear deformation.

Early modelling was analytical, using geometric mapping-based schemes with some non-mechanical, particle-based approaches appearing in the 1990s that saw reasonable success outside of engineering applications. Among the more popular approaches employed today, continuum based methods have been achieving sufficient fidelity with a relative simplicity and efficiency. Alternatively, detailed discrete and semi-discrete approaches (as discussed in Section 2.1.3) are also becoming popular as computational capacity increases. These are also showing great promise but, in many cases, remain limited to smaller scale simulations.

As the capabilities of numerical modelling and computational power keeps advancing, the study of complex phenomena (that have been previously ignored) is slowly becoming possible. Wrinkling, in particular, poses a significant problem during manufacturing and development of parts in industry, and is a behaviour that has been largely neglected in the past. Recently though, some studies have emerged in various fields to try to characterise and realistically simulate this phenomenon; resulting in varied applicability and success. One group of researchers has characterised the nature and severity of wrinkling in stretched thin sheets with some thorough numerical scaling analyses [16]. Another group however, has managed to develop a draping model for composite reinforcements that can reasonably replicate the wrinkling phenomenon during forming through the inclusion of appropriate bending properties [17]. In most cases though, it is sufficient to use a more basic model to identify areas where wrinkling could become a problem and instead optimise the manufacturing approach to avoid them entirely. The following sections summarise some of the pertinent draping models identified in literature.

2.1.1 Geometric mapping and particle based methods

Early modelling techniques for tracking fibre orientation during forming processes were geometric mapping based schemes. First described by Mack and Taylor in 1956 [18], these models represented the fabric as a pin-jointed net, with yarns assumed to be inextensible and fixed at crossovers, such that they were free to rotate over each other without slipping. In the last 25 years, these geometric models (also known as fishnet or kinematic models) have been replicated through numerical simulations with increasing sophistication [19]. They are simple, fast and fairly efficient, however they have limitations. Firstly, they do not account for static boundary conditions or tow-level deformations (like yarn slippage, decrimping or internal compaction due to tool pressure) and they have difficulty predicting mechanical phenomena

such as stresses. Additionally, they do not incorporate the effects of shear locking, wrinkling or processing conditions and may not find feasible solutions for parts with holes, bridges or non-uniform curvatures. These are considerable limitations for engineering applications where the primary purpose of modelling is often stress analysis of complex structures. Hence, these methods have been quickly dropped from favour.

In the 1990s an alternative, particle-based fabric simulation method was developed, primarily for the computer animation and apparel industries [11]. This method represented fabrics as discontinuous sheets of micro-mechanical structural elements, termed ‘particles,’ incorporating limited material properties. A model by Breen et al. [20] was most notable, with energy-based particle interactions and asymmetric permutations providing simulations with seemingly realistic textile behaviour. However, this method focused on appearance rather than deformation or stress, and thus does not seem to have been pursued for technical applications, instead being used for real-time simulation in interactive media [11]. These approaches are now largely neglected in preference of the continuum and discrete methods that are able to achieve greater realism for engineering applications.

2.1.2 Continuum methods

The continuum simulation of fabric draping was originally presented in literature as simply an extension of common metal forming processes, like deep drawing or diaphragm forming [21], which had seen extensive FEA study. Continuum-based models for textile reinforcements rely on the simplification of the fabric at the macro-scale, homogenising the complexities of the fabric architecture. This allows for the use of standard finite elements (typically shell or membrane elements) to perform the modelling, and hence, the accuracy of the simulation depends mostly on the material characterisation and constitutive model used for the homogenised fabric. Though typically deemed reasonable [22, 23], these models also assume that there is no significant sliding between fibres and generally neglect out-of-plane behaviour.

Constitutive models for continuum simulations of fabric reinforcements are varied in literature, focussing on tracking and updating the fibre orientations as the fabric deforms, using non-orthogonal or anisotropic formulations. These updating material behaviour laws subsequently show improved results over simple orthogonal methods. This is because, as shear is applied to the fabric material, the yarn orientations will not remain orthogonal, but will instead rotate in-plane relative to each other, with the magnitude of rotation determined by the shear angle (see Figure 5). Two of the more successful approaches in literature for constitutive modelling of fabric reinforcements are the hyperelastic and hypoelastic models, which represent the current state-of-the-art in continuum-based methods.

Hyperelastic methods are based on the calculation of stress from a strain energy functional [24], and are typically used for materials that behave elastically in response to very high strains. These constitutive models account for large deformation, anisotropy and non-linear elasticity making them reasonable for the simulation of fabric reinforcement material behaviour, even though they are more commonly used for rubbers or elastic foams. Work by Ten Thije et al. [25] shows a method developed by Huétink [26], derived from the Helmholtz free energy theorem. Similar to many hypoelastic models, accurate tracking of multiple fibre directions is possible with this method, where the traditional Jaumann or Green-Naghdi approaches

(commonly used in Finite Element Analysis (FEA) packages) merely provide approximations [25].

Hypoelastic models, on the other hand, relate stress increments directly to strain increments with a constitutive tensor containing the material moduli [24]. These focus more on materials that exhibit reversible non-linear behaviour and are often used in finite element analyses at large strains [27]. Though more typically used for isotropic materials, there have been some non-orthogonal models, including those by Yu et al. [28] and Xue et al. [29], set up in conjunction with these hypoelastic laws for fabric reinforcement simulation. Several research groups have studied the potential of these approaches [22, 30], limited in some cases to meso-scale modelling and tracking of a single fibre direction [27]. More recent work has shown validation of the technique for full scale thermoforming simulation of bi-directional composite fabric reinforcements [31-33] (see Figure 6), proving the potential of this continuum modelling approach for composites manufacturing.

Although most of these continuum approaches reduce the complexity of their models by representing fabric sheets with membrane elements, shell elements have also been used for their ability to incorporate some bending behaviour in the form of an asymmetric axial modulus [30]. However, some issues with the current models remain. For example, hypoelastic models do not always allow for complete recovery after a closed loop loading path (though hyperelastic models typically will). Additionally, despite the advances and widespread use of continuum-based methods, none can realistically simulate many of the more complex interactions that occur within the fabric architecture, such as yarn slippage. Hence, for even more detailed simulations of textile draping, discrete and semi-discrete approaches have also been developed.

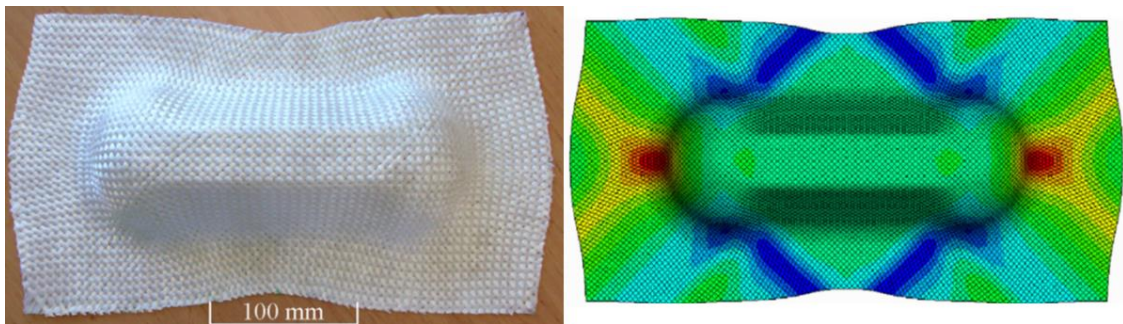


Figure 6: 'Double dome' forming simulation by Khan et al. [31] using a continuum finite element method.

2.1.3 Discrete and semi-discrete methods

Modelling approaches that physically represent the structure of the textile reinforcement at the meso or micro-scales are often considered to be 'discrete' or 'semi-discrete', as the degree of homogenisation is greatly reduced, and the material is no longer being represented as a simple continuum sheet. In these methods the focus of simulation is on representing the arrangement and interaction of the discrete yarns or fibres. Due to the complexity of fabric architecture, and the sheer number of fibres in yarns, these methods are also subject to various degrees of simplification and assumptions before feasible models can be implemented. In many cases the fibres or yarns are represented by beam or truss elements, with interactions

and shear effects sometimes modelled by springs [34]. These approaches still typically neglect yarn slippage and do not realistically account for bending behaviour. Thus, similar to the continuum models, they can overestimate stiffness for applications where slippage can become significant, such as the ‘bias extension test’ [34]. However, conditions for real forming applications are likely to experience less yarn slippage than such idealised characterisation experiments.

Researchers have also modelled individual fibres as beams with complex interaction and contact algorithms as seen in Figure 7. This approach relies on an enriched kinematic beam model with the aim of overcoming issues with large rotations and cross-sectional deformation that can arise from the use of basic beam models [35]. The strength of this work is in the sophisticated fibre friction and contact modelling at the micro and meso scales that results in the simulation of macro scale fabric behaviour. Nevertheless, these models are still limited to smaller scales (8 tows of 48 fibres, significantly below the several thousand necessary to completely model every fibre in a single reinforcement yarn [35]). This state-of-the-art method shows potential because the assumptions of material continuity are restricted to only the individual fibres, hence it can simulate yarn (and even fibre) slippage along with macro scale tensile, shear and bending behaviour. However, it loses practicability, due to high computational expense, for larger scale applications. Furthermore, this type of discrete modelling may also neglect some unforeseen material phenomena, since only the fibre beam and interaction behaviour is simulated. Particularly as these properties are not easily characterised and subsequently rely on qualitative approximation.

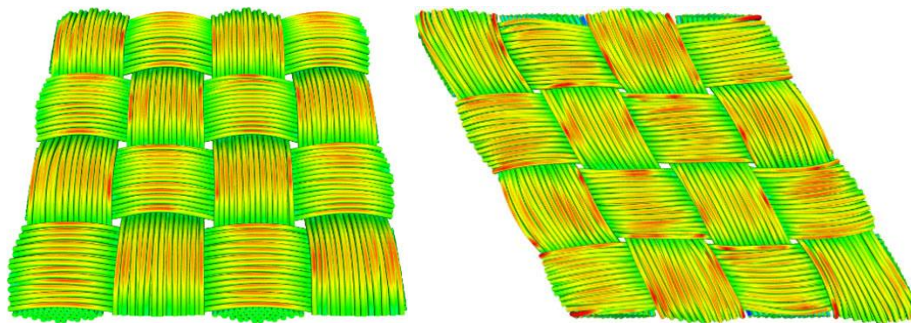


Figure 7: Example of a discrete fibre model by Durville [35], before and after shear deformation.

Other discrete approaches use similar principles at the meso-scale, where tows are represented by truss elements joined at crossovers within Repeated Unit Cells (RUCs). Alternatively, several researchers are simulating the yarns within the RUCs with 3D solid elements [27, 36]. With appropriate definition of yarn deformation and contact interactions these approaches could offer potential for realistic modelling that also predicts yarn slippage. However, the required number of elements and subsequent computation times for these discrete methods are again a major limitation. Therefore it is not yet a practical method for simulating an entire part, although it is being used as a method of material characterisation for continuum modelling [37].

Combining these discrete methods with continuum FEA practices has lead researchers to pursue semi-discrete methods where the fabric is represented as a continuous sheet of specialised elements, each made up of a discrete number of woven unit cells [38]. These

methods return to the assumption of no sliding between yarns, but can perform a rather efficient simulation of fabric behaviour with a less comprehensive material characterisation regime than is required for continuum modelling, and have even been developed to include bending effects [39] for better wrinkle characterisation [17]. Such semi-discrete approaches aim to avoid the use of stress tensors and instead define unit cell loading from the yarn tension, in-plane shear and bending. Researchers with experience working on a range of fabric simulation methods report their semi-discrete approach to have the greatest success [40]; though it comes at the cost of considerable complexity.

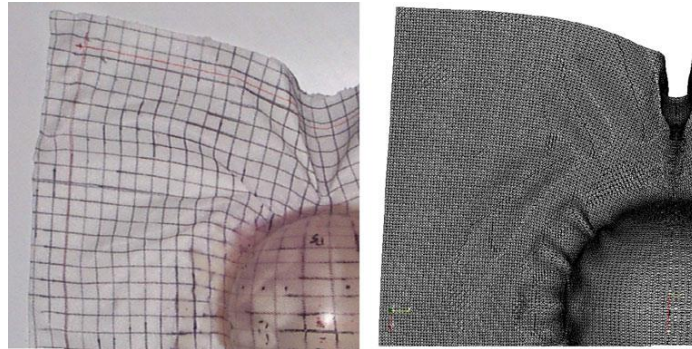


Figure 8: Experimental hemisphere forming and a semi-discrete simulation [40].

Ultimately, whichever of these approaches is adopted in the simulation of fabric reinforcement draping, there is typically a need for supporting experimental material characterisation to create a valid model.

2.2 Determination of mechanical properties

The material characterisation requirements of each simulation approach depend on the fundamental theory and assumptions of the chosen technique. For a discrete micro-scale model, where only the individual fibres (or small groups of fibres) are being modelled, the elastic properties of the fibres are required, along with any contact interactions. In the meso-scale, whole yarns are typically considered to be homogenous, in which case yarn behaviour and friction need to be determined. Generally for macro-scale models, in-plane shear is considered to be the dominant mechanism of fabric deformation [41]. Tensile properties are also significant due to the very high stiffness of yarns (particularly for carbon fibre materials). Bending stiffness is often neglected in the existing literature, since it is very small in fabric materials. However, it has been identified as influential to the shape of wrinkles in association with the shear properties [42]. Compaction is of greater significance during the infusion process, as it affects resin flow in addition to the ultimate fibre volume fraction and part quality [43].

There are two common approaches of material characterisation for establishing homogenised properties across the textile. The first relies entirely on experimental work; the second combines simplified meso-scale modelling with reduced experimental testing as an alternative [37]. The latter approach is preferable when studying fibre architecture during the design process where changes to the fabric weave can be quickly implemented and incorporated into a new simulation. The first approach consisting of only experimental work aims to characterise an existing fabric, reduces the modelling complexity, and requires only a few mechanical test

methods. However, if new fabrics are to be used or altered it does require further experimentation.

2.2.1 Experimental material characterisation

As previously noted, the tensile and shear properties are considered to be the most influential parameters on draping simulation for continuum modelling. Hence, it is typically the shear and tensile moduli of these fabric reinforcement materials that need to be experimentally determined. There are a number of challenges in working with, and testing, textiles though; primarily caused by the loose nature of the material, which facilitates unravelling, fraying and yarn slippage during handling. Cutting and mounting of material samples must be performed with great care in order to preserve the state of the fabric architecture and yarn orientations prior to testing. Free edges (at material cuts) need to be monitored carefully to ensure minimal interference where yarns can easily unravel. Due to these complications there is a lack of standardisation in the field, and a variety of competing experimental techniques have been used to determine both properties. Furthermore, bending characterisation is also gaining in popularity as modelling requirements increase.

2.2.1.1 Tensile methods

Due to the nature of fabric reinforcement materials, standard tensile coupon tests are not applicable and alternative methods need to be employed. A primary concern is the susceptibility of these materials to damage, and deformation during handling, however there are also further challenges specific to tensile testing. For carbon fibre fabrics in particular, tensile loads are incredibly high, meaning that the clamping forces need to be very strong in order to prevent any specimen slippage.

In practice, there are a few competing approaches for tensile testing, although biaxial testing is popularly performed for tensile characterisation due to the interconnected nature of the warp and weft yarns in a fabric [37]. In this method, square or cruciform shaped specimens are gripped at all four sides with various loading ratios in the two perpendicular directions as shown in Figure 9, recording a complete tensile curve for the material response. Experimental rigs for biaxial testing are challenging to set up, particularly since they need to accommodate the very high tensile strength of yarns for a range of warp/weft loading ratios. Though extensive, there is a lack of standardisation for the biaxial approach, leaving uniaxial tests such as the 'grab' [44] and 'strip' [45] tests as another option under the assumption that biaxial behaviour is negligible. Both of these standardised approaches require fabric specimens to be clamped and loaded axially, parallel to either of the principal fibre directions, observing the load and displacement relationship during testing. However the grab test uses a sample wider than the clamp width and reduces the effect of free boundaries, as seen in Figure 9. However, since these tests are uniaxial, they are unable to account for biaxial phenomena such as crimp interchange and are therefore only reasonable for applications where biaxial behaviour is not significant.

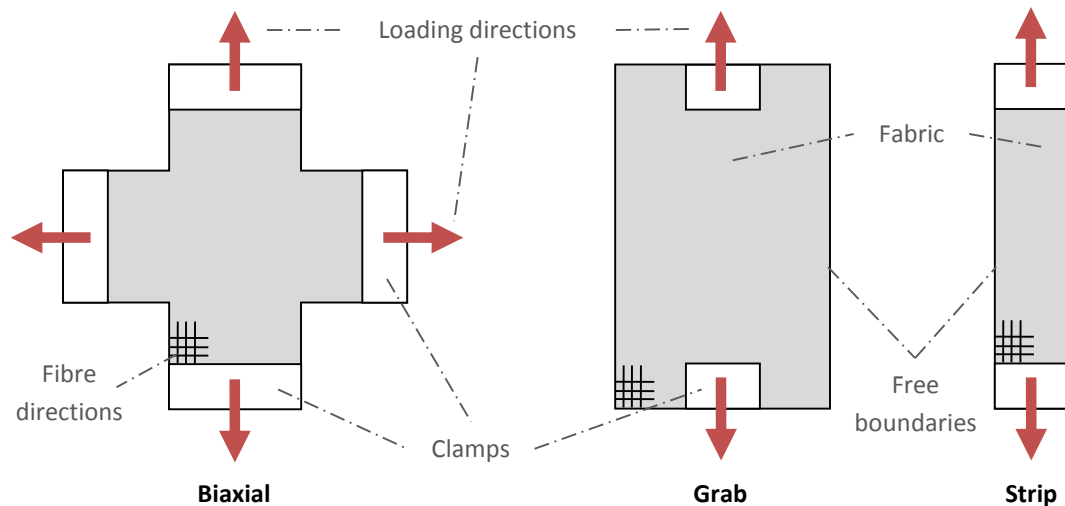


Figure 9: Biaxial, grab and strip tensile test methods.

2.2.1.2 Shear methods

The shear behaviour of fabric reinforcement materials tends to be highly non-linear under relatively low loading. This is due to the finite trellising of the warp and weft yarns, after which yarns become ‘locked’ and resistance to shear deformation greatly increases. Since shearing loads are so small in the undeformed state, mechanical tests are particularly sensitive to manual handling, which poses further difficulty to the selection of an appropriate method.

Historically, in shear testing, the Kawabata simple shear test has been used [46], although its application is limited to small shear deformation (only up to 8° shear angles in one case [47], far below the 50° angles achieved with other methods in the same study). The ‘picture frame’ test has more recently been adopted, where square or cruciform samples are clamped into a deformable trellis shaped rig [48], as shown in Figure 10. This approach shows reasonable repeatability and offers homogenous deformation behaviour but requires a specialised rig that must be carefully developed to ensure that the fabric clamping method does not negatively affect testing. It has been observed that induced tension from clamping and misalignment pose problems for the picture frame method [49].

Additionally there is a third method used by many researchers called the ‘bias extension’ test, which operates in the same fashion as uniaxial tensile testing, however samples are cut and oriented in the ‘bias’ direction, such that the warp and weft yarns are $\pm 45^\circ$ relative to the loading direction (see Figure 10). This approach is highly repeatable, only requires a simple rig, and does not have the same tension and clamping problems as the picture frame test. It has also been shown to have good agreement with the low range results of the Kawabata Evaluation System shear tester [47]. However, since the test samples exhibit heterogeneous shear deformation and often experience yarn slippage, optical strain measurement techniques are usually required for accurate results [49]. Figure 11 displays this heterogeneous shearing behaviour, where samples tend to reveal three distinct regions of varying shear deformation. Notably, region ‘C’ experiences no shear deformation since the yarns in this area are confined by the clamps. Region ‘A’, on the other hand, exhibits a pure shear deformation and is the primary region of interest. Lastly, the areas labelled ‘B’ (between regions ‘A’ and ‘C’) commonly

experience shear angles half of those in region 'A'. A further criticism of this approach is that these tests are often limited to a smaller range of shear angles because of yarn slippage [49].

Again there are no standard shear characterisation methods, despite ongoing work by an international collaborative effort to establish testing benchmarks [50], and as such the method choice may require further validation.

Recently a detailed study has also looked at the coupling of shear and tensile properties using a modified biaxial bias extension test to introduce varying transverse loads. The findings showed that additional tension in the yarns influenced the shear behaviour, and by increasing transverse tension, the onset of out-of-plane buckling (wrinkling) could be somewhat mitigated [51].

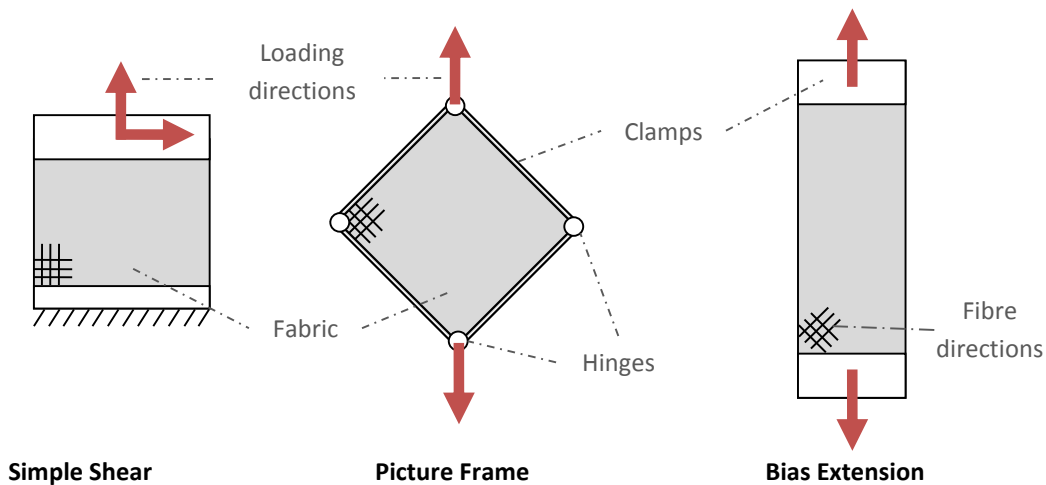


Figure 10: Comparison of the three main shear testing approaches: simple shear, picture frame and bias extension.

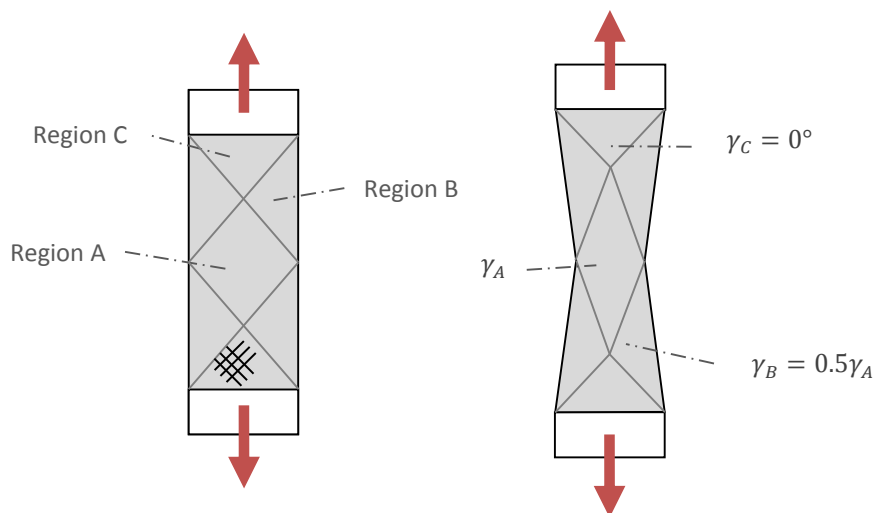


Figure 11: Heterogeneous deformation in bias extension testing.

2.2.1.3 Bending methods

More recently, the study of composite reinforcement bending behaviour has gained popularity as a result of the growing desire to simulate wrinkling. The bending behaviour of fabric

reinforcement materials is known to exhibit hysteresis during loading and unloading as a result of friction among the yarns and fibres [52, 53]. Thus, the traditional cantilever bending tests that assume the material to have linear elastic bending behaviour are not realistic. Similarly, the Kawabata Evaluation System Bending Test for Fabrics (KES-FB2 test) that was designed for testing clothing materials is not often suitable for thicker and stiffer composite reinforcement textiles.

Hence, a replacement test has been devised [52], using a combination of basic mechanical and optical measurement techniques based on the original cantilever model, to measure curved deflection and characterises non-linear and non-elastic bending behaviour. The recent work on biaxial bias extension testing for shear-tension coupling by Harrison et al. [51] has also been used to demonstrate an alternative means of inversely characterising bending properties by fitting several parameters into a bending stiffness model. Though such an approach has not been validated.

In some cases, performing these tensile, shear and bending tests can be quite involved, and some research is turning instead to meso-scale simulation for the purpose of characterisation. When multiple fabric weaves and types are under consideration, simulations serve as a more efficient and economical option.

2.2.2 Simulating fabric behaviour

For simulated material characterisation, the aim is to model the underlying structure of a fabric in order to determine the macro-scale behaviour. This involves setting up detailed models of yarn geometry and architecture at the micro or meso-scale, typically using Representative Volume Elements (RVEs) or RUCs [54]. Often this work is facilitated by external software packages such as TexGen [55] or WiseTex [56], which can quickly generate fabric geometries for subsequent modelling. These meso-scale models also require some experimental material characterisation, although this is typically just the tensile properties of the yarn and an approximation of yarn interactions. In practice, small scale 3D simulations have been performed to characterise biaxial tensile properties, showing reasonable agreement with experiments [37, 57].

These approaches tend to add complexity to the entire process, as work needs to be performed in, and integrated between, several software packages, with the persisting need for some experimental testing. However, it is most applicable in the development stage of textile reinforcement parts, since alterations in fabric architecture can be rapidly studied without the need for an entirely experimental characterisation process.

2.3 Fabric permeability

In order to model resin infusion, several key properties need to be determined for the fluid and fabric material. For Newtonian fluids travelling at low velocities, Darcy's law is commonly used to describe the flow behaviour. Here \mathbf{v} is the phase-averaged flow velocity, \mathbf{K} is the permeability tensor for the material, μ is the viscosity of the fluid, and ∇p is the pressure gradient:

$$\mathbf{v} = -\frac{K}{\mu}\nabla p \quad (1)$$

The viscosity of the fluid can easily be determined as a function of temperature according to various standardised methods [58]. Similarly, the pressure gradient is able to be monitored and controlled in most processes. However, fabric permeability poses a much greater challenge in its determination, where Darcy's law provides only a macroscopic continuum description of the flow behaviour through a porous material.

Permeability is a measure of how easily fluid flows through a porous material under the influence of a driving pressure gradient. Despite being well documented and summarised in recent years [59], there is still no standardised method for permeability characterisation. The competing experimental approaches currently in use also show great variability, as highlighted by initial benchmarking attempts [60]. Although the internal geometry of textiles seems conveniently periodic, the flow through these materials is quite complex because it occurs at two different scales: viscous flow in macropores between the yarns, and capillary flow (related to surface tension) in the micropores between the fibres within each yarn [61]. Furthermore, the weaving process actually results in a stochastic distribution of tow geometry and spacing in fabrics, which undermines the repeatability of permeability characterisation testing. Although most applications focus on planar testing, and negate through-thickness effects, transverse permeability also adds further complexity. Often, the in-plane permeability properties of textiles are actually anisotropic, so flow needs to be defined for at least two principal directions. This anisotropy is also enhanced when the material is sheared or deformed. If multiple layers are stacked, nesting effects will also greatly influence fluid flow [62, 63], further compounding on the stochastic nature of the material. Subsequently permeability should be considered as a statistical estimate for fluid flow through a porous material, rather than a clear deterministic value. As a result of all these difficulties, initial benchmarking exercises observed large variations in results, not only in tests performed by different lab groups (with results varying by a whole order of magnitude) but also internally using the same methods (with relative standard deviations over $\pm 30\%$) [60].

Permeability is typically characterised experimentally, although there is also growing interest in the development of predictive models for permeability estimation [64-66]. Newer predictive permeability modelling offers significant improvements in efficiency [13], however these methods tend to oversimplify and merely approximate the real flow behaviour through porous textile materials. Stochastic variables can be simulated as well (such as tow spacing and nesting)[67, 68], however the validity and accuracy of these approaches is difficult to demonstrate without extensive experimental testing. Hence, the experimental approaches remain widely practiced and well established, despite being time consuming and having repeatability issues.

2.3.1 Experimental permeability characterisation

There are two main experimental approaches for in-plane permeability characterisation that are widely practiced by monitoring fluid flow through the material, even if neither has been adopted as a standard. The first method, using linear flow experiments, is designed to restrict flow to one dimension, such that the fluid travels evenly down the length of a rectangular sample with a perpendicular flow front. In order to achieve this, the fluid needs to be

introduced evenly along the complete width of the sample. Alternatively, two-dimensional ‘radial’ flow experiments are performed with a small circular inlet at the centre of samples and fluid is observed to flow radially.

These basic methods can be run with either saturated (pre-wetted) or unsaturated (dry) material. For saturated samples using either approach, the determination of permeability using Darcy’s law [69] relies on measuring the mass flow and fluid density in order to calculate the fluid flow rate. For the unsaturated (dry) samples, the flow front is measured as a function of time, and permeability is calculated based on the Laplace-equation derived from Darcy’s law and the continuity equation for incompressible flow [70].

A further consideration is whether to run tests using constant pressure or constant flow rate control. Under a constant pressure control scheme, the variable inlet speed can become undesirably slow (meaning the fluid flow may be dominated by surface tension effects in the form of capillary flow, rather than viscous flow). Though conversely, using flow rate control to achieve a constant flow rate, the required pressure gradient can become unreasonably high.

Linear methods typically exhibit better repeatability, as has been demonstrated by the latest international benchmarking exercise where principal permeability values characterised by seven different institutions resulted in a relative standard deviation of around $\pm 20\%$ [71] (a significant improvement on the results from several years earlier [60]). However for anisotropic fabric materials, a large number of tests are required. When the anisotropy of the material is not known prior to testing, experiments need to be carried out in at least three different orientations (0° , 45° and 90° relatively), such that the two principal permeability values (K_1 and K_2) and the principal permeability direction (φ) can be found (Figure 12). When the principal permeability directions are known *a priori*, tests are only required in those two orientations, although all tests need to be repeated a number of times to ensure that results are consistent.

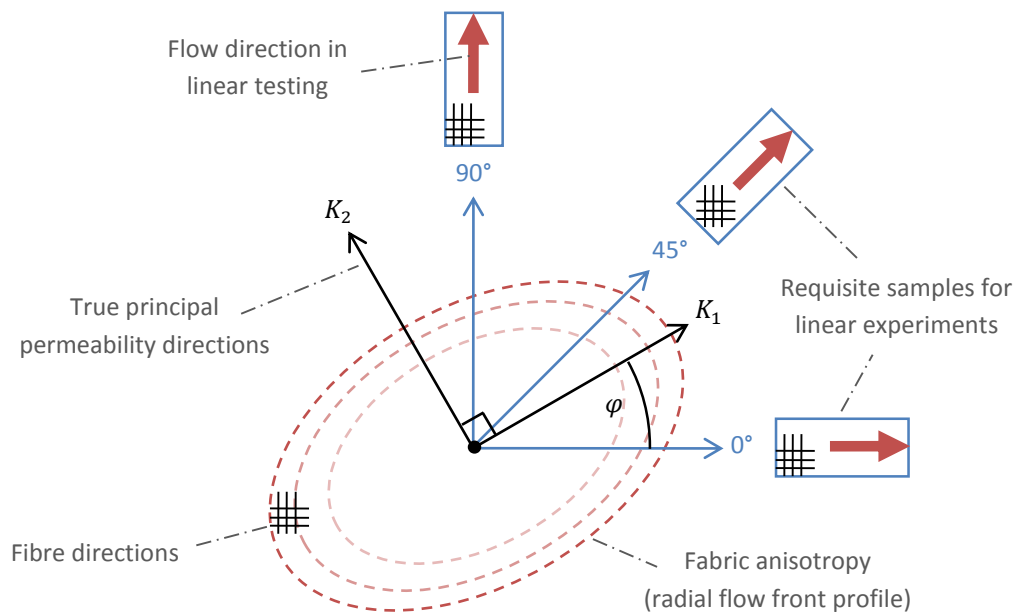


Figure 12: Linear testing of anisotropic permeability in textile materials.

Linear experiments are also prone to ‘race-tracking’ at the sample edges, where gaps or edge effects can undesirably enhance the flow such that it advances non-linearly. Radial permeability experiments instead monitor 2D flows through planar samples, with fluid flowing radially in all directions from a small central inlet. Hence, there are not the same race-tracking issues as radial experiments do not rely on a linear flow front and there are no free edges for race-tracking to occur.

Radial testing is predominantly run with unsaturated samples and the permeability is typically calculated based on flow front measurements rather than an outlet mass flow rate. This method allows for the determination of anisotropic permeability from a single test (although multiple tests are still required to analyse the consistency of the results), but is not suitable for monitoring full 3D or through-thickness flow. The advancing planar flow front can be measured in all directions, and captures the full 2D anisotropic behaviour of the material. However this means that tests can be difficult to control and often exhibit greater variability than linear experiments [72].

These two competing experimental approaches have been summarised extensively in recent literature [59, 60]. Overall a large variety of measurement techniques have been employed over the years for both approaches. Most commonly, the displacement of the flow front is monitored either visually [73], using fibre optics [74], or with sensors (thermistors [75], electronic resistance, ultrasonic waves, or pressure sensors [76]). However, it is important to note that due to the conductivity of carbon fabrics, electrical sensors are not suitable for testing such materials. Furthermore, inclusion of many of these sensors (or necessary wiring) can negatively influence fluid flow or cause race-tracking. Determination of the mass flow rate for saturated tests can be done by measuring the outlet fluid flux and the pressure field using pressure transducers.

Ultimately though, the most simple and prevalent method for monitoring the flow front is by using cameras [72, 73]. In such a case, at least one of the tool faces for the experiment must be transparent. Subsequently, to ensure the cavity thickness remains constant and the tool surface is not deflecting under the imposed pressure gradient, the transparent tool must be sufficiently stiff or well supported. Despite the academic interest in this field, there is still no clearly preferred method, and experimental permeability characterisation remains unstandardised.

2.3.2 Predictive modelling

Due to the repeatability issues with experimental permeability characterisation, and its tedious nature, there has also been a significant effort to predict permeability properties using various simulation approaches.

The first predictive method for permeability determination was proposed by Kozeny and subsequently modified by Carman [77]. The Kozeny-Carman equation represents flow through a porous material as a bundle of tubes of varying radii, through which flow is laminar, and is reliant on the definition of several geometric and dimensionless parameters that cannot be strictly measured. Since the predicted permeability is highly dependent on these dimensionless parameters this method is quite prone to error. More recently, Gebart proposed a lubrication model for predicting permeability in unidirectional reinforcements [78], though

it assumed fibres were packed in square or hexagonal arrangements for modelling. However, both of these approaches are designed for the prediction of single-scale porous media, and therefore are not strictly applicable to textile reinforcements where there are both intra-yarn and inter-yarn porosity considerations.

Other models have simulated small Repeated Unit Cells (RUCs) of the fabric architecture using the Navier Stokes equations with appropriate boundary conditions and considerable geometric simplifications [79]. An example of a typical RUC created for a plain weave using TexGen is shown in Figure 13. Several similar attempts have been made with 3D meso-scale models of RUCs [65], and with the lattice Boltzmann method for the flow simulation [80], although the latter was considered computationally expensive. Most of these approaches rely on the approximated geometry of tow cross sections and waviness that has a significant effect on the predicted permeability. Alternatively, Optical Coherence Tomography (OCT) imaging has even been used to extract details from the microstructure of woven reinforcements in order to study permeability [81]. However, this approach is expensive and time consuming, meaning it is not realistic for applications outside academia.

To capture the dual scales of fabric permeability, a two-step approach has been considered by Nedanov et al. [82] and Takano et al. [66]. This method first calculates the yarn permeability from the micro scale inter-fibre flow, then flow through the meso scale yarn architecture is investigated to find the effective fabric permeability. Other models using 3D Representative Volume Elements (RVEs) have also seen some success [64] along with voxel based finite difference methods [83]. Additionally, reduced dimensional 'grid' approaches have also been developed to increase efficiency and simplify predictive modelling [13, 84]. In many cases, as a result of the micro cavities between fibres, yarn permeability is considered to be two orders of magnitude smaller than that of the fabric architecture [82], and is driven by the cavities between the yarns. Subsequently, this internal yarn permeability is often neglected, although it can also be approximated and incorporated using statistical fibre volume fraction data for the yarns or using methods like the two-step approach [66, 82]. Ultimately, for all these modelled approaches, fundamental assumptions have to be made on the arrangement and geometry of fibres in yarns, or of yarns in the fabric, which are not strictly realistic and are lacking in experimental validation.

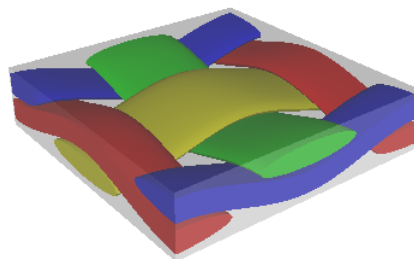


Figure 13: Example of a plain weave Repeated Unit Cell (RUC) created in TexGen [55].

2.3.3 Permeability and shear angle relationship

Fabric shearing, which occurs in the draping process, also has a significant effect on permeability. The rearrangement of yarns during shear deformation affects the local porosity (or fibre volume fraction) of the fabric, in addition to the obvious changes to fibre orientation.

This contributes to a change in the local permeability of the fabric, which research has quantified in many cases to be greater than 50% over the possible shear deformation range of a material [13, 64, 84, 85].

When manufacturing simple panels, this is not an important consideration since the fabric preforms experience very little shearing. Subsequently the porosity and permeability remain somewhat uniform throughout the parts. With increasing part complexity though, the permeability will vary due to local shearing, and is more likely to result in a failed infusion due to unanticipated dry spots or macro voids.

Hence, for the purposes of complex forming simulations, it is important to characterise permeability over a range of shear angles that may result from draping. In radial permeability testing, sheared fabrics tend to exhibit increasingly anisotropic behaviour and produce an elliptical-shaped flow front [70]. A number of studies have attempted to characterise this relationship, although the focus tends to be on glass fabrics. Hammami et al. [85] observed the anisotropy of a stitched, bi-directional, non-crimp fabric to increase by a factor of four as the material was sheared. This was due to increasing K_1 principal permeability values and decreasing K_2 values over the shear angle range. Similarly, Slade et al. [86] reported comparable trends working with both stitched and woven fabrics.

Conversely, Endruweit et al. [76] performed experimental and modelling work for a variety of different fabric architectures, resulting in a general reduction in both K_1 and K_2 principal permeability values as shear angles were increased. However, many of their samples initially showed some anisotropy in an undeformed configuration, suggesting that the fabrics may have been unbalanced (a K_1/K_2 ratio of 1.43 was recorded for one plain weave material). These decreasing permeability trends have also been observed in experimental and modelling work by Smith et al. [87] and Loix et al. [64] respectively.

The modelling work by the latter group predicted lower principal permeability values for tests with a single material layer compared to thicker stacks, although greater anisotropy was also predicted [64]. Unfortunately, this work is lacking appropriate experimental validation to support these predictions. Experimental studies for carbon and glass fabrics, by Lai et al. [88], again resulted in increasing anisotropy with decreasing principal permeability values. However, their work on layup thickness observed higher principal permeability values for tests with fewer layers. This difference between the two groups may be attributed to nesting effects and an increasing fibre volume fraction with layup thickness in the experimental work, where the models represent an idealised and unrealistic stacking arrangement. Ultimately, it is clear that this effect is significant and should be incorporated into infusion modelling for improved realism.

2.4 Infusion modelling

In the composites manufacturing industries, despite resin infusion being seen as a relatively low-cost approach, empirical design and development practices are often wasteful. This is particularly true for complex parts, where the rate of rejection is high due to unforeseen problems with infusion strategies. As such, further cost savings can be made by accurately simulating the infusion process; eliminating any flaws in the process that could lead to part rejection prior to any actual forming experiments.

The primary aim of an infusion model is to predict the transient flow front profile, and ensure that the total fill time is within the gel time for the selected resin system. Secondary to this, simulation can be used as a tool for identifying potential dry spots and macro voids that may result from a particular infusion strategy. Furthermore, infusion modelling is being increasingly adopted at the component design stage, in order to predict an optimal manufacturing strategy including the location of inlets and outlets.

Macroscopically, the simulation of flow through porous materials is typically based on generalised forms of the Navier-Stokes equations and Darcy's law, including both advection and diffusion terms. In reality, there are a number of complex interactions related to the flow within the fabric architecture, such as the tortuosity of the flow paths, dispersion or the true porosity, which can only be approximated. In addition, many cases of infusion are performed in non-isothermal conditions. This can be because the resin cures only at elevated temperatures (and thus a tool might be heated, or the infusion might take place in an oven) or because the curing reaction is very exothermic. Either way, because the resin viscosity is temperature dependent, these conditions can become very important to include in simulations. Subsequently, non-isothermal simulations are sometimes necessary to account for heat transfer phenomena in addition to fluid velocity and pressure considerations.

Due to the complexity of manufacturing and material interactions, there are a number of further complications that should be considered in the development of an infusion model. For example through-thickness effects, tool compaction, and void formation/transportation can all be significant during infusion processes. For many mould filling applications, parts are assumed to be sufficiently thin that through-thickness effects can be neglected. This is supported by the position that transverse permeability is generally one or two orders of magnitude smaller than the principal in-plane values [89]. Subsequently, it is common to represent these parts as shells for the purpose of simulating planar resin infusion. However, there are also many examples where through-thickness and 3D flow cannot be neglected. This is often the case for thick (multiple ply) preforms, or in vacuum-assisted infusion processes where distribution media is used to enhance resin flow and compaction modelling can become necessary [43, 90-92]. In terms of modelling however, these predictions of compaction behaviour primarily remain one-dimensional for simplicity and disregard post-filling relaxation (while resin pressure in the mould equalises).

In practice, infusion manufacturing of composite components also relies on successfully achieving a high degree of saturation and minimal void content. The simulation and prediction of voids in these processes is also an area of growing interest. A recent study has demonstrated that void formation at the flow front can be correlated with the dimensionless 'modified capillary number', which is effectively a ratio of viscous force and surface tension [61]. This research accounts for void formation, bubble compression and void transport to more accurately predict void content, on the basis that mechanical entrapment is the main cause for void creation.

Ultimately, most modelling approaches simplify infusion to a continuum-based approximation and neglect through-thickness effects, saturation, compaction and heat transfer, as is reasonable on a case-by-case basis. There are a number of different modelling approaches that

have been developed over the years, with varying degrees of complexity. Early methods like the Boundary Element Method (BEM) had some issues with the conservation of mass within the system. Meshless methods and a Lagrangian Finite Difference (FD) approach showed some success but were computationally demanding and limited to simple geometries respectively [93, 94]. There have also been a number of pure Finite Element (FE) based methods of varying sophistication, from early implicit modelling under isotropic conditions, to detailed approaches that incorporate heat exchange, compaction and full 3D flows [95]. A more unique 'Level Set' method has also been developed with promising 2D results [96], but has not been extended to more advanced cases. However, the most recent and popular methods tend to be variations of the Control Volume / Finite Element (CVFE) approach and the Volume of Fluid (VOF) method. Both have demonstrated some success, although typical examples rely on homogenous permeability and flow properties throughout the infusion domain in relatively simple geometries (where this assumption is reasonable).

2.4.1 Control Volume / Finite Element (CVFE) methods

The most popular approach for infusion modelling is the combined Control Volume and Finite Element method (CVFE), as it has proven to be relatively efficient and accurate in applications of varying sophistication [89, 97-100]. It is capable of simulating merging flows and variable preform thickness (for cases where compaction is significant). This formulation breaks down the infusion problem by only considering the resin phase (and not the air within the porous material) and simplifies the transient filling problem by solving small successive steady-state problems (explicit integration in the time domain).

An example of the CVFE approach is the Flow Analysis Network (FAN) method described by Phelan et al. [100], which can be summarised as follows. First, the computational domain is discretised into elements and nodes, with independent control volumes assigned to each node. Then, based on Darcy's Law and the mass continuity equation for an incompressible Newtonian fluid, the pressure gradient between the inlet and flow front is determined using the FE method (although technically Finite Volume (FV) or Finite Difference (FD) methods can also be used). From the pressure gradient, the velocity field is calculated and then the filling times are found for all the control volumes adjacent to the flow front. The minimum time to fill one of these cells determines the length of the next time-step, thus guaranteeing the flow front advances by at least one control volume but does not overflow. Hence, the rest of the adjacent volumes are partially filled and the new numerical flow front position is known. Figure 14 depicts the CVFE discretisation and the advancing flow front.

Using this approach only one differential equation needs to be solved, thus the process is efficient and stable even for coarse grids (although there can be problems discretising complex geometries) [10]. However, as the approach aims to only fill one control volume at a time (unless multiple volumes have the same fill time for that step), cases with a large number of control volumes can be slower to solve (but flow-aligned regular grids can speed this up).

Bruschke and Advani [97] used an early CVFE method to model 2D, isothermal, anisotropic flow through fibre preforms, before other authors developed similar models [99]. Kang et al. [98] were able to smooth out the advancing planar flow front in a CVFE approach using a Floating Imaginary Nodes and Elements (FINE) method. Using the Liquid Injection Moulding

Simulation (LIMS) software developed at the University of Delaware, Šimáček and Advani [89] have also added the capability to include artificial fibre tow saturation modelling with the incorporation of a sink term.

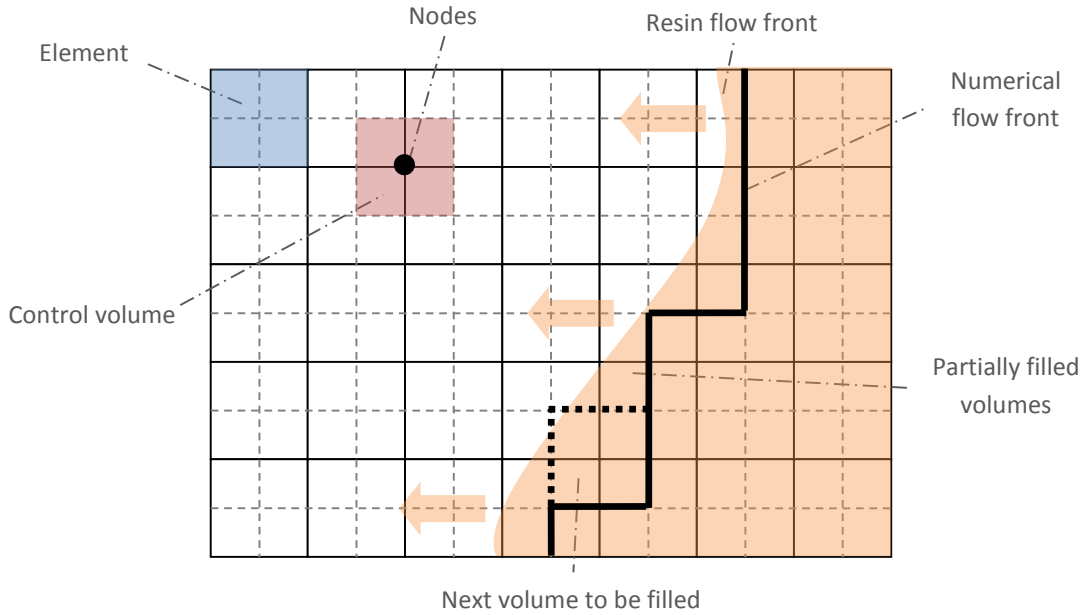


Figure 14: Control Volume / Finite Element (CVFE) method.

2.4.2 Volume of Fluid (VOF) methods

Based on the Marker Cell (MAC) approach, which combines a computational Eulerian mesh with a set of Lagrangian marker particles that move through it [99], the Volume of Fluid (VOF) method became popular for infusion modelling as it required less computational storage than the MAC approach [101]. VOF can be used to model multiphase flows with two or more inviscid fluid phases that are well defined but cannot occupy the same volume. Within control volumes the volume fraction of all phases sum to one and a single set of continuity, volume fraction and momentum equations are applied to all fluid phases:

$$\frac{\partial \rho}{\partial t} + \nabla \cdot (\rho \mathbf{u}) = 0 \quad (2)$$

$$\frac{\partial (\rho V_{fp})}{\partial t} + \nabla \cdot (\rho V_{fp} \mathbf{u}) = 0 \quad (3)$$

$$\frac{\partial (\rho \mathbf{u})}{\partial t} + \nabla \cdot (\rho \mathbf{u} \times \mathbf{u}) = -\nabla p + \nabla \cdot \boldsymbol{\sigma} + \rho \mathbf{g} + \mathbf{S}_K \quad (4)$$

Where V_{fp} is the phasic volume fraction, $\boldsymbol{\sigma}$ is the stress tensor, and \mathbf{S}_K is a source term related to flow resistance in the porous material:

$$\mathbf{S}_K = -\frac{\mu}{K} \mathbf{u} \quad (5)$$

Averaged viscosity and density properties are defined in terms of volume fraction for use in the governing equations:

$$\rho = V_{fp}\rho_{resin} + (1 - V_{fp})\rho_{air} \quad (6)$$

$$\mu = V_{fp}\mu_{resin} + (1 - V_{fp})\mu_{air} \quad (7)$$

This method works by solving a set of four simultaneous partial differential equations in 2D (or five for full 3D simulations), and subsequently can suffer from convergence issues that means grid refinement and time discretisation must be carefully established. Darcy's law is effectively considered by incorporation of the resistive source term in the momentum equation, coupled with the porosity information that is defined across the modelling domain to establish the allowable fluid volume in each cell. One advantage of this approach is that it can be used to solve problems with regions of significantly different permeability characteristics (for example areas with porous reinforcement adjacent to areas without any viscous resistance, like an open channel) that are not solvable with CVFE methods [10]. This is particularly important for this research, since permeability is expected to be variable as a result of the draped fabric deformation.

2.5 Process modelling

In order to completely simulate the manufacturing process for complex, resin-infused, composite structures, an unprecedented combination of all of the previously mentioned research must be considered. Mechanical material characterisation practices are needed to enhance the fidelity of a suitable draping model. This model results in a detailed distribution of shear deformation that can be coupled with a realistic shear angle and permeability relationship (characterised either experimentally or through predictive simulation) to describe the local anisotropic permeability properties of a textile preform. Then the deformed part geometry and distributed permeability properties can be implemented into an infusion model to determine an effective fill strategy and predict the fill time or any potential defects in the part. Each of these individual areas have seen extensive study as described above, although there continues to be room for improvement (particularly for the permeability characterisation approaches that remain unstandardised). However, there have been very few attempts to demonstrate the combination of all these aspects into one complete process model. In light of the growing demand for larger and more complex structures (outlined in Chapter 1), this is an area in need of significant research.

Lomov et al. have prominently proposed the concept of an 'integrated design tool' that can incorporate all the detail and steps necessary for a full process model for over ten years [12, 13]. As referenced in these works, commercial software developers like ESI group (PAM-FORM and PAM-RTM) have been actively engaged in improving the capability of process modelling for industrial application. However, there remains no true demonstration of a process model that can accurately predict material draping, define a complex permeability distribution through the part, and ultimately run a realistic infusion simulation through the part. This thesis is intended to fulfil this need.

3 Draping simulation

3.1 Motivation

The draping simulation makes up the first major component of the overall process model for Liquid Composite Moulding (LCM). This chapter focuses on the development, evaluation and implementation of a successful draping model. As discussed in Section 2.1, this requires the ability to accurately predict the change in yarn orientations during deformation from realistic material characteristics in order to determine the ultimate geometry of a deformed layup. As the fabric preform conforms to a specific shape, the yarns reorient themselves, resulting in localised shear changes that are typically quantified by the shear angle, γ (see Figure 5, Section 2.1).

For this research, a hypoelastic, continuum-based approach has been adopted due to its proven success [31-33] and relative efficiency compared to discrete and semi-discrete approaches [35, 39]. It is important to note that continuum methods, like most approaches, do not account for yarn slippage and for particularly loose weaves, or certain forming processes, this could be an issue. In which case, the discrete and semi-discrete methods may be more capable at simulating slippage behaviour provided the fibre and yarn interactions are well characterised for the material.

The continuum approach discussed in this chapter incorporates tensile and shear characteristics of the material in order to simulate the fabric deformation behaviour, ultimately highlighting regions of large deformation that could cause difficulties during the manufacturing process. The model also provides a detailed shear angle distribution for use in subsequent components of the Complete Process Model (CPM).

3.2 Continuum model

As discussed in Chapter 2, continuum-based draping models can offer efficient and realistic results. A hypoelastic continuum method was developed using customised material subroutines within Abaqus [102] similar to those in use by other researchers [22, 31]. Layers of fabric material were treated as continuous sheets of membrane or shell elements. The intricate effects of the underlying fabric architecture were incorporated as complex material behaviours in the VFABRIC or VUMAT subroutines. Both subroutines assume the independence of yarn tensile properties from the shear response of the fabric material, and are intended to accept non-linear material properties that have been characterised experimentally.

The model has been developed for Abaqus/Explicit due to the degree of geometric and material nonlinearity expected in draping analyses, where implicit solvers become less efficient. Shell and membrane elements were chosen because the material behaviour is considered to be in-plane for woven fabric reinforcements. Specifically, S4R and M3D4R elements were selected which are both four-node elements with reduced integration. Although the reduced number of integration points can sometimes cause spurious modes of

deformation in Finite Element Analysis (FEA) packages, Abaqus incorporates sophisticated hourglass controls to monitor and restrict the effect of such problems.

Bending was largely neglected, as it is primarily demonstrated in literature to influence the nature of free wrinkling in fabrics [40], and because accurate shear modelling will still predict the location and potential onset of wrinkling. Typically, drape modelling aims to avoid wrinkling and as such, the realism of the wrinkling behaviour is only of secondary importance for this work.

3.2.1 VFABRIC subroutine approach

The VFABRIC material subroutine has been available in Abaqus for a number of years but has only briefly been discussed in literature [17, 103], despite its apparent suitability for draping models. As with all subroutines for Abaqus, VFABRIC is written in the FORTRAN programming language.

Primarily, the VFABRIC subroutine accounts for the orientation of fabric yarn directions and simulates the shear trellising behaviour between yarns. Hence it is capable of modelling anisotropic and non-linear behaviour. The VFABRIC subroutine is applicable for materials that exhibit two principal structural directions that need not remain orthogonal as the material is deformed. By default, yarn directions are defined initially to match the in-plane base orthogonal system, although they can be specified otherwise if necessary.

When modelling with the VFABRIC subroutine, the tensile and shear properties must be defined as constitutive properties in order to relate the calculated strain increments in each time-step to updated stress values. This subroutine was designed for adiabatic analyses, and is suitable for simulating the draping process, which is effectively operated under isothermal conditions. However it may not be valid for rapid forming processes with temperature dependent materials, where inelastic strain and thermal variations occur during deformation.

In its operation, the VFABRIC subroutine is fed information for blocks of material points at each time increment, such as the initial fabric stress, incremental nominal fabric strains, engineering shear strain and other solution-dependent state variables in the local system. Based on this data and the user-input constitutive relationship, the nominal fabric stresses are updated and passed back to the continuing Abaqus analysis.

VFABRIC works with plane stress elements such as shells and membranes; when using shell elements however, transverse shear stiffness needs to be defined separately to account for bending calculations. Fabric thickness is incorporated into the analysis, however it only becomes significant with the use of shell elements or when an accurate bending response is required.

Although this VFABRIC approach has been created specifically for modelling fabric behaviour, the details of its full formulation and theoretical background were not available. Furthermore, the implementation of this subroutine requires manual changes to the input file keywords that can conflict with any operations performed in the Abaqus CAE interface. Subsequently, a generalised user material subroutine (VUMAT) has also been developed for simulating fabric behaviour to facilitate greater control and eliminate the implementation issues.

3.2.2 VUMAT subroutine approach

The VUMAT subroutine has been coded in FORTRAN to describe the hypoelastic constitutive behaviour of the dry textile reinforcement for the Abaqus software package. As with the VFABRIC material subroutine, this approach requires the definition of the constitutive model and assumes that the tensile yarn and shear behaviour are independent. However, in addition to this, the VUMAT subroutine requires a completely custom algorithm to track the non-orthogonal yarn orientations during deformation based on the orthogonal, planar strains and deformation gradient tensor. Subsequently, the VUMAT subroutine allows for greater control and customisation.

The theory which constitutes this subroutine is outlined below and is based on the work by Khan et al. [31]. This approach was founded on the Hypoelastic law, applicable for reversible non-linear behaviour:

$$\sigma^{\nabla} = \mathbf{C} : \mathbf{D} \quad (8)$$

Where σ^{∇} is an objective derivative of the Eulerian 2nd order tensor of Cauchy stress, σ ; \mathbf{D} is that of the strain rate, and \mathbf{C} is the 4th order constitutive tensor oriented along the fibre directions. Because this constitutive tensor is referenced to the fibre directions, it is necessary to update the current fibre directions throughout the analysis. Within Abaqus/Explicit the physical behaviour of the material is traced using the deformation gradient tensor, \mathbf{F} , and the right stretch tensor, \mathbf{U} . Through the polar decomposition of the deformation gradient, the rotation tensor, \mathbf{R} , can be found:

$$\mathbf{R} = \mathbf{F}\mathbf{U}^{-1} \quad (9)$$

In Abaqus this rotation is the average orthogonal rotation of the material axes and is based on the Green-Naghdi (GN) approach. Subsequently a set of, ever orthogonal, GN axes can be determined for the current configuration, \mathbf{g}_{α} , which can be related to the initial GN axes configuration, \mathbf{g}_{α}^0 , with the rotation tensor (where the index α can take the values 1 or 2, signifying two independent directions):

$$\mathbf{g}_{\alpha} = \mathbf{R} \cdot \mathbf{g}_{\alpha}^0 \quad (10)$$

To further simplify the calculations; the initial GN axes are made coincident with the local material coordinate system of the Abaqus model. It is therefore important to define a local material coordinate system that reflects the initial fabric yarn orientations during the model generation. Subsequently, the definition in Equation (11) is reasonable since each of the fibre axes initially corresponds with the local material coordinate system.

$$\mathbf{g}_1^0 = \begin{bmatrix} 1 \\ 0 \end{bmatrix}, \quad \mathbf{g}_2^0 = \begin{bmatrix} 0 \\ 1 \end{bmatrix} \quad (11)$$

Next, the current warp and weft fibre directions, \mathbf{f}_{α} , can be calculated from the initial fibre axes, \mathbf{f}_{α}^0 , and deformation gradient in Equation (12). It is also reasonable to assume that the fibre axes are aligned with the GN axes in the initial state, since this is a condition that can be enforced during the simulation set up.

$$\mathbf{f}_\alpha = \frac{\mathbf{F} \cdot \mathbf{f}_\alpha^0}{\|\mathbf{F} \cdot \mathbf{f}_\alpha^0\|} = \frac{\mathbf{F} \cdot \mathbf{g}_\alpha^0}{\|\mathbf{F} \cdot \mathbf{g}_\alpha^0\|} \quad (12)$$

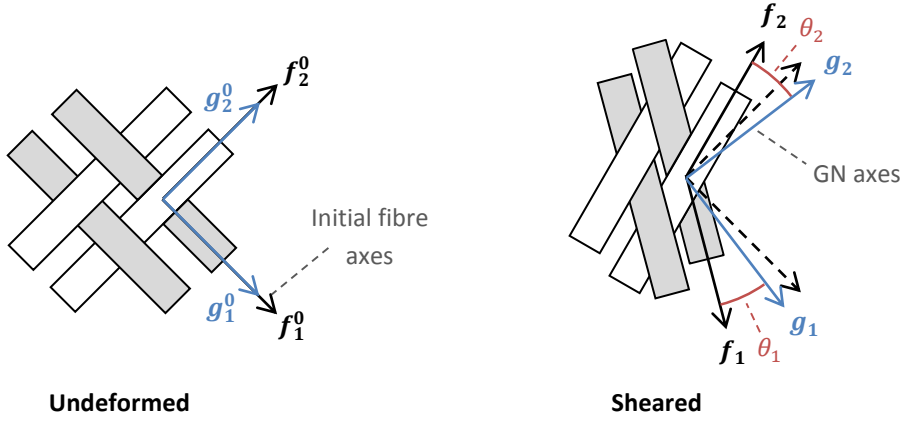


Figure 15: Rotation of both Green-Naghdi and fibre axes as a result of deformation from an initial state.

Figure 15 shows the physical representation of the GN and fibre frames in the initial and deformed states. Here it can be seen that the yarn fibre directions are first enforced to be aligned with the GN frame prior to rotation. The angles between the two independent fibre frames and the orthogonal GN axes can be determined from the trigonometric definitions in Equation (13).

$$\sin \theta_\alpha = \frac{\mathbf{g}_\alpha \times \mathbf{f}_\alpha}{\|\mathbf{g}_\alpha\| \|\mathbf{f}_\alpha\|}, \quad \cos \theta_\alpha = \frac{\mathbf{g}_\alpha \cdot \mathbf{f}_\alpha}{\|\mathbf{g}_\alpha\| \|\mathbf{f}_\alpha\|} \quad (13)$$

These relationships convert the properties determined in the GN frame to equivalent properties in the two independent fibre frames. Thus, two transformation matrices, \mathbf{T}_α , are established to facilitate the conversion of stress and strain matrices:

$$\mathbf{T}_\alpha = \begin{bmatrix} \cos \theta_\alpha & -\sin \theta_\alpha \\ \sin \theta_\alpha & \cos \theta_\alpha \end{bmatrix}, \quad \alpha = 1, 2 \quad (14)$$

For VUMAT subroutines, Abaqus calculates and stores the incremental strain, $d\boldsymbol{\varepsilon}$, relative to the average rotation (the GN frame). In order to use the proposed constitutive equation, this strain tensor needs to be transformed and split into the two independent fibre frames, $d\boldsymbol{\varepsilon}^{f_\alpha}$, using the above transformation matrices according to Equation (15).

$$d\boldsymbol{\varepsilon}^{f_\alpha} = \mathbf{T}_\alpha^T d\boldsymbol{\varepsilon} \mathbf{T}_\alpha \quad (15)$$

Then the constitutive law can be applied for each warp and weft fibre direction, \mathbf{C}^{f_α} , and solved for incremental stress in the fibre frames using Equation (16).

$$d\boldsymbol{\sigma}^{f_\alpha} = \mathbf{C}^{f_\alpha} d\boldsymbol{\varepsilon}^{f_\alpha} = \mathbf{C}^{f_\alpha} \begin{bmatrix} d\varepsilon_{11}^{f_\alpha} \\ d\varepsilon_{22}^{f_\alpha} \\ d\varepsilon_{12}^{f_\alpha} \end{bmatrix} = \begin{bmatrix} d\sigma_{11}^{f_\alpha} \\ d\sigma_{22}^{f_\alpha} \\ d\sigma_{12}^{f_\alpha} \end{bmatrix} \quad (16)$$

Where,

$$\mathbf{C}^{f1} = \begin{bmatrix} E_{11} & 0 & 0 \\ 0 & 0 & 0 \\ 0 & 0 & G_{12} \end{bmatrix}, \quad \mathbf{C}^{f2} = \begin{bmatrix} 0 & 0 & 0 \\ 0 & E_{22} & 0 \\ 0 & 0 & G_{12} \end{bmatrix} \quad (17)$$

Here the tensile moduli in each of the fibre directions, E_{11} and E_{22} , and the in-plane shear modulus, G_{12} , are the only values needed in the constitutive tensor since they are considered as independent. The accuracy of this behaviour law then relies on suitable characterisation of these properties (experimentally discussed in Chapter 4).

Solution Dependent state Variables (SDVs) are used in the material subroutine to track and store values such as fibre stresses, strains and shear angles between time increments. In order to calculate the new fibre stresses at the end of the current time increment, $\sigma_{New}^{f\alpha}$, in Equation (18), a midpoint integration scheme is applied, where the incremental fibre stresses from Equation (16) are added to the fibre stresses from the previous increment, $\sigma_{Old}^{f\alpha}$. In the initial state, old stresses are set to zero, then at the end of each increment the new fibre stresses are stored as SDVs to be used as the old fibre stresses for the subsequent time increment.

$$\sigma_{New}^{f\alpha} = \sigma_{Old}^{f\alpha} + d\sigma^{f\alpha} \quad (18)$$

Finally, the updated new fibre stresses must be converted back to the original GN frame in Equation (19), for Abaqus to continue the analysis.

$$\sigma_{New} = \mathbf{T}_1 \sigma_{New}^{f1} \mathbf{T}_1^T + \mathbf{T}_2 \sigma_{New}^{f2} \mathbf{T}_2^T \quad (19)$$

This process is summarised in Figure 16, where the section in red represents the work coded into the VUMAT material subroutine and the blue section represents the work performed natively in Abaqus. The orange blocks are those which are defined by the user in the code and the dashed grey lines represent advances in the time increment, which is done within the Abaqus explicit solver. An example of the full VUMAT code is presented in Appendix A.

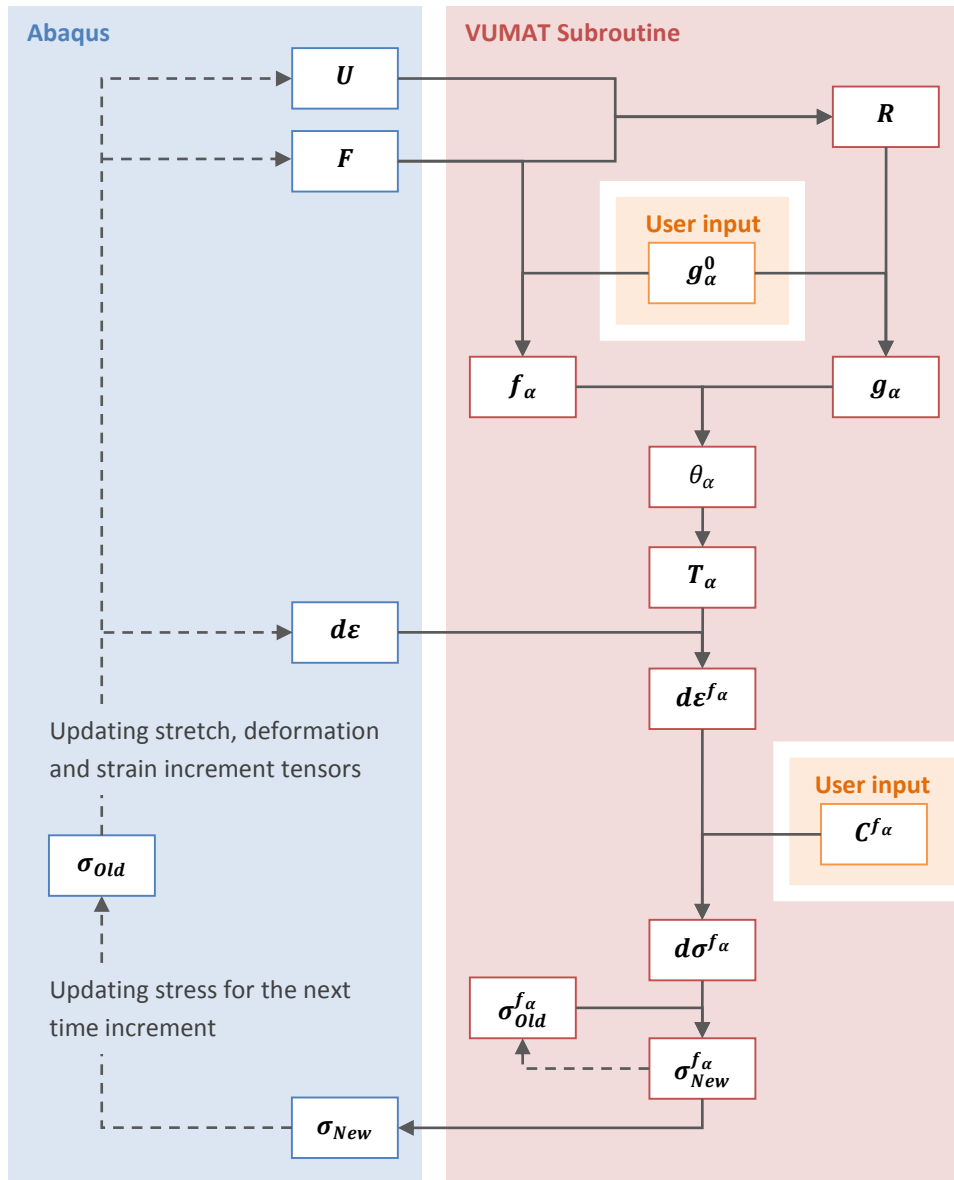


Figure 16: Process diagram for the VUMAT subroutine code, based on work by Khan et al. [31].

3.3 Draping simulation validation

Initial validation trials were performed iteratively for analytical cases. Small scale simulations were first run on single elements to ensure that the subroutines and overall Abaqus modelling processes were performing as intended. Once verified, simulations were scaled up to multiple elements for similar analytical cases before ultimately applying the model to complex cases that had previously been studied in literature. Using similar modelling approaches, work by Khan et al. [31, 103] and Peng et al. [32, 33] provided suitable double dome and hemispherical forming cases for validation purposes.

3.3.1 VFABRIC hemispherical punch simulation

In order to evaluate the potential of the VFABRIC subroutine approach, a hemispherical stamping simulation was run in Abaqus/Explicit for comparison with the implicit (Abaqus/Standard) model and experimental work by Peng [32]. The modelling case was created using four parts: the punch, blank holder, blank and die as depicted in Figure 17. The

blank part represents a single sheet of continuous fabric material, and is the only deformable body in the simulation, with the punch, blank holder and die parts represented by analytical rigid bodies. Due to the symmetrical nature of the simulation (for balanced weave fabrics), and to increase efficiency, the blank was represented as a quarter model with xy and yz planes of symmetry. Figure 17 shows the assembly of the model based on the simulation details provided in the work by Peng et al. [32].

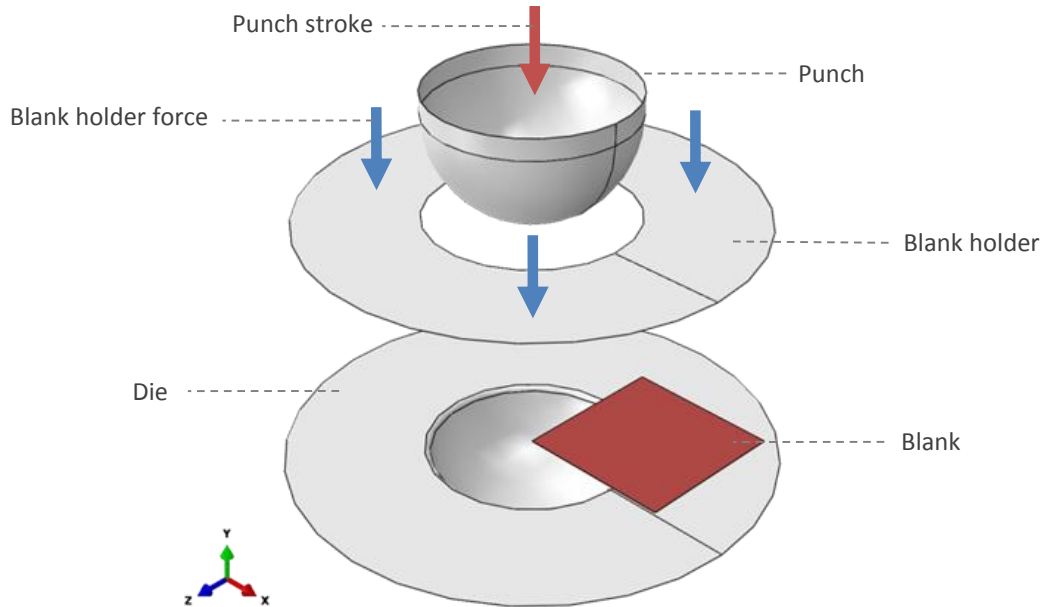


Figure 17: Hemispherical stamping simulation geometry.

The explicit VFABRIC simulation was performed in two steps. First, the rigid blank holder applies a constant force of 50 N down, on top of the fabric blank, holding it in place against the rigid die. Then, the hemispherical punch performs a full downward stroke, pressing the blank into the die cavity over a one second period. In order to accommodate for the rapid stamping duration, artificial mass damping was also included in the model to eliminate unreasonable blank holder vibration. This short simulation time ensured the efficiency of the model by reducing the overall solver wall time (the total time elapsed in solving the problem). Within this fabric-specific subroutine, since Abaqus automatically tracks the incremental stress and strain in fibre directions, only the constitutive relationship needed to be defined. In this case, fabric stresses were related to the fabric strains with the constitutive tensor shown in Equation (20):

$$\begin{bmatrix} \sigma_{11} \\ \sigma_{22} \\ \tau_{12} \end{bmatrix} = \begin{bmatrix} D_{11} & D_{12} & 0 \\ D_{12} & D_{22} & 0 \\ 0 & 0 & G_{12} \end{bmatrix} \begin{bmatrix} \varepsilon_{11} \\ \varepsilon_{22} \\ \gamma \end{bmatrix} \quad (20)$$

Non-linear functions for a glass and polypropylene plain weave fabric, outlined in Equations (21), (22) and (23), were replicated from earlier work by Mohammad et al. [104] and Peng et al. [32]. These were then employed to populate the constitutive tensor in the VFABRIC subroutine.

$$G_{12} = \begin{cases} 0.01|\gamma| + 0.1 \text{ MPa} & \text{if } |\gamma| < 0.5 \\ 17.1|\gamma|^3 - 25.38|\gamma|^2 + 12.72|\gamma| - 2.05 \text{ MPa} & \text{if } |\gamma| \geq 0.5 \end{cases} \quad (21)$$

$$D_{ii} = \begin{cases} 0.1 \text{ MPa} & \text{if } \varepsilon_{ii} < 0 \\ \frac{1200}{1 + e^{-600(\varepsilon_{ii}-0.01)}} \text{ MPa} & \text{if } \varepsilon_{ii} \geq 0 \end{cases} \quad (22)$$

$$D_{12} = 0.02 \min(D_{11}, D_{22}) \text{ MPa} \quad (23)$$

To remain consistent with the simulations run by Peng et al. [32], a uniform mesh of 3600 (60 x 60) shell (S4R) elements was used for the fabric blank, with similar loading and contact conditions. Since friction was merely approximated by choosing an appropriate coefficient that best matched the experimental data in their work, a similar process was performed to find that the same coefficient of friction, 0.2, was required in the explicit VFABRIC model to achieve a similar degree of accuracy.

The successful VFABRIC simulations (Figure 18), were in good agreement with both the implicit simulation and the experimental data, as shown in Figure 19 and Figure 20. The experimental results presented here from Peng et al. [32] actually originate from an earlier paper by Mohammed et al. [104], where the hemispherical draping of a glass and polypropylene plain weave fabric (among others) was studied. The top-down view of the shear angle distribution across the quarter blank part is shown in Figure 18, revealing the greatest shear angles in the region of greatest curvature and least tensile resistance. This coincides with what is commonly known as the fabric bias direction. For a balanced plain weave fabric, the bias direction bisects the two principal yarn directions of high tensile strength.

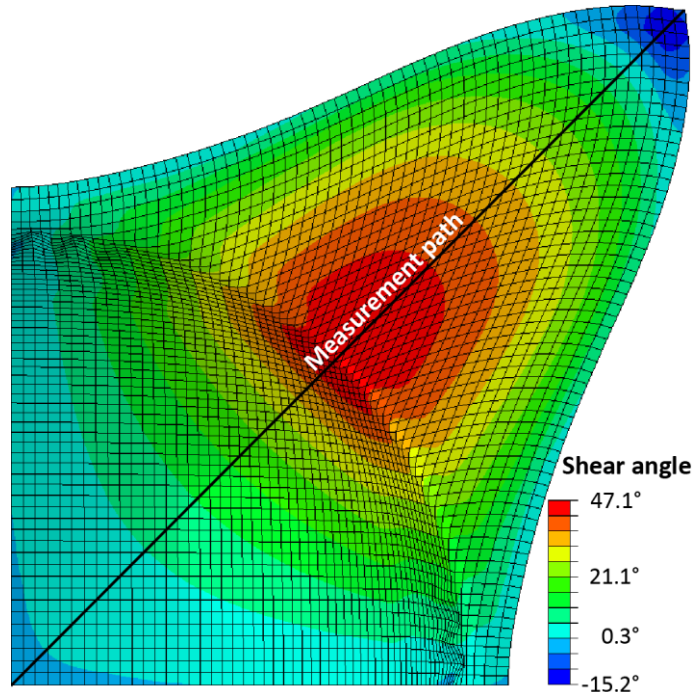


Figure 18: Top-down, quarter view of the hemispherical punch results with coloured shear angle contours and the bias direction measurement path.

For a quantitative comparison of the results, shear angles were measured regularly along the diagonal path displayed in Figure 18 (the fabric bias direction). These values are plotted against results published by Peng et al. [32] for their implicit UMAT simulation, a simple orthogonal simulation (without the non-orthogonal yarn tracking subroutine) and experimental data, in Figure 19. The results of this shear angle comparison shows that the explicit VFABRIC model agrees well with the implicit UMAT model. Both models show reasonable agreement with the experimental results, although the available experimental data is sparse and contains significant error. Most importantly though, it can be seen that a basic orthogonal approach does not replicate the same behavioural trend. This demonstrates why orthogonal modelling is insufficient for process modelling, since it does not realistically track fibre directions as a fabric deforms. Similarly, in Figure 20, the orthogonal draw-in profile for the fabric reveals a very different shape to those of the subroutine models and experimental results. Here the VFABRIC model shows very good agreement with both the implicit UMAT results and the experimental draw-in profile.

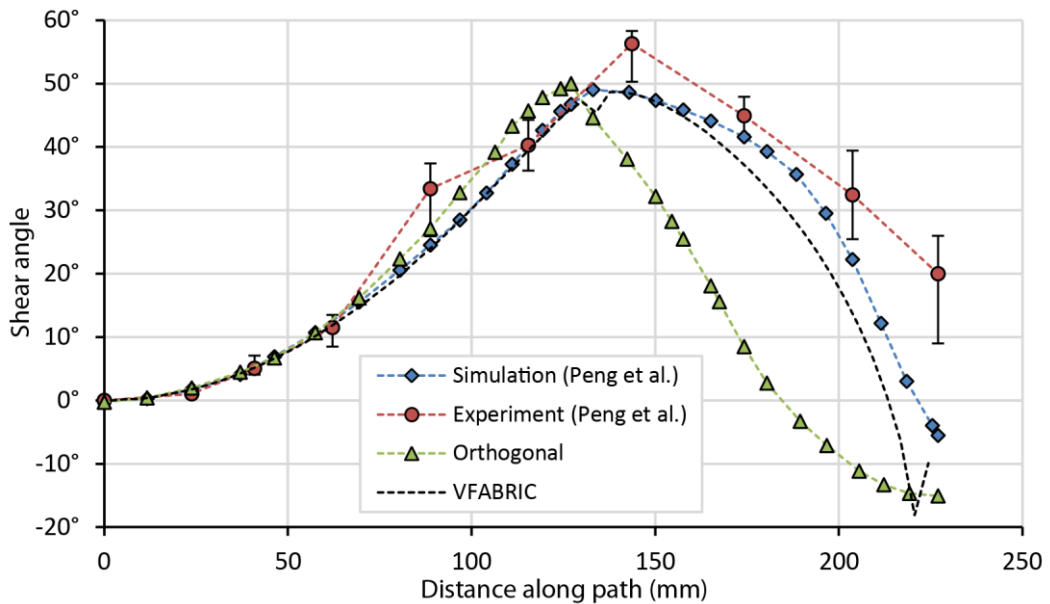


Figure 19: Comparison of shear angles measured along a path in the bias direction (Figure 18) for hemispherical punch forming.

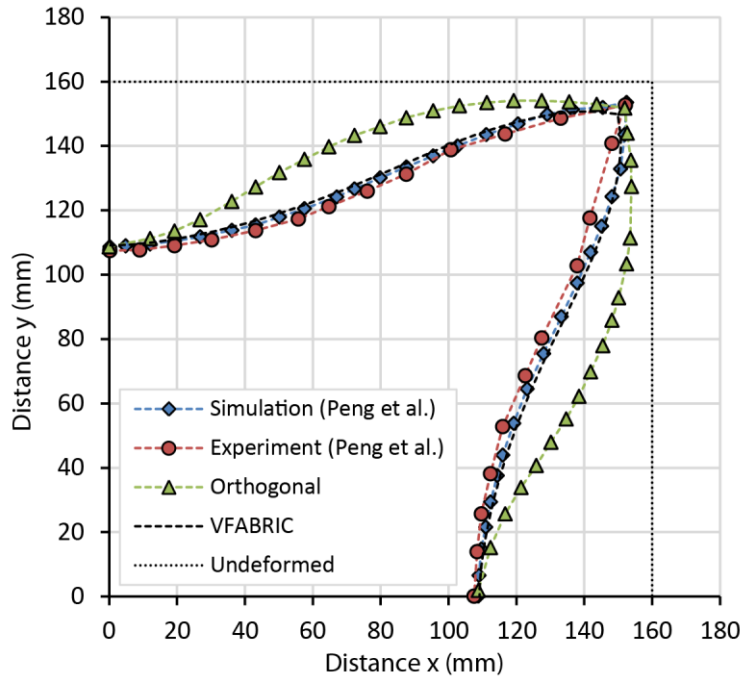


Figure 20: Comparison of the fabric draw-in profile for the quarter blank.

3.3.2 VUMAT double dome punch simulation

Recently, researchers attempting to benchmark fabric reinforcement materials have been working with a more complex ‘double dome’ geometry (Figure 21). Khan et al. [31] and Peng et al. [33] have both used this case to validate their own draping models. For consistency and validation purposes, the VUMAT model discussed in this chapter has also been used to simulate this case.

The experimental results obtained by Khan et al. [31] were found for a balanced plain weave (glass and polypropylene) fabric with sample dimensions 470 mm x 270 mm and thickness 0.78 mm. Full fabric properties are detailed in a previous benchmarking exercise [50]. The physical punching process involved first applying a 100 N blank holder force onto the fabric over the die, then forcing the punch and fabric material into the die cavity at a rate of 20 mm/min. For their work, the fabric was lightly treated with resin prior to forming so that it would cure and keep its shape after the punching process in order to facilitate measurements of the material draw-in and shear angles. This draw-in profile was used to validate the simulation results, along with a number of shear angle values taken at various points of interest across the formed geometry (as seen in Figure 22).

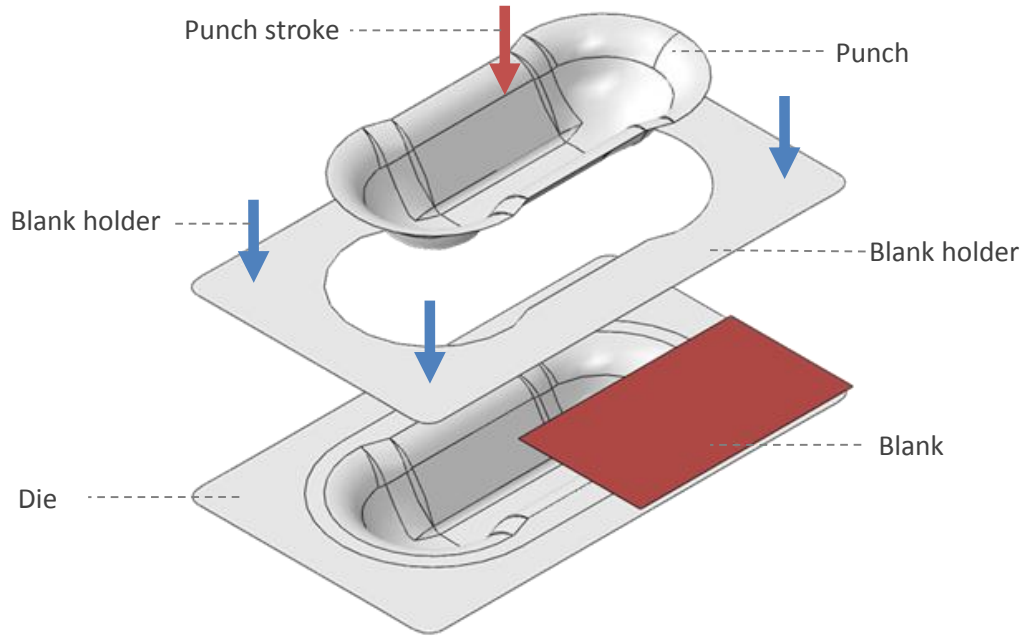


Figure 21: Double dome stamping simulation geometry (based on similar work by Khan et al. [31]).

Like the hemispherical simulation, the double dome case relied on modelling the fabric as a deformable and continuous sheet of elements in quarter symmetry. Rigid blank holder, die and punch parts were used to perform the actual deformation, again in a two-step approach of blank holder force and then punch stroke (refer to Figure 21). A blank holder force of 100 N and a punch stroke of 60 mm were used, with each step occurring over 0.01 second. Given the nature of the problem, such a short step duration is reasonable so long as suitable mass damping properties are included in the model. This enables a significant improvement in computational time, where these simulations are able to run in a matter of minutes (at least 20 times faster than running a realistic stamping rate that achieves near identical results). The blank holder was modelled as a flat plate with space for the punch to penetrate, rather than that used in the experiment which consisted of six 20 mm wide segments forming an oval around the die cavity.

Khan et al. [31] ran a very similar explicit simulation using a VUMAT subroutine using M3D4R elements for the fabric mesh (at the same refinement as the presented model from this thesis, 3555 elements). Peng et al. [33] on the other hand, continued to employ an implicit formulation with UMAT subroutine and S4R shell elements in a finer mesh (8280 elements). All simulations were run with samples of quarter symmetry in order to reduce computational requirements, along with the same assumed friction coefficient of 0.2 and ‘general’ contact conditions (where all bodies are prevented from penetrating other bodies according to the ‘general’ contact rules in Abaqus).

For the constitutive modelling, tensile moduli (E_{11} and E_{22}) were set as constant, 35.4 GPa, and the non-linear shear modulus function, G_{12} , in terms of shear strain, was defined by Equation (24) from literature [103].

$$G_{12} = 8.48\gamma^4 - 12.0972\gamma^3 + 6.1275\gamma^2 - 0.83\gamma + 0.051 \quad \text{MPa} \quad (24)$$

In order to demonstrate the benefits of these improved modelling approaches, a simplistic orthogonal model was also set up for comparison. This assumed that the fibre directions would remain orthogonal throughout the forming process, but incorporated the same tensile and shear moduli as the other models.

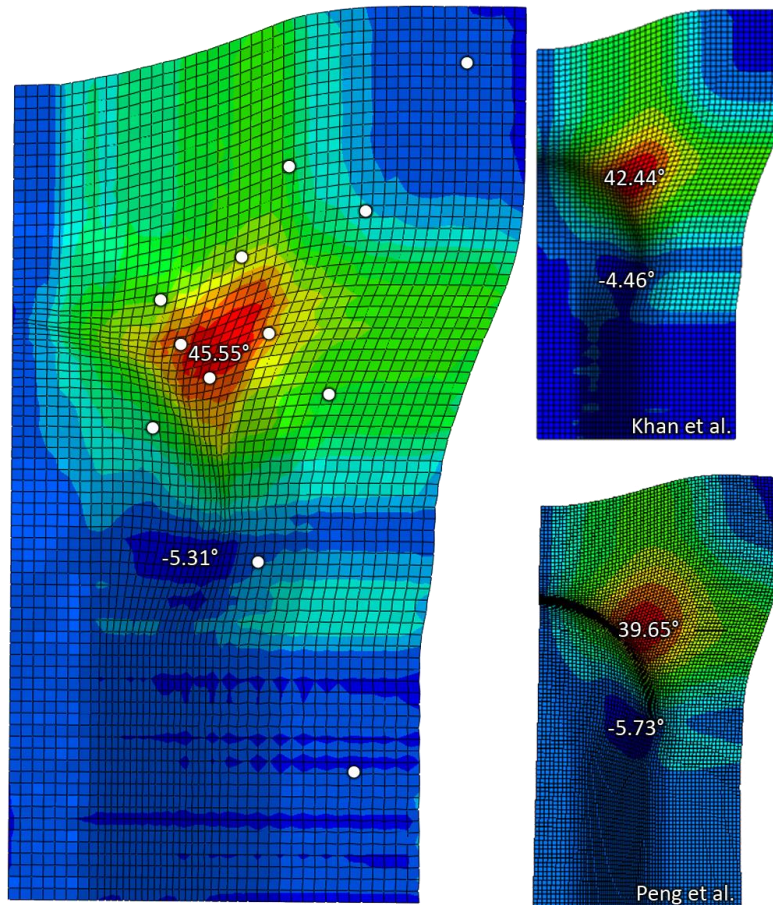


Figure 22: Top-down, quarter view of the double dome punch results with coloured shear angle contours and shear measurement points compared with results from literature [31, 33].

Figure 22 shows the shear angle distribution from the authors simulation results, which range from -5.31° to 45.55° , and compares them with the previous models from literature. The white dots on this figure represent the equivalent position of twelve known experimental shear angle results (similarly represented in Figure 23). This shear angle distribution shows very good agreement with the modelling results from both the other research groups, where the colour contours from the authors models are similar to those of Khan et al. [31]. However, the results reported by Peng et al. [33] have a slightly different colour scale and reduced peak shear angle, but still show a similarly high degree of agreement.

Detailed quantitative draw-in and shear angle results are shown in Figure 23. Due to the similarity between the VUMAT results and those from the model by Khan et al., their results are not displayed in this figure for clarity. The draw-in profile is very consistent between the VUMAT model, the implicit model by Peng et al. [33] and the experimental results from Khan et al. [31]. Similarly, the shear angle results all showed good agreement except in the regions of particularly high shearing. These shear angle results in Figure 23 are plotted relative to distance y , based on the true locations from literature [103], as marked on the profile view.

The orthogonal model showed reasonable fidelity with the rest of the simulated and experimental draw-in results, but were not capable of predicting realistic geometry near the highly sheared zones. The shear angle measurements also support this, showing that the orthogonal model values are well below those from the experimental results, despite using the same material properties.

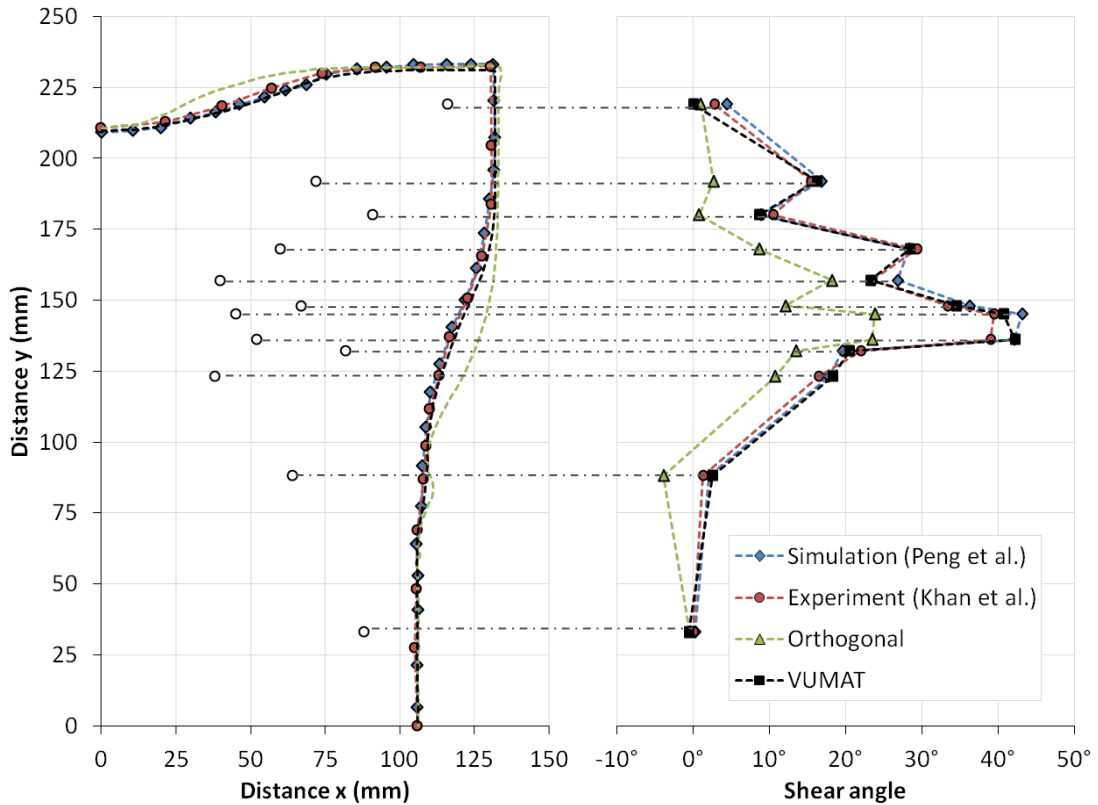


Figure 23: Double dome forming results: Draw-in profile and shear angle values at various points across the material [31, 33].

3.3.3 VUMAT and VFABRIC comparison

In order to directly compare the two subroutines, the double dome draping case is again evaluated. In establishing the VFABRIC model it is necessary to manually alter keywords in the input file prior to running a simulation, even when the model is developed in the Graphical User Interface (GUI), called Abaqus CAE. Ensuring that any conflicts are resolved after doing this, the rest of the modelling and solver process is much the same as when using VUMAT subroutines. Figure 24 shows the draw-in profile and shear angle distribution results for simulations run with both VFABRIC and VUMAT subroutines. There is nothing to differentiate the draw-in results from the two models; however there are subtle differences in the shear angle results as taken at various locations across the deformed double dome geometry. Ultimately though, the two models perform similarly, as is also true for their computational times.

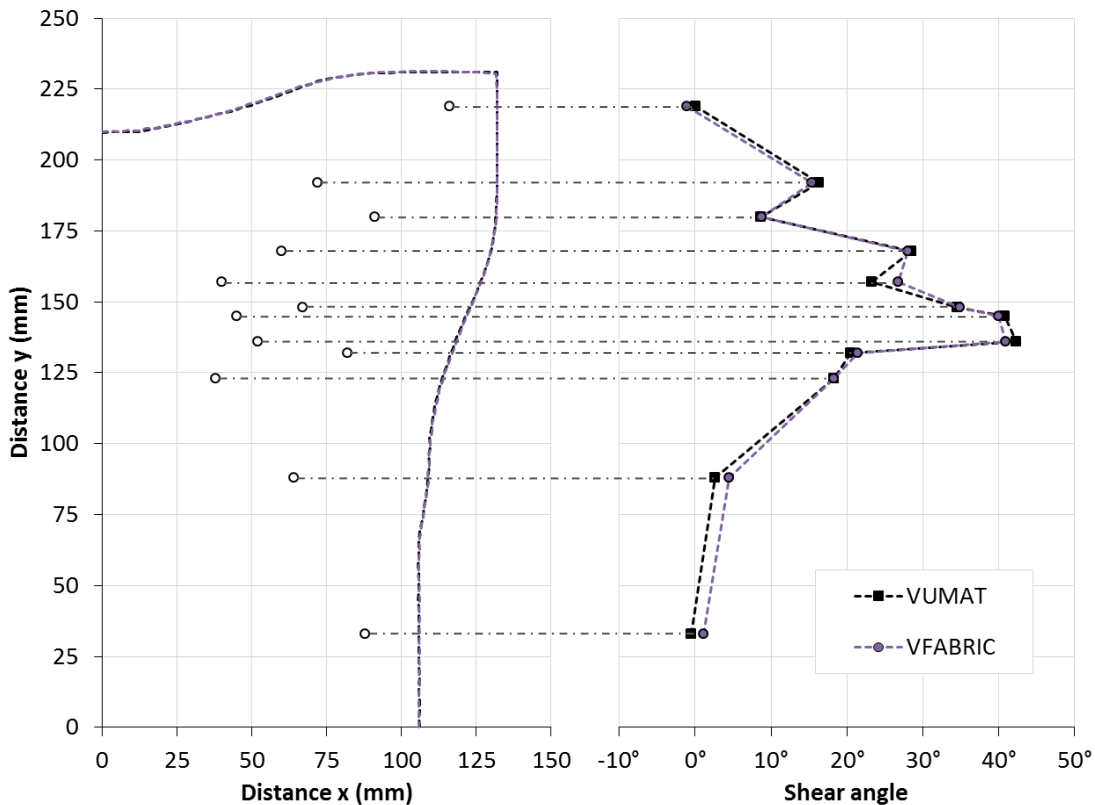


Figure 24: Comparison of VUMAT and VFABRIC double dome forming results.

3.4 Multiple ply modelling

These hemispherical and double dome draping studies demonstrate the accuracy of the VFABRIC and VUMAT continuum models for single ply simulations. However, in practice, draping is typically performed with multiple ply layups. The hypoelastic continuum approach discussed in this chapter is also capable of modelling multiple ply cases. A four ply forming example was simulated over the double dome geometry, with a layup of $[0^\circ, 45^\circ]_s$. Ply interactions were simulated by the same global contact conditions as the single ply case, with 0.2 friction coefficient. Figure 25 shows the results for the top two plies after draping in terms of the shear angle distributions throughout each ply. Ply 1 (with warp and weft yarns initially oriented at 0° and 90° respectively) shows peak shearing in the same zones as in the single ply case. Ply 2 (with yarns initially oriented at $\pm 45^\circ$) however, exhibits -55.23° shear angles at the long ends of the geometry (in dark blue), significantly greater than those experienced in the top ply. Negative shear angles are simply indicative of regions where the fabric has sheared transversely. Due to the symmetry of the layup, the bottom two plies mirror those shown in Figure 25 with negligible differences in shear angle values. These results are similar to those shown by Khan et al. [31] in their own demonstration of multiple ply modelling.

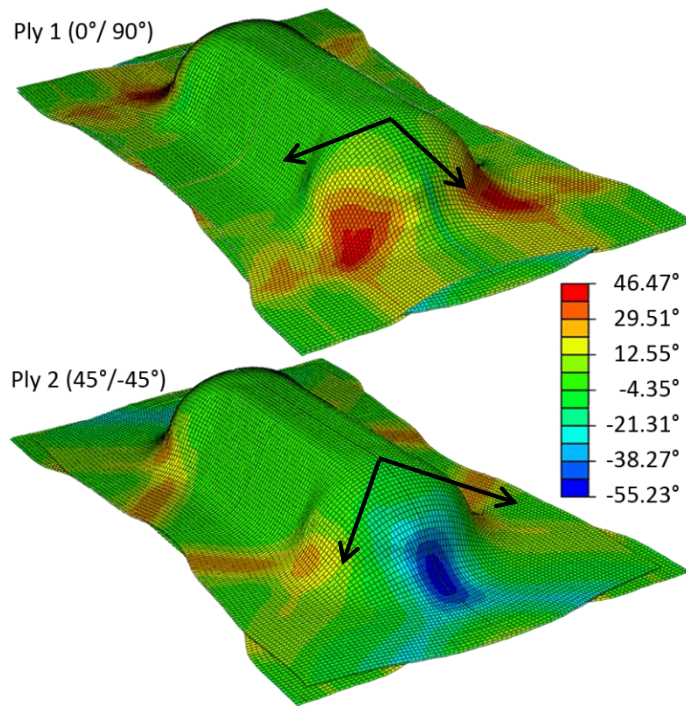


Figure 25: Shear angle distributions in the top two plies of a four ply layup draping simulation, along with yarn directions.

3.5 Conclusions

The demonstrated draping model has shown good agreement with previous simulations and experimental results by employing a VUMAT subroutine within Abaqus/Explicit that tracks yarn directions non-orthogonally. The fabric specific VFABRIC subroutine for Abaqus has also produced realistic results, with marked improvements over orthogonal modelling approaches for the hemispherical draping case and for the double dome case. However, since both the VUMAT and VFABRIC subroutines perform similarly, it is optimal in this research to use the VUMAT subroutine, as it allows for greater control and adaptation. The implementation conflicts that can arise with the VFABRIC subroutine approach, and the lack of any detailed supplementary theory, also detract from its use. For future work it is expected that the VUMAT approach has the capacity to incorporate more realistic material behaviours. In the drive for enhanced realism, it may be possible to include thickness change effects from compaction or a better description of bending and wrinkling behaviour.

Currently, the model is able to accurately predict fabric draw-in and shear angle distributions that result from forming over complex tools. Provided a reasonable material characterisation regime is in place, identification of high shear angles in the fabric can also give a very strong indication of areas where wrinkling is most likely to occur. However, if this is insufficient for a particular forming case requiring a prediction of the nature and size of wrinkling, then an alternative draping model may be preferable. In the Complete Process Model, this draping model could certainly be replaced by a semi-discrete approach that is able to better incorporate bending behaviour [39], or even fundamental hierarchical models like those that discretely modelling individual fibres [35]. However, these tend to be more difficult to implement and can be limited to small scale applications.

4 Mechanical characterisation

4.1 Motivation

In support of the draping model from Chapter 3, mechanical characterisation of the fabric reinforcement provides further realism to the simulated material behaviour. As discussed in Chapter 2, the tensile and shear properties of woven fabrics are the most important to the draping process, the VUMAT subroutine subsequently requires appropriate definition of warp and weft tensile moduli, E_{11} and E_{22} , and in-plane shear moduli, G_{12} .

To this end, appropriate test methods have been developed for both tensile and shear testing of fabric reinforcement materials. Specifically for this project, an aerospace grade carbon fibre fabric was provided (see Figure 26). As a plain weave fabric with 3K tows and a 0.193 kg/m² areal density, it is a relatively basic material in terms of fabric architecture. However, it is representative of any woven fabric reinforcement material that has a repeatable geometry for the purposes of this research.



Fabric Properties	
Weave Type	Plain
Yarn Fibres	3K
Yarns per mm	0.48
Areal Density	0.193 kg/m ²

Figure 26: Roll of aerospace grade carbon fibre fabric and the material properties.

4.2 Tensile testing

4.2.1 Experimental approach

As there is no existing standard for the biaxial tensile testing method, and due to the difficulty in creating a biaxial test rig for fabrics, a uniaxial tensile test was employed. Although this approach did not incorporate the effects of crimp interchange in textile reinforcements, it was deemed reasonable for this project, as the tensile loads imparted on the textile were unlikely to be significantly biaxial in nature during an LCM process.

Uniaxial tensile testing has two standard methods ASTM 'strip' and 'grab'. Due to the very high loads and the geometric clamp requirements of the grab test, the strip test (ASTM D5035-11) [45] was selected and conducted. The strong mechanical grips that were employed for strip testing were unable to facilitate grab testing as they were only open on one side. Although more commonly used to measure breaking force, for the purposes of this research it was also suitable to simply measure the non-linear stress-strain curve and find the tensile modulus.

Under the standard specifications, as shown in Figure 27, the strip tensile test samples were cut for a 75 mm x 75 mm gauge area with a 25 mm x 50 mm clamping section above and below the gauge area. Subsequently 25 mm of yarns were removed from each side of the gauge area such that only the vertical yarns within the clamping width of the specimen remained. This 'ravelling' process is recommended by the ASTM standard to ensure that the loaded yarns are influenced less by edge effects, and that transverse yarns do not slip out. The width of the gauge section meant that testing was performed across 13 yarns in each sample.

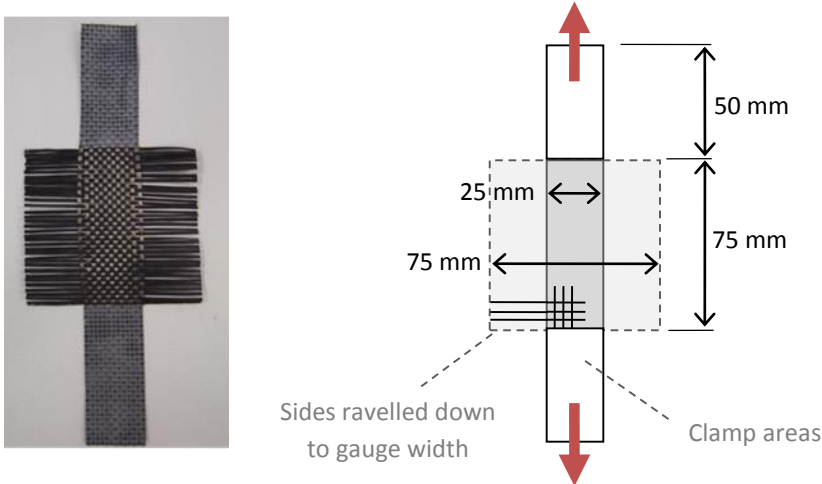


Figure 27: Strip test sample and dimensions.

Tensile Test Rig	
Frame	Instron 4505
Electronics	Instron 5500R
Load Cell	5 kN
Test Mode	Constant Rate of Extension (CRE)
Loading Rate	0.5 mm/min



Figure 28: Tensile test rig details and method.

Samples were cut in both the 0° and 90° orientations to ensure that both warp and weft fibre directions were tested. This was also to account for any directional behaviour that could result from the manufacturing process; even through the material was technically 'balanced'. A

minimum of five tests were run for each 0° and 90° direction. The clamping areas of test specimens were covered in a layer of adhesive tape to ensure the samples were sufficiently stable for handling, and to provide a better gripping surface for the clamp jaws. Testing of the samples was conducted on an Instron 4505 frame with updated 5500R electronics, using a 5 kN load cell under a 0.5 mm/min constant rate of extension. Details of the tensile test rig set up can be seen in Figure 28.

4.2.2 Tensile strip test results

From observation, all samples appeared to be well gripped in the clamp jaws, with no noticeable slippage until extremely high loading (greater than 1500 N). It is interesting to note that as the longitudinal yarns straightened under the tensile loading, the transverse yarns exhibited greater undulation (or crimp) to accommodate them. This is demonstrated by the splaying of the ravelled yarns in Figure 29.

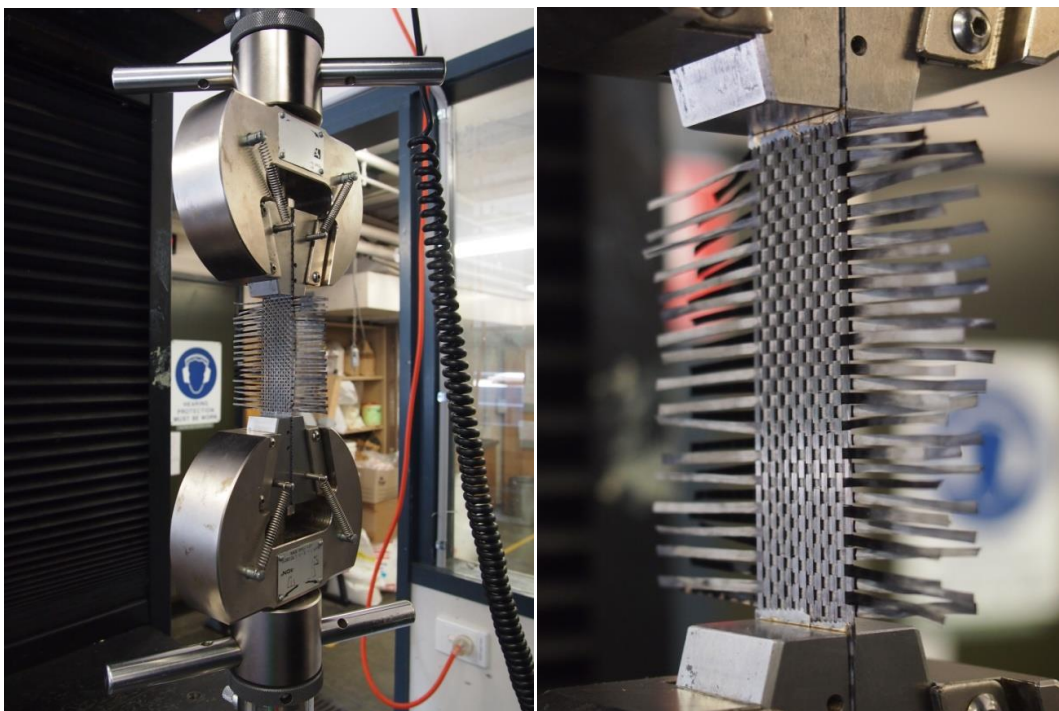


Figure 29: Tensile strip test in progress and a close up view of the ravelled yarns splaying.

From the raw load-extension curves for batches of warp and weft tensile samples, test results appear to be consistent, showing a good degree of repeatability, as seen in Figure 30. All the texts exhibited an almost immediate, rather rapid increase in load, up until a peak load of around 1700 N, which corresponds to an extension of around 1.7 mm. After reaching this peak there is a similarly rapid loss in the load, to around 30% of the peak. One sample was ultimately tested all the way to 15 mm extension, for which loading continued to display a steady decline to around 10% of the peak value. Although it is not clear what exactly causes the deficient tensile behaviour past the peak load, yarn slippage and fibre breakage are likely explanations. On close inspection of the samples post-testing, there were clear signs of fibre breakage (a few broken and curled fibres were visibly protruding from yarns), although these were not numerous enough to explain a rapid 60% loss in strength. Simultaneously, yarn or fibre slippage might also have occurred, where the grips were no longer able to provide enough

force to keep the ends of the yarns from slipping. This would describe the behaviour quite well, as observed in other trials; however, there was not any of the expected visual evidence to support this.

For this work, the loads encountered in the draping and manufacturing process are likely to be quite low, certainly lower than the peak loads from these tensile tests. Thus, this research is only really interested in the near-linear section of the results where fibre breakage and slippage were not occurring.

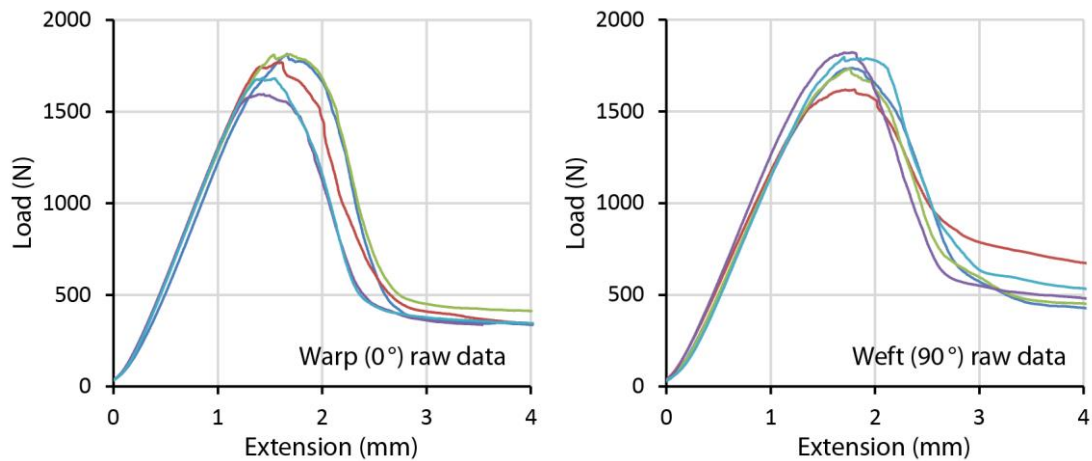


Figure 30: Warp and weft tensile strip test load-extension results.

Based on this raw data, averages were taken for each of the warp and weft test batches, and with the gauge dimensions of 75 mm x 25 mm x 0.3 mm the stress and strain were calculated. It is important to note that the thickness used here is only an approximation and the fabric samples are considered as a homogenous continuum, such that a simple rectangular cross section of 25 mm x 0.3 mm is assumed. For the purposes of simulated draping this is reasonable; the models use the same approximation for each ply of material, hence the simulation results will reflect the measured experimental behaviour. Engineering strain was calculated from knowledge of the initial gauge length and the measured extension from testing.

Since tensile stresses are generally quite low during draping, interest lies primarily in the low strain results. Hence, only the results from testing up to 0.015 strain have been considered and the tensile modulus has been characterised for this range. It is important to confirm that tensile strains do not exceed 0.015 in the modelling though, as the approximated curve fit is likely to stray significantly from reality when extrapolating from this low strain data.

As can be seen in Figure 31, for this low strain range the warp (0°) and weft (90°) average stress-strain curves are quite similar, with slightly lower stresses in the weft direction (which may be a result of residual stresses from the weaving process). As such, they are to be considered as identical and a mean of these curves is fit to develop the non-linear relationship for modelling in both tensile directions. The warp and weft stresses vary by less than $\pm 5\%$ from the mean at all points along the curves, which is considered to be negligible.

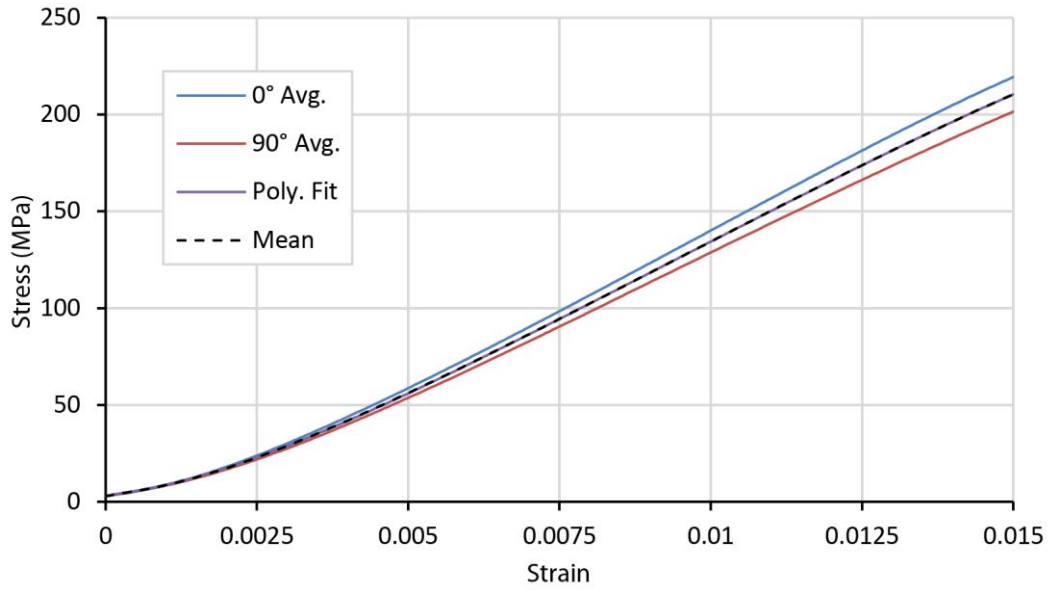


Figure 31: Average stress-strain curves for warp and weft directions as well as their mean and a polynomial curve fit of the mean.

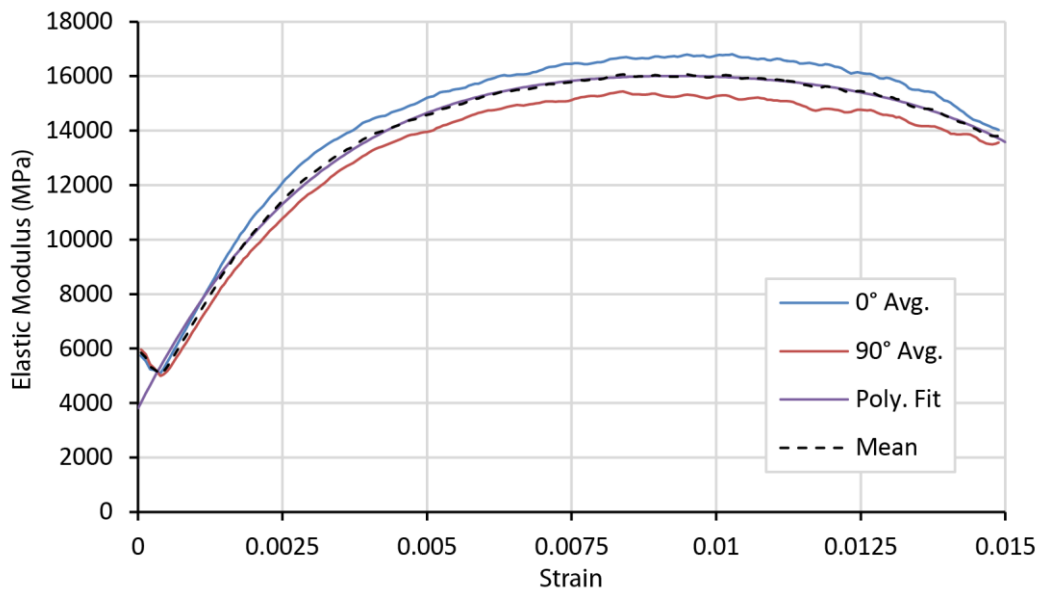


Figure 32: Relationship between tensile modulus and strain for the warp and weft averages, their mean and a polynomial curve fit of the mean.

A fourth order polynomial curve fit has been produced for the mean elastic modulus as a function of strain and is plotted in Figure 32. It can be seen here that the curve fit shows very good agreement with the experimental data after 0.0003 strain. Initially however it is not able to replicate the local minima exactly, although this small deviation, which results only in a slightly less stiff tensile property at very low strain, is not expected to affect the modelling significantly. This quartic function is outlined in Equation (25):

$$E_{ii} = -8.951 \times 10^{11} \varepsilon_i^4 + 3.458 \times 10^9 \varepsilon_i^3 - 5.525 \times 10^8 \varepsilon_i^2 + 4.180 \times 10^6 \varepsilon_i + 3800 \text{ MPa} \quad (25)$$

Similarly, the integral of this function can be found for a predictive stress-strain polynomial:

$$\sigma_{ii} = -1.790 \times 10^{11} \varepsilon_i^5 + 8.645 \times 10^9 \varepsilon_i^4 - 1.842 \times 10^8 \varepsilon_i^3 + 2.090 \times 10^6 \varepsilon_i^2 + 3800 \varepsilon_i + 2.936 \text{ MPa} \quad (26)$$

This is plotted in Figure 31 and for confirmation, as expected, shows excellent agreement.

4.3 Shear testing

4.3.1 Experimental approach

Shear testing was more difficult to establish due to the lack of standardisation in the area, despite the significant benchmarking efforts previously discussed in Section 2.2. Of the competing methods, picture frame and bias extension testing are the most popular. The picture frame test typically requires a complex rig that introduces clamping and alignment issues [49]. Bias extension testing, on the other hand, has its own problems with shear measurement, since the sample is not sheared uniformly. Hence, both methods are commonly run with optical strain measurement techniques for the greatest accuracy. To overcome the reliability issues associated with kinematic and mechanical calculation of fabric strain in bias extension samples, Digital Image Correlation (DIC) was used to obtain accurate shear strain readings. Typically specialised software and cameras are used in DIC, however an in-house DIC code has been developed in MATLAB that takes advantage of an inbuilt image processing package, discussed in Section 4.4.

Similar to the tensile testing, shear testing was performed with a Constant Rate of Extension (CRE) control. However, as the expected loads were smaller, and a higher resolution and accuracy was desired for lower loads, an Instron 5948 MicroTester machine was used. A relatively rapid loading rate of 10 mm/min was used for these tests due to the large shear deformation possible with these woven composites.

In order to facilitate the DIC analysis, a standard 12 Megapixel Active Pixel Sensor (APS) camera was set up on a mount (shown in Figure 33) and aimed at the test region with images taken at regular 2 second intervals to capture 0.33 mm changes in bias extension according to the CRE. Regions of interest were speckled with silver markings on the samples, to enhance the reliability of the DIC analysis.

Two alternative specimen types have been used in literature [47], with very little work on comparing them. The first, 'narrow' sample type is a strip with length recommended to be two times its width [41]. The second is a wider test specimen, which is tested in a similar manner to the tensile grab test, with the width of the fabric protruding noticeably from the clamp jaws (see Figure 34). Both samples exhibit the same central, diamond shaped region of theoretically pure shear deformation that is the main area of interest for the DIC shear angle calculation.

Preparation of test samples was performed carefully due to the very low loads required to shear these fabrics. A careless operator could detrimentally shear a sample or ruin the weave architecture without noticing. As such, the most appropriate way to prepare and load test samples in the rig was to use adhesive tape around the perimeter of the gauge area to provide sufficient strength to resist deformation that might result from manual handling. Again, as with the tensile tests, adhesive tape was also used to cover both sides of the clamping areas (where three further holes needed to be punched for shear tests to fit in the bolted clamp jaws as

seen in Figure 35). Once specimens were clamped in place and ready for testing, the excess and tape-covered edges of the specimens were cut away. As can be seen in Figure 35, silver markings were dotted onto areas of interest for each test sample, this enhanced the capabilities of the DIC code to distinguish and track deformation (which becomes particularly difficult at high shear angles).

Shear Test Rig

Machine	Instron 5948 MicroTester
Load Cell	2 kN
Test Mode	Constant Rate of Extension (CRE)
Loading Rate	10 mm/min



Figure 33: Shear test rig details and method.

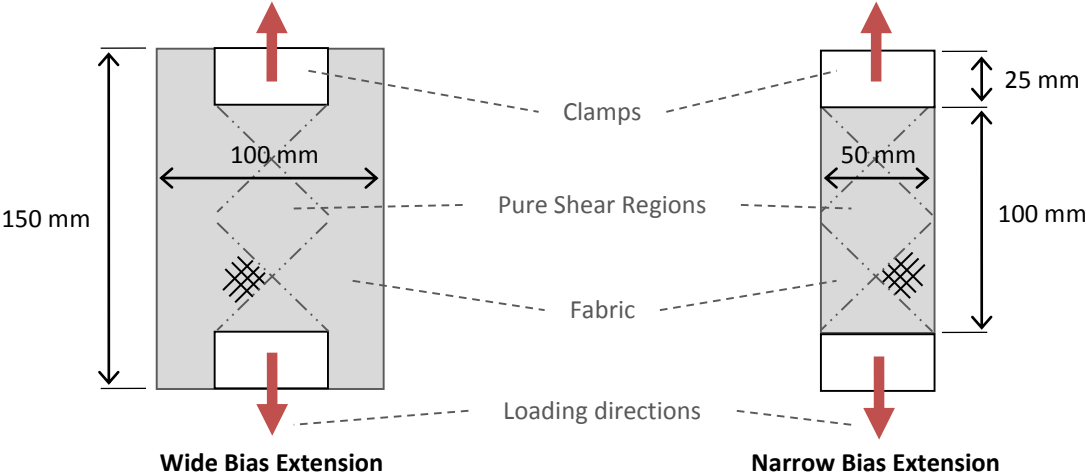


Figure 34: Bias extension test specimen dimensions: wide and narrow.

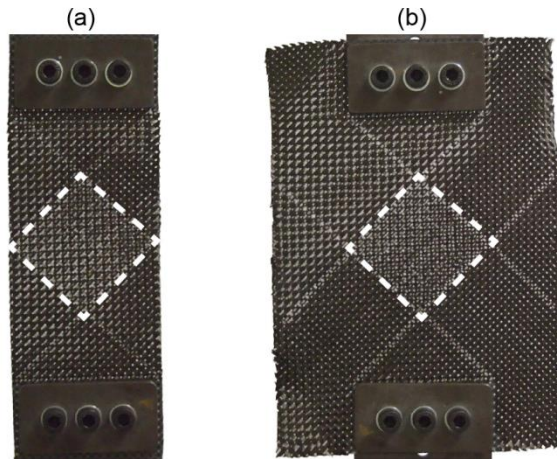


Figure 35: (a) Narrow and (b) wide bias extension test specimens in clamps ready for testing.

4.3.2 Narrow sample mechanical test results

Narrow test samples resulted in very low peak loads for the onset of shear locking in the material, at around 12 N. Hence, narrow sample testing was actually performed with a 0.1 kN load cell to avoid any resolution error that might have been intensified by the 2 kN load cell. A series of tests were still performed on the 2 kN load cell though, showing similar results, discounting any noticeable compliance or sensor error.

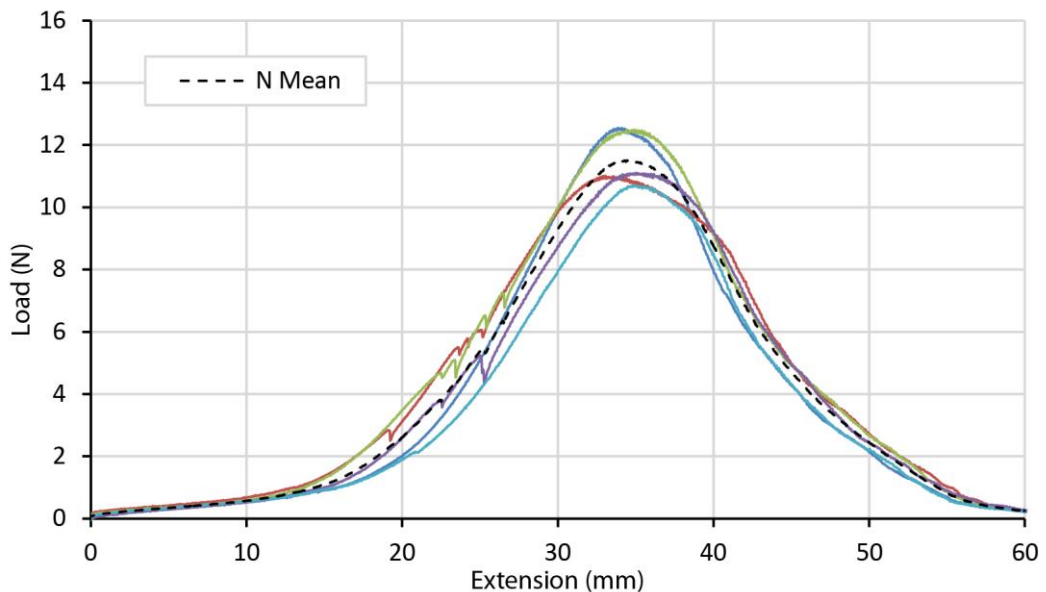


Figure 36: Raw test results for narrow sample shear testing plotted as load against extension.

Tests appeared to be quite repeatable, with only small differences in extension as load dramatically increases. This is likely due to differences in the initial set up of each sample, since it is particularly difficult to ensure that each sample is perfectly undeformed in the initial state. The possible variation between samples is estimated to be up to 2 mm, which is reflected by a shift seen in Figure 36.

From observation, bias extension tests with the narrow specimens initially exhibited a near-pure shear deformation as they were extended. Past an extension of 15-20 mm shear locking began to occur, after which the central shear zone appeared to approach a physical limit of

shear deformation. This resulted in the relatively sharp increase in loading shown in Figure 36, and is also reflected by the asymptotic behaviour seen in Figure 37 as the samples shear past 50°. However, approaching extensions of 30 mm, the weak frictional bonds between warp and weft yarns were being overcome by the higher loading, and resultantly yarn slippage was observed. This yarn slippage is the reason for the sudden drop in loading as the sample extension continued. The shear angle results plotted in Figure 37 have been determined from optical strain measurement techniques discussed in Section 4.4 and also demonstrate the repeatability of this bias extension test method.

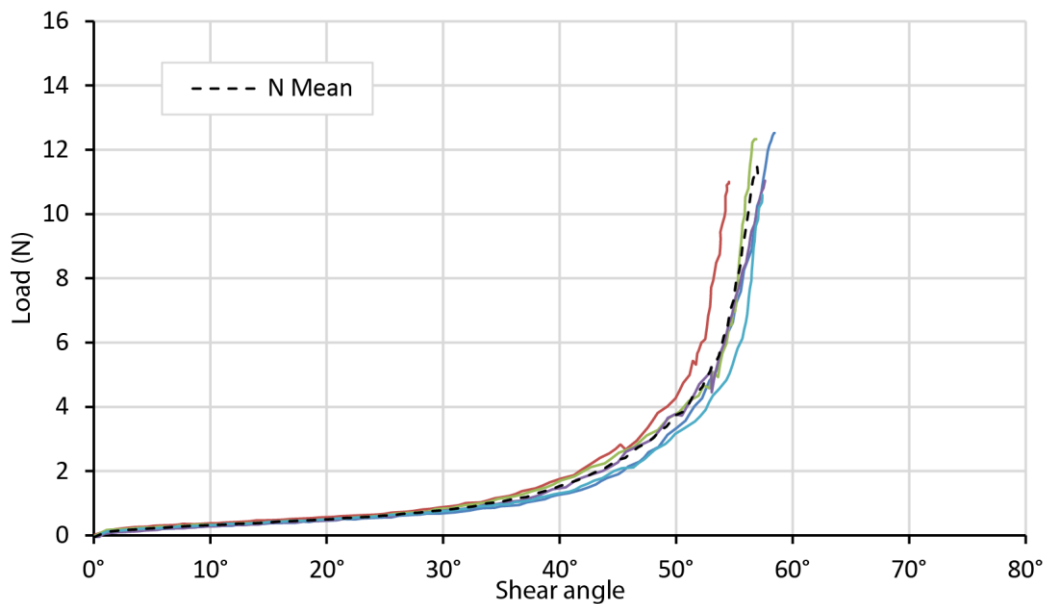


Figure 37: Narrow sample shear test results plotted as load against shear angle (determined from DIC).

4.3.3 Wide sample mechanical test results

In the bias extension testing of wide samples, tests were again very repeatable, all demonstrating the same behaviour (Figure 38). With the 2 kN load cell these tests recorded peak loads around 140 N. Although this is less than 10% of the load cell capability, the Instron 5948 MicroTester machine still provides a high accuracy in this range.

These wide sample tests displayed near pure shear deformation prior to shear locking, however as the warp and weft yarns locked, extension in the bias direction was additionally facilitated by some out-of-plane buckling. This mode was observed past 20 mm extension as small amplitude waves and wrinkles in the central shear zone, oriented with the bias and loading direction. As the loads increased the number of wave oscillations in this region increased with reducing periodicity. The amplitudes of these wrinkles only appeared to be of the order of a few millimetres. This type of wrinkling has been previously seen in similar high shear tests [51]. Once specimens were reaching extensions of 45 mm or more (at around their peak loading) these wrinkles would dissipate and the central shear zone would flatten out again.

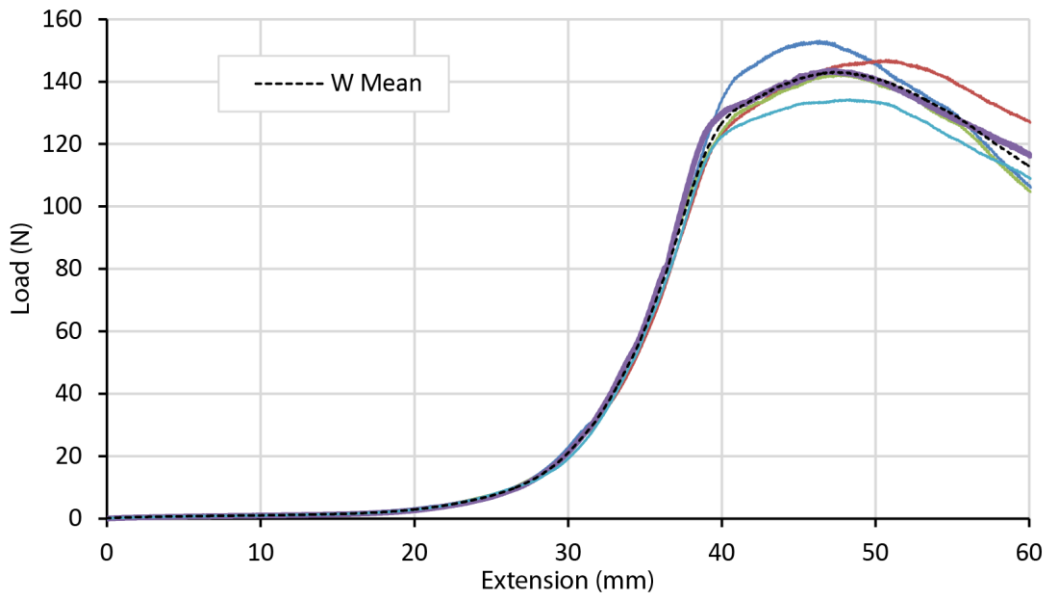


Figure 38: Raw test results for wide sample shear testing plotted as load against extension.

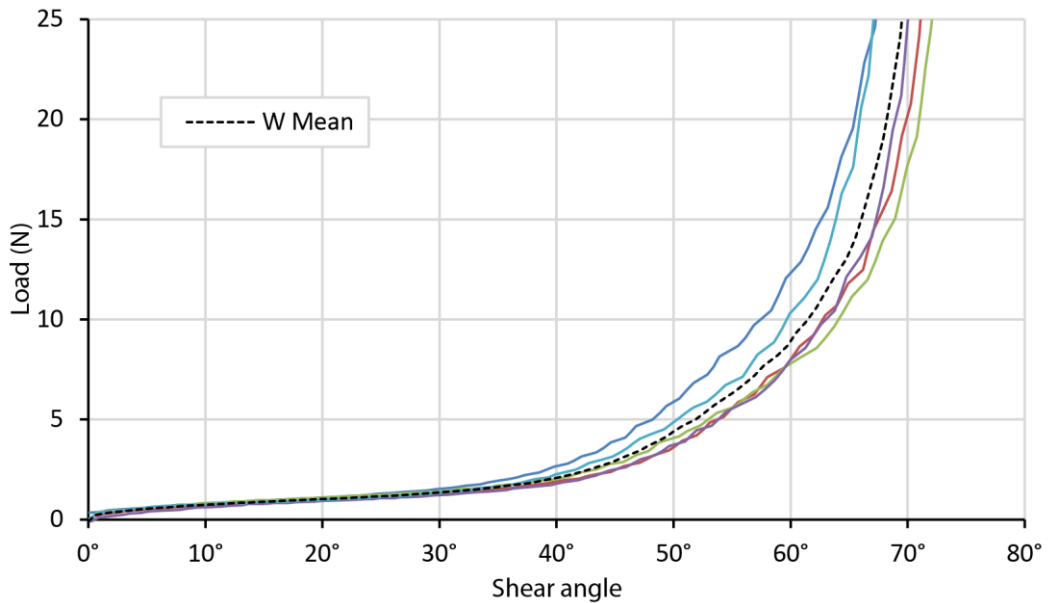


Figure 39: Wide sample shear test results plotted as load against shear angle (determined from DIC).

At extensions over 40 mm the results from different tests are seen to diverge somewhat, alluding to the late onset of slippage effects that then cause the loads to diminish. This would also explain the aforementioned disappearance of wrinkles as slippage becomes the primary mechanism for facilitating extension.

In the case of wide bias extension samples, there is some variation in the shear stiffening of the fabric as shown in Figure 39. This is expected to be a result of both the variation in initial specimen condition and the out-of-plane wrinkling having an effect on optical shear measurements. Again, the shear angle values reported in Figure 39 are from optical strain measurement techniques discussed in Section 4.4.

4.3.4 Comparison of test results from different samples

The two bias extension shear test samples (wide and narrow) exhibited quite different results despite the gauge lengths and clamping areas remaining the same (along with all the other test parameters). The first observation is that the wide bias extension samples are able to achieve much higher loads and even shear angles. This is clearly demonstrated by the comparison of mean sample values in Figure 40, where peak loads for wide samples are ten times greater than those for narrow samples. Wide samples also exhibit slightly higher loads even at lower extensions, which is likely to be caused by the additional resistance of the excess material around the gauge area. Figure 41 compares the shear stiffening behaviour of the two sample types, where narrow samples exhibit a reduced range of shear angles.

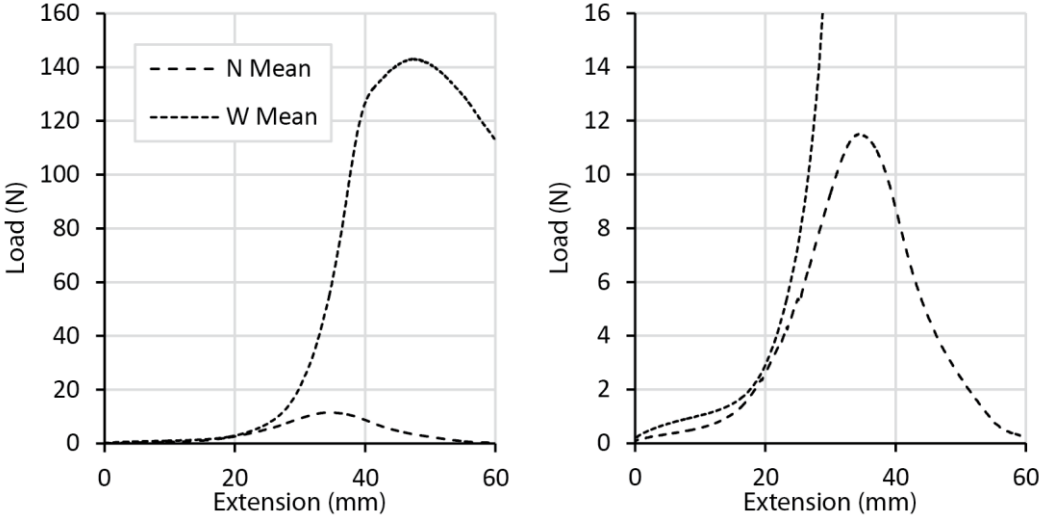


Figure 40: Comparison of wide and narrow bias extension sample load-extension results at two different scales.

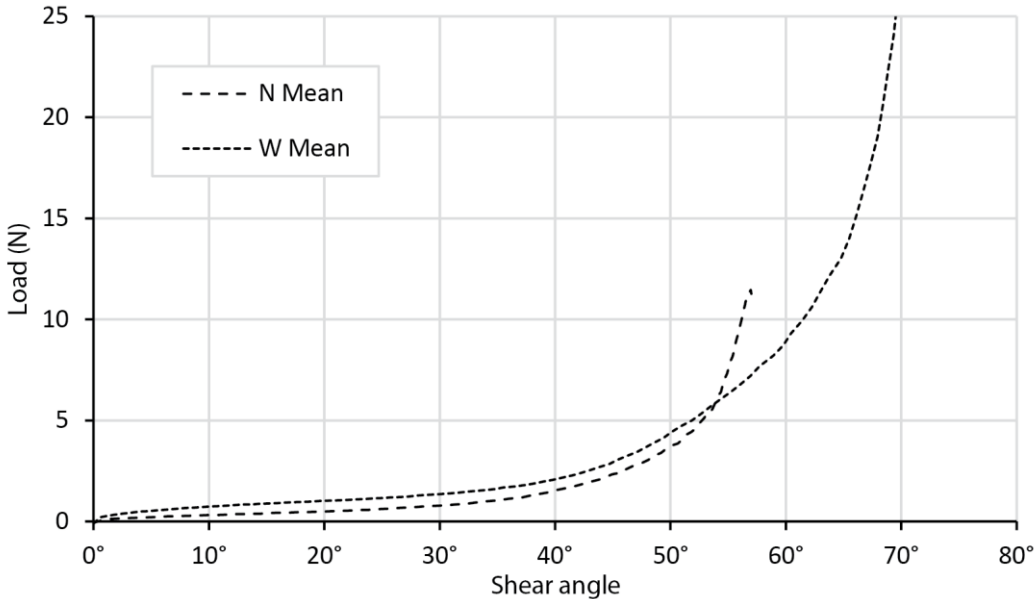


Figure 41: Comparison of wide and narrow bias extension sample load-shear-angle results from DIC.

Overall it is the frictional effects in the peripheral fabric architecture of wide specimens that is restricting and preventing yarn rearrangement and slippage. It is expected that this is the cause

for such different results between the two samples. Without yarn slippage to facilitate the extension of wide test samples, higher loads and shear angles are achievable, and out-of-plane bending effects are subsequently introduced.

4.4 Optical shear measurement

4.4.1 Method development

Optical measurement techniques used in material characterisation testing can be quite varied, ranging from primitive observational approaches to sophisticated 3D digital camera systems. Obviously, with the availability of low cost digital imaging, it is now most common to use digital Active Pixel Sensor (APS) or Charge-Coupled Device (CCD) cameras to record images of deforming test materials, although other low cost systems have been developed using flat-bed scanning technology [47]. Lately, the most popular technique for optical strain measurement is Digital Image Correlation (DIC) where sequential digital images of material deformation are correlated in computational software to determine changes and ultimately calculate the strains in the sample. Several complete package systems are often used, however they can be quite expensive and are generally designed for axial strain applications. Because the calculation of fabric shear strain relies on accurate yarn tracking (not simply speckle feature tracking), these costly generic packages can only be employed with considerable post-processing calculations. Hence, an alternative, low-cost system designed specifically for fabric shear testing and yarn tracking was desirable.

For the bias extension method, interest lies solely in the in-plane shear response of the fabric material, and as such a two camera, 3D system was deemed unnecessary; particularly as these systems can actually be less accurate for tracking in-plane deformation than a single camera system. Additionally, since the desired output for these tests is an angular change, there is no need for any image calibration (unlike axial strain applications). Thus a regular APS digital camera (12 Megapixel) was used to take the series of still images used in the Digital Image Correlation (DIC).

A rather comprehensive DIC code has been developed in MATLAB for the optical tracking and measurement of shear deformation inspired by the freely available code for axial strain developed by Eberl et al. [105]. The new code, initially purposed for fabric shear testing, has also been published for free on the MathWorks File Exchange website [106] so that it may be used and improved upon by other researchers, rather than requiring other expensive DIC systems and software.

Although primarily intended to determine the shear strain (shear angles) in bias extension tests, this code can easily be adapted to other shear test methods such as the picture frame test. The following section outlines the workings of this code.

4.4.2 MATLAB Digital Image Correlation (DIC) code

The Matlab DIC code first automatically generates a list of the sequential image file names based on user identification of the first image in the sequence. At this point, time information is also extracted from the meta-data of each image file to be later linked with the output shear angle data. The user is also required to identify the region of interest and a spacing parameter between grid points for the cross correlation process. In the case of bias extension testing this

is the gauge section of the fabric sample, between the two clamps. An initially regular grid, based on the chosen grid spacing, is then generated over this region (where each grid location acts as a correlation point). Thus an initial grid of correlation points is fed into the image correlation section of the code along with the sequential image library, as depicted in Figure 42.

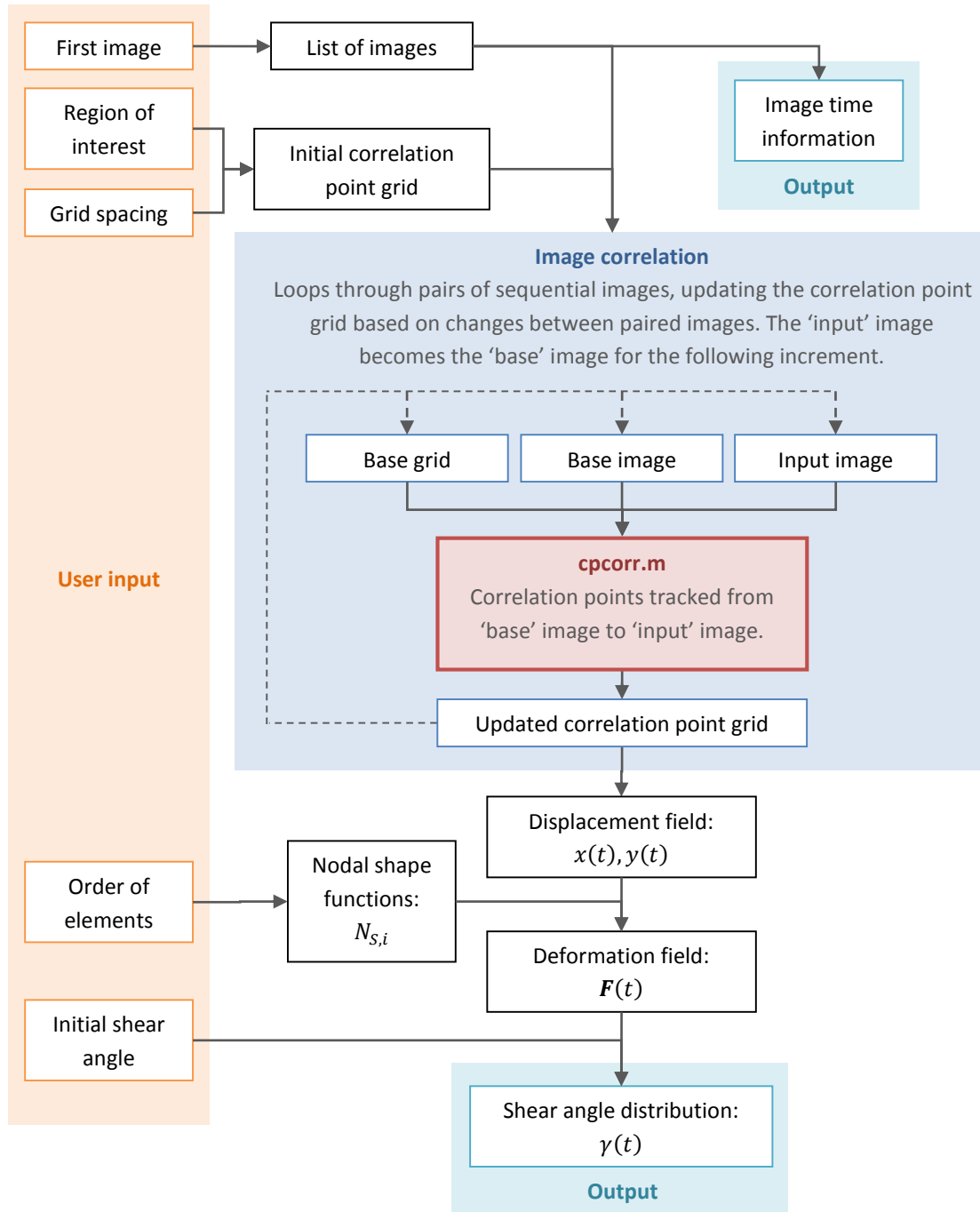


Figure 42: Process diagram for the MATLAB DIC code.

The actual image correlation is performed through a number of nested functions starting with 'cpcorr.m' (represented by Figure 43) from the MATLAB Image Processing Toolbox. Pairs of images (an initial 'base' image and a consecutive 'input' image) are incrementally passed into the cpcorr.m function along with a reference grid for the base image, in order to find a

displaced grid of reference points for the input image (to be used in the next image pair increment). Within the function, the two images are each broken down into smaller elements to enhance the efficiency of the cross correlation. For the input image, elements of size 40 x 40 pixels are created for, and centred on, every correlation point specified in the grid. Similarly for the base image, larger elements of size 80 x 80 pixels are created for, and centred on, the same correlation points.

Iteratively, for each correlation point in the grid, the associated elements or sub-images from the base and input images are then analysed using normalised 2D cross correlation with 'normxcorr2.m'. This process effectively compares the input and base sub-images by finding a 'correlation coefficient' for every possible pixel displacement within the base sub-image region. This can be thought of as a process of superposing the input sub-image (using its central correlation point pixel) over each pixel of the base image and calculating a correlation coefficient based on how well the images match at each different overlay position. A simplified example of this cross correlation process is described in Section 4.4.3.

The actual analytical theory being implemented within the normxcorr2.m function correlates the two sub-images using either the 2D convolution in the spatial domain or 2D discrete Fourier transforms in the frequency domain (depending on which is expected to be faster). As outlined in the MATLAB documentation [107], the cross-correlation is then normalised to find correlation coefficients, largely based on work by J.P. Lewis [108].

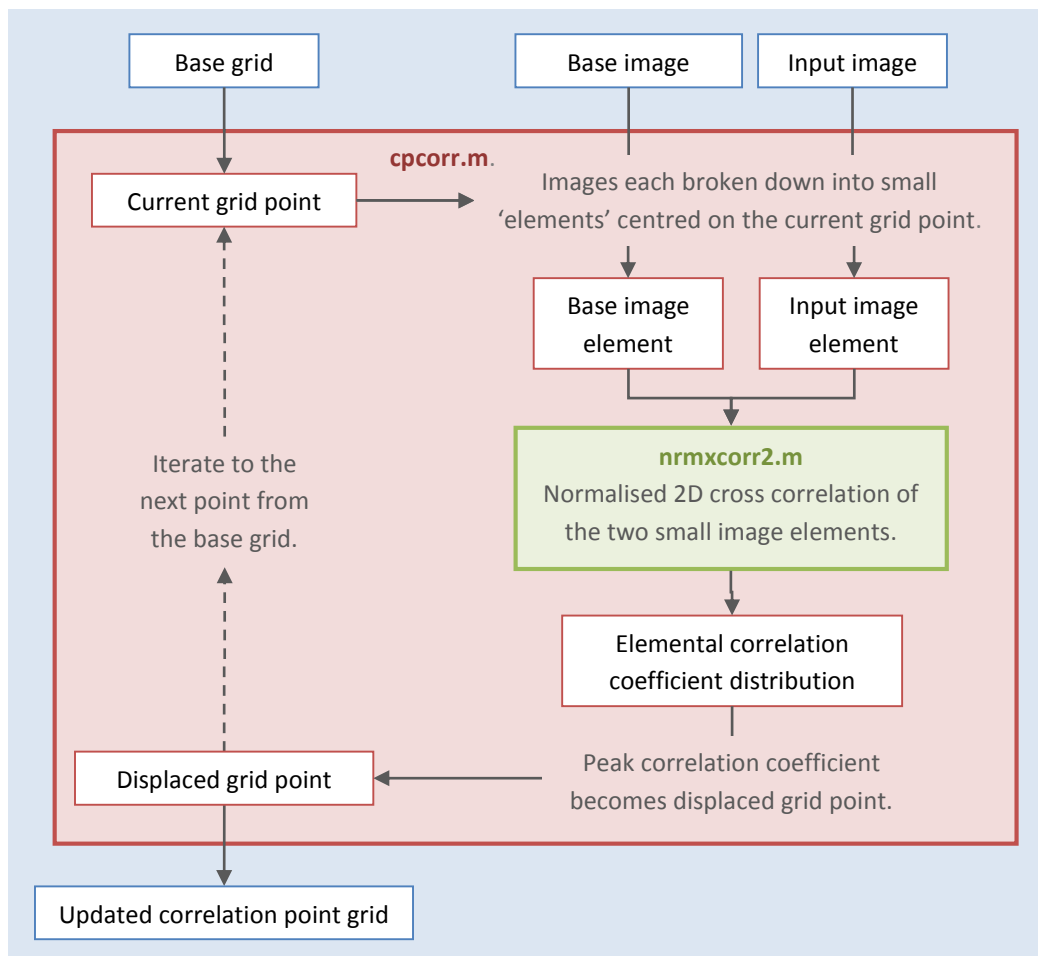


Figure 43: Process diagram for the inset cpcorr.m component of the MATLAB DIC code.

The elemental correlation coefficient distributions from normxcorr2.m for each grid point are post-processed in cpcorr.m to eliminate any poor or undesirable correlation results. The peak correlation coefficient of each normalised elemental distribution corresponds to the displaced location of a specific grid point from the base image to the input image. These displaced grid points are then combined to generate the updated correlation point grid for use with the next incremental image pair. This process continues to loop through image pairs, updating changes to the correlation point grid with respect to the image time-stamp information until the whole image sequence has been analysed.

After the image correlations have been performed for every correlation point and for every pair of images in the sequence, the x and y displacements of each correlation point corresponding to each image through time are known. Subsequently, the shear strain (and shear angles) in the fabric specimen are calculated as follows for the central shear zone based on this known displacement field.

Firstly, adjacent points from the correlation grid are grouped to form linear four-node or biquadratic nine-node elements, depending on the desired order of elements, as shown in Figure 44. For each element type, shape functions and spatial relationships are outlined in Table 2. Where x and y are the deformed displacements at any point within the element based on the deformed nodal displacements x_i and y_i . Similarly, X and Y are the displacements of the initial state for any point within the element based on nodal displacements X_i and Y_i .

With the known shape functions and spatial relationships (for either the 4 or 9 node configurations), the deformation gradient tensor, \mathbf{F} , can be determined:

$$\mathbf{F} = \frac{d\mathbf{x}}{d\mathbf{X}} = \begin{bmatrix} \frac{dx}{dX} & \frac{dx}{dY} \\ \frac{dy}{dX} & \frac{dy}{dY} \end{bmatrix} \quad (27)$$

Hence the deformation gradient tensor, \mathbf{F} , is determined from the known derivatives of x , y , X and Y . From this point on the method for calculating the shear angle essentially follows the same theory as was outlined in Section 3.2 for the VUMAT subroutine; tracking the fibre directions non-orthogonally. The stretch tensor, \mathbf{U} , and rotation tensor, \mathbf{R} , are calculated as follows:

$$\mathbf{U} = \sqrt{\mathbf{F}^T \mathbf{F}}, \quad \mathbf{R} = \mathbf{F} \mathbf{U}^{-1} \quad (28)$$

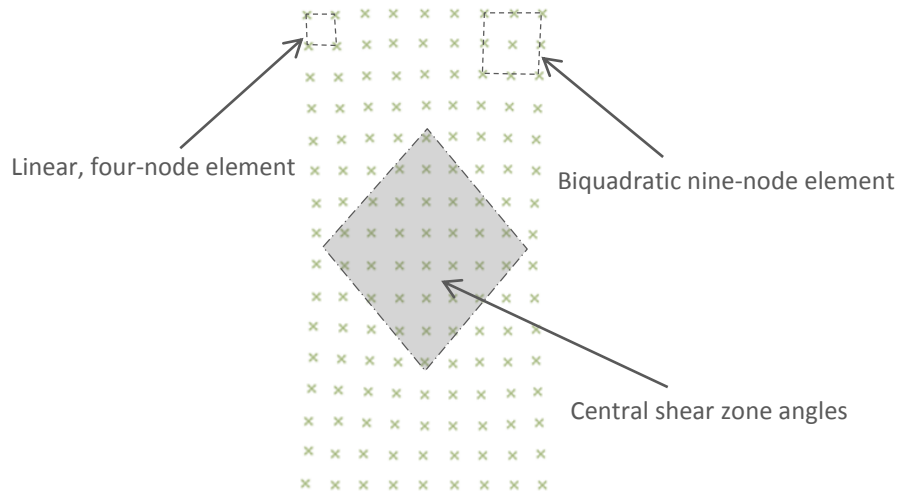


Figure 44: Example of bias extension test correlation point grid after some deformation.

Table 2: Comparison of the two different order elements.

	Linear, four-node elements	Biquadratic, nine-node elements
Element composition		
Shape functions	$N_{S,1} = \frac{1}{4}(1 - \xi)(1 - \eta)$ $N_{S,2} = \frac{1}{4}(1 + \xi)(1 - \eta)$ $N_{S,3} = \frac{1}{4}(1 + \xi)(1 + \eta)$ $N_{S,4} = \frac{1}{4}(1 - \xi)(1 + \eta)$	$N_{S,1} = \frac{1}{4}(1 - \xi)(1 - \eta) - \frac{1}{2}N_{S,5} - \frac{1}{2}N_{S,8} - \frac{1}{4}N_{S,9}$ $N_{S,2} = \frac{1}{4}(1 + \xi)(1 - \eta) - \frac{1}{2}N_{S,5} - \frac{1}{2}N_{S,6} - \frac{1}{4}N_{S,9}$ $N_{S,3} = \frac{1}{4}(1 + \xi)(1 + \eta) - \frac{1}{2}N_{S,6} - \frac{1}{2}N_{S,7} - \frac{1}{4}N_{S,9}$ $N_{S,4} = \frac{1}{4}(1 - \xi)(1 + \eta) - \frac{1}{2}N_{S,7} - \frac{1}{2}N_{S,8} - \frac{1}{4}N_{S,9}$ $N_{S,5} = \frac{1}{2}(1 - \xi^2)(1 - \eta) - \frac{1}{2}N_{S,9}$ $N_{S,6} = \frac{1}{2}(1 + \xi)(1 - \eta^2) - \frac{1}{2}N_{S,9}$ $N_{S,7} = \frac{1}{2}(1 - \xi^2)(1 + \eta) - \frac{1}{2}N_{S,9}$ $N_{S,8} = \frac{1}{2}(1 - \xi)(1 - \eta^2) - \frac{1}{2}N_{S,9}$ $N_{S,9} = (1 - \xi^2)(1 - \eta^2)$
Spatial relationships	$x = \sum_{i=1}^4 N_{S,i}(\xi, \eta) x_i, \quad y = \sum_{i=1}^4 N_{S,i}(\xi, \eta) y_i$ $X = \sum_{i=1}^4 N_{S,i}(\xi, \eta) X_i, \quad Y = \sum_{i=1}^4 N_{S,i}(\xi, \eta) Y_i$	$x = \sum_{i=1}^9 N_{S,i}(\xi, \eta) x_i, \quad y = \sum_{i=1}^9 N_{S,i}(\xi, \eta) y_i$ $X = \sum_{i=1}^9 N_{S,i}(\xi, \eta) X_i, \quad Y = \sum_{i=1}^9 N_{S,i}(\xi, \eta) Y_i$

Now considering a set of axes for the initial state of the fibre directions, \mathbf{g}_α^0 (which are determined by the initial shear angle), by multiplication with the rotation tensor a set of current axes, \mathbf{g}_α , changed only by a rotation can be found (where $\alpha = 1,2$ signifies the two independent principal fibre directions, and the 0 superscript represents the initial undeformed state):

$$\mathbf{g}_\alpha = \mathbf{R} \cdot \mathbf{g}_\alpha^0 \quad (29)$$

Next the actual fibre directions, \mathbf{f}_α , can be calculated from the initial fibre axes, \mathbf{g}_α^0 , and deformation gradient, \mathbf{F} :

$$\mathbf{f}_\alpha = \frac{\mathbf{F} \cdot \mathbf{g}_\alpha^0}{\|\mathbf{F} \cdot \mathbf{g}_\alpha^0\|} \quad (30)$$

The angles between the actual fibre axes, \mathbf{f}_α , and the simply rotated axes, \mathbf{g}_α , are calculated from the trigonometric definitions in Equations (31) and (32).

$$\cos \theta_\alpha = \frac{\mathbf{g}_\alpha \cdot \mathbf{f}_\alpha}{\|\mathbf{g}_\alpha\| \|\mathbf{f}_\alpha\|} = \frac{g_{\alpha,1}f_{\alpha,1} + g_{\alpha,2}f_{\alpha,2}}{\sqrt{g_{\alpha,1}^2 + g_{\alpha,2}^2} \sqrt{f_{\alpha,1}^2 + f_{\alpha,2}^2}} \quad (31)$$

$$\sin \theta_\alpha = \frac{\mathbf{g}_\alpha \times \mathbf{f}_\alpha}{\|\mathbf{g}_\alpha\| \|\mathbf{f}_\alpha\|} = \frac{g_{\alpha,1}f_{\alpha,2} - g_{\alpha,2}f_{\alpha,1}}{\sqrt{g_{\alpha,1}^2 + g_{\alpha,2}^2} \sqrt{f_{\alpha,1}^2 + f_{\alpha,2}^2}} \quad (32)$$

Then finally the shear angle is calculated by finding the difference between the two angles. This is the shear angle resulting from the change between the initial and the current state, at the centroid of each element in the formulation. In bias extension testing the main region of interest is the central shear zone (as highlighted by Figure 44). The calculated change in shear angle for each element in the central shear zone is then added to the input initial shear angle, resulting in the actual shear angle for each point, which can then be averaged across the central shear zone. This whole process is visualised in Figure 42 and Figure 43.

Additionally, because the fibre directions are monitored with this method, the effective normal strain in yarn directions can also be calculated by the DIC code, providing an additional measure for sample analysis. Normal strains from the stretch tensor, \mathbf{U} , can be converted from the global directions to the two fibre directions with the transformation matrix, \mathbf{T}_α , as described by Equation (33). Effective strains in each of the yarn directions are then $\varepsilon_{11}^{f_1}$ and $\varepsilon_{22}^{f_2}$.

$$\mathbf{T}_\alpha = \begin{bmatrix} \cos \theta_\alpha & -\sin \theta_\alpha \\ \sin \theta_\alpha & \cos \theta_\alpha \end{bmatrix}, \quad \alpha = 1,2 \quad (33)$$

$$\mathbf{U}^{f_\alpha} = \begin{bmatrix} \varepsilon_{11}^{f_\alpha} & \varepsilon_{12}^{f_\alpha} \\ \varepsilon_{21}^{f_\alpha} & \varepsilon_{22}^{f_\alpha} \end{bmatrix} = \mathbf{T}_\alpha^T \mathbf{U} \mathbf{T}_\alpha = \mathbf{T}_\alpha^T \begin{bmatrix} \varepsilon_{11} & \varepsilon_{12} \\ \varepsilon_{21} & \varepsilon_{22} \end{bmatrix} \mathbf{T}_\alpha \quad (34)$$

One important note is that the code assumes the initial shear angle is uniform across the fabric sample, which is not strictly true. This is because the bias extension method results in three

clear shear zones: the central diamond which is expected to have shear angle γ , the triangular regions next to the clamps which are expected to have no shearing, and the rest of the sample which will typically shear at $\gamma/2$. Hence if the initial shear angle in the central diamond (where the user is meant to measure as an input) is not zero, then other 2 shear regions will not be equivalent. This also ignores any slight natural variations in shear angle. However, as the desired results are from the central shear region, and the initial shear angle should not be much greater than zero, this assumption is justified. Any DIC shear angle measurements outside the central shear zone, in samples with a non-zero initial shear angle, will be less accurate though.

Ultimately, the advantage of the MATLAB DIC code, is that it can calculate and display shear angle distributions across samples specific to textile shear testing. Moreover, the design of the code facilitates the calculation of strains in the actual yarn directions, not simply in the assumed orthogonal material directions, which again is not an option in the more generalised DIC software packages.

4.4.3 Simplified cross correlation example

As a demonstration of the cross correlation procedure employed in the MATLAB DIC code, the following example is described. Two sequential images (51 x 51 pixels) are shown below in Figure 45, where a light grey cross moves from an off-centre position (first image) to a central position (second image). Sequential images such as these are termed ‘base’ and ‘input’ images respectively, as the movement of features is tracked from the initial base position to the input position.

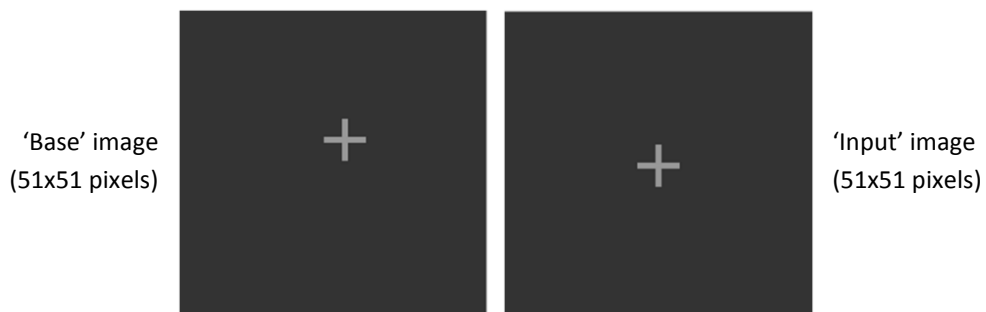


Figure 45: Sequential ‘base’ and ‘input’ images of a moving cruciform feature.

Assigning only a single correlation point to both images (located at the same central grid point), a subset image element is taken from both the base and input images centred at the correlation point (of sizes 22 and 11 pixels squared respectively) as seen in Figure 46. Here the base image element is larger in size so that the features visible in the input image can be matched with similar features that have only moved a short finite distance (within the base image element) in the time between images.

As noted in the process diagram (Figure 43), the two image elements are passed into the cross correlation function, `normxcorr2.m`, which then finds a normalised correlation coefficient distribution. This is done by effectively comparing every possible position of the input image element (which is expected to have ‘moved’ but still lie within the larger base image element region) relative to the base image element. As the centre point of the input sub-image could have potentially moved to the edges or corners of the base sub-image, the greater distribution

becomes 31x31 pixels (22+11-1) as seen in Figure 47. The relative overlay position of the peak result is shown on the right of this figure, with the peak of this distribution being 1 and coloured white where the cruciform feature of the input image element lines up exactly with that of the base image element. Once the peak correlation point is identified, the displacement of the cruciform feature from image to image can be determined. As seen in Figure 47, the desired displacement of the correlation point, AB, can be found, since the relative displacements OA and OB are known. Obviously this can be extended to larger images with multiple correlation points and less distinct features, as is the case for the bias extension DIC.

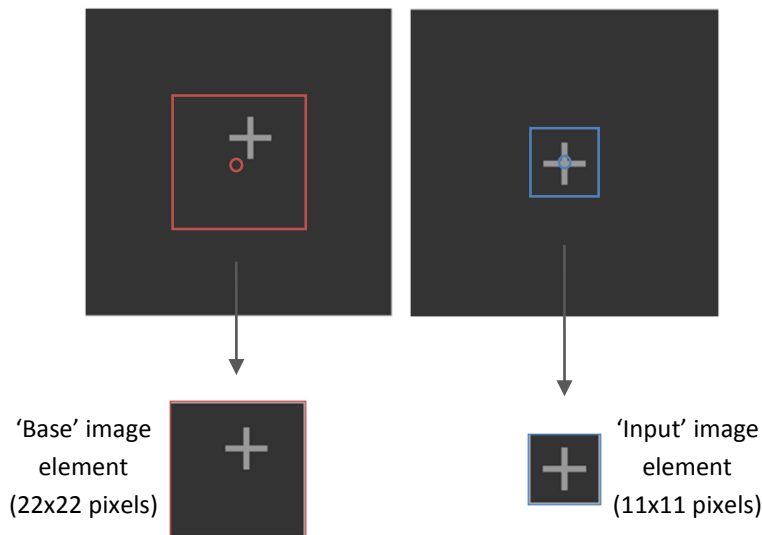


Figure 46: 'Base' and 'Input' image elements selections from sequential images.

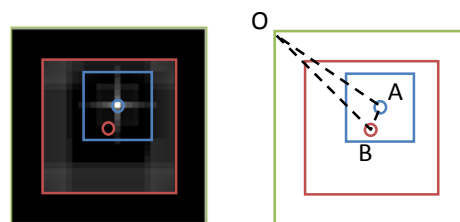


Figure 47: Normalised correlation coefficient distribution with image elements overlaid at the location of peak correlation, and the vectors used to calculate the displacement.

4.4.4 Evaluation of DIC results

The Digital Image Correlation (DIC) code was employed to calculate the fabric shearing across narrow and wide bias extension test samples. In order to validate these results, 'manual' measurements of the shear angle in the central shear zone were also taken for the comparison shown in Figure 48. These were measured directly from the digital images from each test, one image at a time. There is generally a very good agreement, however at high shear angles the manual measurements actually became prone to greater error as yarns became increasingly difficult distinguish with the human eye. This error stands out most with the narrow (N) sample results, although the problem was the same for the wide (W) samples and the measured results above 50° became unreliable for validation purposes. As a result, the DIC shear angle predictions actually appeared to be more accurate than human measurements. This is not unreasonable as subtle differences in tones and colours can be objectively compared by the coding approach. However, definitive validation for shear angles above 50° would need to be

undertaken in order to confirm this. For the purpose of this work, the easily measured angles below 50° have shown good validation of the DIC approach within the expected draping range.

Upon careful evaluation of the results in Figure 48, one could interpret the difference between wide and narrow samples to be significant (for a given load at shear angles below 2 N there might be a 15° difference in shear angle). However, for the purposes of shear modulus characterisation this difference indeed becomes negligible (as is demonstrated and discussed in Section 4.5).

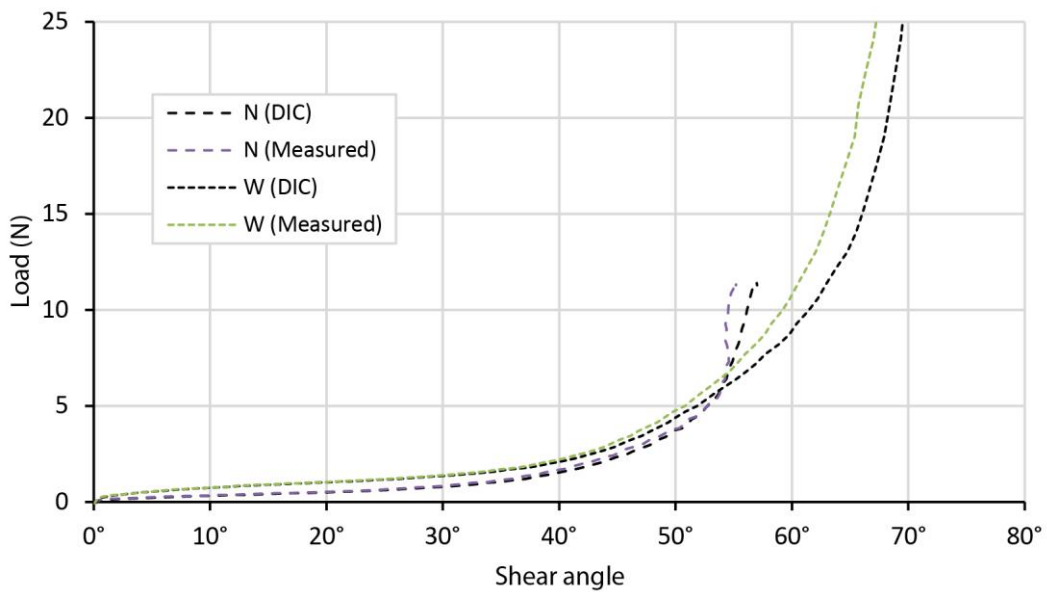


Figure 48: Load and shear angle results from DIC and digital measurement.

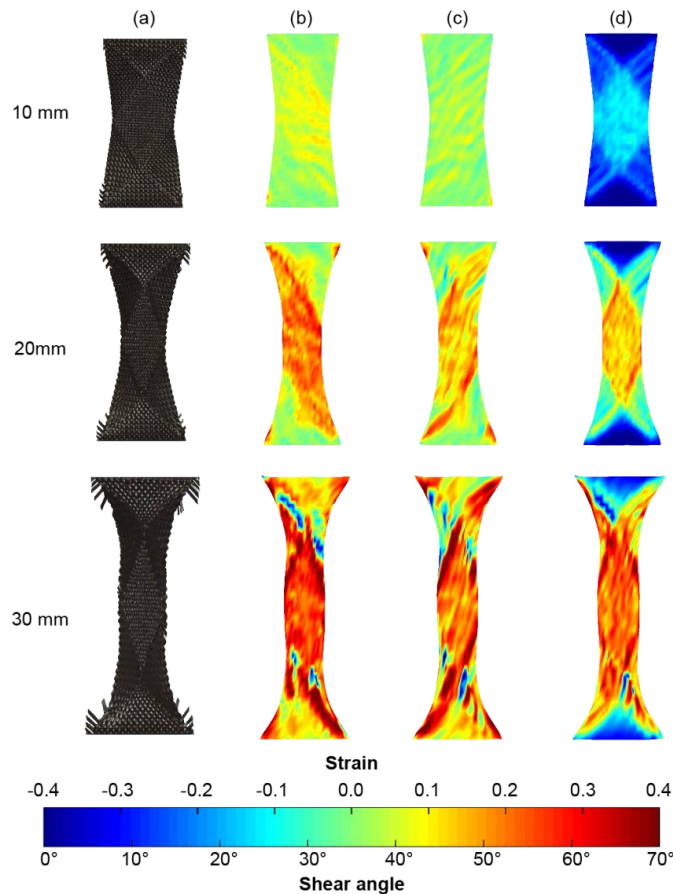


Figure 49: Narrow bias extension test results: (a) images, (b) warp yarn artificial strain, (c) weft yarn artificial strain and, (d) shear angle distribution from DIC.

For a detailed look at the DIC results for both the narrow and wide samples, Figure 49 and Figure 50 compare them with images of the actual samples at 10 mm extension increments. The qualitative change in the DIC correlation point region shows very good agreement with the changing shape of the test samples in these figures. In addition to the shear angle determination (d), the ‘artificial’ tensile strains in the warp (b) and weft (c) yarn directions have also been calculated by the code and are displayed in these figures.

These artificial strains are calculated from the transformation of stretch values into each of the fibre directions. The artificial strain values include contributions from yarn strain, yarn slippage and any error in the DIC. Since yarn strain is expected to be negligible (at less than 0.002 for the experienced loads) the artificial strain visualised in these figures is primarily an indicator of yarn slippage.

Focusing on the shear angle distribution results from DIC, it can be seen that, in general, the three distinct zones of shearing show reasonable agreement with theoretical assumptions. The triangular regions adjacent to the clamps exhibit negligible shearing, with peak shear values seen in the central diamond that are twice that of the adjacent intermediate regions.

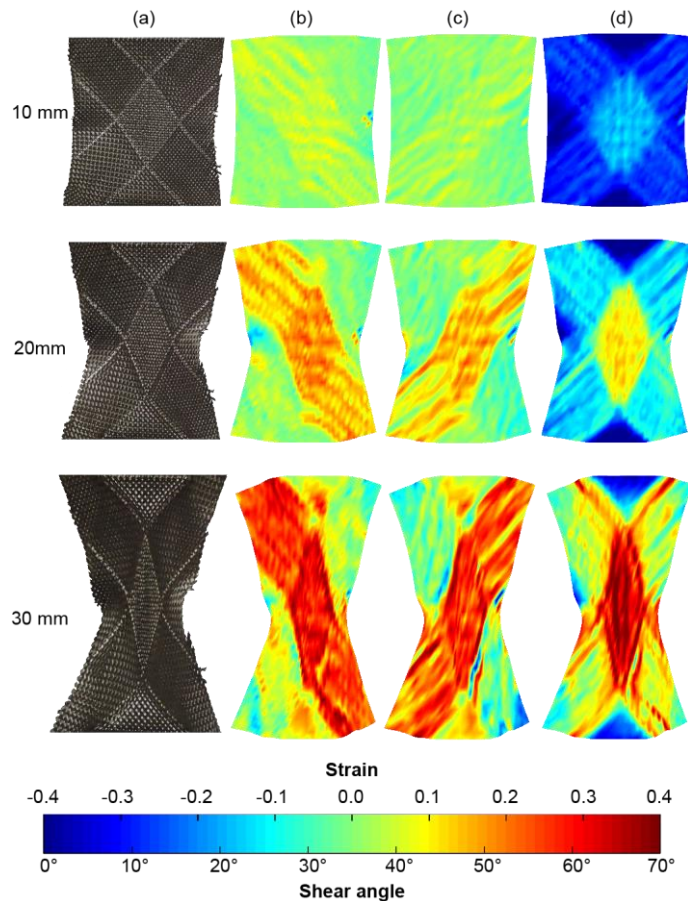


Figure 50: Wide bias extension test results: (a) images, (b) warp yarn artificial strain, (c) weft yarn artificial strain and, (d) shear angle distribution from DIC.

However, there is also increased shearing calculated at the interface of the different shear zones, more so for the narrow samples at lower extension. It is likely that the increase of calculated shearing in the zone interfaces, coupled with higher artificial yarn strains, is actually being caused by yarn slippage since these are the areas where yarn slippage is well documented to occur [109]. This slippage is also evidenced from the actual photos, where yarn fraying can be seen in the narrow sample edges. The wide samples do not show the same problem, and at 30 mm extension the DIC results appear to be much more reliable (with none of the local correlation errors or discontinuities that are visible in the narrow DIC results). Similarly, the artificial strains calculated in the warp and weft yarn directions are more consistent in the wide samples than the narrow samples (where there are greater stress concentrations).

The 30 mm extension results reveal the limitations of the narrow test samples, where wider samples are capable of achieving much higher shear angles with reduced slippage. In the wide samples some of the out-of-plane wrinkling behaviour is even observed by the DIC code, vertical lines of artificially increased shear angle are recorded, these correspond with the walls of wrinkles from the test images. Though this out-of-plane behaviour will clearly have an effect on the accuracy of the 2D DIC, it is only observed at high shear angles (above 55°) and therefore the DIC results for the more realistic draping range (below 55°) are still reliable from the 2D system.

4.5 Shear modulus determination

With detailed force, extension and shear angle data from the bias extension experiments and Digital Image Correlation (DIC), the next step is to reduce this description of the fabric material behaviour down to the shear modulus. In order to determine the non-linear shear modulus, a theoretical normalised shear force (and subsequent shear stress) is determined as outlined by Lebrun et al. [110]. This process is founded on some basic theoretical assumptions [50]. Firstly, that samples are divided into three distinct and uniform shear zones (A, B and C in Figure 51), within which the shear angles are uniformly: γ , $\gamma/2$ and zero respectively. Secondly, in this particular case, the samples must have a height that is twice the width. Furthermore, it is assumed that samples experience no yarn slippage, and though unrealistic, it provides a reasonable foundation for determining the shear modulus.

The theoretical shear angle, γ , in a bias extension sample is related to the change in angle of the sample from an undeformed state (assuming $\theta_0 = 45^\circ$), the geometric height, H , and width, W , of the sample and the extension during testing, δ , as shown in Equation (35).

$$\gamma = 2\theta_0 - 2\theta, \quad \text{where } \theta = \cos^{-1}\left(\frac{H - W + \delta}{\sqrt{2}(H - W)}\right) \quad (35)$$

This geometric calculation of the theoretical relationship between shear angle and extension is shown in Figure 52 against the experimental DIC results for both the narrow and wide bias extension tests. From this, it can be seen that the theoretical relationship diverges from the actual test results since it is based on simplistic assumptions of the deformation behaviour. The majority of the deviation is expected to be due to yarn slippage, which is not accounted for by the theoretical predictions.

Next, the normalised shear force (per unit length), $F_{sh}(\gamma)$, expected in bias extension testing can be calculated and expressed in terms of shear angle, γ , normal bias force, F_b (as recorded from testing), height and width:

$$F_{sh}(\gamma) = \frac{1}{(2H - 3W) \cos \gamma} \left[\left(\frac{H}{W} - 1 \right) F_b \left(\cos \frac{\gamma}{2} - \sin \frac{\gamma}{2} \right) - W F_{sh} \left(\frac{\gamma}{2} \right) \cos \frac{\gamma}{2} \right] \quad (36)$$

Since this requires the shear function of the half shear angle, it is an iterative process to calculate the full range of force-shear curves based on the initial assumption:

$$F_{sh} \left(\frac{\gamma}{2} \right) = \frac{F_{sh}(\gamma)}{2} \quad (37)$$

Then any values of shear force at half shear angle that have not been previously determined are simply interpolated between the known values. To calculate the shear stress, the normalised shear force needs to be multiplied by the edge length of the central shear zone, and then divided by the cross section area of this zone:

$$\tau(\gamma) = \frac{W F_{sh}(\gamma)}{\sqrt{2} A} \quad (38)$$

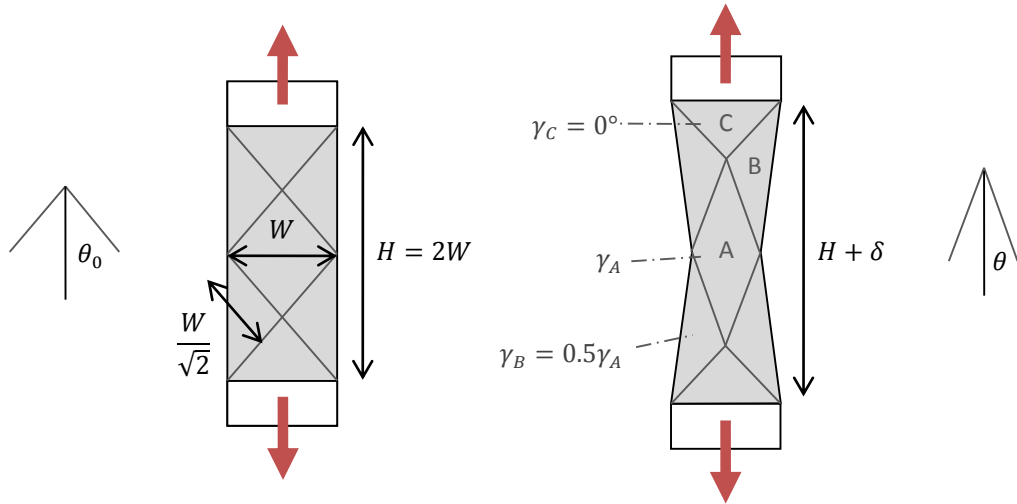


Figure 51: Schematic for bias extension testing theory.

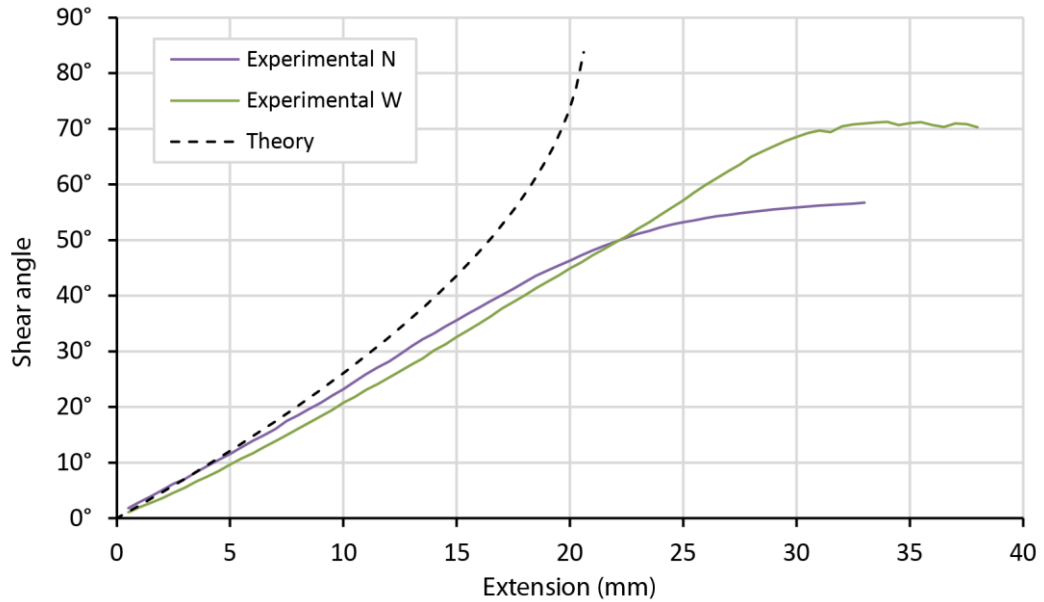


Figure 52: Shear angle and extension relationship for bias extension theory and both narrow (N) and wide (W) experiments.

This function of shear stress is then fit with an appropriate function approximation. In the case of fabric shearing, a double exponential function of the form seen in Equation (39) is used to represent the shear stress.

$$\tau(\gamma) = ae^{b\gamma} + ce^{d\gamma} + k \quad (39)$$

The derivative of this forms the shear modulus of the fabric behaviour in terms of shear angle (shear strain) in Equation (40).

$$G_{12}(\gamma) = \frac{d\tau}{d\gamma} = bae^{b\gamma} + dce^{d\gamma} \quad (40)$$

Using the shear angle results from DIC in conjunction with the raw experimental measurements, the calculated shear stress function has been determined for both sample types and is shown in Figure 53. The double exponential curve fit for both narrow and wide

cases is also plot, based on the parametric values outlined in Table 3. These curve fit functions show very good agreement with the calculated shear stress values, and similarly when the derivative function, Equation (40), is graphed against a numerical derivative of the calculated shear stress the good agreement remains (Figure 54).

Table 3: Parametric values for the shear stress and shear modulus functions of narrow and wide samples.

	Narrow	Wide
<i>a</i>	0.001933 MPa	0.001247 MPa
<i>b</i>	4.240	4.896
<i>c</i>	1.0560×10^{-11} MPa	4.336×10^{-18} MPa
<i>d</i>	23.690	31.480
<i>k</i>	0.00 MPa	0.01 MPa

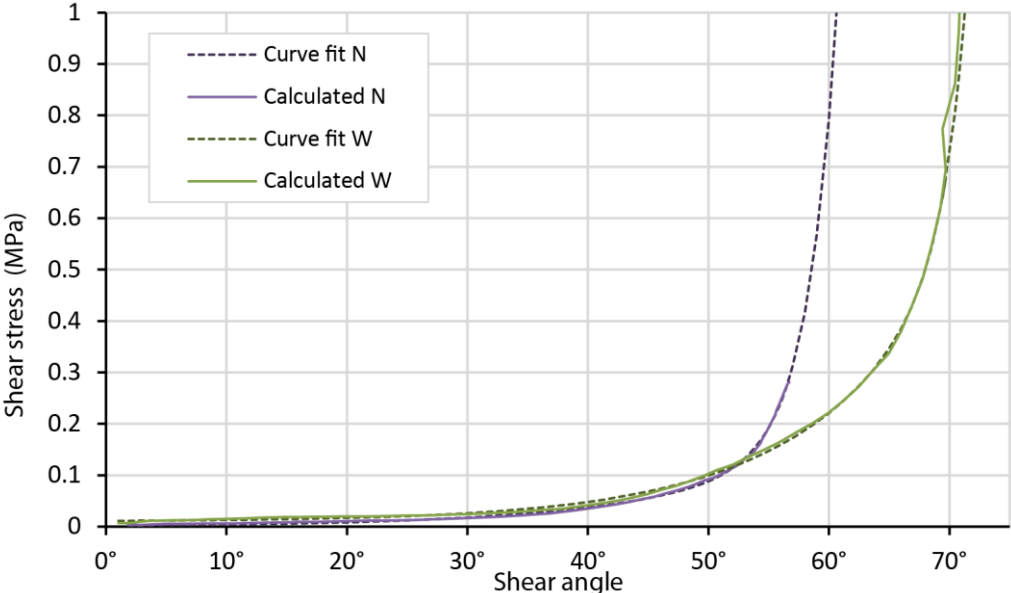


Figure 53: Shear stress and shear angle relationship for narrow (N) and wide (W) bias extension cases including curve fitting functions.

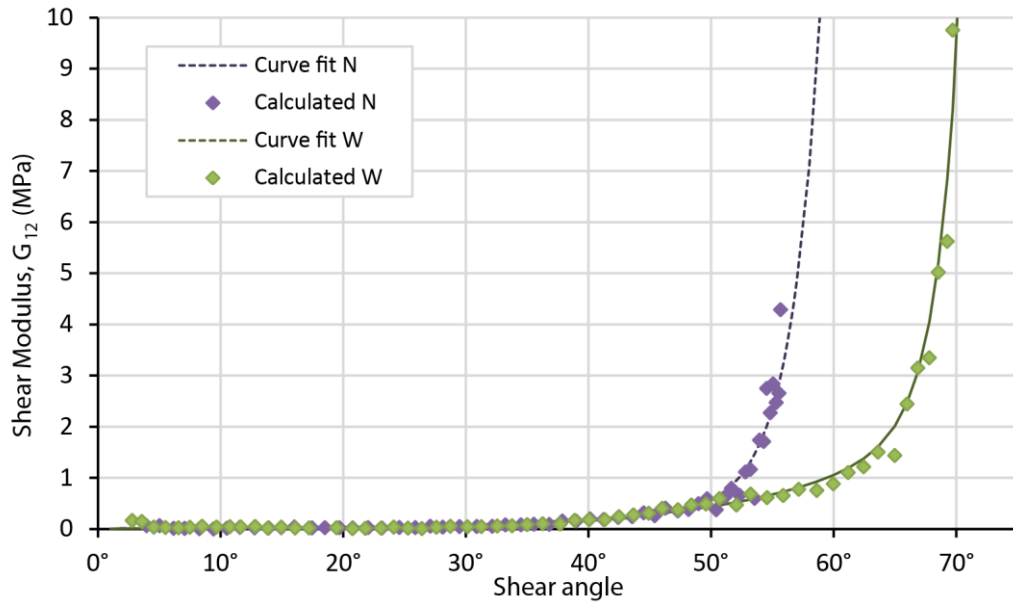


Figure 54: Shear modulus and shear angle relationship for narrow (N) and wide (W) bias extension cases including curve fitting functions.

In order to evaluate these shear modulus curves for modelling purposes, simulations of the bias extension tests were performed using the draping model discussed in Chapter 2. For both sample types, the simulated bias extension tests produced quite good agreement with the experimental load and shear angle curves (Figure 55). However, because the model also does not account for yarn slippage there is a greater disparity between the simulated and experimental results for shear angle and extension data in Figure 56. Here the simulations show greater agreement with the simple theoretical curve, with the exception of the improved modelling of the shear locking phenomenon. As a result of this deviation, the shear stress and shear angle results also show a reduction in agreement with the experimental calculations in Figure 57.

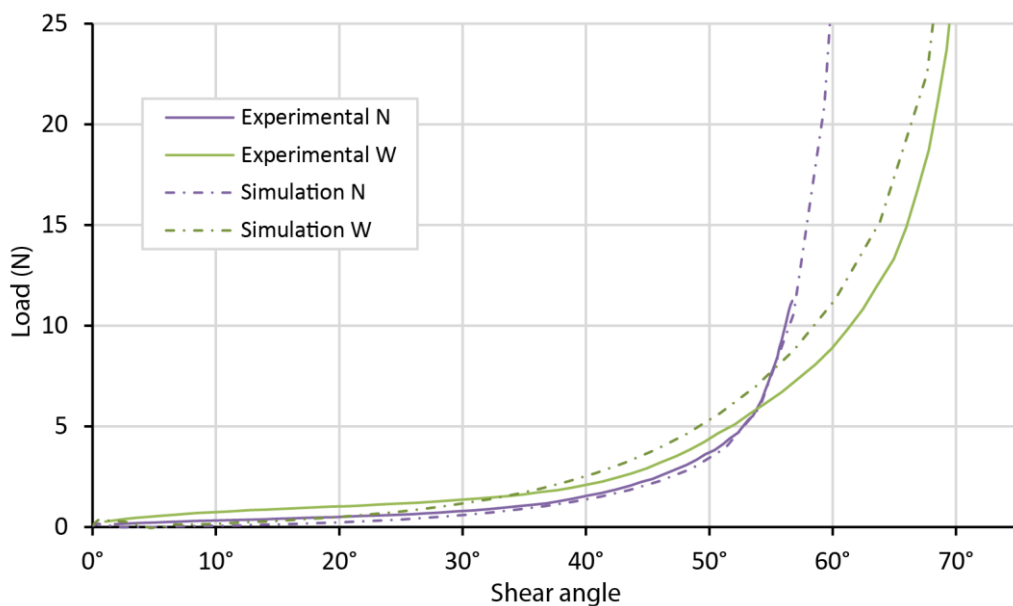


Figure 55: Bias extension simulation and experimental load-shear angle results for narrow (N) and wide (W) samples.

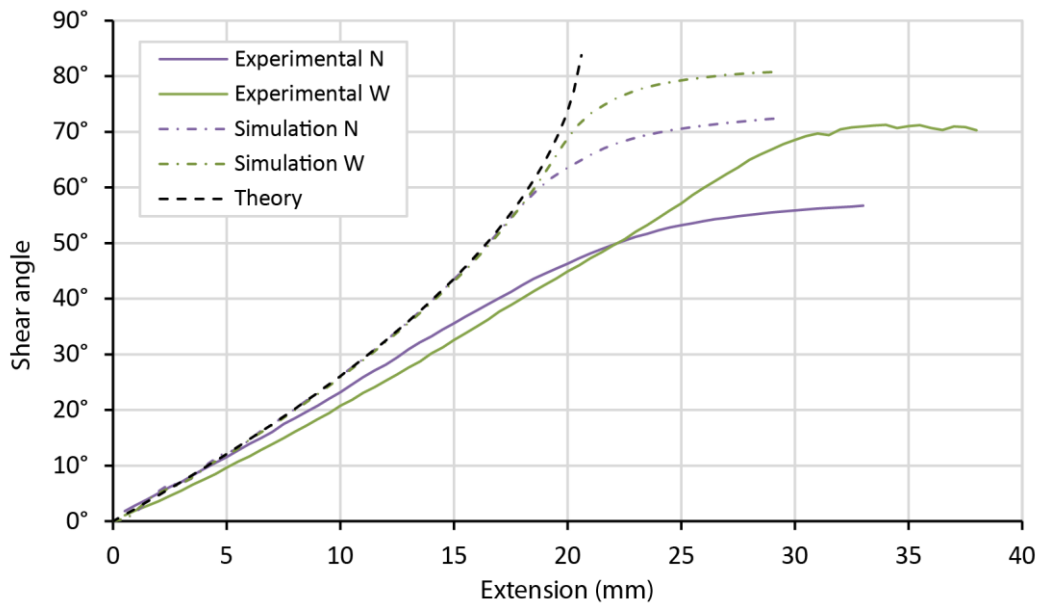


Figure 56: Bias extension simulation, experimental and theoretical results for shear angle-extension of narrow (N) and wide (W) samples.

Ultimately though, these results were considered sufficient to support the use of these calculated shear moduli for simulations with the knowledge that the model is not able to replicate yarn slippage and is most appropriate for applications where yarn slippage is expected to be small (as is reasonable for many draping processes).

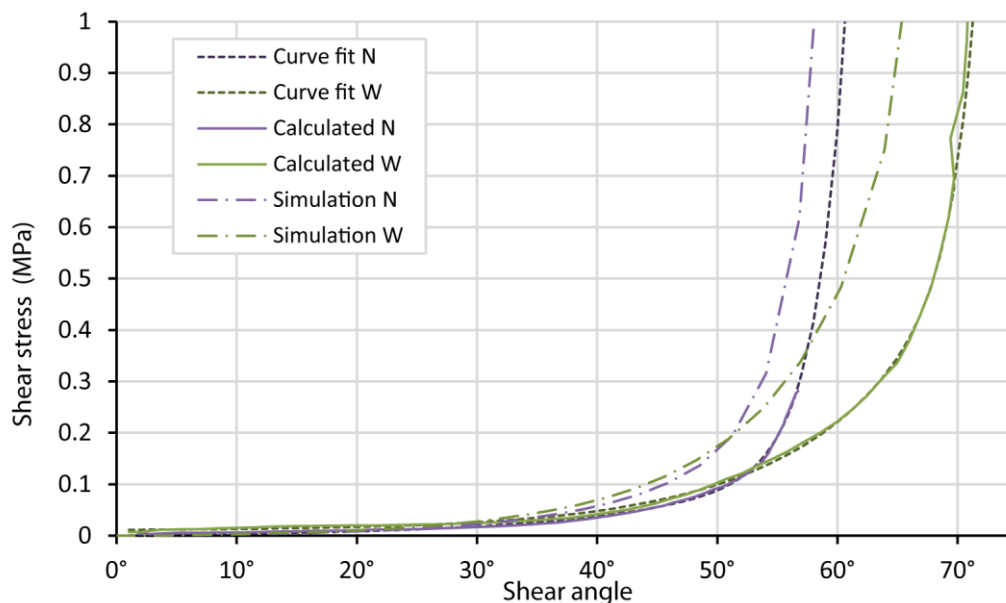


Figure 57: Bias extension simulation and calculated shear stress-shear angle results for narrow (N) and wide (W) samples.

4.6 Material characterisation discussion and conclusions

This material characterisation work is supplementary to the draping model discussed in Chapter 2. Uniaxial tensile strip testing was performed to determine the non-linear elastic modulus for the warp and weft fibre directions. Although fabric reinforcement materials are biaxial in nature, this uniaxial approach has been adopted for this research due to its simplicity

and standardisation. If further accuracy is required for future modelling, a biaxial characterisation method can certainly be adopted in its place to enhance the Complete Process Model.

To determine the shear characteristics of the fabric reinforcement material, the bias extension test was employed. This required only a very simple rig, but a suitable DIC code had to be developed in order to measure the degree of shearing in the material tests. The MATLAB DIC code is relatively simple, but has been developed specifically for the shear testing of fabric materials. As such, it offers some advantages over common commercial DIC systems, which do not account for non-orthogonal material deformation (such as yarn rotation) and cannot predict yarn strains or even shear angles without further modification. The MATLAB code can be used with simple camera systems, thus proving to be less expensive as well.

The comparison of different bias extension test samples has revealed that a wide sample may provide better results for characterisation purposes than the more common narrow samples. The raw test results saw narrow samples to achieve loads one tenth of the maximum load observed in wide samples, and also revealed extensive yarn slippage. Wide samples were consistently more stable and capable of higher shear angles (and even out-of-plane wrinkling) associated with greater loads and reduced yarn slippage. The DIC results supported these observations, with indications of yarn slippage at an earlier onset for narrow samples, particularly when looking at the shear angle and yarn strain distributions. This significant improvement from the narrow to the wide bias extension results is comparable to the benefits noted in literature for the picture frame test [109], which suggests that testing with wide samples could overcome some of the previous limitations of the bias extension approach. However, as there are no picture frame results with the same plain weave fabric for a direct comparison, this conclusion is not definitive.

This improved resistance to yarn slippage can be explained by the frictional effects in the excess material of wide sample, where the extra length of yarn crimp helps yarns to resist sliding out from the rest of the weave. Looking at the characterisation results, the excess material does not appear to have a significant effect, where the moduli calculated from narrow and wide testing are quite similar. The major difference is that for highly deformed geometries, the shear modulus determined from narrow samples will be an extrapolation from experimental data, and though this will still often provide a reasonable result, it is not ideal. Using the draping model, applications are likely to avoid simulating free edges near regions of high deformation where yarn slippage may become significant. Hence, the wide bias extension tests are believed to provide a better indication of localised shear behaviour in the continuum draping model. Particularly as the inclusion of extra frictional resistance to yarn slippage provides a more accurate representation of shear behaviour away from free edges.

5 Permeability characterisation

5.1 Motivation

The previous chapters have discussed the simulation of fabric draping, including the characterisation of fabric mechanical behaviour. With this work in place, the next stage of the project focuses on modelling the actual resin infusion. In order to simulate fluid flow through porous media, the permeability properties of the material need to be characterised. This is particularly important for reinforcement materials because of the complex woven architecture. Furthermore, it is well documented that fabric permeability is influenced by the deformation of the material [83]. This effect is highly localised, and as such, it is not typically considered in modelling attempts, despite its significance. The material permeability is instead commonly assumed to be homogenous or is adjusted artificially. The focus of this chapter is to characterise the permeability of a woven composite reinforcement material in relation to the fabric shear angle, which is predicted by the draping model.

As documented in Chapter 2, there are a number of ways to try to define permeability as a function of local deformation (shear angle) in fabrics. These range from experimental characterisation regimes to very simple two-dimensional models and even complex meso-scale flow simulation. Although modelling is an appealing option that generally reduces the need for tedious experimental work, these approaches are still in their infancy and may not yet be suitable for industrial use. This is compounded by the need for supplementary experimental validation anyway. Since an experimental approach is unavoidable to verify the characterisation method, the use of an enhanced experimental method for the characterisation of fabric permeability properties is demonstrated. Although, as predictive models improve, this experimental approach could be easily substituted by simulation in future work.

5.2 Experimental approach

In order to link the draping simulation with infusion modelling, experimental permeability characterisation was performed over a range of shear angles. As previously mentioned, despite extensive study in the area over the years, there are no standard methods to experimentally determine permeability for textile reinforcements. Recent efforts to benchmark the common approaches ultimately found that tests carried out under similar conditions exhibited significantly scattered results, varying by as much as an order of magnitude [60]. Hence there are a number of important considerations to be made in the planning of an experimental approach.

Firstly, even though linear flow experiments are generally considered to exhibit less variability and have been even more recently benchmarked with some success [71], an unsaturated radial flow experiment was preferred because the principal permeability directions were not known prior to testing at the various shear angles. This approach also allowed for greater data collection from a single test, facilitating permeability calculations in any direction to better describe the anisotropic flow. Secondly, the experiments were run under a constant injection

pressure, rather than with a constant inlet velocity, because the latter often require very high pressure gradients. For this study the pressure differential across the system was imposed by drawing a vacuum at the outlet, with an oil reservoir open to ambient conditions. Vacuum pressure was measured with a standard pressure gauge and was observed to be constant throughout each test. The permeability test configuration is shown in Figure 58 and Figure 59, where it can be seen that the test sample is sandwiched between a glass plate (8 mm thick) and a polycarbonate caul plate (10 mm thick), with white breather cloth placed around the periphery to ensure an even vacuum within the test cavity.

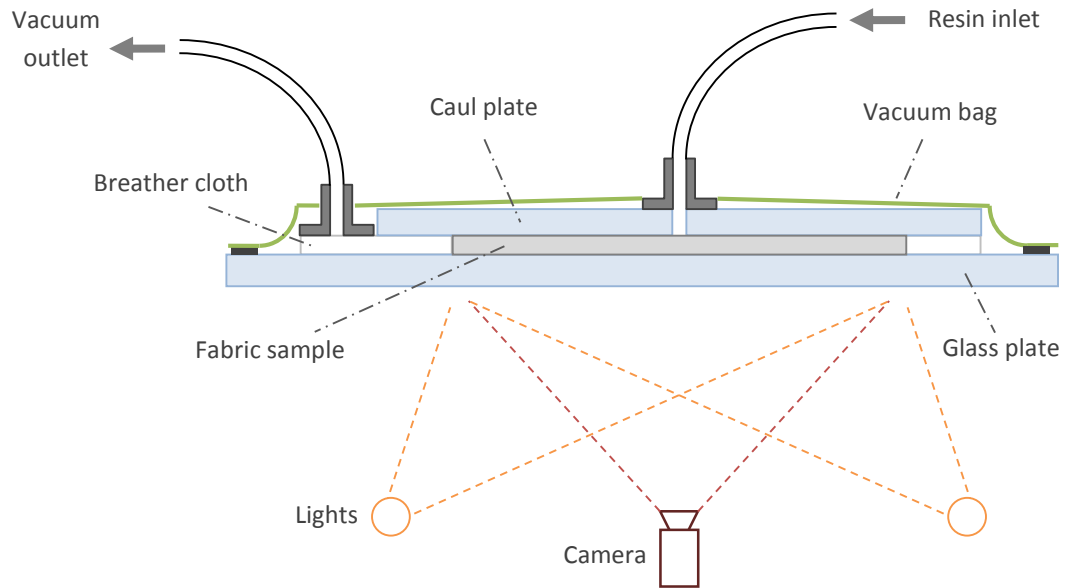


Figure 58: Diagram of the permeability test configuration including lights and camera.

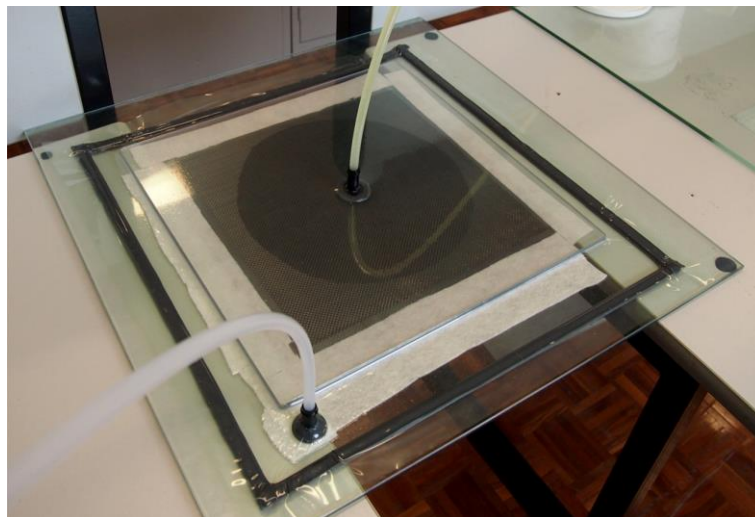


Figure 59: Experimental permeability testing configuration for an unsheared sample.

Single plies of the plain weave carbon fibre fabric with 3K yarns were tested in batches of at least six samples at various shear angles from 0° to 40° . Through-thickness flow and gravitational effects were neglected since the preform was only one ply thick, and testing was considered solely in 2D. Test samples were cut to 300 mm by 300 mm dimensions from the

unsheared material, using adhesive tape around the border of samples in order to prevent yarns from fraying. The corners of samples, where the taped borders intersected, were removed in order to allow manual, uniform shearing of samples prior to permeability tests. A 3 mm radius circular hole was drilled into the caul plate to act as the fluid inlet. An inlet size at least 20 times smaller than the sample size is recommended for highly anisotropic materials [111], in order to minimise the error that results from calculation assumptions of the inlet being elliptical. In this case, the maximum flow front distances were 50 times greater than the inlet radius. Since the samples were so thin, it was unnecessary to cut holes from the material underneath the inlet port (as is indeed necessary for thicker samples).

As plate deflection and cavity thickness change have a significant influence on tests such as this, the experimental set up was carefully monitored to ensure that the vacuum and plate configuration maintained a constant cavity thickness. As is discussed in Section 5.4.3, there is a high confidence that this experimental configuration does not produce any deflection or thickness change issues (since these would result in clear behavioural trends during the regression analysis for the permeability calculations).

The fluid used for these tests was a Newtonian olive oil, assumed to be incompressible, isothermal and chemically inert for the duration of each permeability test. Viscosity data was obtained, as seen in Table 4, for a range of lab temperatures using a cone and plate rotational viscometer. Prior to each permeability test the temperature of the oil was recorded to ensure an accurate viscosity value for subsequent analysis.

Table 4: Oil viscosity values at different temperatures.

Temperature (°C)	Viscosity (Pa.s)
15.0	0.1062
22.4	0.0754
30.1	0.0561

Tests were conducted with a digital video camera looking through the lower glass plate to record the radial flow pattern as a function of time. This method was used instead of alternative sensor methods which are often more difficult to set up, yield limited data, and may even negatively influence the fluid flow through the test cavity [112]. As discussed in the literature [60], fibre optic sensors, thermistors, pressure transducers or ultrasound and electrical resistance measurements can be used as alternatives. However using digital video meant the principal permeability directions did not need to be known in advance, and also provided greater flexibility in post processing and analysis as discussed in the following Section 5.3.

5.3 Flow front tracking and permeability calculation

In these experiments the full flow front was monitored using a digital video camera, though typically flow front propagation is only measured in a limited number of directions (as required by the popular methods for permeability characterisation). However in this work, the theory has been extended to allow for a more comprehensive definition of the permeability in all directions. This may initially appear unnecessary, however the detailed inclusion of flow data

from all directions subsequently allows for the determination of principal permeability values with greater confidence, by taking a statistical mean from the broader data set. It should also be noted that since the whole flow front was monitored, the more detailed approach required no additional effort.

MATLAB code was developed to process the video images from experimental testing, track the flow front in any number of directions, at any number of time intervals, and ultimately calculate the permeability. Details of the underlying theory and code development are discussed below.

5.3.1 Extended permeability theory

Characterising anisotropic permeability from radial flow experiments was popularly introduced by Adams et al. [70], to describe fluid motion by combining the Laplace equation (as derived from the continuity equation for incompressible flow) with Darcy's law. Subsequent work by Weitzenböck et al. [111, 112] expanded on the implementation of this method for anisotropic textile permeability characterisation, and focused on the reduced definition of permeability with 3 parameters: principal permeability values, K_1 and K_2 , and an orientation, φ . These parameters were retrievable from the transformed quasi-isotropic calculation of permeability in any set of three known directions (recommended as 0° , 45° and 90° relatively).

By monitoring the flow front in all directions using digital video, a quasi-isotropic permeability is instead able to be determined in every direction, rather than a limited few (as is the case for many sensor based flow front monitoring techniques). This provides the complete anisotropic permeability of each test sample (where traditional methods would instead rely on calculating an effective permeability for each direction based on the assumption of an elliptical flow front and knowledge of the principal permeability values). For simplicity, the quasi-isotropic calculations effectively treat each directional measurement independently, as if flow was isotropic (circular) for the particular flow front radius. As the number of directions being measured increases, the error of this approximation becomes negligible, and the resolution of the directional permeability characterisation includes every flow front anomaly and fluctuation.

In most practical applications the inclusion of data from flow anomalies and fluctuations is undesirable, and such detailed permeability definitions may prove unnecessary. However, using traditional methods it is difficult to ensure that the limited data is not affected by common anomalies. Hence, the advantage of performing such detailed flow front monitoring and permeability definition is that the data can be easily reduced down to the same three characteristic properties (K_1 , K_2 and φ) with greater confidence as a result of statistical analysis.

Before discussing the details of the video processing and permeability characterisation, it is important to mention the porosity and fibre volume fraction approximation that has been used.

$$\epsilon = 1 - V_f, \quad V_f = \frac{n\rho_A}{\rho_f h} \quad (41)$$

The porosity, ϵ , relies on the approximate calculation of the fibre volume fraction, V_f , based on the number of fabric layers, n , the fabric areal and fibre densities, ρ_A and ρ_f respectively, and the cavity thickness, h . Although this is only an estimate of the true fabric porosity, it is deemed reasonable for the purposes of this study, to demonstrate the relative change in permeability based on shear angle variance. It is also important to note that the areal density will change as a fabric is sheared, hence, the undeformed areal density is divided by the cosine of the shear angle to find an improved approximation. Although this has been acceptable in this work, standardised methods for porosity measurement such as the ASTM D2584 [113] ignition loss approach are recommended when finding true values.

5.3.2 Development of MATLAB code

In order to facilitate the automated calculation of anisotropic permeability from video footage of the experimental permeability tests, a new code was written for MATLAB. This code analyses video frames to track the fluid flow front, before characterising permeability in all directions using Darcy's law. Like the DIC code from Chapter 4, this MATLAB code has been made freely available on the MathWorks File Exchange website [114]. This section discusses the design of the MATLAB code and the underlying approach.

The code is designed to calculate the raw permeability in every direction, although it also reduces this data down to more practical principal permeability values. The primary requirements for the code to be effective are that the lighting in the videos is consistent and that the flow front is clearly discernible. When running the code, several input parameters are required from the user: the number of fabric plies, cavity thickness, specimen shear angle, areal density and fibre density. Additionally, the viscosity and differential pressure also need to be specified for each test, along with a metres-per-pixel conversion factor and the inlet radius. Depending on the clarity of the flow front progression in the video there are also several modifiable video processing parameters that help control the quality of the results.

5.3.2.1 Raw directional permeability calculation

Essentially the operations in the MATLAB code are reliant on three loops: one advancing through time, a second loop of increasing angle (signifying different measurement directions) and a third inner loop for increasing radius (see Figure 60). The first loop identifies a pair of video frames with finite time spacing between them, δt , and iteratively advances through the footage by updating image frames until the conclusion of the test at time t_f . The two frames are distinguished to identify changes between the frame at time t and the frame at time $t + \delta t$. Effectively this comparison results in a clear elliptical annular shape caused by the difference in the radial flow of fluid from frame to frame. The differential image from this process is then enhanced using a pillbox (or disk) filter for noise reduction, and converted to a high-contrast binary format. Figure 61 shows an example of this image processing approach: where two video frames are differenced, filtered, converted to binary and used to find a discretised flow front.

The second loop, for changing measurement direction, is nested inside the outer time loop and simply sweeps through angular increments, from 0 to 2π radians. While the last nested loop incrementally increases a radial length parameter, r , by δr from the fluid inlet until the annular flow front is detected (at a binary value of 1). Theoretically without any noise, this will always

linear regression of N_i is taken as a function of time, F_i , and the quasi-isotropic permeability, K'_i , for each radial direction, i , is calculated.

$$N_i = \left(r_{ff,i}^2 \left(2 \ln \left(\frac{r_{ff,i}}{r_{0,i}} \right) - 1 \right) + r_0^2 \right) \quad (42)$$

$$K'_i = \frac{\mu \epsilon}{4 \Delta p} F_i \quad (43)$$

This raw, quasi-isotropic, permeability for every direction accurately represents the results of each test in detail; however, the code can also be used to simplify and reduce this data down to principal permeability values, K_1 and K_2 , which are often more practical.

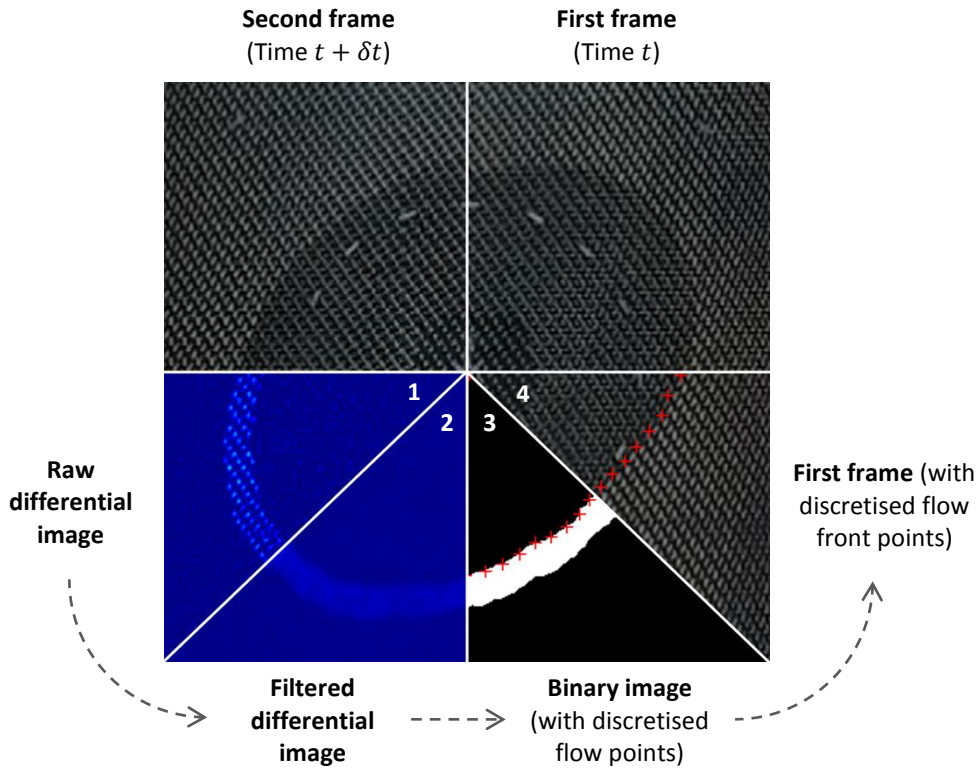


Figure 61: Video processing example for a carbon fibre plain weave sample sheared at 20°.

5.3.2.2 Data reduction for practical use

In accordance with the work by Weitzenböck et al. [112], K_1 and K_2 values can be determined from measurements taken in three directions ($I = 0^\circ$, $II = 45^\circ$ and $III = 90^\circ$ relatively) at any arbitrary orientation, φ , from the actual principal permeability direction. The following equations are used to calculate these principal permeability values in the MATLAB code:

$$K_1 = \frac{\mu \epsilon}{4 \Delta p} \frac{A - D}{\left(A - \frac{D}{\cos 2\varphi} \right)} F_I, \quad K_2 = \frac{\mu \epsilon}{4 \Delta p} \frac{A + D}{\left(A + \frac{D}{\cos 2\varphi} \right)} F_{III} \quad (44)$$

Where:

$$\varphi = \frac{1}{2} \tan^{-1} \left(\frac{A}{D} - \frac{A^2 - D^2}{F_{II}D} \right), \quad A = \frac{F_I + F_{III}}{2}, \quad D = \frac{F_I - F_{III}}{2} \quad (45)$$

and,

$$F_i = \frac{1}{t_i} \left(r_{ff,i}^2 \left(2 \ln \left(\frac{r_{ff,i}}{r_0} \right) - 1 \right) + r_0^2 \right) \quad (46)$$

These equations are based on the same quasi-isotropic method outlined earlier, assuming the flow front is a perfect ellipse and again that the inlet is similarly elliptical (or small enough for its shape to be insignificant). Here φ is the angle between the measured principal directions and the true principal permeability directions. In the case where $\varphi = 0$, measurements are aligned with the principal permeability directions.

Once principal permeability values K_1 and K_2 are known, an effective permeability can also be calculated for any direction θ degrees from the principal permeability direction according to the following equation from literature [112]:

$$K_{eff} = \frac{K_1 K_2}{K_1 \sin^2 \theta + K_2 \cos^2 \theta} \quad (47)$$

It is important to note however, that this reduction approach only uses data from three directions and thus can be prone to error as a result of local fluctuations in the flow front during testing. Hence, using data from the flow front in all directions, this reduction process is repeated for every possible orientation triplet, such that the code determines a statistical range of K_1 and K_2 principal permeability values and a similar range for the calculated principal permeability direction. From this the mean values can be taken with greater confidence for subsequent practical use.

5.4 Single-ply test results

5.4.1 Observations

Experimental permeability tests were recorded in high definition (1920 x 1080 pixel resolution) with a standard APS digital camera. Due to the variability of natural light, some tests observed large changes in lighting that negatively affected the video processing. However, this was overcome by the selection of suitable video frame pairs such that the results from all tests were still reliable. In general the permeability tests appeared to be quite consistent, and as expected, the flow front for the unsheared material configuration was near-isotropic. Unsurprisingly, the samples with the greatest degree of shearing also showed the greatest anisotropy in the form of an elliptical flow front (as seen in Figure 62). For all tests the flow of oil was initially quite rapid but quickly slowed under the constant pressure control.

Although the experiments were generally consistent, there were a couple of early tests that produced unexpected flow behaviour which was only identified after the conclusion of the tests. The experimental data from these tests has been eliminated from the reported results since the causes for error were subsequently discovered and monitored for all other tests. In one case, for example, the join between the caul plate and the inlet port was not sufficiently fixed, such that eclipsing occurred and resulted in a marginalised flow with greater anisotropy.

However, the remainder of the reported test data still contains some outlier results that could not be similarly explained or justified for elimination from observations or conditional changes.

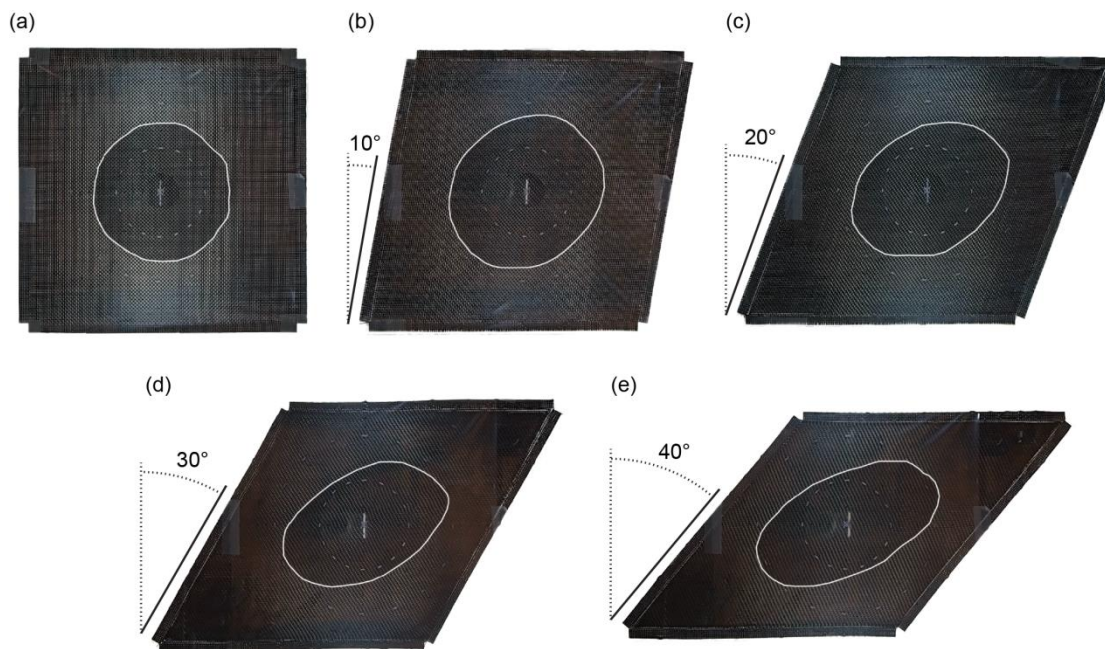


Figure 62: Photos from permeability characterisation experiments (at 75 s) for, (a) 0° shear angle, (b) 10°, (c) 20°, (d) 30° and, (e) 40°. Flow front profiles are highlighted for clarity.

5.4.2 Raw results

Following the method outlined in Section 5.3.2.1, permeability was calculated for every test sample, in all directions (at $\pi/32$ radian increments) to generate the raw directional permeability plots shown in Figure 63. The mean of directional results for each shear angle group are depicted as a dashed black line on each plot, which are all directly compared in Figure 64. All results are displayed in accordance with the actual test conditions where the warp yarn direction remained constant (horizontal) and the weft yarns were sheared to the desired configuration (represented by solid black lines in Figure 63). From these results, it can be seen that the tests conducted at low shear angles exhibited a greater variance between tests, particularly compared to tests at 30° and 40° shear. Quantitatively, the relative standard deviations for the directional results in the first three batches ranged from $\pm 20\text{-}30\%$, compared with only $\pm 4\text{-}15\%$ for the highly sheared configurations. As has previously been noted, such significant variance is common for permeability testing, as reported by benchmarking efforts in literature [60].

In accordance with the observations from testing, these raw permeability values show a tendency to isotropic behaviour for the unsheared (0°) samples, and increasing anisotropy with increasing shear angle. A further trend is observed from the anisotropic results, where peak permeability values appear to align with the fabric bias direction (bisecting the warp and weft yarn directions). The permeability minima direction also appears to be perpendicular to this direction of the peak permeability, as expected [70].

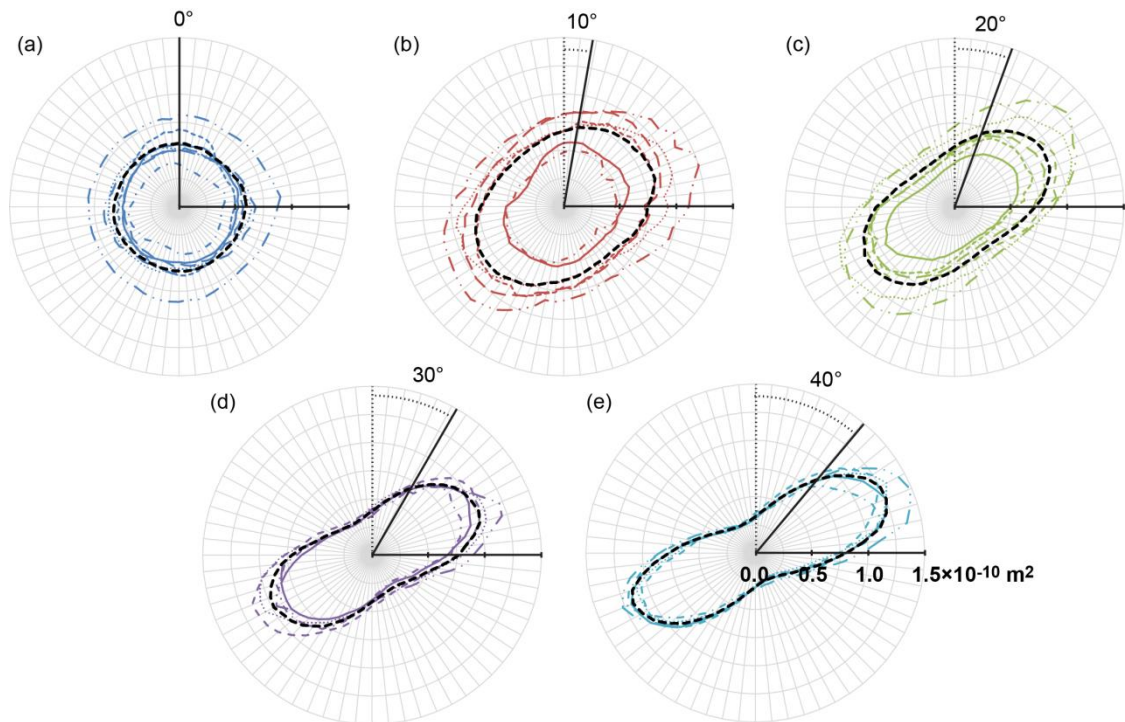


Figure 63: Raw directional permeability results for experiments at, (a) 0° shear angle, (b) 10°, (c) 20°, (d) 30° and, (e) 40°. Mean curves are presented as dashed black lines.

Combining the mean results from tests at all shear angles into a single plot, Figure 64 shows the change in permeability as a function of both flow orientation and shear angle. The flow direction results in this plot are relative to the experimental conditions where the warp yarn direction is 0° on the horizontal axis. The observed relationship of increasing anisotropy with increasing shear angle can be seen by the growing permeability amplitude. The peaks and troughs are also seen to repeat predictably over a 180° flow direction cycle in accordance with the peak permeability values. Furthermore, the peaks are seen to shift with increasing shear angle as a result of the test 0° direction remaining aligned with the warp yarn direction. Hence the principal permeability direction (which is generally aligned with the fabric bias direction) changes as the fabric is sheared.

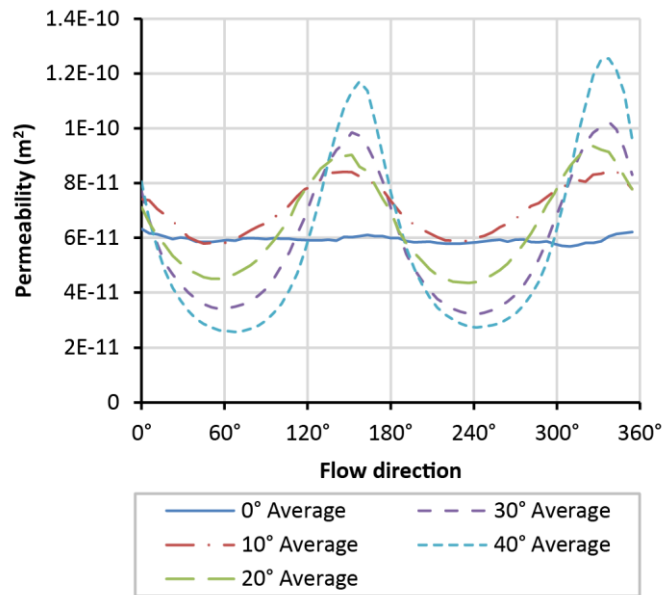


Figure 64: Raw permeability results for each shear angle batch in all flow directions.

5.4.3 Regression model validation

In order to ensure that both the experimental set up and calculation method were reasonable for the constant pressure flow assumptions, a regression analysis was performed for the theoretical term N_i , defined in Equation (42). Any non-linear deviation or trend in the calculated N_i values over time might have suggested a transition to capillary driven flow in the experiments, unreasonable deformation of the test cavity or simply that the chosen calculation approach might have been flawed. Hence, regressions were comprehensively analysed in every direction for several specimens from each shear angle batch, totalling around 500 studies. The linearity of the data was interpreted by; firstly, how well the data points fit a linear trend line (quantified by the coefficient of determination, R^2); and secondly, by the randomness of the residuals. Depending on the fluid flow in experiments, the regressions typically consisted of 10-15 N_i data points through time.

The full regression results for different shear angles, samples and flow directions have all been extensively analysed. Overall, the regressions fit linear trends very well, with R^2 values typically greater than 0.99 (where 1 represents an exact fit), and only a few cases at around 0.98. Figure 65 shows the linear regression of N_i values over time from a 20° shear angle specimen. For simplicity, regressions from only 3 flow directions in the sample are shown (the principal permeability direction, φ , and two further 45° increments) along with their corresponding R^2 values. This one case is representative of the regression results for all different shear angles and samples. In all cases, further scrutiny of the residuals revealed random behaviour, with no observable trends that might have contested the use of a linear model. Thus, there is great confidence in both the method and experimental approach in the construction of this permeability data.

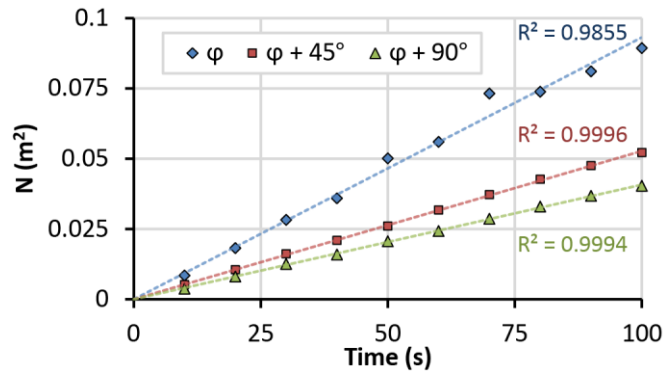


Figure 65: Linear time regression of N_i terms from a 20° shear angle specimen, for the principal permeability direction, ϕ , and increments of 45° and 90°.

5.4.4 Data reduction and comparison with traditional methods

Although it is interesting to characterise and plot the raw permeability data in all directions, this information is not always the most practical for subsequent modelling. As outlined earlier in Section 5.3.2.2, a traditional method can be employed to reduce data triplets from the full directional data down to principal permeability values, K_1 and K_2 , and a principal permeability direction, ϕ . In theory, for a perfectly elliptical flow front, these three calculated parameters will be the same regardless of the triplet orientations. In reality, the flow front often has significant irregularities that subsequently change the principal permeability estimates. To overcome this problem, the full directional measurement can be used to calculate approximate reduced parameters (K_1 , K_2 and ϕ) based on triplets from all orientations. This ensures that all the irregularities of the flow front can be accounted for by determining the statistical mean of each parameter.

The full principal permeability results (K_1 and K_2) of this reduction method (employing the three-direction method discussed by Weitzenböck et al. [112]) can be seen in Figure 66 for each test. In this figure, the markers represent the mean of the estimated principal permeability values, with error bars representing one standard deviation. Dashed lines of anisotropy are depicted for each shear angle group, along with the associated value of anisotropy (defined as the ratio K_1/K_2). In accordance with initial observations and the raw results, the unsheared (0°) specimens exhibited near isotropic behaviour, with a principal permeability ratio of 1.13. Although this does suggest some slight anisotropy, there was no consistency in the directionality of these samples and experimental variability is the likely cause of this deviation from true isotropy. For the rest of the samples, anisotropy is quantitatively seen to increase with shear angle, up to a ratio of 3.71 for the 40° tests.

Figure 66 shows a relatively large variance in the principal permeability values from test to test, particularly at lower shear angles (0°, 10° and 20°) where the relative standard deviations are greater than $\pm 20\%$. However, as was noted in the raw results, at 30° and 40° the tests were more consistent with relative standard deviations of around $\pm 7\%$ and $\pm 4\%$ respectively. More interestingly though, despite the significant variance in the principal permeability values, the ratio of anisotropy for specimens in each shear angle batch was very consistent. Unsheared sample results have a relative standard deviation of $\pm 6\%$, with the sheared specimen groups all below $\pm 4\%$.

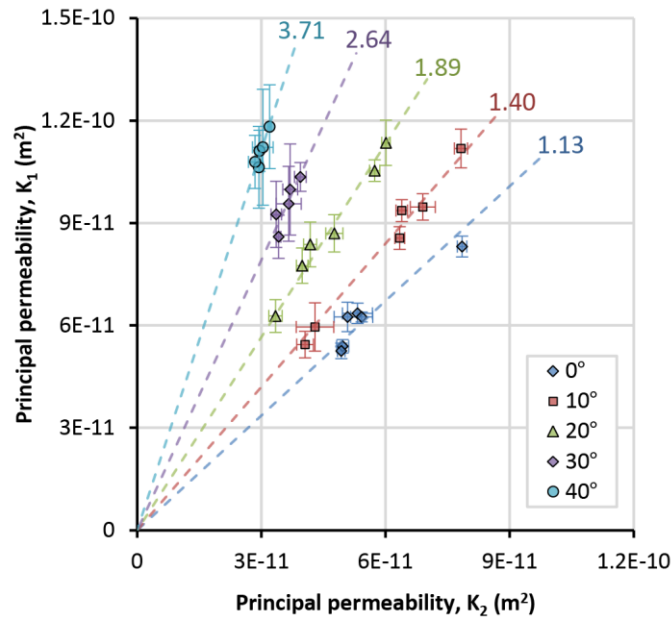


Figure 66: Distribution of all the reduced principal permeability results.

In addition to the principal permeability values, the three-direction method also estimates the principal permeability direction, φ , associated with them. Figure 67 plots the estimated principal permeability directions against shear angle for all the sheared sample permeability tests (relative to the experimental warp yarn direction). Again, each marker represents the average of values determined from different measurement orientations in the same test, with standard deviation error bars. Evidently, samples that exhibit low anisotropy observe a greater variance in the predicted principal permeability direction as can be seen in the 10° shear angle values, and the results for the (near-isotropic) unsheared case were so scattered they were deemed irrelevant. Not only were the predicted φ values highly variable among tests at 10°, but they were also strongly influenced by the measurement orientation used in their calculation, with relative standard deviations in excess of $\pm 25\%$. Principal permeability direction results from tests at shear angles 20° and higher proved to be more consistent and less sensitive to the measurement orientation used in their calculation (with relative standard deviations ranging from $\pm 2-12\%$). Also plotted in Figure 67, the line of the bias direction fits well with the experimental results, as was observed in the raw results. Hence, it is reasonable to assume the principal permeability direction coincides with the fabric bias direction for this particular balanced plain weave material.

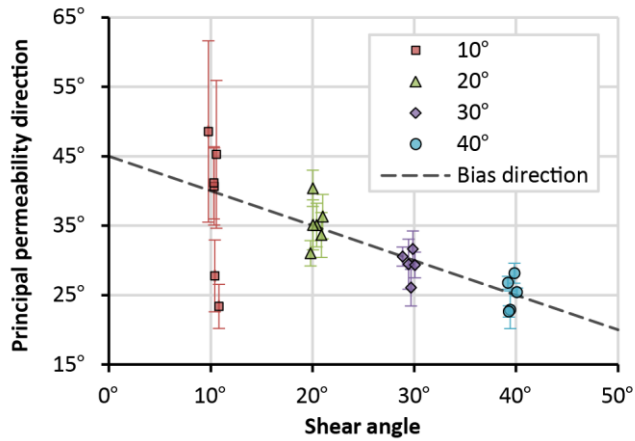


Figure 67: Distribution of the predicted principal permeability direction results.

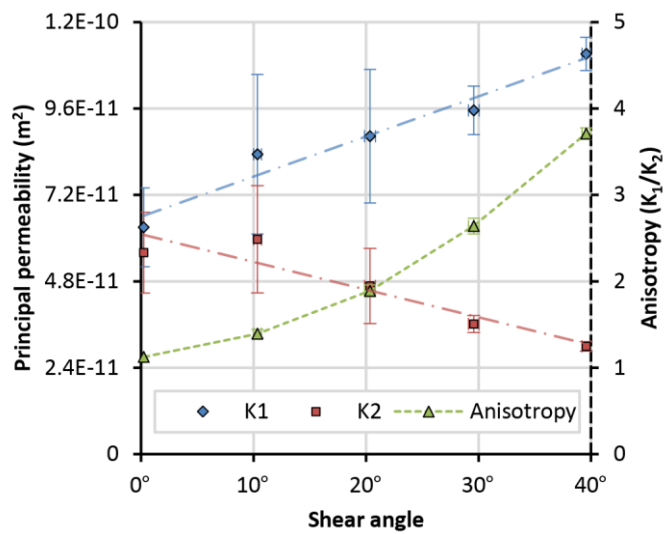


Figure 68: Relationship between principal permeability values, anisotropy and the fabric shear angle, including linear trend lines for principal permeability values

Taking the mean of all results for each batch of shear angle samples, Figure 68 shows the simplified relationship between principal permeabilities, anisotropy and the fabric shear angle. Here a large variance in K_1 and K_2 values is observed, particularly at the lower shear angles. However, as noted earlier, the anisotropy results are very consistent for each batch. Overall, with increasing shear angle the trends show increasing K_1 values, decreasing K_2 values and a subsequently large increase in anisotropy. Although the K_2 values are observed to increase slightly at 10°, this may only be due to the large variance in the results. Linear trend lines have also been plotted for the principal permeability values in Figure 68, and are seen to lie within the standard deviation of results.

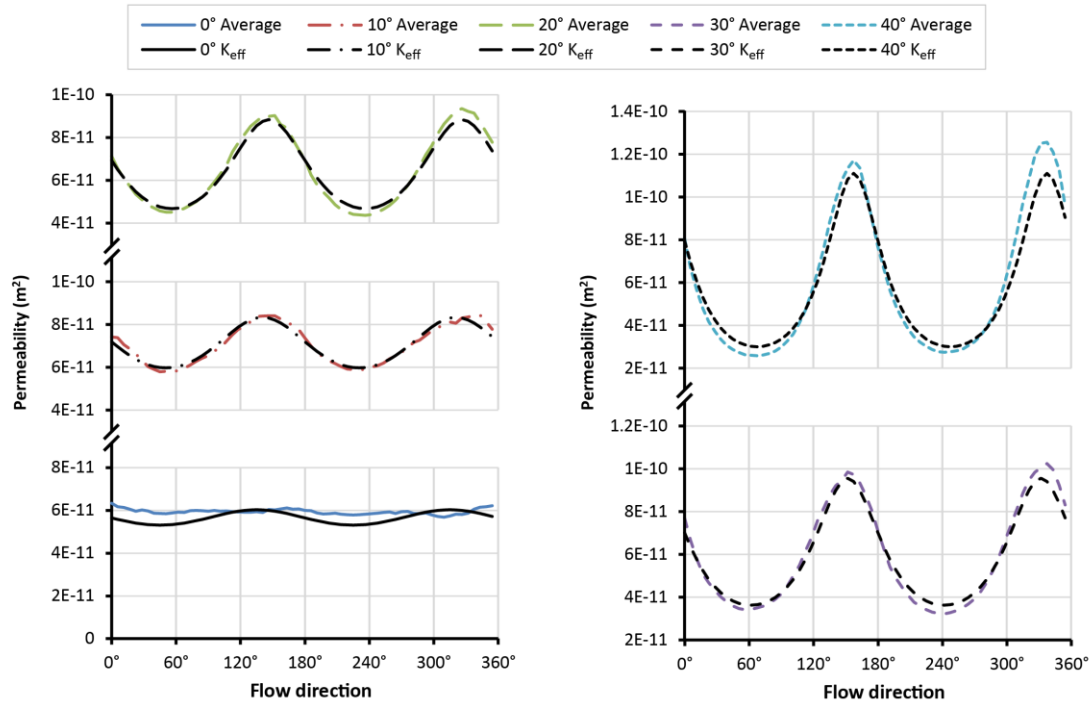


Figure 69: Comparison of the calculated effective permeability (from mean principal permeability values) with raw experimental permeability in all directions.

With the principal permeability parameters (K_1 , K_2 and φ) defined, Equation (47) can be used to calculate an effective permeability for any direction. Figure 69 compares the mean calculated effective permeability in all directions for each shear angle batch, with the corresponding mean of the raw experimental results (from Figure 64). Aside from some experimental irregularities for the highly sheared sample results and some increased anisotropy at 0° shear angle, the reduced effective permeability data shows good agreement with the raw experimental data. The general shape and magnitude is very well captured, although this is primarily attributed to the detailed statistical approach that has been employed to define K_1 , K_2 and φ .

5.5 Discussion and conclusions

Similar to these results, previous permeability research has observed significant increases in anisotropy with increasing fabric shear angles [85-88, 115], however, there appears to be little else to correlate between studies. This is not surprising given the use of different materials, methods and test configurations; not to mention the known variability issues with permeability test methods themselves [60]. In some cases, results similar to this study have been observed with increasing K_1 principal permeability values related to increasing shear angle [85, 86], while other research has seen K_1 values decrease [87, 88, 115]. The operating conditions and test parameters in each of these studies do not reflect any clear correlation between the results. It is likely that the relationship between shear angle and permeability is dependent on a large number of these experimental parameters, and the diversity of the reported studies does not help to clarify the problem. Recent literature summarises sources of uncertainty with textile materials [116], attributing the scatter of permeability results to manufacturing conditions, nesting, weave, architecture and ultimately to an insufficient number of tests in order to determine statistically relevant results.

Among the research community there is a preference for performing experimental permeability tests on thick, multiple ply samples rather than a single layer (as was used in this study). Generally, the aim is to minimise the influence of wall effects and characterise the permeability from a more realistic layup for manufacture. However, the stacking of plies greatly increases the complexity of the flow paths inside the layup, since the nesting of plies is particularly difficult to control or measure. It is well documented that changes in the nesting configuration significantly alters permeability [67], in some cases by as much as an order of magnitude [65]. For this reason the single ply test has been performed to increase repeatability, where the impact of wall effects is likely to be more consistent even if it is acknowledged that results are affected. The use of a single fabric layer has meant that the porosity of the samples was 20-30% higher than is common for composite aircraft structures. Subsequently, this may be the reason for the increasing K_1 values at higher shear angles, where larger flow channels may be enhancing the positive effect of flow-aligned yarns. Ultimately though, the reduced fibre volume fraction and significant wall effects in the single-ply tests were deemed acceptable for this work, as the experiments were designed to primarily demonstrate the method, describe the relationship between fabric deformation and permeability, and support the Complete Process Model.

These results serve as a very effective validation of the experimental method and calculation approach. By monitoring the complete flow front and implementing an intelligent video processing code, it is possible to determine permeability in all directions from a single test (although repeated tests are required for consistency). Furthermore, the extensive data this provides can be scrutinised statistically and reduced to principal permeability values with greater confidence. Alternatively, the traditional three-directional method for permeability characterisation, using very limited data sets, is more susceptible to error. Measurements taken from only a small number of directions can be greatly affected by common flow anomalies. For example, selecting only a single set of three-directional measurements from one of the 40° shear tests can estimate a peak K_1 value 55% higher than the statistical mean found by analysing all the data. Another positive aspect of this approach is the fact that it is a very low cost experimental method, as there is no need for sophisticated or expensive in-situ sensors.

Most significantly, the detailed mean results of this study show very consistent anisotropy between like tests, despite a greater variance in principal permeability values. This is a promising outcome, suggesting that 2D radial permeability testing can be much more consistent than previously thought. Although linear tests are generally accepted to be more consistent, a combination of both methods may prove to be the best approach for permeability characterisation. Assuming the anisotropy can be reliably determined from radial testing, linear tests could be used to determine one principal permeability value, which could then be extended to an effective permeability definition based on the characterised anisotropy for each shear angle configuration. This would effectively reduce the necessary amount of experimental work (from three linear tests to one linear test and one radial test), and may require fewer repeated tests before consistent results are obtained than simply the radial method.

On a final note, experimental permeability measurement approaches are widely used due to their maturity, although they continue to elude standardisation. Furthermore, they tend to require a large number of time consuming experiments for a single fabric architecture, while still exhibiting a large scatter in results. Predictive permeability modelling is therefore an attractive alternative, provided it can achieve reasonable accuracy and reliability [84]. There are currently several different modelling approaches that show some good agreement with experimental testing: ranging from full 3D Computational Fluid Dynamics (CFD) analysis of flow through a Representative Unit Cell (RUC) [13], to highly efficient dimensionally-reduced approximations [84]. However all of these methods still require some degree of homogenisation, geometric simplification or similar assumptions and are not yet well established.

6 Infusion modelling

6.1 Motivation and software options

The last major component of the Complete Process Model is the infusion model. Primarily, the aim of this model is to realistically predict the flow front profile and fill time of any given LCM infusion process. In fulfilling this aim, there are several challenges to simulating anisotropic flow through a porous material. Firstly, the simulation must be transient, with the capability of simulating both the resin and air fluid phases; including the interaction between them that constitutes the fluid flow front. Secondly, the model needs to be capable of incorporating the anisotropic permeability characteristics of a woven material. In this research, interest lies in accounting for permeability and porosity as functions of local deformation in complex geometries.

For the preliminary demonstration of the CPM, infusion has been considered only for isothermal conditions, neglecting the complexities of saturation and compaction. Although this is a significant simplification of the infusion process, this work is intended to highlight the importance of defining variable anisotropic permeability across a preform. With these simplifications in mind, the infusion model has been developed to ensure there is the capacity for improvement and enhancement in future work.

As a framework for this research, there are a variety of sophisticated Computational Fluid Dynamics (CFD) software packages capable of infusion modelling, and subsequently several of the most capable have been studied where available. Although the draping model discussed in Chapter 3 was developed in Abaqus and continued modelling on this platform would be ideal, the recently released Abaqus CFD package is limited to applications without transient flow and does not have the same customisation options for writing user subroutines. Unfortunately this only became evident after the development of the draping model and a different package had to be found for the infusion.

PAM-RTM is an established commercial package by ESI group that is widely used in industry and designed to simulate infusion processes for composite materials. However, without access to this software (or the details of its full capabilities), this research has focussed on using the more generalised CFD simulation packages (FLUENT and CFX) available in ANSYS. Both FLUENT and CFX are highly capable and widely used by both academia and industry; as such they have been evaluated here for LCM infusion modelling.

The infusion model is particularly important to the CPM as it is the final component that incorporates detailed data from all the preceding work of draping and material characterisation. It relies on the generation of a porous domain based on the deformed mesh from the draping model, and incorporates the shear angle distribution through a part as local permeability changes based on the experimentally determined relationship between the two properties. This chapter focuses on the development and validation of the basic infusion approach for variable, anisotropic, multiphase flow through a porous domain; including a comparison of both FLUENT and CFX packages for this application.

6.2 Modelling Theory

As two of the most prominent, and enduring, general purpose CFD software packages, FLUENT and CFX are both capable of modelling a diverse array of CFD problems. With regards to solving transient resin infusion problems, both packages offer very similar approaches. Within both packages, the fundamental theory can be divided into three main components: the multiphase modelling approach, the porous media model and the solver algorithm, which are covered briefly below.

6.2.1 Multiphase modelling

Both models for multiphase flow employed in FLUENT and CFX are based on a Eulerian-Eulerian VOF approach (as introduced in Chapter 2) where different phases are considered as interpenetrating continua and the volume of one phase cannot be occupied by any of the other phases. The volume fraction of each phase traces fluid flow through the domain and is used to calculate averaged cell properties in areas of the model with multiple phases. With these cell-averaged properties, a common flow field is shared among all the phases and the transported quantities (other than volume fraction) are the same for all fluid phases. This is typical of VOF approaches (termed a ‘homogenous’ model in CFX) and means that only one set of governing equations needs to be solved for all phases. The momentum equation used in these simulations, Equation (48), neglects interphase mass transfer, but includes gravitational acceleration, \mathbf{g} , and source terms, \mathbf{S}_K (related to the flow resistance of the porous material for infusion applications).

$$\frac{\partial}{\partial t}(\rho \mathbf{u}) + \nabla \cdot (\rho \mathbf{u} \times \mathbf{u}) = -\nabla p + \nabla \cdot [\mu(\nabla \mathbf{u} + \nabla \mathbf{u}^T)] + \rho \mathbf{g} + \mathbf{S}_K \quad (48)$$

To account for the multiple fluid phases, this momentum equation is essentially a single-phase transport equation with variable viscosity and density according to the volume fraction of each phase in the cell, as described through Equation (49).

$$\rho = V_{fp} \rho_{resin} + (1 - V_{fp}) \rho_{air}, \quad \mu = V_{fp} \mu_{resin} + (1 - V_{fp}) \mu_{air} \quad (49)$$

Here the viscosity, μ , and density, ρ , properties are simply averaged by the fractional content in each cell. Next the continuity and volume fraction equation, Equation (50), also assumes mass transfer between phases to be negligible and that there are no additional source terms.

$$\frac{\partial}{\partial t}(V_{fp,\alpha} \rho_\alpha) + \nabla \cdot (V_{fp,\alpha} \rho_\alpha \mathbf{u}) = 0 \quad (50)$$

$V_{fp,\alpha}$ is the resin volume fraction of phase α , and the volume fractions of all phases sum to unity:

$$\sum_{\alpha=1}^{N_p} V_{fp,\alpha} = 1 \quad (51)$$

Before being passed on to the solver, Equation (50) is then divided by phasic density and summed over all the phases, where N_p is the number of phases:

$$\sum_{\alpha=1}^{N_p} \frac{1}{\rho_{\alpha}} \left(\frac{\partial}{\partial t} (V_{fp,\alpha} \rho_{\alpha}) + \nabla \cdot (V_{fp,\alpha} \rho_{\alpha} \mathbf{u}) \right) = 0 \quad (52)$$

For most infusion applications there will only be two phases: resin and air. For non-adiabatic processes an energy equation can also be included in the set of governing equations, although these modelling trial simulations are assumed to be adiabatic. By default, CFX incorporates a standard free surface flow model into the homogenous model, although this negatively affects anisotropic flow and needs to be turned off for improved results.

6.2.2 Modelling porous media

The effects of porosity are simply represented with the inclusion of a directional momentum loss model in the fluid domain. This is implemented as a momentum source (or ‘sink’) term to the governing momentum equation. In both packages a superficial velocity, calculated from the volumetric flow through the porous region, is used in the porous media formulation. It is noted that this generally provides a good representation of the bulk pressure loss through porous media, however it does not predict, nor account for, the increase of true velocity through a porous region. Since flow is expected to be laminar (with low Reynolds number) for resin infusion processes, the superficial velocity formulation is reasonable and inertial losses can be neglected. Hence, the momentum source term reduces to only a viscous loss term, separated into orthogonal streamwise (x') and transverse (y' and z') components:

$$S_{Kx'} = -\frac{\mu}{K_S} u_x, \quad S_{Ky'} = -\frac{\mu}{K_T} u_y, \quad S_{Kz'} = -\frac{\mu}{K_T} u_z \quad (53)$$

Here K_S and K_T are the streamwise and transverse permeability values respectively, μ is the fluid viscosity, u_i is the velocity and S_{K_i} is the corresponding source term in the i direction. In the case of textile reinforcements, the local fibre volume fraction (or porosity) simply prescribes the ‘usable’ volume of each cell for fluid flow calculations.

6.2.3 Solution algorithm

For low velocity flows such as infusion, where the aim is to predict multiphase fluid flow, a pressure-based solver algorithm is preferred. This approach is generally categorised as a ‘projection method’, for which the constraint of velocity-field mass conservation is imposed by solving a pressure equation that is derived from the continuity and momentum equations. Due to the coupled and non-linear nature of these equations, the solution must be found iteratively, stepping the solution towards convergence.

Solutions for the governing equations can be calculated sequentially (by iterating each of the component momentum equations separately) or simultaneously (by solving them together), making up the ‘segregated’ and ‘coupled’ methods, respectively. Using the segregated algorithm requires significantly less memory, but can be relatively slow, as the coupling between equations is only treated indirectly. As indicated, the coupled algorithm instead simultaneously updates all the component discretised equations at each iteration; as a result it tends to converge more quickly and is more appropriate for transient problems, generally allowing a larger time-step. Subsequently, the coupled algorithm is employed for this infusion model.

The iterative process of this pressure-based and coupled algorithm can be divided into the following steps. First, based on the current (or initial) solution, the fluid properties (such as density, volume fraction and viscosity) are updated, then the coupled system of momentum and continuity equations are solved in order to update the face mass fluxes. In the case of multiphase flow, necessary for this infusion model, the volume fraction equation is then solved separately (although it is also possible to couple this equation into the previous system of simultaneous equations). Next the source terms, such as the directional porous momentum loss term, are updated. Then lastly, there is a check for convergence before beginning the next iteration or advancing the time-step.

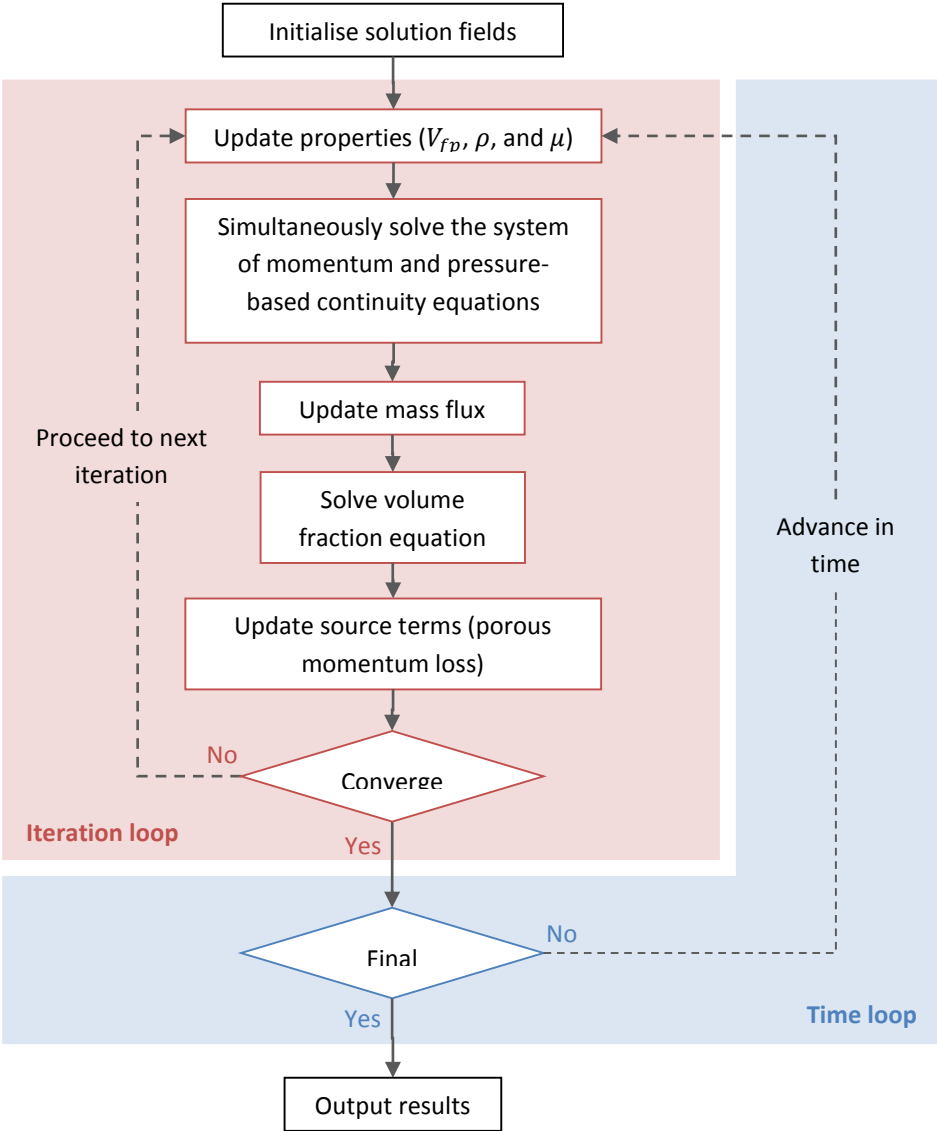


Figure 70: Process diagram for the pressure-based coupled algorithm.

6.2.4 Discretisation and interpolation

Up to this point the two models in FLUENT and CFX are nearly identical, it is only some of the discretisation and interpolation methods that differentiate the two packages. Similar second-order accurate spatial discretisation methods have been set up for both packages, although the way gradient terms are calculated differentiates them.

In FLUENT, a second-order upwind scheme is used for the spatial discretisation of the advection terms in the governing equations. Face values, ϕ_f , are computed using Equation (54) based on the upstream cell-centred value, ϕ , its gradient, $\nabla\phi$, and the displacement vector from the upstream cell centroid to the face, \mathbf{d}_f . The gradient term is subsequently determined in FLUENT using the Least Squares Cell-Based approach.

$$\phi_f = \phi + \nabla\phi \cdot \mathbf{d}_f \quad (54)$$

In CFX a specified ‘blend factor’ can be tuned to reduce discretisation error, where 0 corresponds to the first-order upwind differencing scheme, and 1 effectively switches to the second-order upwind scheme (as used in this study). However, for the volume fraction equation in multiphase simulations, a second-order upwind advection scheme cannot be used, and CFX defaults to its own ‘high resolution’ scheme that is different to the FLUENT approach. Furthermore, the gradients in CFX are determined using a method based on Gauss’ divergence theorem.

Pressure interpolation between cells relies on a Pressure Staggering Option (PRESTO) in FLUENT, whereas CFX performs linear-linear interpolation instead. The pressure-velocity coupling is subsequently based on a staggered approach in FLUENT, as opposed to a co-located grid that is implemented in CFX.

Temporal discretisation in both packages is implemented using a first-order implicit time integration method, that must be solved iteratively. Because it is implicit, it is theoretically unconditionally stable with respect to time-step size while the convergence criteria are met. Face fluxes are thus obtained using a standard Finite Difference (FD) interpolation scheme.

6.3 Model validation

In order to validate the FLUENT and CFX models for multiphase flow simulations through porous media, cases of increasing sophistication have been modelled and compared against analytical and experimental tests. Initially, simple cases of isotropic flow through blocks of porous material were simulated and compared to analytical results determined from Darcy’s Law. Once satisfied with the modelling results from several such basic cases, validation efforts shifted to running simulations of the permeability experiments outlined in Chapter 5.

Both isotropic and anisotropic cases of flat, single material plies (undeformed and sheared to 20° or 40°) have been studied to determine the effectiveness of the model in simulating fluid flow for an infusion-type process. The multiphase models from both CFX and FLUENT were run in double precision for all cases, neglecting gravity effects due to the 2D nature of the experiments. As is necessary for any computational modelling work, mesh and time-step sensitivity were studied to ensure that fluid flow was within 2% of the independent results, and convergence was carefully monitored throughout each simulation.

For both the isotropic and anisotropic simulations the transient flow front was observed via the increasing resin (or in the case of the permeability experiments, oil) volume fraction in cells through the modelling domain. The location of the flow front, as predicted by simulation, was expected to occur where the resin volume fraction was 0.5, such that the empty volumes of

cells (based on the porosity/fibre volume fraction) were half-filled with resin and half-filled with air.

6.3.1 Simulation of isotropic permeability tests

These simulations focussed on assessing the validity of the multiphase and porous media modelling approach by comparing the predictions with known experimental results. Simulations in CFX and FLUENT were run using the same mesh of 2658 elements, with a 1 second time-step and over a total time of 150 seconds. A 300 mm squared and 0.4 mm thick domain was modelled in accordance with the experimental set-up, including a 3 mm radius circular inlet at the centre of the sample. In order to simulate the experimentally-measured vacuum pressure drop (98.0 kPa), the ambient inlet pressure was assumed to be 101.325 kPa, and an outlet pressure of 3.325 kPa was set for the four edge faces of the domain. The top and bottom surfaces were modelled as free-slip walls, since the permeability properties were originally calculated by neglecting wall effects. The porosity and isotropic permeability were set to be 0.724 and $0.570 \times 10^{-10} \text{ m}^2$ respectively (as determined in Chapter 5), and the resin viscosity was 0.08819 Pa.s in accordance with the recorded values from experimentation. Air was considered as an ideal gas with initial density 1.204 kg/m^3 and viscosity $1.8 \times 10^{-5} \text{ Pa.s}$. The full list of these parameters is provided in Table 5.

Based on the assumption that the simulated flow front occurs where the resin volume fraction is 0.5, the flow front propagation from the inlet is compared with experimental results for both the CFX and FLUENT simulations in Figure 71. There is very good agreement between both software packages and the experimental results for the whole test duration.

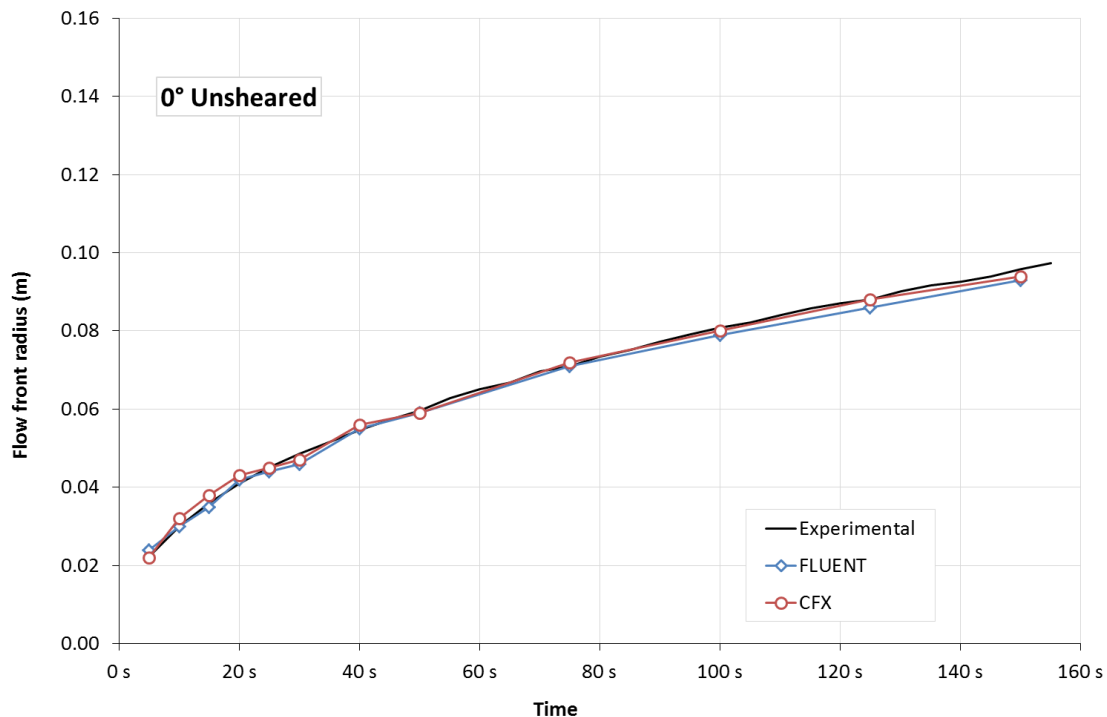


Figure 71: Plot of simulated and experimental flow front results for the unsheared (0°) fabric.

Qualitatively, Figure 72 compares the simulation and the actual experimental results at 75 seconds. In the simulations, the flow front is illustrated by the distribution of resin volume

fraction, where red contours represent resin rich areas and blue describes dry, air-filled regions. Thus there is greater diffusion of the simulated flow front than in the actual experiment; where the resin and air interface produces a more distinct and discrete boundary. However, treating the midpoint of this diffusive flow front (where resin volume fraction is 0.5) as the effective flow front still provides an accurate prediction, as evidenced by Figure 71. There appears to be greater diffusion and irregularities (at a low resin volume fraction) in the CFX simulation results, despite both simulations being run with similar approaches (with an identical mesh and time-step).

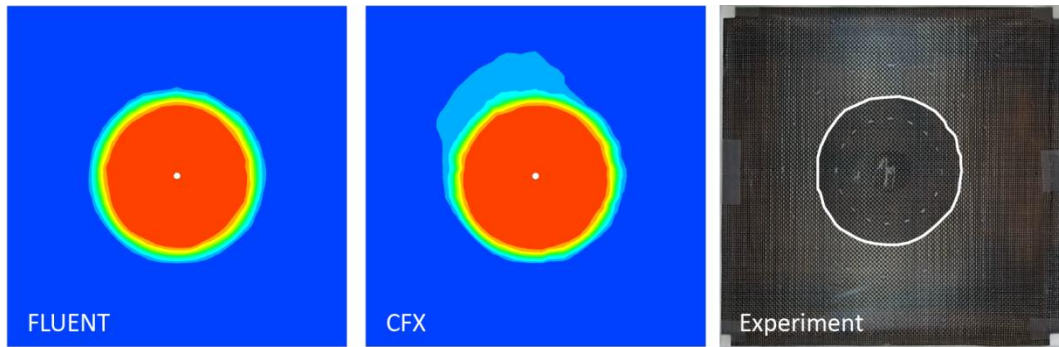


Figure 72: Unsheared (0°) fabric results from FLUENT and CFX simulations compared with the experiment at 75 seconds.

6.3.2 Simulation of anisotropic permeability tests

Adding a further degree of complexity, anisotropic permeability properties were next included in the simulations to validate the model against the experimental 20° and 40° shear angle samples. As with the isotropic simulations just described, details of each modelling case were the same for FLUENT and CFX (outlined in Table 5). The inlet pressure, domain thickness, time-step, total time, and inlet radius for the anisotropic cases remained the same as the isotropic case and the free-slip wall conditions were maintained. The parallelogram domains of these sheared cases also had 300 mm edge lengths but were simply skewed by 20° and 40° respectively. To account for the anisotropic behaviour of the fabric, separate ‘streamwise’ and ‘transverse’ permeability values were assigned (based on the principal permeability values calculated in Chapter 5), along with the definition of the streamwise direction for both cases.

Table 5: Permeability test simulation parameters for 0°, 20° and 40° shear cases.

Fabric shear angle	0°	20°	40°
Mesh	2658	2040	2458
Fluid viscosity, μ	0.08819 Pa.s	0.08421 Pa.s	0.08046 Pa.s
Outlet pressure, p_o	3325 Pa	2825 Pa	2825 Pa
Porosity, ϵ	0.7240	0.7066	0.6401
Streamwise permeability, K_S	0.570 × 10 ⁻¹⁰ m ²	0.880 × 10 ⁻¹⁰ m ²	1.110 × 10 ⁻¹⁰ m ²
Transverse permeability, K_T		0.470 × 10 ⁻¹⁰ m ²	0.300 × 10 ⁻¹⁰ m ²
Streamwise direction vector	-	0.819, 0.574, 0	0.906, 0.423, 0

Again, values of 0.5 resin volume fraction were taken to mark the position of the flow front from the inlet, however to capture the anisotropic behaviour, measurements of flow front radius are taken separately in the streamwise (S) and transverse (T) directions. Figure 73 plots the simulated results from FLUENT and CFX for both the streamwise and transverse directions against the experimental results for the 20° shear case. Here both simulations demonstrate a strong capability to accurately capture the anisotropic behaviour, showing good agreement with the experimental results. The qualitative results from the simulations and experiment are shown in Figure 74, where there is a similar degree of flow front diffusion to that of the unsheared fabric. The streamwise (S) and transverse (T) directions are shown for the experimental results in Figure 74, which correspond with the flow front maxima and minima respectively.

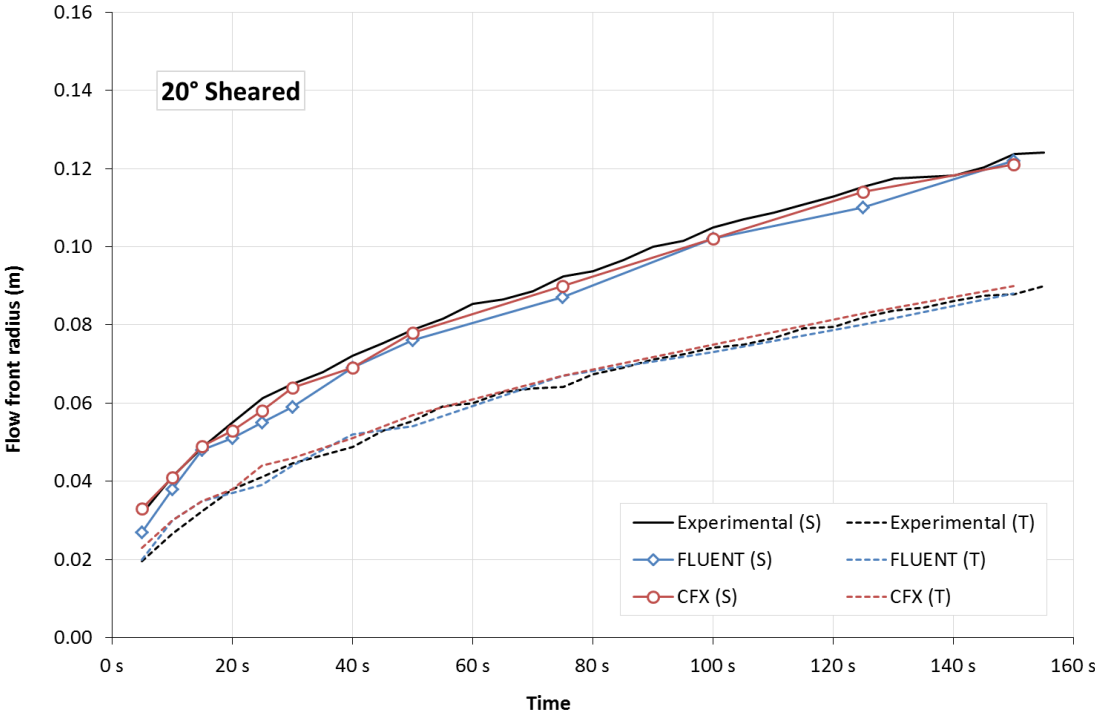


Figure 73: Plot of simulated and experimental results for the sheared (20°) fabric, in the streamwise (S) and transverse (T) directions.

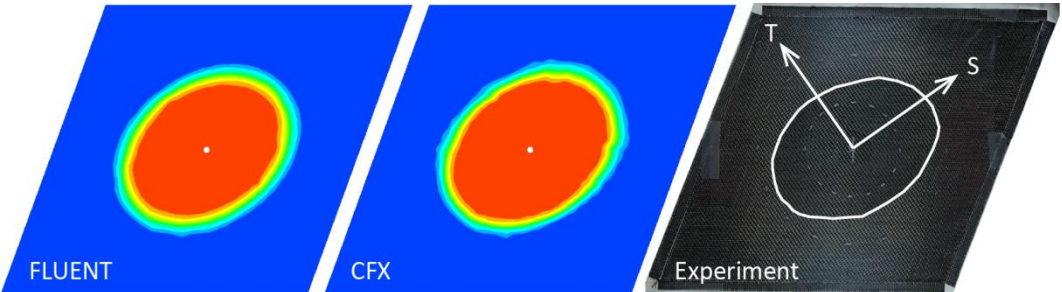


Figure 74: Sheared (20°) fabric results from FLUENT and CFX simulations compared with the experiment at 75 seconds.

For the 40° shear case, the simulations continue to show very good agreement with the experimental results for anisotropic flow. In both the streamwise and transverse directions the software packages predict flow front propagation with high fidelity (Figure 75). In this

configuration the experimental results end at 110 seconds, although this does not affect the validation of both CFX and FLUENT models.

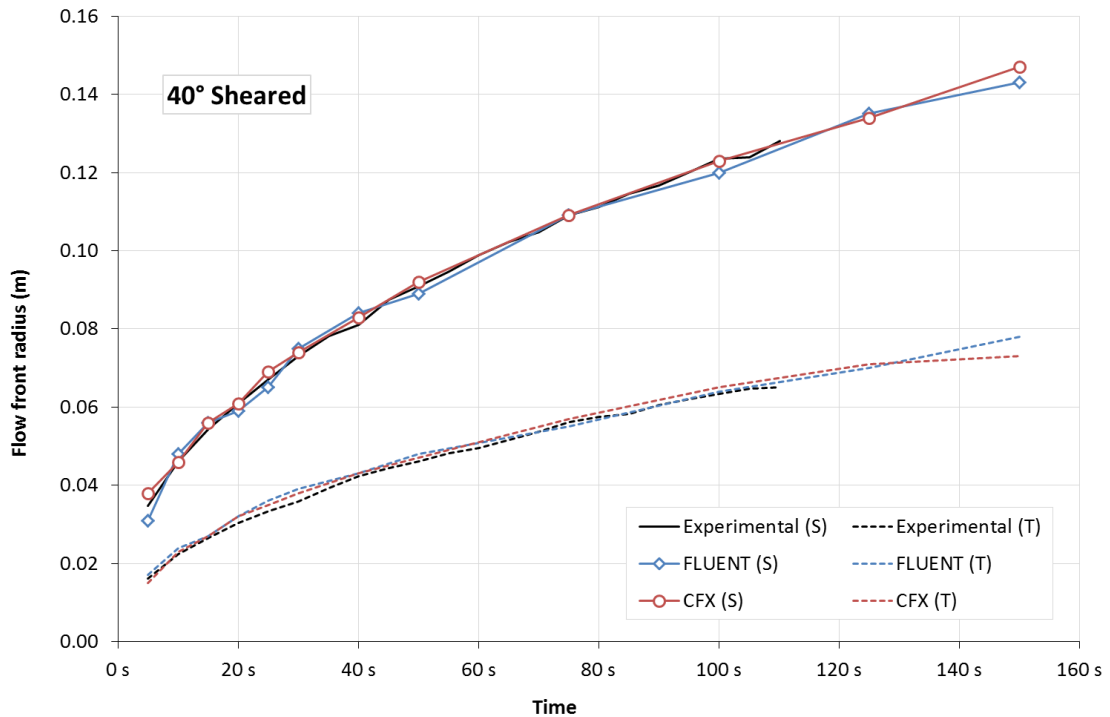


Figure 75: Plot of simulated and experimental results for the sheared (40°) fabric, in the streamwise (S) and transverse (T) directions.

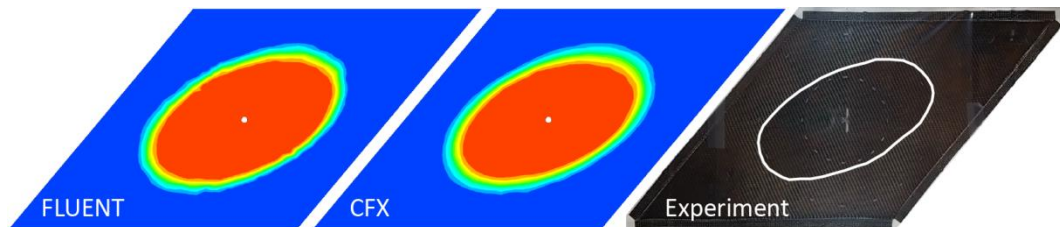


Figure 76: Sheared (40°) fabric results from FLUENT and CFX simulations compared with the experiment at 75 seconds.

6.4 Comparison of CFX and FLUENT models

Since both FLUENT and CFX perform well to this point, further analysis has been undertaken to determine which package would be more robust and suitable for advancement to more complex modelling cases. Mesh and time-step sensitivity studies have primarily been performed to differentiate the two software packages, although the solve time has also been considered. These studies have been performed for the 40° shear permeability experiment case as it provides sufficient complexity to differentiate the two models.

6.4.1 Mesh dependence

In order to evaluate the sensitivity of each modelling approach to changes in the domain mesh, simulations were run with meshes of varying refinement under identical conditions and a 1 second time-step. Starting with a 'coarse' mesh of 491 elements, the mesh was refined to a 'regular' mesh of 2458 elements and once again to a 'fine' mesh of 11384 elements for both

CFX and FLUENT. As expected, the results (measured as the flow front radius in streamwise and transverse directions) were observed to converge with mesh refinement. However, for both packages the initial coarse mesh still provided reasonable agreement with experimental results and the difference between the regular and the fine mesh results was negligible. Subsequently, it is only the comparison of the coarse and regular mesh results for CFX and FLUENT that is discussed in this section.

The relative error of the simulation results from the experimental data for flow in the streamwise and transverse directions was calculated, with the coarse mesh results plotted against time in Figure 77. The error (in both flow directions) using the regular mesh is below 10% for the entire time domain for both packages, and below 4% after 40 seconds. However, using the coarse mesh, there is significant error (greater than 10%, and as high as 49%) in the transverse flow direction when modelling with CFX for the first 30 seconds. FLUENT does show slightly increased error in the transverse flow direction with the coarse mesh until 15 seconds, though it remains below 13%.

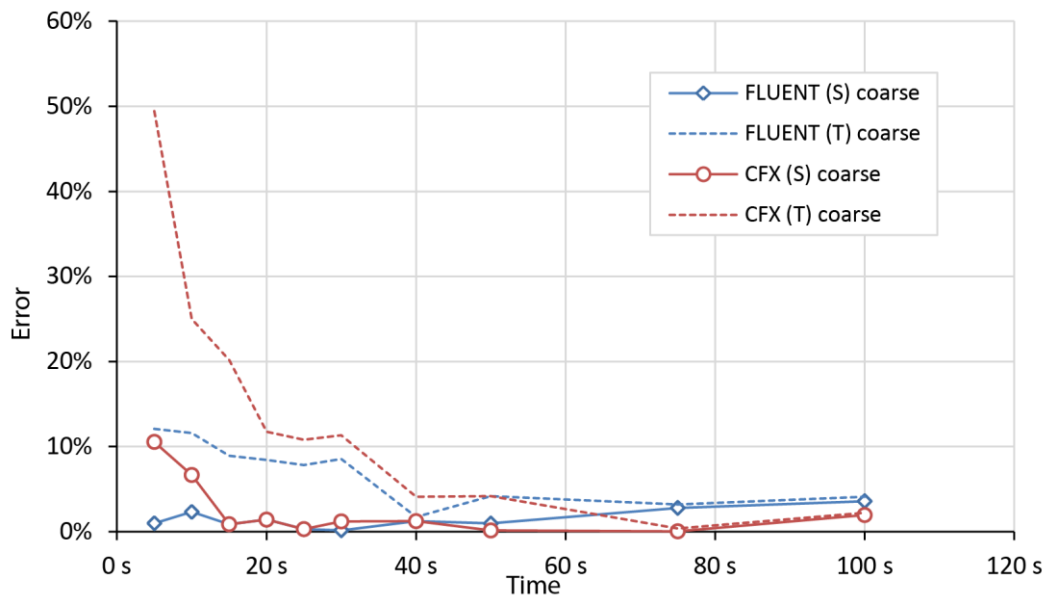


Figure 77: Simulation error for coarse and regular meshes in the streamwise (S) and transverse (T) directions.

Table 6 shows the error for each mesh-dependent simulation as an average of the flow front radius deviation from experimental results for the full time domain. For both packages, the error in the coarse mesh is higher, although the FLUENT results appear to show reduced mesh dependence as the results are more consistent. However, the regular mesh results from CFX have the least error overall. The flow front diffusion in Table 6 is an averaged, relative measure of the resin/air interface size throughout the full time domain for each simulation. Since the flow front radius is taken as the point where resin volume fraction is 0.5 in this interface, the diffusion measure is taken as the relative distance of cells with resin volume fraction values ± 0.4 from the flow front. Again, as expected, the flow front diffusion reduces with mesh refinement for both CFX and FLUENT. CFX also shows less diffusion than FLUENT regardless of the mesh, meaning that the flow front appears to be slightly more distinct in CFX simulations. However, the CFX diffusion is still significant (above 20% even when using the regular mesh)

due to the modelling approach. The simulation wall time using a single core is also compared, with a notable increase in computational time for the regular mesh in CFX, but a negligible change for FLUENT which performs reasonably well for both meshes (although slower than CFX for the coarse mesh).

Table 6: Mesh sensitivity of CFX and FLUENT simulations for the 40° case with a 1 second time-step.

Software	CFX		FLUENT	
Mesh	491 (coarse)	2458 (regular)	491 (coarse)	2458 (regular)
Wall time	133 s	268 s	192 s	188 s
Average flow front diffusion	26.8 %	20.2 %	28.1 %	25.3 %
Average error	8.2 %	2.7 %	4.3 %	4.0 %

Looking at the simulation results qualitatively, CFX appears to exhibit greater diffusivity of the resin volume fraction values, particularly in areas where these values are low despite the quantitative mean results in Table 6. Figure 78 compares the simulation results with both meshes against the actual flow experiment at 10 seconds. From this figure it appears that CFX has a greater sensitivity to the mesh, with an irregular flow front prediction in the early stages of the simulation, even for the regular mesh. FLUENT on the other hand, exhibits very little sensitivity to the mesh; with slightly more diffusion observed at the flow front for the coarse mesh. Unlike the CFX results, the diffusive zones predicted by FLUENT are very consistent for the whole flow front regardless of the mesh geometry and refinement.

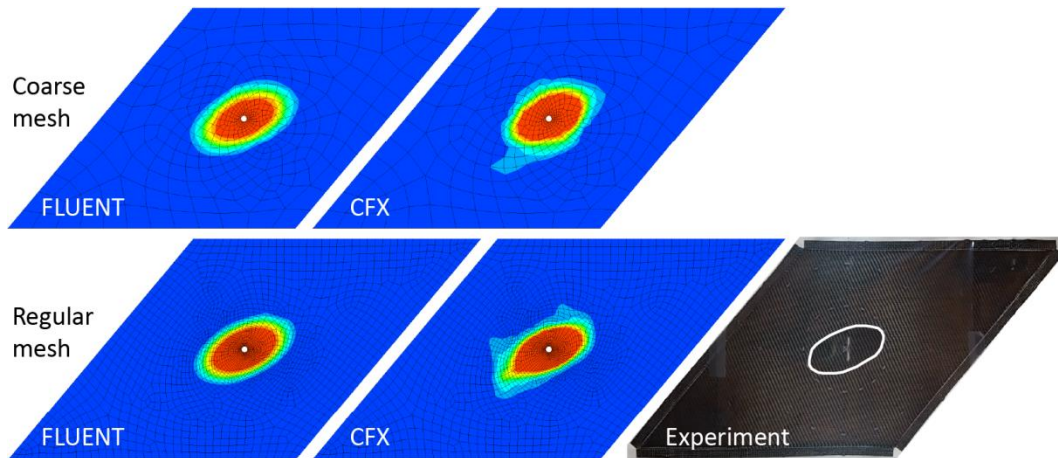


Figure 78: Comparison of meshing effects with FLUENT and CFX for 40° shear samples at 10 seconds against experimental results.

6.4.2 Time-step dependence

Based on the regular (2458 element) mesh for the 40° shear case, further simulations were run with various time-steps (0.1, 1 and 5 seconds) to evaluate the time-step dependence of the two software packages. As expected, both CFX and FLUENT observed a general convergence with time-step reduction (at the cost of increasing computational times).

Again the relative flow front error for both streamwise and transverse directions, as predicted by the various time-step simulations, was calculated. The 5 second time-step results are plotted against time for both FLUENT and CFX in Figure 79, since error in the smaller time-step

simulations was less significant. Unsurprisingly, the greatest error was generally observed at the start of tests (likely due to the peak flow rates occurring at that time). However, the streamwise CFX results show a much greater, persistent error (above 10%) for the whole duration of the simulation with a 5 second time-step. Error results for the 1 second and 0.1 second time-steps were generally below 10% for both directions and both software packages. The only exception was for the transverse CFX results (with the 0.1 second time-step), which also had exceptionally high error (above 20%) for the first 15 seconds of the test; greater even than any error observed in the 1 second time-step simulation.

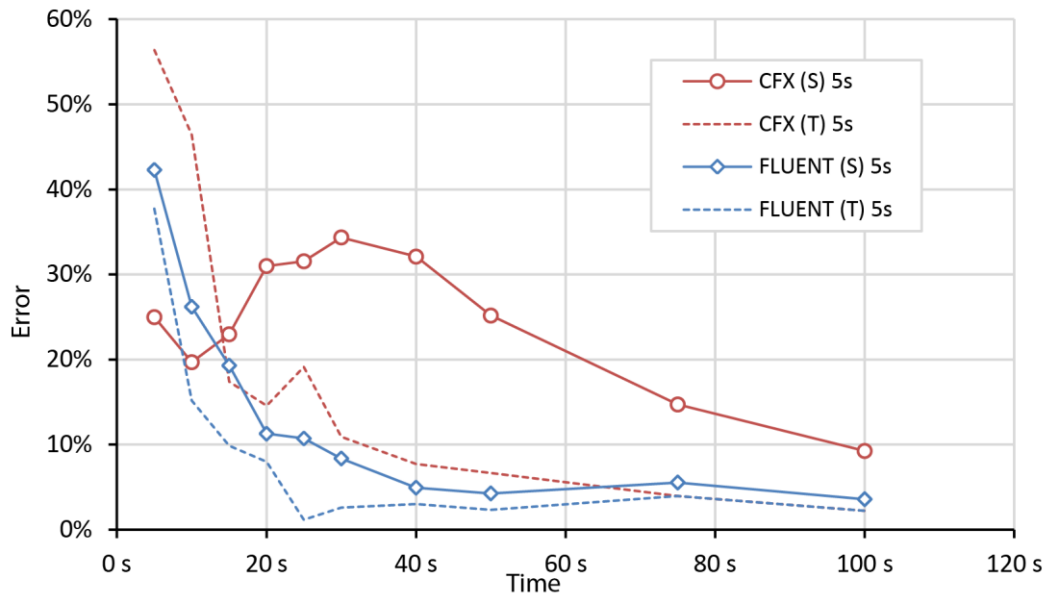


Figure 79: Error for FLUENT simulations with three different time-steps, in the streamwise (S) and transverse (T) directions.

The wall time, flow front diffusion and error are shown in Table 7 for the three different time-step simulations in each software package. As the time-step size reduces (and the required number of time-steps increases) the solution time increases for both packages. Flow front diffusion is similar in both packages for like tests, with diffusivity reducing along with time-step. The error is greatest in the simulations with long time-steps (primarily as a result of the initial peak velocities that cannot be reasonably resolved with a 5 second time-step). However, the unexpectedly high error in the 0.1 second time-step CFX simulation is not so easily explained. This is likely to be a result of discretisation error, since FLUENT does not have the same problem using slightly different discretisation techniques.

Table 7: Time-step sensitivity of CFX and FLUENT simulations for the 40° case with a regular mesh.

Software	CFX			FLUENT		
	0.1 s	1 s	5 s	0.1 s	1 s	5 s
Time-step	0.1 s	1 s	5 s	0.1 s	1 s	5 s
Wall time	727 s	268 s	88 s	992 s	188 s	86 s
Average flow front diffusion	18.6 %	20.2 %	33.5 %	17.4 %	25.3 %	31.5 %
Average error	9.9 %	2.7 %	21.6 %	4.2 %	4.0 %	11.1 %

Figure 80 shows the qualitative results of this time-step study at 25 seconds. As with the mesh sensitivity results, FLUENT is capable of very consistent results and achieves a realistic flow front profile where the diffusion variance is the only notable change resulting from time-step modification. CFX on the other hand, for all simulations displays the same irregularities in the flow front profile that have been observed in the other results, even for the short time-step simulation that would be expected to be the most accurate. With a 5 second time-step, the CFX flow front profile is clearly dominated by error. This error eventually resolves into a more realistic elliptical shape, although it still does not match the fidelity of the FLUENT simulation.

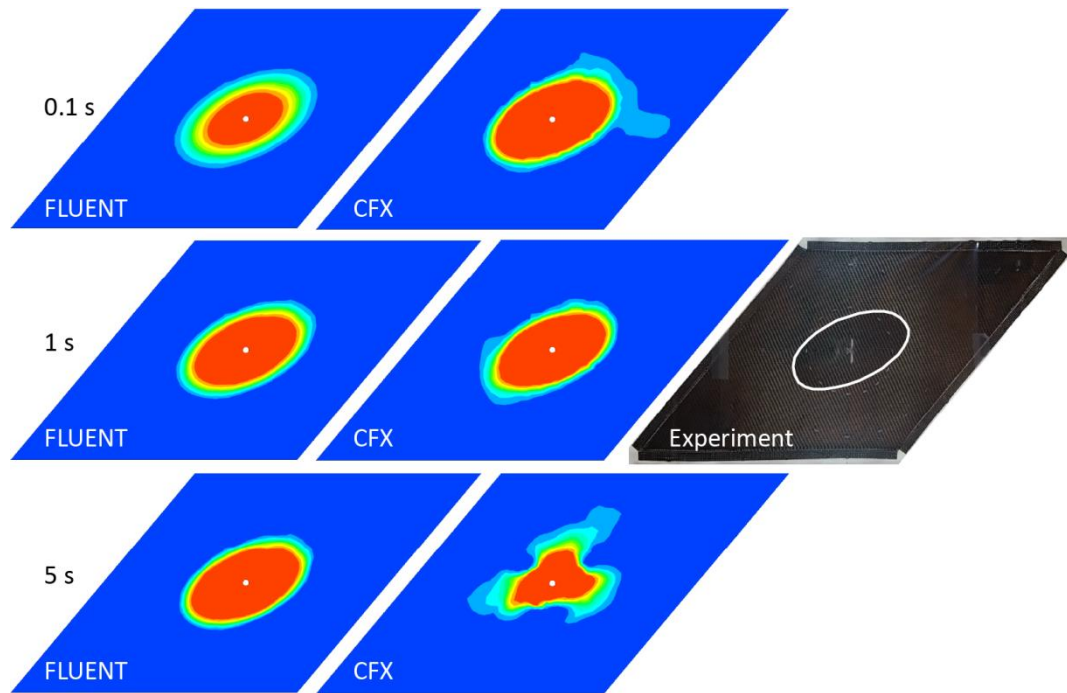


Figure 80: Comparison of time-step variation in FLUENT and CFX for 40° shear samples at time 25 seconds.

6.5 Further modelling capabilities

The validation results in this chapter demonstrate the ability to simulate resin flow through a porous material with anisotropic permeability characteristics. Despite the planar nature of these initial trials, the models are actually capable of simulating flow through more complex 3D domains, as is demonstrated by the Complete Process Model in Chapter 7. In addition to this, for the CPM, the goal is to run simulations with a complex distribution of variable permeability properties throughout the domain (that result from local shearing during the draping process). This is possible within CFX and FLUENT, as user subroutines can be coded to assign material properties on a cell-by-cell basis (the implementation of which is discussed in Chapter 7). Multiple plies of material at different orientations can also be evaluated using the models described in this chapter provided each material ply is represented by its own layer of elements in the full domain mesh. However, future work would need to be conducted to determine feasible permeability properties for each ply in the stack.

At this stage, the models still rely on a number of assumptions and simplifications of the true infusion behaviour; however, these CFD packages are capable of significant enhancements and improvements. Firstly, provided the temperature dependence of fluid properties has been

adequately characterised, the model can easily incorporate a shared-phase energy equation into the governing equations and account for heat transfer. This is useful for simulating cases where resin is heated prior to infusion, or where a heated tool surface is implemented to enhance resin flow. Similarly, surface tension and wall adhesion effects can also be included in these VOF models for cases where it is unreasonable to simulate infusion with free-slip boundaries. The simulation of the actual curing reaction might also be desirable during the infusion of large parts, in which case mass transfer terms can be included in the volume fraction equation to account for the migration of gaseous species from the resin bulk into the air phase. This may further be coupled with the exothermic curing behaviour of the resin system by incorporating the energy equation.

Another popular area of model enhancement is in the prediction of void content, since both software packages are capable of including user subroutines this may also be possible to include in future work. Lastly, preform compaction and thickness change during the infusion process may also be of interest for thicker parts. Currently, the models assume a constant ply thickness based on experimental permeability test results; however thickness change can be modelled artificially as an alteration to the porous media momentum source term by dividing the permeability by the relative thickness change. Alternatively, the ANSYS suite of modelling packages that includes CFX and FLUENT is also capable of running sophisticated Fluid-Structural Interaction (FSI) simulations. Such simulations combine CFD and structural FE methods to simultaneously predict the effect of transient interactions between fluids and solids. The application of this would be to simulate resin flow inside a deformable vacuum bag, where the advancing flow of resin is known to affect the local bag thickness [43, 90-92]. However, such modelling approaches would require details of the vacuum bag elasticity and plasticity from further material characterisation testing and there was not sufficient time to explore this option.

6.6 Discussion and conclusions

This chapter has documented the theoretical background and implementation of infusion modelling approaches in two general-purpose CFD software packages, FLUENT and CFX. Although some previous research has shown the infusion specific software PAM-RTM to perform slightly better than CFX for a similar application [10], the generalised packages have been adopted due to their overall flexibility and capacity for improvement. The VOF-based multiphase and porous media modelling approaches have been validated against the experimental permeability test results, and demonstrate sufficient capability for implementation in the Complete Process Model.

Specifically comparing the FLUENT and CFX modelling results from the validation simulations, both provided realistic predictions of the flow front profile for isotropic and anisotropic cases. However, the qualitative analysis of the results revealed that the CFX models were generating diffusive irregularities for areas of low resin volume fraction in many of the simulation cases, regardless of the modelling set-up. Furthermore, the mesh and time-step dependence trials highlighted problems with the CFX model, which proved much less robust than FLUENT and revealed unreasonable qualitative results. As there was little difference in the theoretical foundations of the two modelling approaches, the differences in the spatial discretisation methods are expected to be the primary reason for the undesirable behaviour observed in the

CFX models. Otherwise, the CFX simulations often resulted in slightly better accuracy, marginally less diffusion in the flow front and were slightly faster to solve. However, these benefits were minimal overall, and as such, the FLUENT model was selected for implementation in the Complete Process Model.

7 Complete Process Model (CPM)

7.1 Motivation

Thus far, each component of the Complete Process Model (CPM) has been discussed individually. First, a draping model was developed and validated against results from existing literature. Then, tensile and shear characterisation methods were implemented for a plain weave carbon fibre fabric, including the development of customised DIC code. Similarly, permeability testing was performed over a range of shear angles using optical measurement techniques. Lastly, an infusion model was evaluated and validated against experimental results.

Fundamentally, the CPM is designed to predict and account for changes in the flow properties of a material that result from forming, and subsequently simulate infusion through the deformed material more accurately. This is an improvement over existing models, which assume that the fabric properties are homogenous (even in a deformed configuration). Such an assumption is reasonable for cases where the formed geometry is very simple, like flat panels; however for complex structures the effect of fabric deformation on flow properties needs to be accounted for.

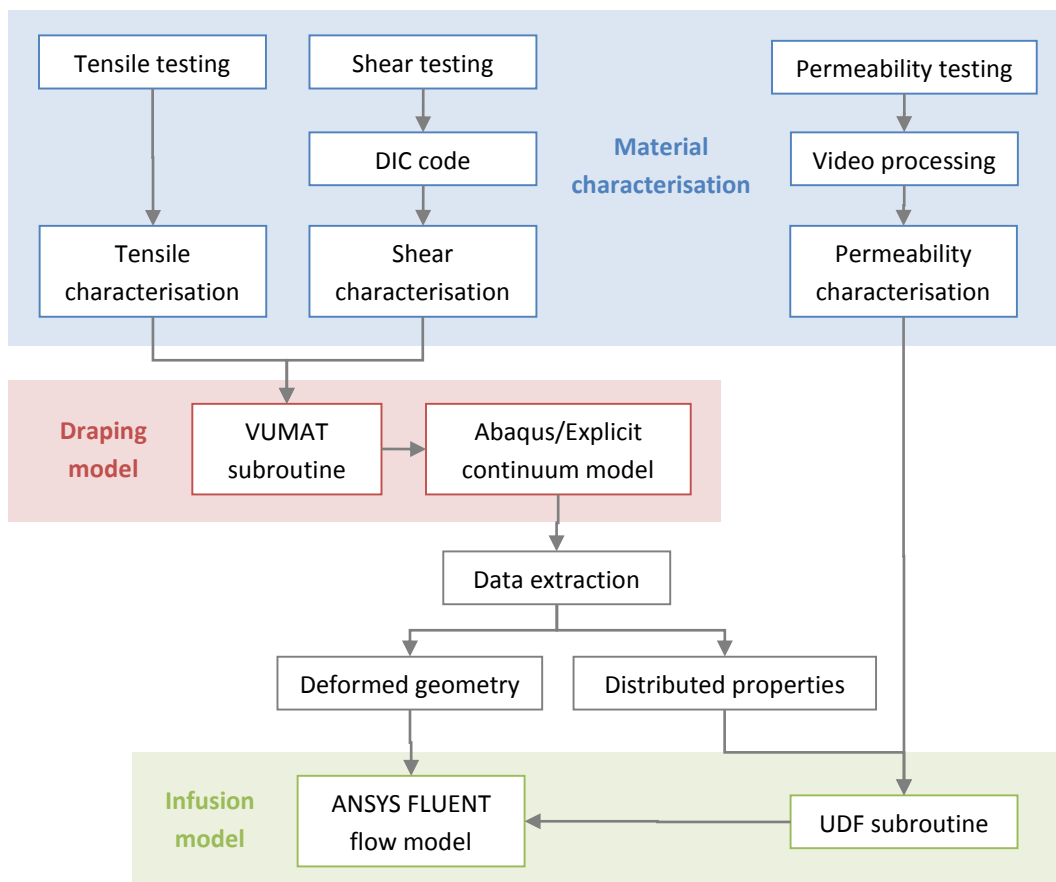


Figure 81: Flow chart for the Complete Process Model (CPM).

Since draping and infusion have both been independently simulated quite effectively in the past, the most important component to this research is in linking the results of the draping model with the infusion model. This chapter details the linking of these models: extracting the geometry and distributed properties that result from the draping model, and then importing this information into the infusion model. A flowchart of the Complete Process Model is shown in Figure 81. In the latter part of this chapter, a detailed validation of the CPM is presented against the experimental draping and infusion of a double dome part, followed by a discussion of future work and potential.

7.2 Extracting information from the draping model

As the simulation results from Abaqus are not directly compatible with FLUENT, the detailed information from draping needs to be extracted and stored in a format appropriate for the infusion model to reference. Simulations run within the Abaqus infrastructure produce a binary output database (odb) file, in which all the modelling and results data is stored. The information in the output database file can be accessed either through the Graphical User Interface (GUI) (called Abaqus/CAE) or through the Abaqus Scripting Interface. Although Abaqus/CAE is useful for visualisation of the results and post-processing, it does not allow access to the detailed data necessary (notably the local material directions can be visualised, but not exported for the deformed geometry in the GUI). Additionally, the extraction of large data sets can be somewhat tedious in Abaqus/CAE. Hence, the scripting interface has been used in this work to allow for greater automation, accessibility and increased efficiency. The Abaqus Scripting Interface is based on an object-oriented programming language, Python, and acts as an Application Programming Interface (API) to the data and models used by Abaqus. A purpose-written Python script has been developed to perform the necessary data extraction for the Complete Process Model, and is fully documented in Appendix B.

The Python script takes all the relevant information stored in the Abaqus output database file and returns two convenient text files to support the infusion modelling in ANSYS. One file contains all the nodal position data such that remodelling of the final part shape (as determined from the draping model) can be easily performed in ANSYS. The second file contains the shear angle and material orientation results associated with elemental locations (also from the draping simulation) so that a FLUENT User Defined Function (UDF) subroutine can perform interpolation and other calculations.

Once the Abaqus output database is generated from the draping model the Python script can be run through the Abaqus GUI or command prompt. The code operates autonomously, under the assumption that the desired results are associated with the final frame of the final step in the simulation. Initially the script identifies the Solution Dependent state Variable (SDV) for shear angle, along with the stress and displacement field outputs. Element type is also retrieved (for M3D4R or S4R element meshes), and the sizes of variable arrays are determined. Since the order of values in the field output arrays is not numerical, preliminary loops through the nodal and elemental lists are run to associate and store indices for later referencing. At this point, since the mesh is assumed to be a regular grid, the connectivity of the first element is queried. This serves to determine the number of rows and columns in the regular elemental grid.

The core section of the script loops through instance points (the locations within each element for which values are calculated), storing vectors for the three local material directions and the local shear angle. Nested within this loop, average elemental coordinates are also calculated from the adjacent nodal coordinates (accounting for initial position and final displacement).

The final component of this script writes the element coordinates, local material directions and shear angles to ASCII (text) files. Two separate output files are created: one to store the nodal coordinates in a column by column format (to assist in geometry generation); and the other to store the element number, coordinates, material directions and shear angle for each element in the model (to be referenced by the infusion model). These make up the deformed geometry and distributed properties modules in Figure 81 respectively.

7.3 Importing information into the infusion model

The process of importing information (that has already been extracted from the draping model) into the infusion model has two stages. First the deformed geometry needs to be recreated before the infusion model can be established, and then the infusion model needs to retrieve the relevant distributed properties upon initialisation.

7.3.1 Recreating the deformed geometry

Due to incompatibility between Abaqus and ANSYS, the deformed mesh from the draping model is not able to be simply imported into the infusion model. However, the Abaqus mesh is created as a regular grid of flat elements prior to deformation, thus columns of the nodal positions can instead be used to recreate the deformed geometry in DesignModeler (the geometry generation module within ANSYS). This information is extracted from Abaqus and stored in the deformed geometry ASCII file as discussed earlier. In DesignModeler, these columns of coordinates can be simply imported as multiple 3D curves in a single operation. Then the 'skin/loft' feature can be used to regenerate the full deformed geometry to the desired thickness based on the 3D curve skeleton. This process is relatively quick and simple thanks to the formatting of the deformed geometry text file. However, it does require some degree of user interaction each time a different deformed geometry is generated from the draping model. Once the geometry is regenerated, the ANSYS meshing package also has to be used to recreate a suitable mesh for the domain. Figure 82 shows this regeneration process from the initial Abaqus deformed geometry to the new ANSYS mesh for a double dome simulation case.

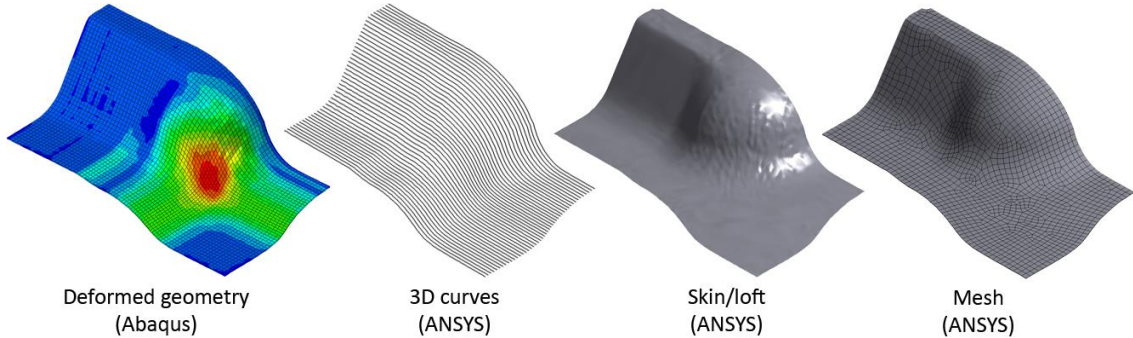


Figure 82: Geometry and mesh regeneration process for a double dome simulation with quarter symmetry.

7.3.2 Referencing to the distributed properties

In order to incorporate distributed properties from the draping simulation into the infusion model, a UDF subroutine has been developed in the C programming language for FLUENT. This defines a number of macro functions such that the subroutine reads data from the distributed properties ASCII file and assigns local variable values to each centroid in the meshed domain. The subroutine includes a single 'INIT' macro function, followed by nine 'PROFILE' macro functions, which are outlined in greater detail below. A complete example of the code is also supplied in Appendix C.

7.3.2.1 INIT macro function

The core INIT macro function reads the values that have been exported from Abaqus in the distributed properties text file, and calculates permeability and porosity values based on user-input functions related to shear angle. Similarly, the material directions are used to calculate and assign the local streamwise and transverse flow directions of the material in relation to principal permeability values. The macro function works by initially reading through each line of the distributed properties ASCII file iteratively and storing values into long array structures for: element number, coordinates, material directions and shear angle. Then, the code iteratively loops through every cell in the new infusion domain. For each cell, the location of the cell centroid is noted and compared to the location of each element from the Abaqus model in order to calculate the distance between them. This process serves to find the three closest points from the Abaqus model such that values at the cell centroid of the FLUENT model can be estimated via interpolation. The 3D interpolation is performed by an inverse distance-based weighting method where the value of ϕ at a cell-centred location x , is determined from the values, ϕ_i , of the nearest 3 locations as follows:

$$\phi(x) = \sum_{i=0}^2 \frac{w_i \times \phi_i}{W_{sum}} \quad (55)$$

Where the weighting function, w_i , is the inverse cubic of the distance, d_i , between the location x and the nearby point x_i . A cubic power parameter is used in Equation (56) for this three-dimensional case to achieve a reasonable degree of smoothing and account for significant contributions from each of the closest points since the 3D grid of points is quite regular. The sum of the three weighting values, W_{sum} , is defined in Equation (57).

$$w_i(x) = \frac{1}{d_i^3} \quad (56)$$

$$W_{sum} = \sum_{i=0}^2 w_i(x) \quad (57)$$

Based on the material direction values that have been interpolated for the current centroid, a bias direction vector (bisecting the material directions), a normal vector (cross product of the material directions), and a transverse vector (cross product of the bias and normal directions) are determined.

Next, several calculations are performed depending on the value of the local shear angle for each centroid. First there is a check to see if the shear angle is negative at this point, if so, then

the bias and transverse directions are swapped, and the shear angle is corrected to become positive. The equations for determining viscous resistance (in the bias and transverse directions) and porosity are hard-coded by the user, based on experimental results and curve fitting. In this case they are simply the inverse of polynomials relating shear angle with permeability, and porosity is calculated from the initial unsheared porosity, ϵ_0 , and the shear angle, γ , according to Equation (58). The last part of the INIT macro function stores all the values of interest in User Defined Memory (UDM) locations for use by FLUENT and the subsequent 'PROFILE' macro functions.

$$\epsilon = 1 - \frac{(1 - \epsilon_0)}{\cos \gamma} \quad (58)$$

The INIT macro function is designed to be hooked to the initialisation of the model, each time the simulation is initialised this function is then called. During the solver phase, this function is not called since all the relevant cell values are defined upon initialisation and stored in the UDM locations for the solver to access. Hence the model remains efficient as the external files need only be read once, and the distributed values remain constant.

7.3.2.2 PROFILE macro functions

The PROFILE macro functions are simply property definitions that are called upon throughout each time increment and iteration for the cells in the mesh domain. Of the nine different functions, three are for the porosity, streamwise viscous resistance and transverse viscous resistance. The remaining six make up the x, y and z components of the streamwise and transverse direction vectors. All nine of the PROFILE macro functions operate in the same manner: looping through each cell centroid in the domain, recalling and assigning a given property value based on the associated UDM that is stored during initialisation by the INIT macro function.

7.4 Complete Process Model (CPM) demonstration

In order to demonstrate the Complete Process Model (CPM) capabilities, an experimental 'double dome' geometry has been selected, since it is a complex form that has been commonly used for similar studies [31, 33]. The significant double curvature of this geometry is typically avoided in the aerospace industry due to the manufacturing challenges that are associated with such complex forming. Hence, a comparison of experimental and modelled infusion for the double dome was intended to serve as a good demonstration for the innovation that the CPM can bring to industry.

7.4.1 Experimental method

An experimental double dome tool was created based on the geometry from literature [31], at twice the original scale (to further reduce the influence of meso and micro scale flow behaviour). The tool itself was constructed from structural foam before being coated to provide additional strength and prevent fluid permeation. This male tooling was recessed 120 mm deep into an outer frame (950 mm x 550 mm), in order to facilitate improved forming and bag conformity.

Tests were conducted with single plies of the carbon fibre plain weave material being placed over the mould, before being covered with a vacuum bag. This configuration was chosen in

preference of a rigid mould for several reasons. Firstly, observation and measurement of the flow front was desired, hence the upper mould needed to be transparent. A clear, rigid mould would be particularly difficult to manufacture, compared to simply using a vacuum bag. Furthermore, the dimensional tolerances for a clear rigid mould were expected to be relatively poor and unable to maintain a constant thickness throughout the complex domain (especially for sub-millimetre accuracy). The effect of any cavity thickness variance would then have an unpredictable effect on the flow front behaviour (unless a detailed set of thickness measurements were also taken for the whole cavity domain). The vacuum bag, on the other hand, is maintained by the constant ambient pressure with good conformity and more predictable deformation behaviour (with reduced cavity thickness only occurring in areas where interior pressure is highest, primarily near the inlet). Use of a vacuum bag is also more consistent with the intended industrial manufacturing case. However, as is noted in Section 7.6.2 there remain several issues with this approach.

Three different (warp/weft) material orientations were tested: $0^\circ/90^\circ$, $-45^\circ/45^\circ$ and $90^\circ/0^\circ$. The material samples were marked with silver grid lines at 50 mm intervals to facilitate optical measurements from both forming and infusion. A vacuum port located on top of the fabric, at the centre of the double dome geometry was used to induce a vacuum and form the material to the mould shape under the bag. Several layers of flow distribution media were placed under the central vacuum port to ensure a rapid and isotropic flow into the fabric material for the start of each infusion. Distribution media was also placed at the ends of the mould to facilitate an even vacuum towards secondary vacuum ports that were activated during forming once the bag reached the bottom of the mould (by puncturing tubing through the bag). At this point, the first vacuum port was closed off and connected instead to an oil reservoir that was open to ambient conditions.

Prior to infusion, the vacuum bag and material were checked for conformity to the mould, taking particular care to ensure that the material in the concave regions at the base of the double dome shape were not exhibiting bridging (where bag forces could hold the material such that there would be a gap between the fabric and the mould).

Temperature and pressure readings were taken, then the inlet port was opened to commence the infusion while the secondary ports remained under a constant vacuum. Time-stamped images of the fluid flow were taken to monitor the advancing flow front. As with the experimental permeability tests performed in Chapter 5, olive oil was used as the infusion fluid, with properties outlined in Table 4 (Section 5.2). In these experiments the aim was to focus on the effect of changing permeability as a result of fabric deformation. Olive oil provided a relatively low viscosity fluid that behaves similarly to a heated resin, but flows more quickly. Hence, it was preferable for these experiments. For a true resin infusion with such a complex and large component, additional flow distribution media would typically be used to speed up the infusion process before significant curing could occur. The Complete Process Model is capable of including additional layers of highly permeable distribution media for a more realistic infusion, but the focus of this study was on the effect of local permeability change and a resin infusion without flow distribution media might have led to partial curing before complete filling. Hence oil was selected as a representative fluid to serve as the best

demonstration and evaluation of the CPM. Diagrams for the experimental forming and infusion are presented in Figure 83, highlighting the two-stage process and port configurations.

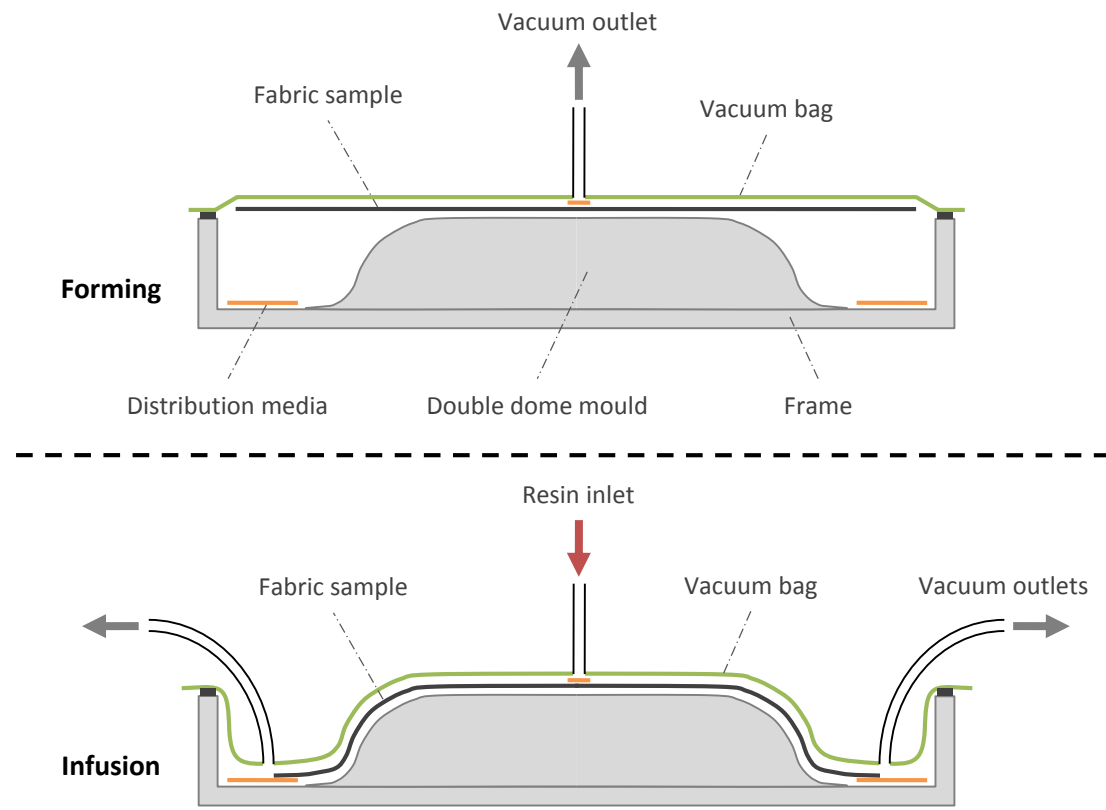


Figure 83: Diagram for the set up of experimental forming and infusion.

7.4.2 Simulation approach

The simulation of these experiments was performed using the Complete Process Model, including all the material characterisation properties, draping and flow simulations discussed in the previous chapters of this thesis. Components of the CPM were linked together to provide the complete package of results, as discussed at the beginning of this chapter, though the two main stages of the simulation approach were draping and infusion.

The deformation of fabric samples was performed using the Abaqus/Explicit draping model, with a similar configuration to the double dome case presented in Chapter 3, but at twice the scale. The model actually simulated the vacuum forming with a stamping configuration, where a deformable blank (of the fabric material) was held in place between a rigid blank holder plate and a female tool die. Then a rigid punch formed the material to the tool geometry. The fabric blank was simulated to be 0.4 mm thick, in quarter or half symmetry (depending on the fabric orientation, a quarter symmetry blank was not suitable for the later infusion simulations with the $-45^\circ/45^\circ$ case). This thickness was selected to remain consistent with the permeability characterisation properties (for the infusion simulation). The tensile and shear properties from characterisation testing of the carbon fibre plain weave (Equation (25) and Equation (40) respectively), were included in the VUMAT subroutine for the draping model. Figure 84 shows an exploded view of the simulation assembly using the quarter symmetry blank (for the $0^\circ/90^\circ$ and $90^\circ/0^\circ$ cases). A global contact condition for friction, with a coefficient of 0.15, was used

across the model as is typical for these types of models [31, 33]. Simulations were run with a regular mesh seed size of 10 mm, such that the deformable material was made up of 1000-2000, M3D4R membrane elements. The results from the completed draping simulations were extracted and reformatted using the Python code discussed in Section 7.2, to prepare the data for use in the flow simulations.

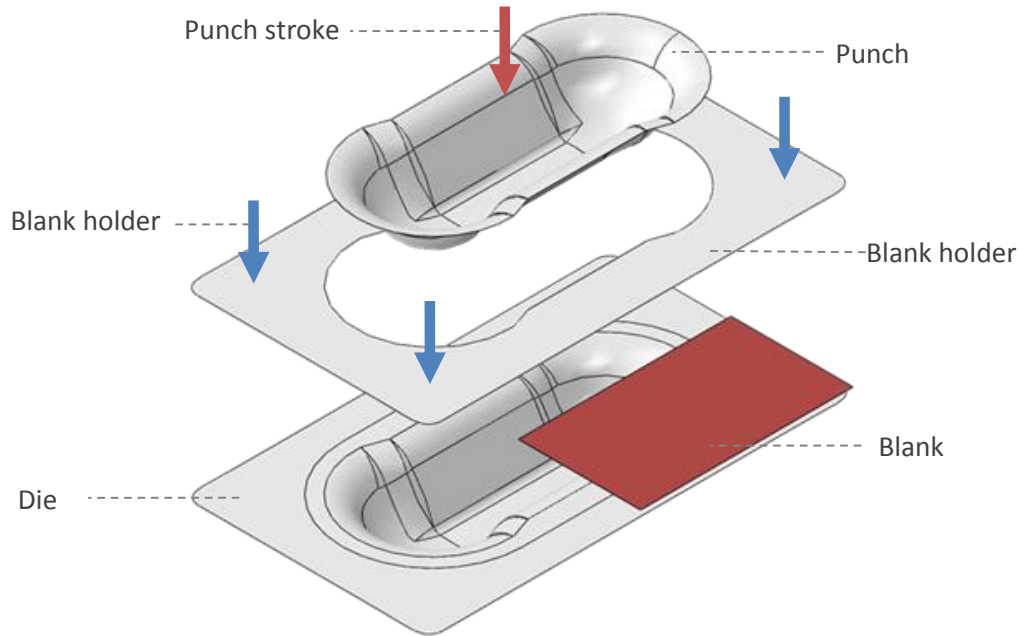


Figure 84: Double dome forming simulation geometry (for quarter symmetry models).

The deformed geometry from draping was recreated in the ANSYS suite with a central inlet of 50 mm diameter cut from the blank and the domain thickness was set to be a constant 0.4 mm. Since several layers of highly permeable distribution media were placed in the 50 mm diameter space under the oil inlet, the effect of any fabric underneath the inlet was negligible and thus excluded from the model. Due to the symmetry of the models, a single outlet condition was defined for the far end of the material as shown in Figure 85. Aside from the inlet and outlet, the remaining faces of the simulated domain were assigned symmetric (free-slip) wall conditions, as were used for the permeability experiment modelling in Chapter 5.

Table 8: Flow model conditions and parameters.

Orientation case	0°/90° and -45°/45°	-90°/0°
Inlet pressure	101.325 kPa	
Outlet pressure	0.3 kPa	
Oil viscosity	0.0993 Pa.s	0.0756 Pa.s
Temperature	16 °C	22 °C
Base porosity	0.724	

A User Defined Function (UDF) subroutine assigned elemental properties throughout the domain, based on the results from draping (as detailed in Section 7.3). Hence the porosity, principal permeability values (K_1 and K_2) and directions were all defined on a cell-by-cell basis in relation to the shear angle distribution, local material directions and the experimentally

characterised permeability functions. Detailed properties from the simulations are shown in Table 8. Although most of the experimental conditions remained consistent for the three different cases, the 90°/0° experimental case was run in warmer temperatures and subsequently the change in oil viscosity had to be accounted for. The shear dependent permeability properties and polynomial functions are also outlined in Equation (59) based on the parameters in Table 9.

Table 9: Permeability function parameters (m²).

	K_1	K_2
a_i	-6.641×10^{-10}	-7.700×10^{-10}
b_i	1.328×10^{-9}	1.466×10^{-9}
c_i	-8.414×10^{-10}	-9.261×10^{-10}
d_i	2.400×10^{-10}	1.605×10^{-10}
e_i	6.028×10^{-11}	5.313×10^{-11}

$$K_i = a_i\gamma^4 + b_i\gamma^3 + c_i\gamma^2 + d_i\gamma + e_i \quad (59)$$

In accordance with the results of the permeability characterisation tests, the principal permeability direction was aligned with the fabric bias (bisecting the two yarn directions) at higher shear angles. However, below a shear angle of 20° this behaviour was less clear, and based on observations from the double dome infusion experiments (where the weft yarn direction showed greater flow) a simple function for defining the principal permeability direction was developed (Equation (60)). Here θ is the angle between the weft yarn direction and the principal permeability direction, as a function of shear angle, γ .

$$\theta = \begin{cases} 45^\circ - \frac{|\gamma|}{2} & \text{if } |\gamma| > 20^\circ \\ \frac{|\gamma|}{20^\circ} \left(45^\circ - \frac{|\gamma|}{2} \right) & \text{if } |\gamma| \leq 20^\circ \end{cases} \quad (60)$$

Flow simulations were run with similarly sized meshes of 1000-2000 elements and a constant 1 sec time-step for 2500 seconds. Mesh convergence, time-step dependence and convergence criteria were all studied to determine these parameters, as a balance of solution time and accuracy. Flow front predictions for simulations run with these parameters exhibited less than 2% variance from the mesh and time-step independent results. Figure 85 shows the oil inlet and vacuum outlet definitions for the quarter symmetry 0°/90° orientation case. This figure also depicts the distribution of principal permeability vectors that are assigned throughout the domain based on the shear angle contours and definitions from experimental characterisation. In this case, the principal permeability direction is initially aligned with the weft yarn direction but rotates towards the fabric bias direction (bisecting the warp and weft yarn directions) as the shear angle increases.

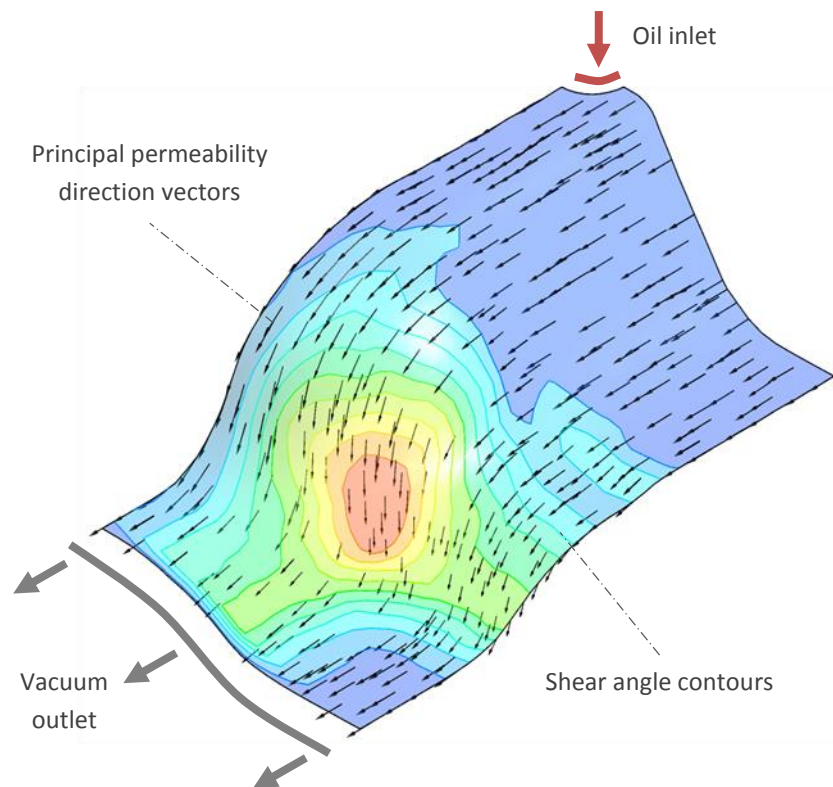


Figure 85: Quarter symmetry simulation for 0°/90° orientation case, with distributed properties and boundary conditions.

7.5 Demonstration forming results

Three main criteria were evaluated for the demonstration results: draw-in, shear angle distribution and fluid flow front location. This section focuses on the simulated forming process and the results from physical draping.

In the presented experimental configuration, the vacuum bag (and fabric material) was able to conform very well to the complex geometry without wrinkling. However, earlier attempts to run this experiment without recessing the male mould into an exterior frame resulted in bag wrinkling that would significantly affect the flow behaviour and cause race-tracking [117]. Figure 86 and Figure 87 show the results of the vacuum forming process for the double dome mould in both the 0°/90° and -45°/45° orientations (the 90°/0° orientation forming results are the same as the 0°/90° orientation). There appears to be good symmetry in these forming cases, and there are no signs of wrinkling or other defects aside from frayed yarns at the sample edges. The initial comparison of the simulation geometry (in Figure 88) with experimental forming appears to be quite good, although the following sections reveal a more thorough quantitative analysis.



Figure 86: Carbon fibre fabric, formed to the double dome tool with 0°/90° orientation.



Figure 87: Carbon fibre fabric, formed to the double dome tool with -45°/45° orientation.

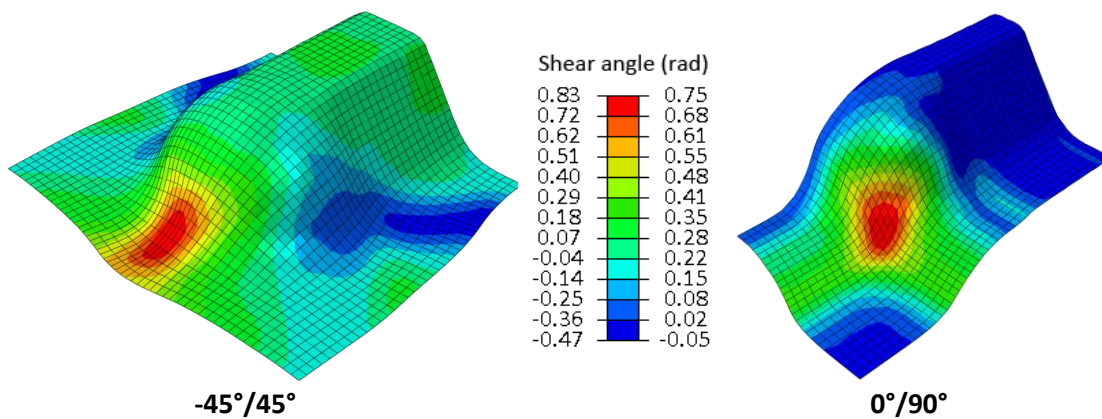


Figure 88: Deformed geometry results from the draping component of the CPM, with shear angle contours.

7.5.1 Material draw-in

In order to quantitatively analyse the simulated and experimental deformation, the x and y locations of the grid intersection points have been measured and compared in Figure 89 and Figure 90. Experimental measurements were determined optically from photographs, carefully correcting for image perspective since the tool geometry and image scale were known. Due to the inherent symmetry of the double dome tool, these ‘draw-in’ results are presented for one

quarter of the geometry in each orientation case, where the centre of each sample is the origin. Each axis represents the relative distance of points from the inlet origin in millimetres. Simulation results from the Complete Process Model (CPM) and a basic orthogonal model have been compared to the mean experimental data (that includes information from all corners of multiple forming cases), with error bars depicting the standard deviation. The $0^\circ/90^\circ$ and $90^\circ/0^\circ$ orientations are represented in Figure 89, since the mechanical behaviour of the fabric is balanced in both directions. Figure 90 shows the $-45^\circ/45^\circ$ orientation forming case. For all orientation cases the CPM shows very good agreement with the experimental results. The basic model also shows reasonable agreement, although it is generally less accurate than the CPM, particularly for the $0^\circ/90^\circ$ orientation.

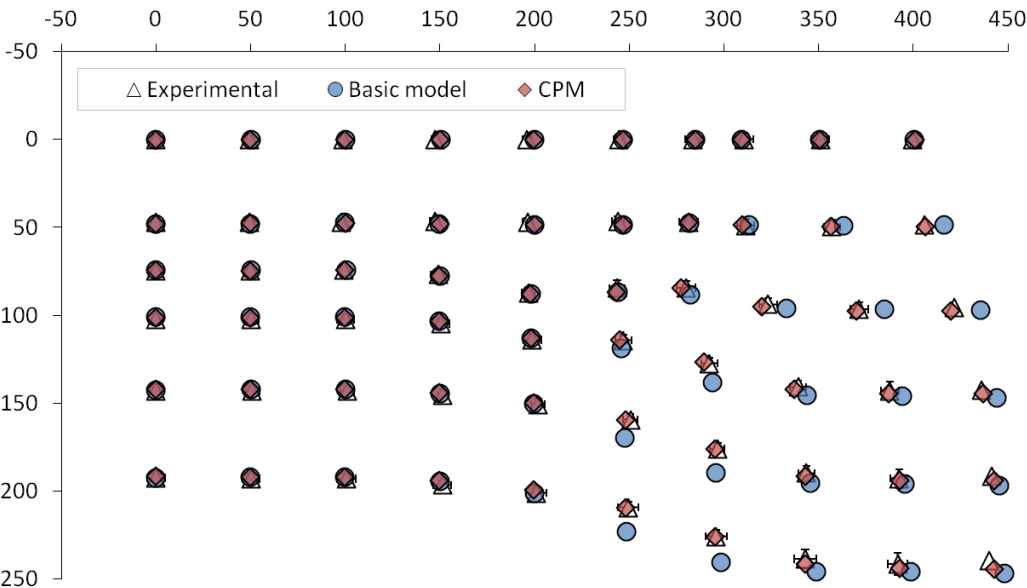


Figure 89: Material draw-in for the quarter symmetry of the $0^\circ/90^\circ$ orientation case.

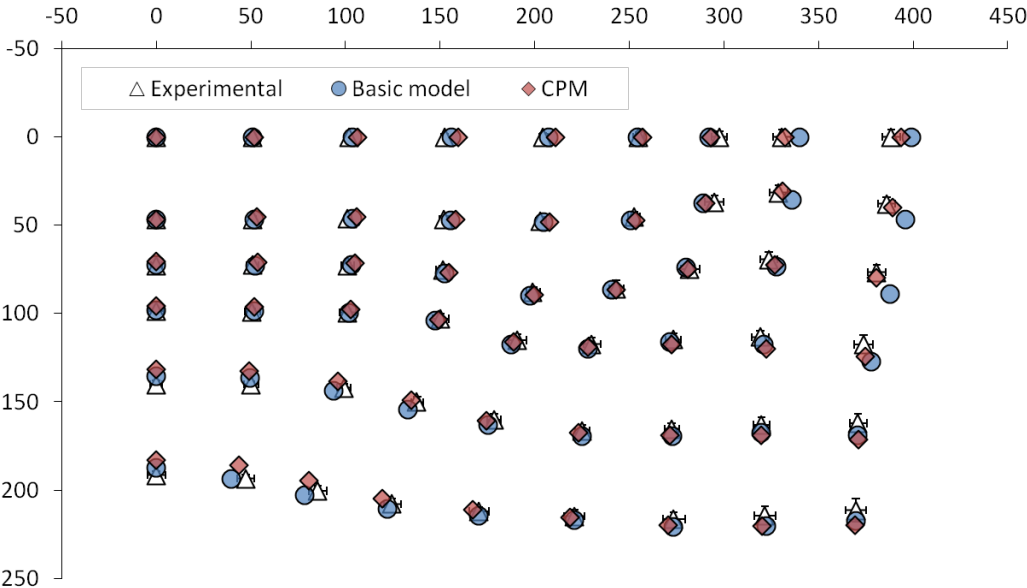


Figure 90: Material draw-in for the quarter symmetry of the $-45^\circ/45^\circ$ orientation case.

7.5.2 Shear angles

Shear angle values have also been measured at various locations throughout each of the formed test samples for comparison with the modelling results. Again, the $0^\circ/90^\circ$ and $90^\circ/0^\circ$ orientation cases are both considered to be identical during forming, and the results from a basic orthogonal simulation have also been included. Measurements were taken along several paths ('A', 'B' and 'C') for the $0^\circ/90^\circ$ orientation case in Figure 91 and the $-45^\circ/45^\circ$ orientation case in Figure 92. For both figures the independent axis represents the y distance of each point from the inlet in millimetres. Overall, the CPM shows very good agreement with the experimental results (that are averaged from all corners and tests). For the $0^\circ/90^\circ$ case in particular the CPM shows a significant improvement over the basic orthogonal model. These results, coupled with the draw-in results, demonstrate both the repeatability of this forming process, and the accuracy of the draping component of the CPM.

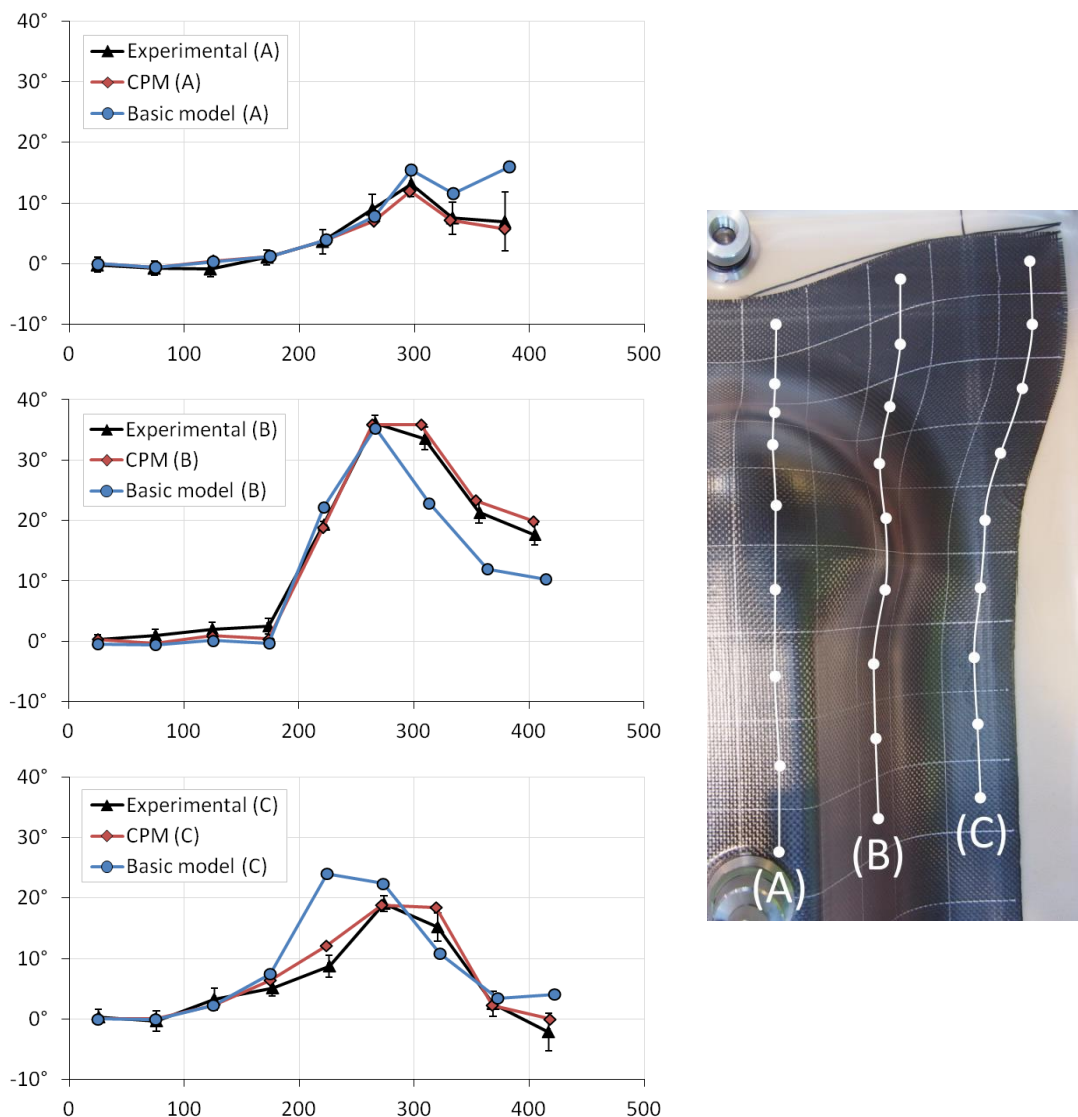


Figure 91: Shear angles along several path lines for the $0^\circ/90^\circ$ orientation fabric sample.

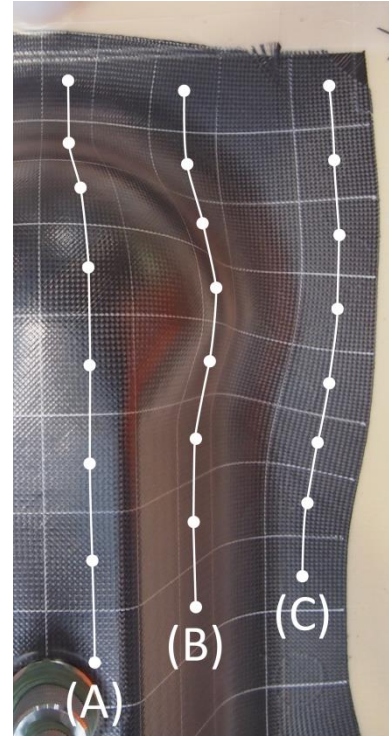
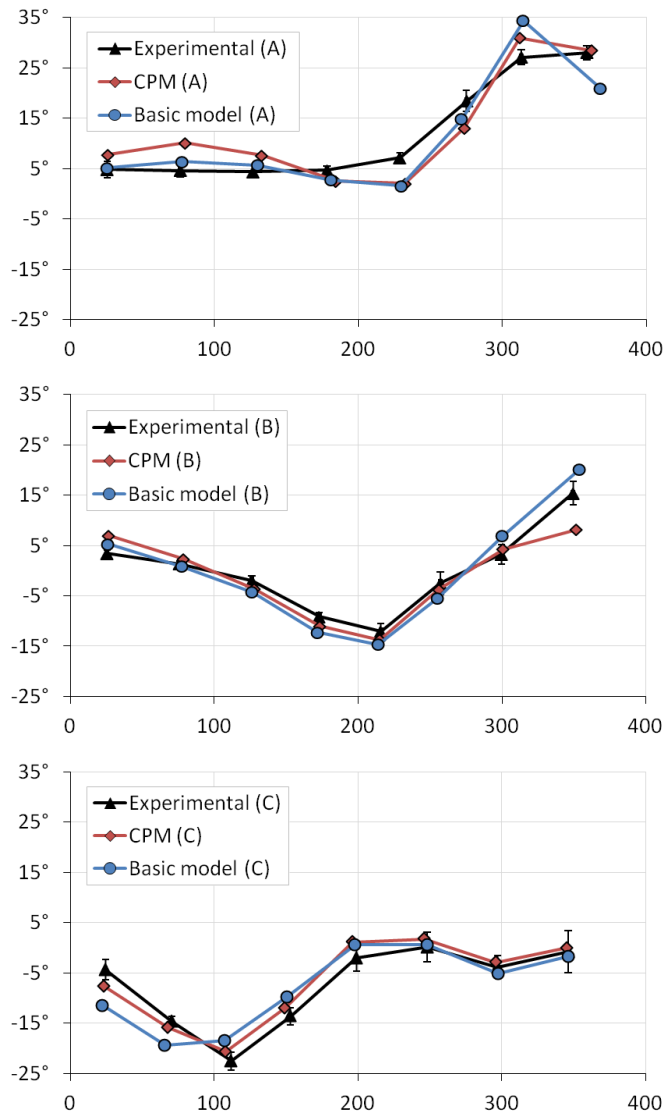


Figure 92: Shear angles along several path lines for the $-45^{\circ}/45^{\circ}$ orientation fabric sample.

7.6 Demonstration infusion results

Infusion served as the second major phase to compare simulated and experimental results for this demonstration. Initially, the Complete Process Model was run using the permeability properties detailed in Chapter 5 and Section 7.4.2. However, further calibration of the CPM is discussed in Section 7.6.2 to improve overall accuracy.

After the forming trials, infusion was simulated for each orientation case ($0^{\circ}/90^{\circ}$, $-45^{\circ}/45^{\circ}$ and $90^{\circ}/0^{\circ}$) and compared to experimental observations and measurements of the advancing flow front. The infusion experiments themselves revealed some important behaviour, as is discussed for the calibrated model, however the importance of checking conformity became evident when some of the tests revealed bridging in the concave curves, which resulted in race-tracking and undesirable results. Data from these tests has been excluded from the presented results, since the sources for error were identifiable and avoidable.

7.6.1 Initial comparison with the Complete Process Model

The following figures depict the advancing flow front for each different orientation case, comparing the CPM results with experimental measurements in two dimensions. These CPM simulations were run using the exact permeability properties that are shown in Chapter 5. Figure 93 shows the advancing flow front for the 0°/90° case where the simulation results show reasonable agreement in the weft yarn direction but poor agreement in the warp direction. Even in the weft direction though, flow is initially underestimated, then ultimately overestimated by the simulation. The results for the -45°/45° case, in Figure 94, reflect some significant variance between the CPM and experiments; again flow in the warp yarn direction is much slower than the model predicts. Flow in the weft yarn direction shows reasonable agreement around 850 seconds, after which the simulated flow is much faster than that of the experiments. For the final 90°/0° case (Figure 95), the CPM captures some of the fluid behaviour quite well, but also reveals faster flow for both the warp and weft directions. Experimentally, the 90°/0° case was run under higher ambient temperatures than the other two cases, as such, the oil viscosity was lower and flow was more rapid. This change in experimental conditions was appropriately included in the CPM for the definition of the oil viscosity and is expected to only influence the speed of the fluid flow, not the nature of the flow. Ultimately, these experimental results show some very different behaviour for each of the orientation cases, which is not well replicated by the previously characterised permeability properties of the CPM.

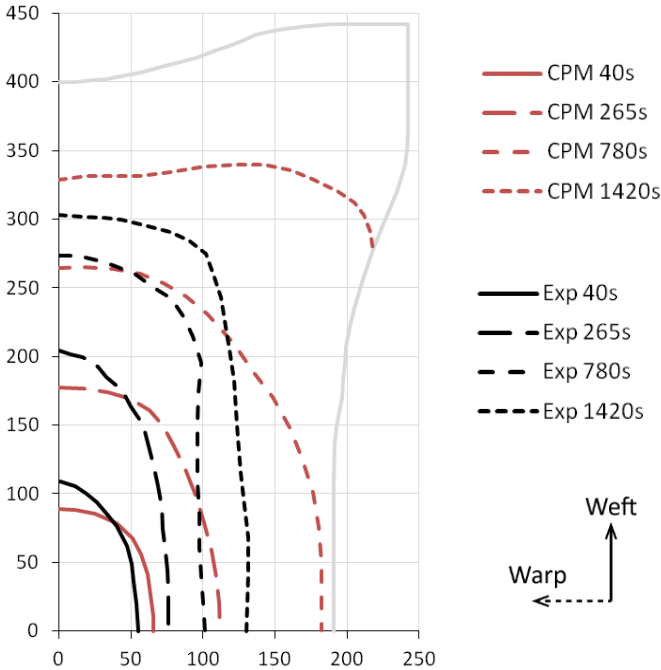


Figure 93: Top-down comparison of the simulated and experimental transient flow front for the 0°/90° case.

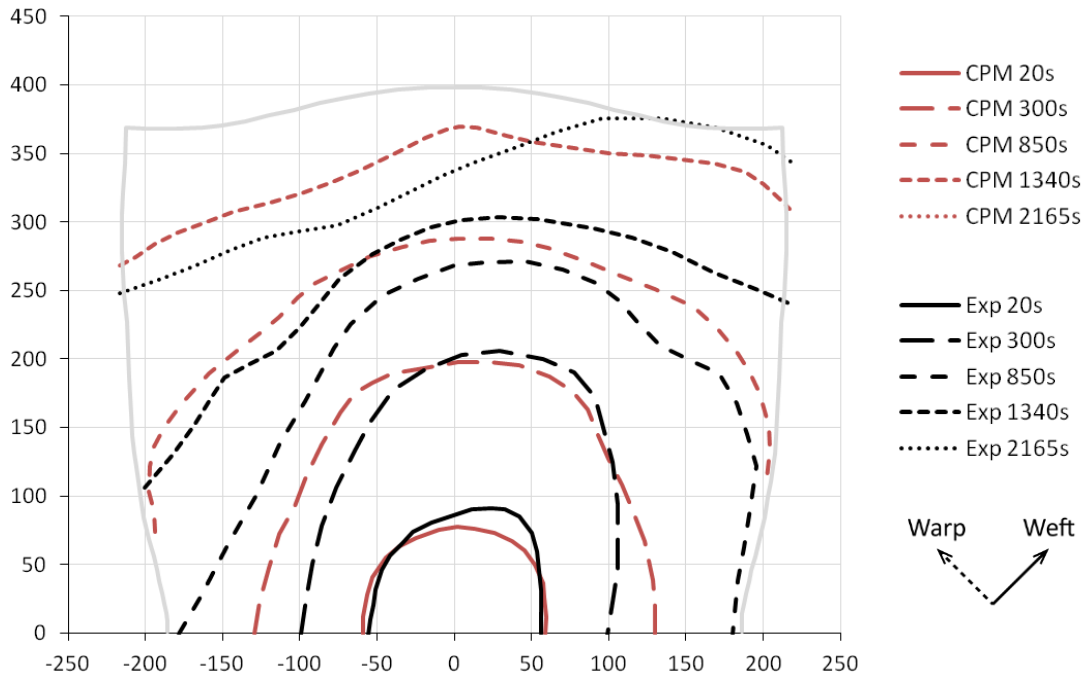


Figure 94: Top-down comparison of the simulated and experimental transient flow front for the -45°/45° case.

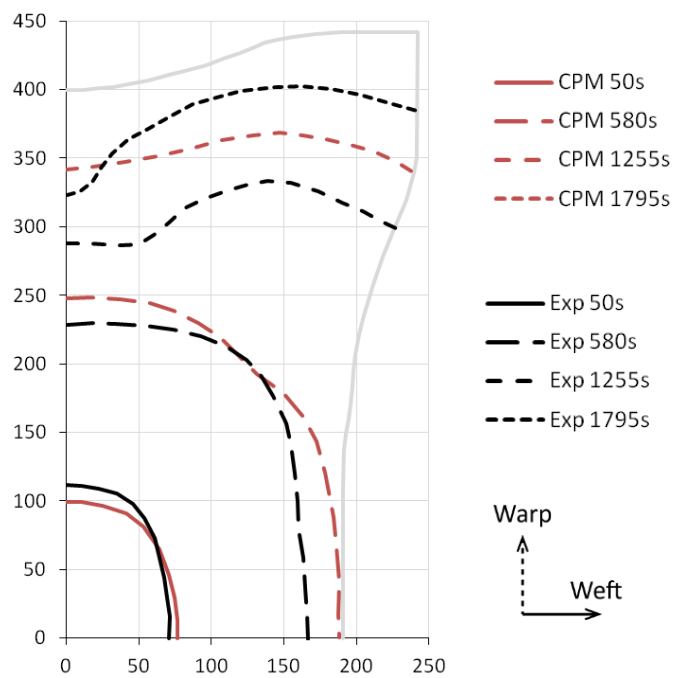


Figure 95: Top-down comparison of the simulated and experimental transient flow front for the 90°/0° case.

7.6.2 Simulation calibration

With the relatively poor performance of the CPM in the initial comparison to the experimental results, further analysis was undertaken to find an explanation for the variance and improve the simulations. Since the tests were repeated to check consistency, experimental variance was an unlikely source for such significant error.

Primarily, the tests at different orientations consistently exhibited a flow bias in the weft yarn direction (despite the mechanical forming results showing no difference between the $0^\circ/90^\circ$ and $90^\circ/0^\circ$ results). This is highlighted in Figure 96, where the fabric orientation was observed to have a clear influence on the flow of the oil. The increased weft direction flow, relative to that of the warp direction, suggests the material has significant initial anisotropy that was not observed for unsheared samples in the experimental permeability characterisation (Chapter 5). Generally the CPM results also predicted faster filling than experimental testing, although the nature of the simulated flow did agree reasonably well with the real behaviour. Based on these observations, it is expected that the fabric permeability properties from Chapter 5 varied significantly from those of the full scale infusion trials. It is possible that the use of different material batches contributes to the explanation, or that increased fabric handling in the permeability experiments was the cause. More likely though, differences in the test conditions have resulted in the overall variance.

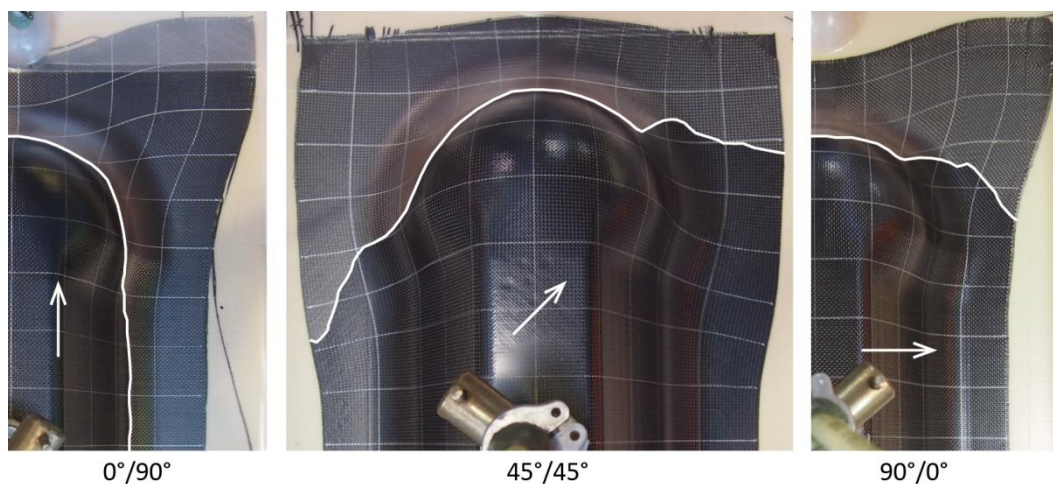


Figure 96: Flow front behaviour, related to the weft yarn direction, for each fabric orientation.

The CPM simulations were run with the assumption of a constant domain thickness, using permeability properties that were characterised from samples between two rigid plates. This difference in experimental conditions has been identified as the most likely reason for the error in the first CPM results. Further inspection of the double dome trials supports this hypothesis. Since the oil was introduced from ambient conditions, significant bag deformation was observed around the oil inlet at the top of the mould. Figure 97 shows this effect quite clearly, where the bag around the inlet bulged under the increased oil pressure. This is expected to have increased the flow of oil in the regions near the inlet, which might explain the faster initial flow of the experimental results, despite the overall reduced flow rates compared to the CPM.

For the rest of the geometry, the bag was formed tightly over the plain weave material, so much so that the surface of the bag bridged the gaps between individual yarns, giving it a dimpled texture (Figure 97). This bridging of macro pores would have reduced the permeability and subsequent flow through the fabric compared to the case of flow between two rigid plates. This also agrees with observations from the initial results comparison and is a strong explanation for the differences between the model and experimental results.

It is also important to note that tight radius convex edges, such as those near the inlet along the top of the mould, typically experience greater pressure and compaction due to the intensification of bag stresses. This is evidenced in the region around the inlet, where the high pressure oil inlet had no apparent effect on the bag thickness for these edges that show very tight compaction of the fabric material in Figure 97.

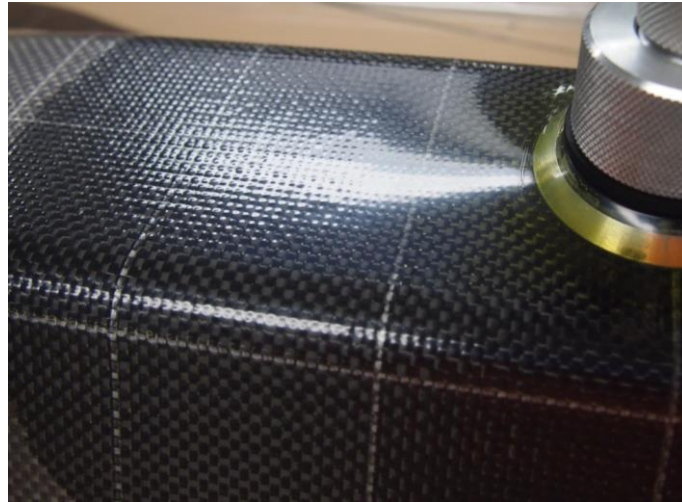


Figure 97: Bag deformation around the oil inlet.

Based on these hypotheses and observations, several calibrations were made to the Complete Process Model to improve its accuracy. Assuming that the deformable bag resulted in both reduced permeability and increased anisotropy (compared to the use of rigid plates), the principal permeability functions (K_1 and K_2 , as outlined in Table 9 and Equation (59)) from experimental characterisation were reduced by 33% and 50% respectively. These values were estimated and confirmed by simulation, although the form of the principal permeability direction function remained the same, as defined in Equation (60). The overall permeability reduction factors (designed to account for bag conditions) can be considered as an equivalent thickness change, or compaction increase, of 33-50% (effectively a 0.133-0.2 mm decrease in domain thickness), which is reasonable given the bridging observations.

Furthermore, to account for the more obvious bag compaction and decompaction effects, two localised conditions for artificial thickness change were included into the UDF subroutine. Since the domain geometry remains a constant thickness (0.4 mm), a change in thickness was artificially applied to the permeability source term as a ratio of the original and adjusted thicknesses.

A first local condition was designed to replicate the increased thickness around the oil inlet. With greater knowledge of the bag pressure and properties a realistic prediction of this thickness increase could be defined in relation to the changing pressure inside the bag. However, for this case a simple linear relationship of increased thickness was established based on distance from the inlet. At a maximum, next to the inlet, the thickness increase was estimated to be 1 mm (a 250% increase) from observations made during the tests Figure 97. However, since the small radius edges along the top of the mould showed higher compaction (despite their proximity to the inlet), this increased thickness effect was limited to a 50 mm wide (75 mm long at a maximum) channel on the top of the mould. These tight radius edges

make up the second region for local thickness adjustments, where the thickness was reduced by an estimate of 0.15 mm in order to replicate the increased bag pressure and compaction.

7.6.3 Results from the calibrated Complete Process Model

The calibrated CPM was once again compared with the experimental results, but also with a basic isotropic flow model (using averaged principal permeability properties) in order to demonstrate the advancement over traditional modelling that this CPM currently offers. The same general permeability reductions and localised calibrations for inlet conditions were applied to all three orientation cases.

A top-down comparison of the experimental and simulated flow fronts at various times is shown in Figure 98 for the 0°/90° orientation case. The calibrated Complete Process Model shows very good agreement with the weft flow, and the overall behaviour is well replicated. However, flow in the warp direction still shows some variance, with the simulation predicting a faster flow. The basic model, on the other hand, does not account for any of the more complex behaviour, showing poor agreement with the experimental results. Images from the two models and the actual oil infusion at 780 seconds are shown in Figure 99, where the solid black line at the 0.5 oil volume fraction contour represents the simulated flow front.

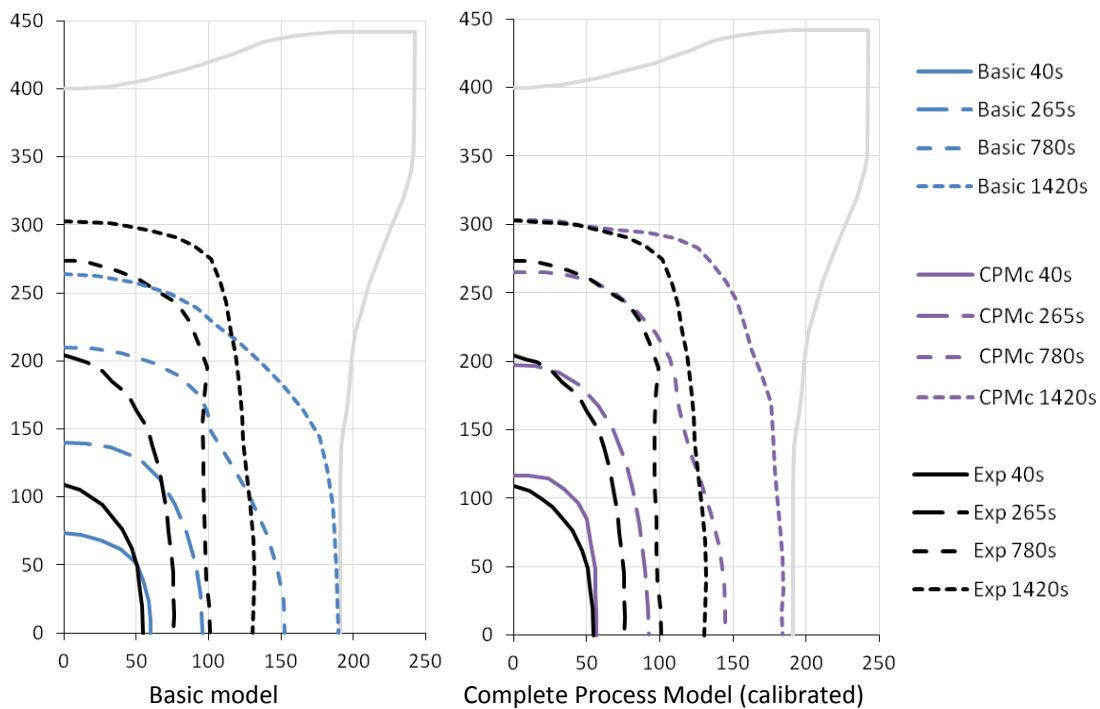


Figure 98: Top-down comparison of the transient flow front (0°/90° case) from a basic model, the calibrated Complete Process Model (CPMc) and experimental measurements.

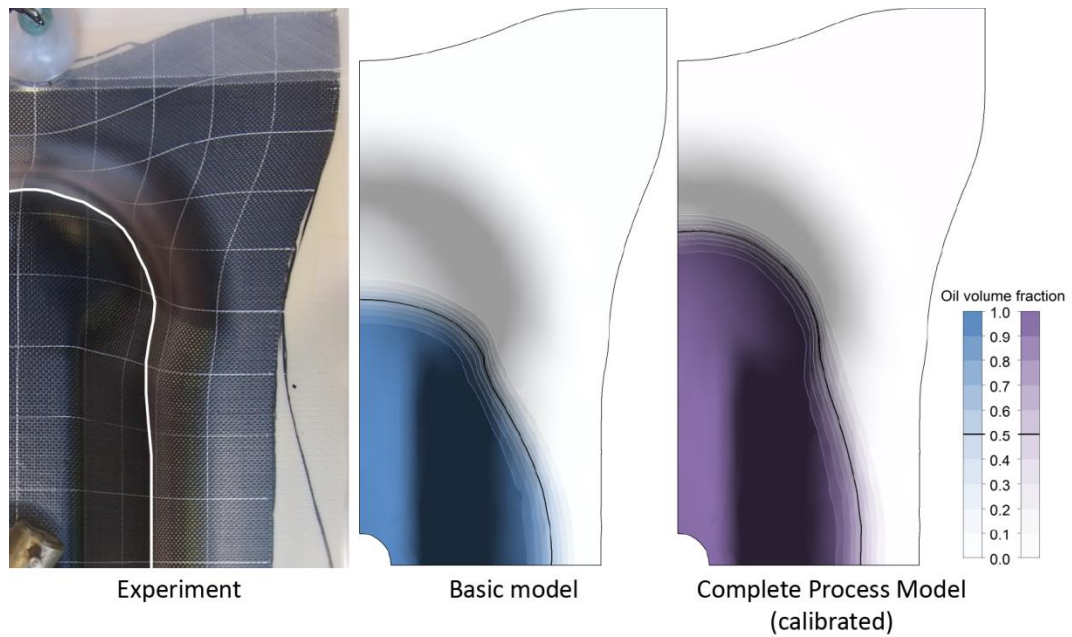


Figure 99: Experimental and modelling images from the 0°/90° case at 780 seconds.

Basic isotropic modelling results for the -45°/45° case are compared to the experimental flow in Figure 100, where again the agreement is quite poor. The calibrated CPM in Figure 101 though, results in very similar flow behaviour to the experimental case. The anisotropy is very well represented by the model, although there is some notable variance between the flow front profiles at 2165 seconds into the infusion. A comparison of images from the experiment and both models at 850 seconds is presented in Figure 102 for the -45°/45° case. From this figure the benefits of the calibrated CPM are clearly observed over the traditional isotropic model.

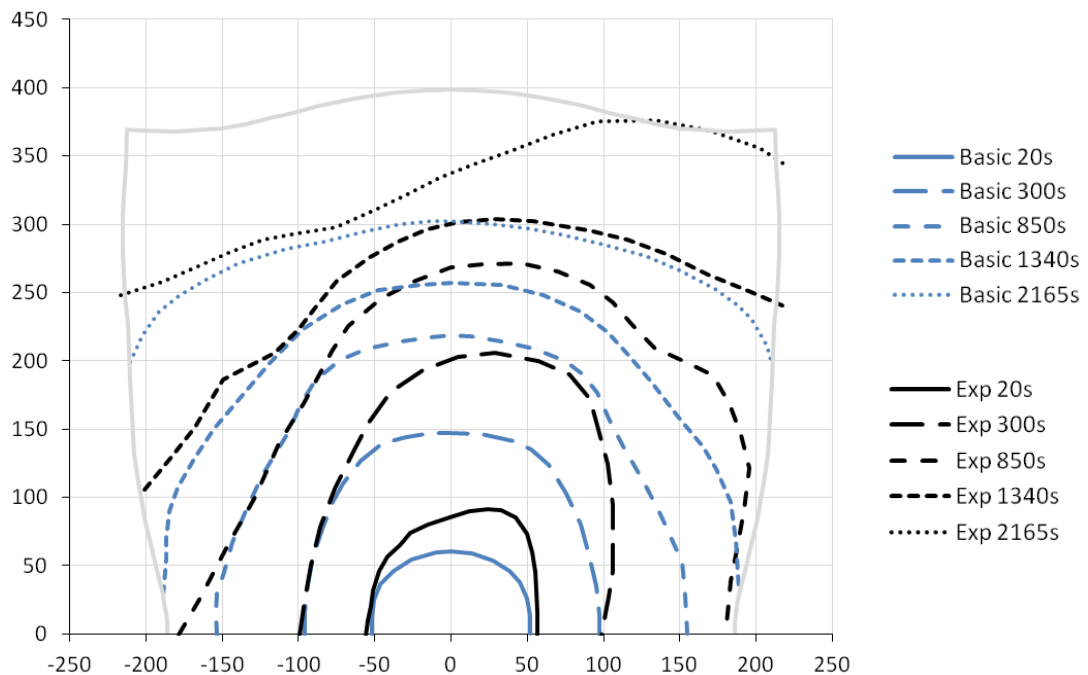


Figure 100: Top-down comparison of the transient flow front (-45°/45° case) from a basic model and experimental measurements.

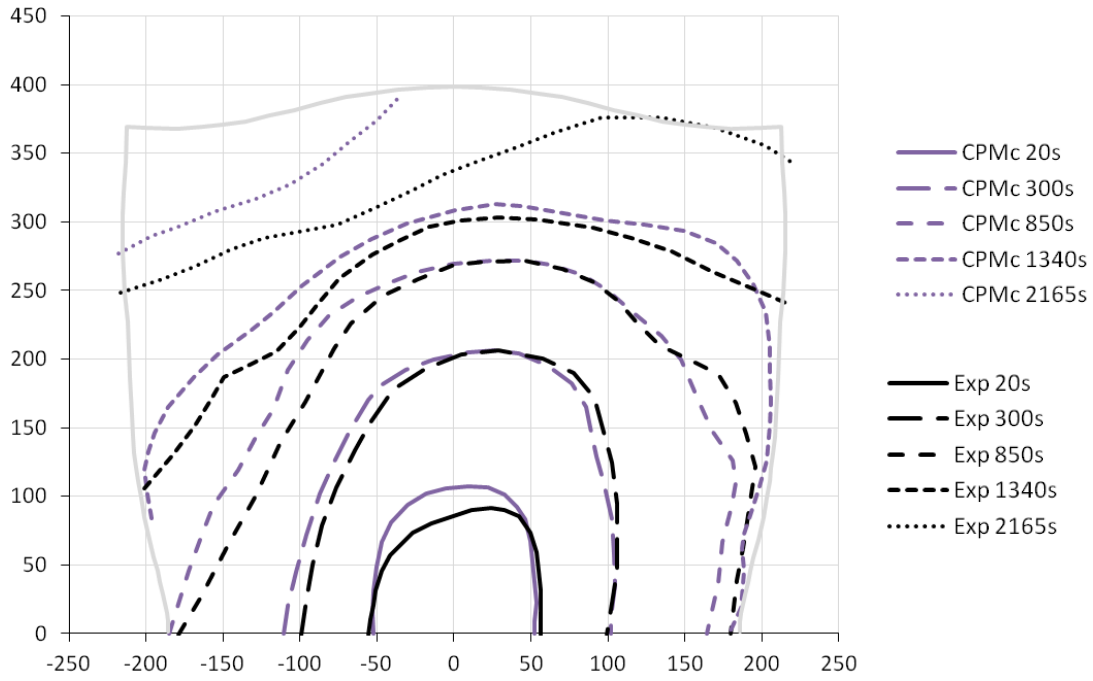


Figure 101: Top-down comparison of the transient flow front ($-45^\circ/45^\circ$ case) from the calibrated Complete Process Model (CPMc) and experimental measurements.

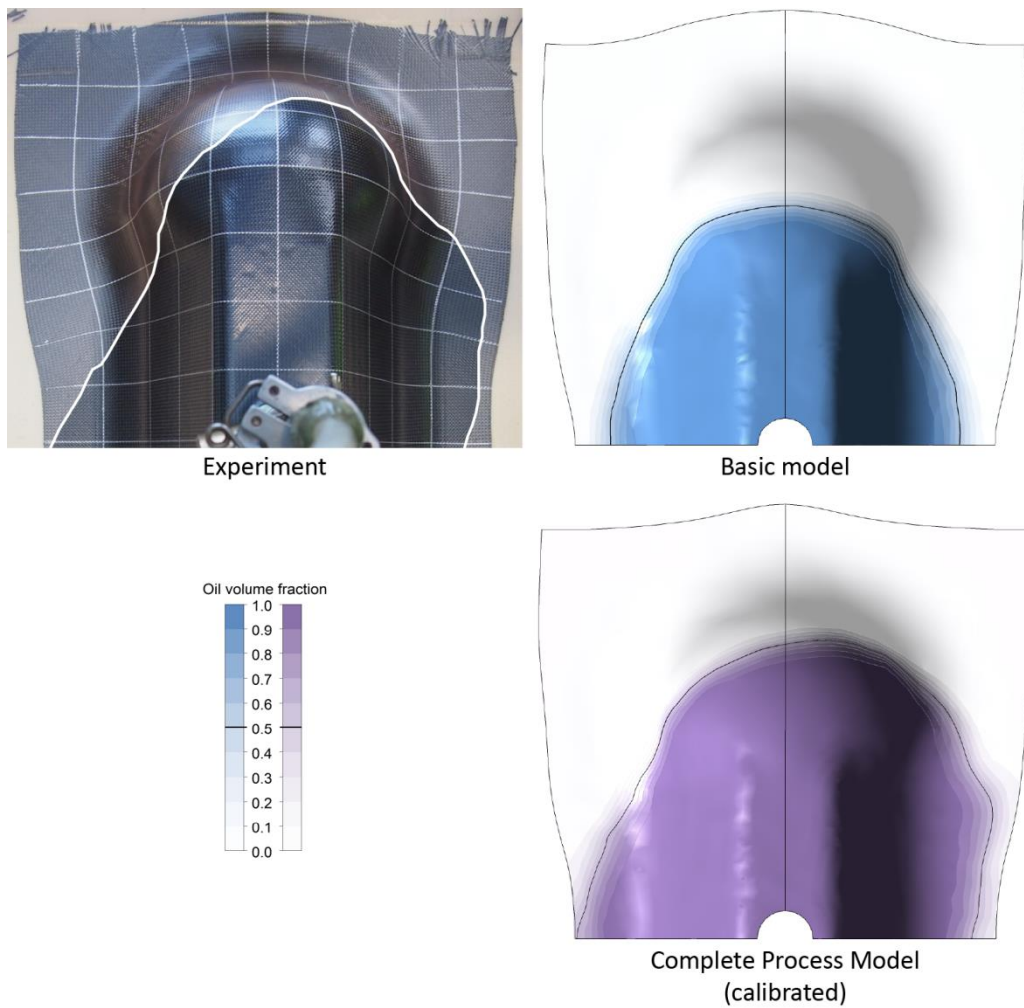


Figure 102: Experimental and modelling images from the $-45^\circ/45^\circ$ case at 850 seconds.

Finally, the results for the $90^\circ/0^\circ$ case are shown in Figure 103, with a comparison of images from the models and experiment at 1255 seconds in Figure 104. The basic isotropic model again shows relatively poor agreement, but the agreement for the calibrated Complete Process Model remains quite good. At 1255 seconds and 1795 seconds, the advantages of the CPM are best demonstrated, despite some variance from the faster experimental flow, as the shape of the flow front is very realistic.

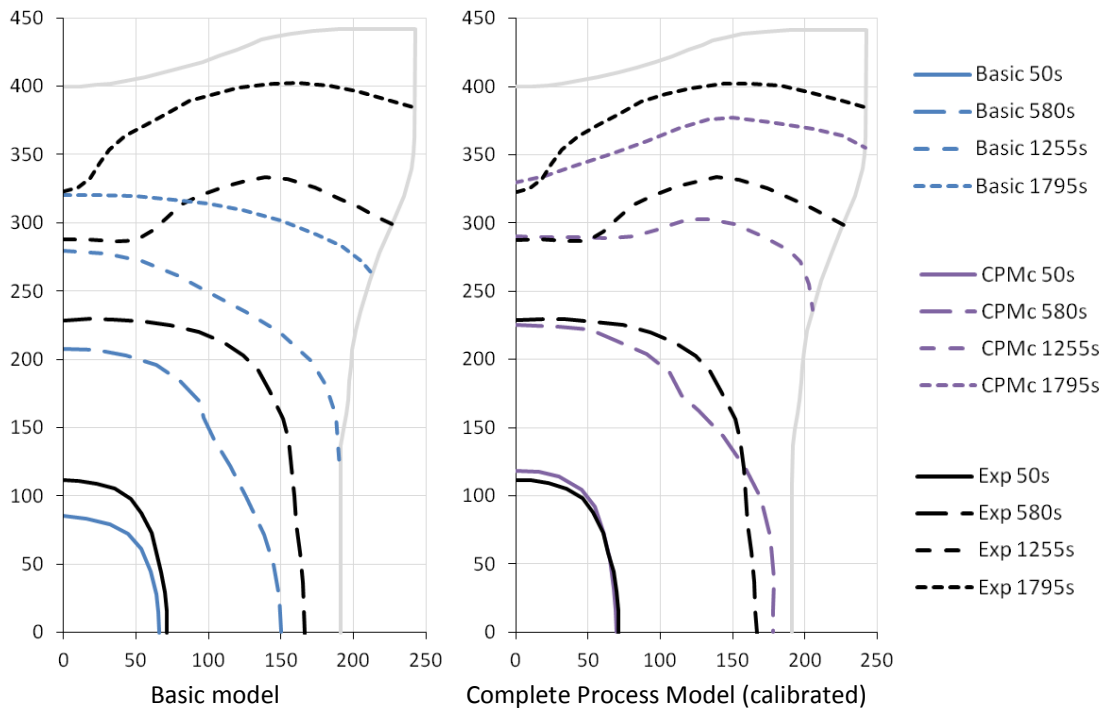


Figure 103: Top-down comparison of the transient flow front ($90^\circ/0^\circ$ case) from a basic model, the calibrated Complete Process Model (CPMc) and experimental measurements.

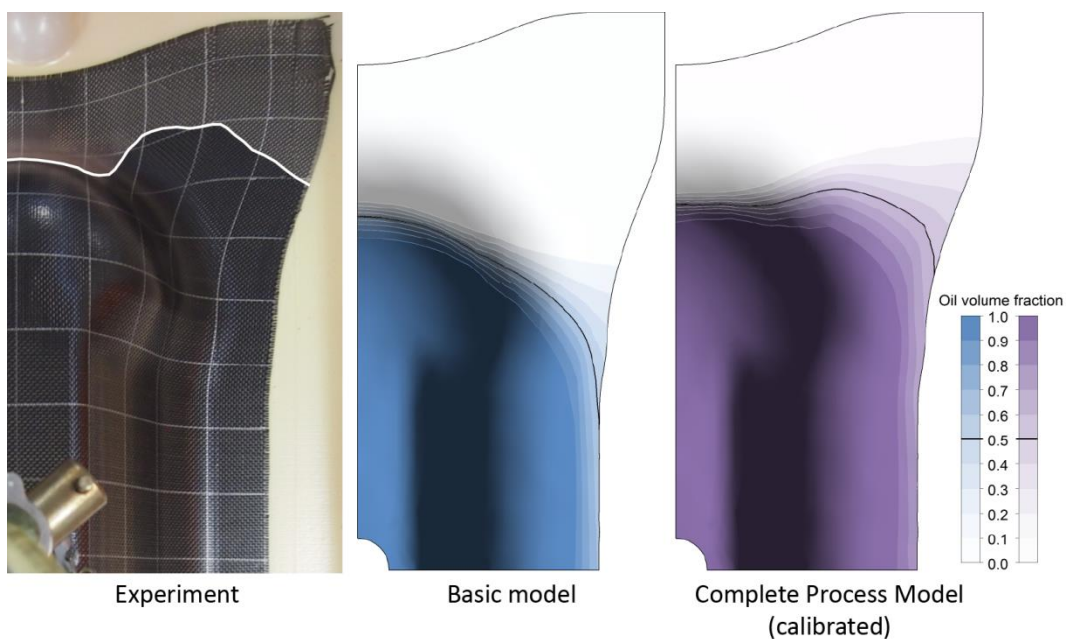


Figure 104: Experimental and modelling images from the $90^\circ/0^\circ$ case at 1255 seconds.

7.7 Multiple ply modelling

The single ply simulations serve as a good initial demonstration of the Complete Process Model, and have been compared against experimental results. However, in reality, large and complex composite aerostructures are made from thicker, multiple ply layups. This section illustrates some of the CPM capabilities for simulating infusion through multiple fabric plies. Specifically, a four ply case for the double dome configuration has been established. Unfortunately, due to the breadth of research required to create the CPM, permeability and experimental testing to validate any multiple ply simulations had to be left for future work.

7.7.1 Four ply simulation

Based on the same double dome geometry (and draping model configuration) outlined in Section 7.4.2, a four-ply $[0^\circ, 45^\circ, -45^\circ, 90^\circ]$ layup simulation was studied. A similar punch forming case was used for the draping in Abaqus, although the gap between the punch and die was increased to account for the additional thickness of the three extra plies (each 0.4 mm thick, as with the single ply simulation). All plies were simulated in half symmetry (with 2000 M3D4R elements each), incorporating the same material properties from Chapter 4. An image of the four-ply draping results, including the shear angle contours, is shown in Figure 105. Due to the mechanical symmetry of the balanced plain weave, the top and bottom plies ($0^\circ/90^\circ$ and $90^\circ/0^\circ$ respectively) behave almost identically. Similarly, the second and third plies ($45^\circ/-45^\circ$ and $-45^\circ/45^\circ$ respectively) also behave the same. Hence, only the top ply and the different profile edges of the second ply are visible in Figure 105.

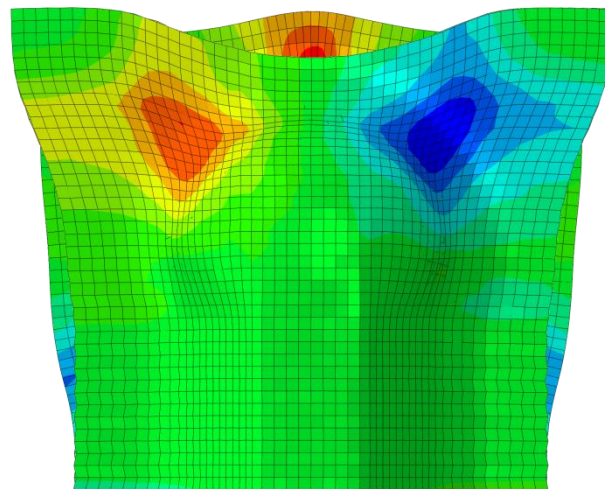


Figure 105: Four-ply $[0^\circ, 45^\circ, -45^\circ, 90^\circ]$ draping results for the double dome geometry.

The python script for extracting Abaqus output database information was also extended to automatically write individual distributed property and nodal geometry files for each ply (the full code is included in Appendix B).

Although each ply could be individually regenerated in ANSYS for the FLUENT infusion model, this posed discontinuity and mesh interaction problems. Instead, a single domain was generated for the infusion model based on a mean surface definition of the four plies. This was cropped to a more realistic part shape (340 mm x 360 mm in half symmetry as shown in Figure 106) that excludes thinner edge regions that would not contribute to the final part geometry. The domain was separated into four even parts through the thickness of the domain, which

allowed for a continuous and regular mesh to be generated across all the plies (four elements thick). Since the plies were linked together with a continuous mesh, fluid flowed freely between the layers during the VOF simulation. As with the single ply models, a 25 mm radius inlet was modelled, and the far edges were treated as the vacuum outlet.

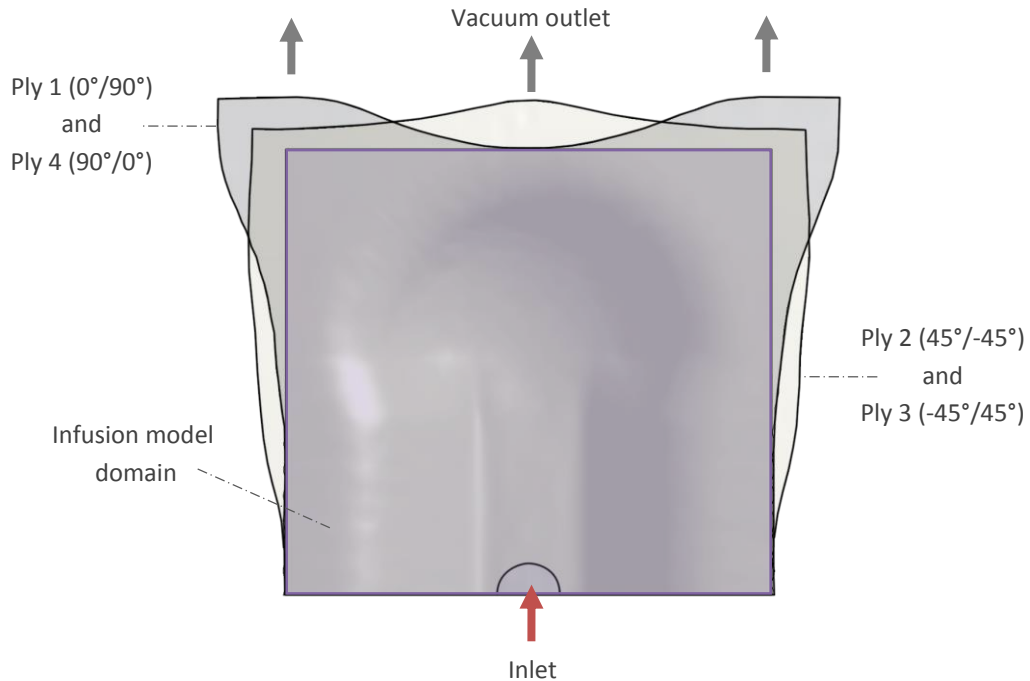


Figure 106: Profile view of the cropped infusion model domain compared with the ply shapes from draping.

The calibrated permeability properties described in Section 7.6.2 were used for each ply and assigned by the UDF subroutine according to the appropriate distributed property files (that originated from the draping model). The UDF subroutine was enhanced to automatically read and allocate the distributed properties from different files, although some user identification of each ply domain was required.

7.7.2 Simulation results

The four ply $[0^\circ, 45^\circ, -45^\circ, 90^\circ]$ layup simulation produces a rather symmetric flow front, with no sign of the weft flow bias that was observed in all the single ply tests. This is not surprising given the layup configuration, where every ply exhibits a different weft direction. Figure 107 shows the superposed, four ply, results from the infusion simulation at 2000 seconds. Since the fabric layers are very thin, and the inlet conditions are uniform across all plies, there appears to be very little difference between the filling behaviour in each ply. This demonstrates that the through-thickness flow, from layer to layer, maintains a rather homogenous planar flow throughout this relatively thin layup. Figure 108 shows the flow in each individual ply at 2000 seconds into the infusion simulation, with only subtle differences between them, despite the varied material orientations.

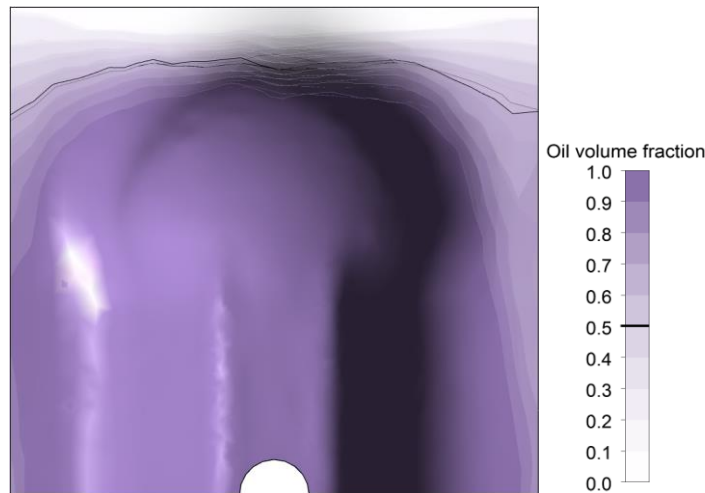


Figure 107: Superposed four ply $[0^\circ, 45^\circ, -45^\circ, 90^\circ]$ CPM infusion results at 2000 seconds.

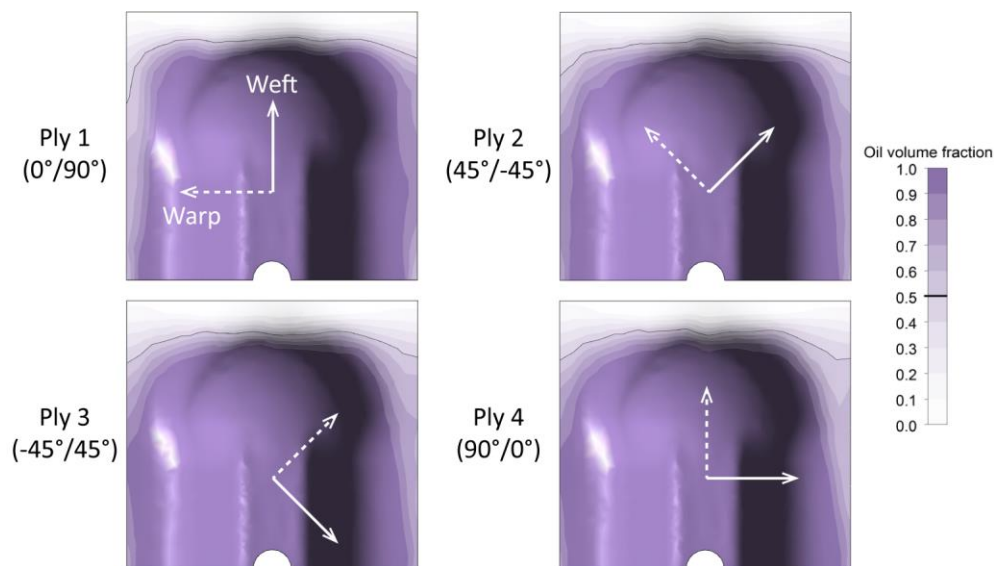


Figure 108: Individual ply CPM infusion results at 2000 seconds.

7.7.3 Evaluation of alternative cases

In practice, the CPM can be used to compare different manufacturing strategies for industrial application. An example is shown here, where the fill times of several different four ply layup configurations are evaluated. Table 10 shows the final fill times for three different stacking arrangements under identical conditions for the calibrated Complete Process Model, and compares these with the results predicted by a basic isotropic model. Of the different layups, the $[0^\circ, 45^\circ, -45^\circ, 90^\circ]$ case shows the fastest fill time, which is attributed to the symmetric flow front. An image from the $[0^\circ, -45^\circ, -45^\circ, 0^\circ]$ configuration at 2000 seconds is shown in Figure 109, and reveals asymmetric behaviour caused primarily by the two aligned -45° plies. Hence this layup results in slower filling of one corner, and a total fill time of 2700 seconds. Since the basic isotropic model cannot account for ply orientation, it predicts an identical 3475 second fill time for any of these configurations; resulting in error which ranges from 14-36%. This study highlights the importance of considering the layup configuration and local permeability changes within each ply, rather than relying on traditional isotropic models.

Table 10: Comparison of different stacking arrangements and basic modelling.

Layup	[0°, 45°, -45°, 90°]	[0°, -45°, -45°, 0°]	[90°, 45°, 45°, 90°]	-
Model	CPM (calibrated)	CPM (calibrated)	CPM (calibrated)	Basic isotropic
Fill time	2540 s	2700 s	3050 s	3475 s

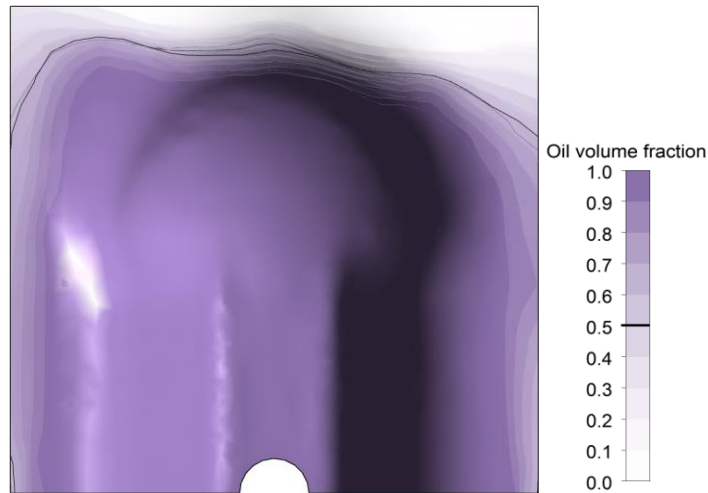


Figure 109: Superposed four ply [0°, -45°, -45°, 0°] CPM infusion results at 2000 seconds.

7.8 Discussion

The predictive results from the Complete Process Model were able to capture some of the general flow behaviour quite well, particularly the influence of local fabric shearing, despite some initially poor agreement with the experimental measurements. This poor agreement was attributed primarily to the permeability characterisation component of CPM, with secondary compaction effects also proving significant. By making some relatively simple adjustments to the permeability properties and adding some artificial thickness effects, a calibrated version of the CPM produced more realistic results. With a more robust and representative method for permeability characterisation, and the inclusion of compaction effects, the model should be able to simulate flow through complex preforms with even greater realism.

It is important to note that wall effects were also neglected in the modelling, since free-slip conditions were assigned to the boundaries of the domain. However, the characterised permeability properties technically included wall effects inherently, which is why simulations of the permeability tests in Chapter 5 were so accurate. Since the characterisation experiments were run between two plates and not directly under a bag, it is possible that the difference in wall conditions posed a significant influence on the flow properties. This is closely coupled with the discussion of compaction and permeability, introduced earlier, as an explanation for the poor agreement in the initial modelling attempt. As such, future permeability characterisation experiments should be designed with similar conditions to the actual infusion. Although, this may not always be possible, as bag deformation has to be monitored in detail or the permeability characterisation will be incorrect. Alternatively experiments could be run under

partial vacuum such that bag deformation is negligible but the wall effects and ultimate permeability better reflect the actual infusion case.

Overall though, the comparisons presented in this chapter have demonstrated a clear improvement of the Complete Process Model over traditional isotropic modelling. By accounting for the effect of shear angle change and coupling a draping simulation with the flow model, the CPM is able to better replicate true flow behaviour through a large and complex component made from fabric material.

7.9 Process model enhancements

This research demonstrates a successful process model for infusion manufacturing processes, although this is only the first implementation; there are considerable improvements that can still be made. Fundamentally, the process needs to be optimised for efficiency before it would be viable for industrial application. Furthermore, the wide range of software and coding languages employed in the various components of the CPM overcomplicate its use. There are also a number of ways in which the process model can be enhanced for greater realism or extended to other applications. The following sections discuss some of the current capabilities that have not been demonstrated in this research and proposed improvements that may be possible with further study.

7.9.1 Software consolidation

The work supporting the current process model requires knowledge of both the Abaqus and ANSYS software packages in setting up the draping and infusion components respectively. From an industrial perspective, the process model should be as simple as possible to run, and require a minimum of commercial software licenses. Hence, it will be important to attempt to recreate the CPM in a single software suite. This is also likely to increase the overall efficiency of the model by eliminating many of the manual steps that are currently necessary due to incompatibilities between software packages. As was discovered in the course of this research (once the Abaqus draping model had already been developed) the Abaqus suite is not currently capable of simulating the whole infusion process. Primarily, this is due to the immaturity of the Abaqus CFD package that is not capable of transient multiphase flow simulations. Subsequently, ANSYS appears to be the most viable option for the CPM, with a mechanical simulation package that could replace the Abaqus draping model, since it is also capable of accepting user defined (UserMat) material subroutines. There was insufficient time to explore this further, although it does appear possible provided the UserMat subroutines can be employed for explicit analyses in ANSYS.

Linked to the use of two different software packages, the supplementary subroutines and scripts required to run the complete process model also require some knowledge of a number of different programming languages. Firstly, the Abaqus draping model requires a VUMAT subroutine, written in Fortran. Then, since the Abaqus output results are not directly compatible with ANSYS Fluent, a Python script is required to export the relevant data to a more accessible format. Ultimately, the UDF subroutine for the Fluent infusion model is coded in C to import, interpret and assign the draping results. In addition to this, the DIC and video processing scripts for the material characterisation have both been written for Matlab.

Evidently, it may be possible to eliminate the Fortran and Python components of the project if the complete process model can be consolidated into ANSYS.

7.9.2 Additional simulation components

Currently, the process model predicts the manufactured part geometry, with detailed information of local fibre volume fraction and fibre directions. In reality, prior to assembly, final machining needs to be performed to result in the final shape and facilitate joining (such as trimming edges and drilling holes). In the aerospace industry it is also typical to perform structural analysis for the anticipated loading conditions, during the development cycle of the final part. The CPM from this research could be extended to include a simulation of the final part geometry for structural analysis. In this case, the mesh from the infusion model would need to be manually modified to account for trimming, drilling or any other machining operations prior to structural analysis. However, the detailed definition of fibre volume fraction and fibre directions across the part would enhance the fidelity of the structural analysis. Particularly when compared with common approaches that do not account for deformation or other effects that result from the manufacturing process.

At the front end of the process model, there is also the potential for replacing experimental material characterisation with predictive modelling. This is an area of active research in academia since many of the experimental approaches are tedious and have not been standardised. Modelling approaches for tension and shear behaviour have been reviewed in recent literature [53], revealing a wide variety of methods. The discrete fibre modelling approach by Durville [35], is capable of predicting fabric behaviour and characterising approximate continuum tensile and shear properties. There are also meso-scale models with similar predictive capabilities, which rely on simulating the yarn interactions of representative Repeated Unit Cells (RUCs) in order to determine macro-scale fabric behaviour [27]. Approaches such as these can eliminate or reduce the need for experimental fabric characterisation, depending purely on fibre or yarn properties and accurately capturing interaction behaviour at small scales. However, the interaction phenomena is not well described and is often simplified to an estimate of friction, meaning the validity of these models for predicting fabric shear and tensile properties still needs to be compared against experimental results.

Similarly, permeability modelling is also an active area of research, as the experiments often show poor repeatability [60]. Based solely on geometric parameters such as yarn height, spacing and fabric weave, a number of approaches are able to approximate the permeability properties in fabric materials. These range from dimensionally reduced simplifications to full 3D CFD simulations [13, 64, 82], and can quite rapidly account for deformation or variation of the fabric configuration. This could offer a large time saving over experimental approaches that are unreliable and wasteful. However, as with the predictive mechanical models, these permeability simulations still require some degree of experimental validation.

These modelling approaches also allow for rapid prototyping and optimisation of the reinforcement material itself, since the need for time-consuming experimental testing can be replaced. There is also the potential for stochastic considerations; as in reality, fabric architecture, properties, nesting and other effects can be variable. As predictive modelling only

relies on the most fundamental of properties such as fibre strength, the geometric parameters can be varied based on statistical estimates and a vast number of simulations can be run in batches [68].

7.9.3 Improved modelling detail and sophistication

The process model demonstration in this chapter is a relatively basic example, primarily designed to indicate the potential capability of the method for simulating the infusion of complex structures. However, the model employed in FLUENT includes additional capabilities. Wall effects can be simulated by a variety of methods in order to better predict phenomena such as race tracking. Additional regions of porous material can be modelled to reflect the presence of distribution media or extra plies, as are common in real manufacturing processes. Multiple inlet and outlet conditions can be modelled as variables for cases where a program-controlled infusion strategy may be employed. Lastly, energy considerations are also capable of inclusion in the fundamental model. This allows for simulation of heat transfer, between a heated tool or preheated resin for example (provided the resin system has been characterised with regards to temperature). However, in this research there has not been time to fully validate all of these features in FLUENT for the CPM.

Further improvements may also be possible in future work. There is potential to simulate the actual curing reaction of a resin system that would account for exothermic effects and partial curing for longer infusions. Modelling of void formation and transportation has been demonstrated in literature [61, 118] to predict part saturation during infusion. A similar model could be implemented into the FLUENT infusion model through a UDF subroutine.

However, the most important behaviour absent from the current process model is compaction. This is an area that has seen significant research for vacuum infusion processes [43, 91, 119, 120]. Notable studies have demonstrated 1D modelling of preform compaction by coupling preform compaction and fluid pressure, and simulating the fibre and resin as a non-linear bed of springs [119]. Other research has performed modelling and experiments to highlight the variance of dry and wet compaction behaviour during different stages of a typical infusion process [43]. More recently, meso-scale Repeated Unit Cells (RUCs) have been implemented in 3D with Finite Element (FE) models to virtually test fabric compaction behaviour and the effects of nesting, shearing and ply orientations [120].

Compaction behaviour is significant to both the draping and infusion stages of manufacturing processes that employ a flexible tooling. One approach to include compaction is to run a combined fluid-structural interaction (FSI), where the force of the flexible tooling is modelled in conjunction with the flow of the fluid, coupling the behaviour of the two. This allows for realistic predictions of cavity thickness change as the increasing pressure in the fluid resists the compaction effect of the bag. Most importantly, this provides a detailed and improved prediction of local fibre volume fraction across the part, rather than assuming a uniform distribution.

Alternatively, compaction behaviour can be artificially incorporated as a modifier to the fabric permeability and porosity, as was demonstrated in the calibrated CPM. This can theoretically achieve comparable fill time predictions with a fully coupled model; however, alterations to the infusion conditions or part geometry will require changes to the effective permeability.

Both methods rely on characterisation of the flexible tooling (typically a nylon derivative, vacuum-bagging material) material or of the preform compaction behaviour, that can be either experimentally or predictively determined (with meso-scale modelling for example [120]).

8 Summary and Conclusions

The research in this thesis presents a strategy to completely simulate the LCM manufacturing process, such that trial-and-error can be minimised in the development of new parts. This Complete Process Model (CPM) is reliant upon an initial draping model, tensile and shear material characterisation, permeability characterisation and a final infusion model, all of which are interconnected. The work related to each of these areas is summarised in this chapter.

8.1 Draping model

The literature reveals a large range of research on draping simulations, for a number of approaches with varying degrees of complexity. The draping model in this work needed to realistically predict fabric deformation with a focus on the shearing behaviour, since this is known to influence the permeability properties of the fabric [84]. A hypoelastic continuum approach was incorporated into Abaqus due to its relative simplicity, efficiency and compatibility with subsequent modelling. This method homogenised the fabric material properties such that each ply was represented by a thin sheet of elements. Using an explicit formulation, this approach relied on a customised VUMAT material subroutine that would track fibre directions realistically. Tensile and shear properties from material characterisation experiments are necessary to support the draping model, which assumes that the influence of bending behaviour is negligible. This maintains the simplicity of the model and is reasonable for the determination of general fabric deformation, however other studies using semi-discrete models have shown that the nature of wrinkling can be more accurately predicted by accounting for bending behaviour [17].

The draping model and VUMAT subroutine were evaluated against other simulations and experimental results for a double dome geometry that was prominent in recent literature [31, 33]. This model showed very good agreement with the experimental results and similar models, while demonstrating that simple orthogonal simulations were not sufficiently accurate. A multiple ply simulation was also performed for the double dome geometry to show off the modelling capabilities for a more realistic layup configuration.

As the first major component of the Complete Process Model, the implementation and evaluation of a state-of-the-art continuum draping model is an important foundation on which the major novelty of this research is developed in later chapters. Additionally, the comparison of the Abaqus VUMAT and VFABIRC subroutines is a study that has not previously been undertaken in such detail.

8.2 Material characterisation

The tensile and shear behaviours of the textile reinforcement material had to be characterised in order to achieve the most realistic draping simulation results. Due to a lack of standardisation, there are ongoing efforts to develop optimal experimental methods in literature [50]. Fabric shear testing, in particular, has seen considerable research in recent years, with several competing methods.

For this research, an aerospace grade, carbon fibre plain weave fabric has been characterised. Tensile testing was performed using the uniaxial ASTM standard strip approach, since the biaxial nature of the fabric was considered to be negligible for the purposes of process modelling. The tensile response of the fabric was found to be slightly non-linear, particularly at low strains where fabric decrimping was the likely explanation. The two yarn directions showed similar behaviour, as expected, since the material has a balanced weave.

The bias extension approach for shear characterisation was employed due to its relative simplicity and because of the known clamping issues associated with the picture frame test. In order to overcome shear measurement problems, a novel Digital Image Correlation code was developed in MATLAB to track sample deformation through a series of images and calculate the fabric shear response. No other DIC software has been designed specifically for fabric shear testing, particularly with such a low-cost method. A more common narrow sample type was compared with a wide sample type for the bias extension experiments. From observation the wide samples showed a significant reduction in yarn slippage, an increase in the achievable shear angles (over 22% higher) and higher peak loads (ten times greater). Out-of-plane wrinkling was also observed in the wide samples but not narrow samples, suggesting that the narrow samples may not have even reached the true locking angle of the fabric. It is expected that these benefits in the wide samples result from the additional frictional resistance in the material outside the gauge area. This is anticipated to be a better representation of draping, where any free edge effects are reduced by design. Such a comprehensive comparison of wide and narrow sample types for bias extension testing forms a significant contribution to knowledge in this field. Notably, this work has revealed that bias extension testing may not be limited to lower shear angle ranges (as was previously believed [49]).

The DIC approach developed in house was found to be accurate, reliable and inexpensive, with several features that are not available in commercial packages (such as predictions of the artificial yarn strains and slippage). The shear modulus determined from this testing approach was verified for modelling purposes, however there remains room for improvement since neither the theory used to calculate the shear modulus, nor the model itself, consider yarn slippage. Ultimately the wide sample characterisation results are expected to be the most reasonable for modelling complex geometries, despite extrapolation of the narrow shear modulus function to be very similar.

8.3 Permeability characterisation

Fabric permeability characterisation is another area that has seen extensive study in literature, particularly for the purposes of modelling infusion. Despite all the literature and recent benchmarking attempts, there remains no standard method for permeability characterisation in textile reinforcements. The two-scale nature of the flow and stochastic fabric architecture mean that tests are difficult to reliably repeat, not to mention the influence of nesting and compaction effects for thicker layups. There have also been efforts to create predictive permeability models in literature, although the validity of these approaches is difficult to confirm without reliable experimental testing.

For this research, a simple 2D radial flow experiment was developed and performed with single plies of the carbon fibre plain weave material. Permeability properties were desired as a

function of shear angle in order to relate fabric deformation from the draping model with flow properties for in the infusion simulation within the Complete Process Model. The 2D experiment provided a more efficient means of measuring anisotropic flow behaviour, even though linear flow experiments are widely regarded as having improved repeatability. Flow front measurements were recorded with digital video footage that was subsequently processed by another customised MATLAB code: designed to calculate all the relevant permeability properties. Overall this experimental approach, run under vacuum with a digital camera, is a low-cost method, and the novel post-processing code allows for detailed and statistical characterisation of the permeability properties. This is a new approach that aims to reduce susceptibility to any deviations from perfectly elliptical flow, which are common in experimental permeability tests.

The results of these characterisation tests revealed increasing anisotropy with shear angle from an initially near-isotropic state for this particular aerospace-grade plain weave. Employing a new method, based on traditional theory [112], the detailed radial description of permeability was found along with principal permeability value distributions for each test. Tests were reasonably repeatable, in terms of principal permeability value predictions (relative standard deviations ranged from ± 4 -20%). However, taking the ratio of principal permeability values (the anisotropy) resulted in very consistent results from the MATLAB code, with relative standard deviations of only ± 2 -6%. This demonstrates that 2D radial permeability testing can be much more consistent than previously thought for determining anisotropy. The principal permeability direction was found to coincide with the fabric bias direction, as is expected for balanced fabrics, and a complete definition for permeability properties was found relative to shear angle and flow direction for use in the CPM.

8.4 Infusion model

Infusion modelling has attracted considerable attention in industry, which has provided renewed impetus within the academic community for modelling this phenomenon. The primary goal of infusion simulation is to predict resin flow through a material (often quantified by fill time) based on part geometry, layup and infusion strategy. Though, sophisticated research has also demonstrated that these simulations have the potential to identify void formation, dry spots and even assist in the very early stages of component design. Generally, simulations simplify the infusion process to a continuum-based approximation, such as the Control Volume Finite Element (CVFE) or Volume of Fluid (VOF) methods that have proven quite successful in research and industrial applications.

In this research, VOF approaches have been developed to simulate the transient flow of multiple fluid phases (resin and air) through a porous material with anisotropic properties. Although this research focuses on isothermal conditions (also neglecting true saturation and compaction phenomena), the approach is capable of greater complexity. Two similar models were developed in ANSYS FLUENT and CFX, with emphasis on the multiphase modelling approach, porous media considerations and solution algorithm. Differences between the two CFD packages were limited to only discretisation and interpolation methods.

Simulations were run for both packages against the experimental permeability tests to evaluate the validity of the models for multiphase fluid flow through porous media, in both

isotropic and anisotropic cases. Generally, both CFX and FLUENT models showed very good agreement with the experimental tests. However, after evaluating the mesh and time-step dependence of the models, CFX was found to be less robust overall. Hence the FLUENT model was selected for implementation in the Complete Process Model.

The evaluation of CFX and FLUENT for infusion modelling presents an interesting comparison of the two CFD packages incorporated in the ANSYS suite. Validation against experimental testing demonstrates the accuracy of such models for infusion applications, particularly in support of the CPM.

8.5 Complete Process Model

Individual components of a Complete Process Model have been previously investigated, but very little research has attempted to combine them, even though the concept has been proposed for a number of years [14].

The major innovation of this work was the linking of the draping model and the infusion model to produce the Complete Process Model with the capability to predict deformation-dependent flow behaviour. This was achieved by first extracting the information describing the deformed geometry and distributed properties (such as shear angle and material orientations) from the Abaqus draping model. Then, these details were imported into the FLUENT infusion model with a custom coded subroutine. Shear angles were translated into local permeability values across the deformed geometry based on the experimental permeability characterisation data.

The Complete Process Model has been demonstrated to be capable of taking complex material deformation behaviour into account for the infusion process using real material properties, which has not been done before. As such, the limitations of traditional models that assume uniform permeability properties have been highlighted by simulating processes involving varied fabric orientations.

Results for a double dome forming case initially showed significant variance from experimental trials. However, this was attributed to permeability properties that were characterised under different experimental conditions and with some reasonable modification to the permeability properties all three different material orientations were well replicated by the CPM. Complex flow behaviour that results from local deformation of the fabric was well represented by the model, showing far superior agreement over traditional isotropic models. Multiple ply modelling was also performed for various stacking arrangements as a demonstration of the CPM potential for industrial applications.

8.6 Conclusive remarks

This work has produced significant research contributions in the fields of draping, material characterisation, permeability testing and infusion modelling by evaluating and improving upon the current state-of-the-art. Specifically, the proposal of wide bias extension testing as a superior approach to the traditional methods, and the development of two new MATLAB codes for DIC and video processing are significant innovations. However, the combination of all these aspects into the Complete Process Model has been the primary and most significant outcome of this novel research. Given the broad scope of the project, there remains a large

body of potential work to reinforce this initial demonstration of the Complete Process Model. As such, a number of future improvements have been recommended.

Firstly, during the double dome infusion trials it became quite clear that the characterisation of permeability properties for vacuum infusion is an area that needs considerable attention. Significant calibration of the closed-tool permeability properties was required in order to implement them effectively in the CPM for comparison against the experimental vacuum infusion. Though this did not detract from the relative improvements that were gained by accounting for deformation-dependent flow properties, a more reliable characterisation approach, or calibration procedure, is required. One option may be to replace experimental permeability characterisation methods with predictive numerical or analytical modelling. If such an approach was also extended to the characterisation of the mechanical properties, then vast improvements could be gained in efficiency and the rapid prototyping of different materials.

Fundamentally, the current demonstration needs to be optimised and simplified before it can be adopted for use in industry. Greater automation between the draping and infusion modelling components is desirable, and would also facilitate rapid parametric analysis for part optimisation. Alternatively, it is expected that operation of the Complete Process Model can be simplified and streamlined by replacing the Abaqus draping model with an equivalent model in ANSYS, which would eliminate the need for knowledge of both Abaqus and Python.

Additionally, the CPM can also be extended to include structural analysis of the final part, taking advantage of the detailed and distributed properties like fibre directions and fibre volume fraction. With further improvements, the current model could also account for more realistic wall effects, compaction behaviour, void formation, heat transfer or even curing reactions. The future of the Complete Process Model has the potential to include all of these advances, however such ambitions were clearly not feasible for this single project.

References

- [1] Comprehensive Composite Materials: Design and Applications: Permagon Press; 2000.
- [2] The research requirements of the transport sectors to facilitate an increased usage of composite materials. Part I: The composite material research requirements of the aerospace industry. EADS Deutschland GmbH; 2004.
- [3] Soutis C. Fibre reinforced composites in aircraft construction. Progress in Aerospace Sciences. 2005; 41: 143-51.
- [4] Roeseler W., Sarh B., Kismarton M. Composite Structures: The first 100 years. 16th International Conference on Composite Materials. Kyoto; 2007.
- [5] Orders & Deliveries. Airbus Group; Accessed: 2014. http://www.airbus.com/no_cache/company/market/orders-deliveries.
- [6] Current orders. The Boeing Company; Accessed: 2014. <http://active.boeing.com/commercial/orders/index.cfm>.
- [7] Poe C., Dexter H., Raju I. Review of the NASA textile composites research. Journal of Aircraft. 1999; 36(5): 876-84.
- [8] Adumitroaie A., Barbero E. Beyond plain weave fabrics: II. Mechanical properties. Composite Structures. 2011; 93: 1449-62.
- [9] Williams C., Summerscales J., Grove S. Resin infusion under flexible tooling (RIFT): a review. Composites: Part A. 1996; 27A: 517-24.
- [10] Luz F.F., Amico S.C., Souza J.A., Barbosa E.S., Barbosa de Lima A.G. Resin Transfer Molding Process: Fundamentals, numerical computation and experiments. Numerical analysis of heat and mass transfer in porous media: Springer; 2012. p. 121-50.
- [11] Long A. Composites forming technologies. Cambridge: Woodhead; 2007.
- [12] Lomov S.V., Huysmans G., Luo Y., Parnas R.S., Prodromou A., et al. Textile composites: modelling strategies. Composites: Part A. 2001; 32: 1379-94.
- [13] Verleye B., Lomov S.V., Long A., Roose D. Permeability prediction for the meso-macro coupling in the simulation of the impregnation stage of Resin Transfer Moulding. Composites: Part A. 2010; 41: 29-35.
- [14] Lomov S.V., Ivanov D., Verpoest I. Predictive models for textile composites. 7th Textile Science International Conference. Liberec; 2010.
- [15] Boisse P., Zouari B., Daniel J. Importance of in-plane shear rigidity in finite element analyses of woven fabric composite preforming. Composites: Part A. 2006; 37: 2201-12.
- [16] Nayyar V., Ravi-Chandar K., Huang R. Stretch-induced stress patterns and wrinkles in hyperelastic thin sheets. International Journal of Solids and Structures. 2011; 48: 3471-83.

- [17] Allaoui S., Boisse P., Chatel S., Hamila N., Hivet G., et al. Experimental and numerical analyses of textile reinforcement forming of a tetrahedral shape. *Composites: Part A*. 2011; 42: 612-22.
- [18] Mack C., Taylor H. The fitting of woven cloth to surfaces. *Journal of the Textile Institute*. 1956; 47: 477-88.
- [19] Van Der Ween F. Algorithms for draping fabrics on doubly curved surfaces. *International Journal for Numerical Methods in Engineering*. 1991; 31: 1414-26.
- [20] Breen D., House D., Wozny M. A particle-based model for simulating the draping behavior of woven cloth. *Textile Research Journal*. 1994; 64(11): 663-85.
- [21] Dong L., Lekakou C., Bader M.G. Processing of composites: Simulations of the draping of fabrics with updated material behaviour law. *Journal of Composite Materials*. 2001; 35(2): 138-63.
- [22] Peng X.Q., Cao J. A continuum mechanics-based non-orthogonal constitutive model for woven composite fabrics. *Composites: Part A*. 2005; 36: 859-74.
- [23] Boisse P., Borr M., Buet K., Cherouat A. Finite element simulations of textile composite forming including the biaxial fabric behaviour. *Composites: Part B*. 1997; 28: 453-64.
- [24] Bathe K.-J.r. *Finite element procedures*. Englewood Cliffs: Prentice Hall 1996.
- [25] ten Thije R.H.W., Akkerman R., Huétink J. Large deformation simulation of anisotropic material using an updated Lagrangian finite element method. *Computer methods in applied mechanics and engineering*. 2007; 196: 3141-50.
- [26] Huétink J. On anisotropy, Objectivity and Invariance in finite thermo-mechanical deformations. 9th ESAFORM conference. Glasgow, U.K.; 2006.
- [27] Badel P., Gauthier S., Vidal-Sallé E., Boisse P. Rate constitutive equations for computational analyses of textile composite reinforcement mechanical behaviour during forming. *Composites: Part A*. 2009; 40: 997-1007.
- [28] Yu W.R., Pourboghrat F., Chung K., Zamploni M., Kang T.J. Non-orthogonal constitutive equation for woven fabric reinforced thermoplastic composites. *Composites: Part A*. 2002; 33: 1095-105.
- [29] Xue P., Peng X., Cao J. A non-orthogonal constitutive model for characterizing woven composites. *Composites: Part A*. 2003; 34(2): 183-93.
- [30] Yu W.R., Harrison P., Long A. Finite element forming simulation for non-crimp fabrics using a non-orthogonal constitutive equation. *Composites: Part A*. 2005; 36: 1079-93.
- [31] Khan M.A., Mabrouki T., Vidal-Sallé E., Boisse P. Numerical and experimental analyses of woven composite reinforcement forming using a hypoelastic behaviour. Application to the double dome benchmark. *Journal of Materials Processing Technology*. 2010; 210: 378-88.
- [32] Peng X., Ding F. Validation of a non-orthogonal constitutive model for woven composite fabrics via hemispherical stamping simulation. *Composites: Part A*. 2011; 42: 400-7.

- [33] Peng X., Rehman Z.U. Textile composite double dome stamping simulation using non-orthogonal constitutive model. *Composites Science and Technology*. 2011; 71: 1075-81.
- [34] Jauffrès D., Fetfatsidis K., Morris C., Sherwood J.A., Chen J. Mesoscopic finite element modelling of woven reinforcements applied to sheet moulding compound forming simulation. 17th International Conference on Composite Materials. Edinburgh; 2009.
- [35] Durville D. Simulation of the mechanical behaviour of woven fabrics at the scale of fibres. *International Journal of Material Forming*. 2010; 3 (Suppl 2): S1241-S51.
- [36] Badel P., Vidal-Sallé E., Boisse P. Computational determination of in-plane shear mechanical behaviour of textile composite reinforcements. *Computational Materials Science*. 2007; 40: 439-48.
- [37] Boisse P., Gasser A., Hivet G. Analyses of fabric tensile behaviour: determination of the biaxial tension-strain surfaces and their use in forming simulations. *Composites: Part A*. 2001; 32: 1395-414.
- [38] Hamila N., Boisse P. A meso-macro three node finite element for draping of textile composite preforms. *Applied Composite Materials*. 2007; 14: 235-50.
- [39] Hamila N., Boisse P., Sabourin F., Brunet M. A semi-discrete shell finite element for textile composite reinforcement forming simulation. *International Journal for Numerical Methods in Engineering*. 2009; 79: 1443-6.
- [40] Boisse P., Aimène Y., Dogui A., Dridi S., Gatouillat S., et al. Hypoelastic, hyperelastic, discrete and semi-discrete approaches for textile composite reinforcement forming. *International Journal of Material Forming*. 2010; 3: S1229-S40.
- [41] Wang J., Page J.R., Paton R. Experimental investigation of the draping properties of reinforcement fabrics. *Composites Science and Technology*. 1998; 58: 229-37.
- [42] Flores F.G., Oñate E. Application of a rotation-free triangle element for finite strain analysis of thin shells and membranes. In: Kröplin B, editor. *Textile Composites and Inflatable Structures*. Berlin: Springer; 2005. p. 69-88.
- [43] Govignon Q., Bickerton S., Kelly P.A. Simulation of the reinforcement compaction and resin flow during the complete resin infusion process. *Composites: Part A*. 2010; 41: 45-57.
- [44] ASTM D5034-09: Standard Test Method for Breaking Strength and Elongation of Textile Fabrics (Grab Test). ASTM International; 2009.
- [45] ASTM D5035-11: Standard Test Method for Breaking Force and Elongation of Textile Fabrics (Strip Method). ASTM International; 2011.
- [46] Kawabata S. The standardization and analysis of hand evaluation. Osaka, Japan: The Textile Machinery Society of Japan; 1980.
- [47] Potluri P., Perez Ciurezu D.A., Ramgulam R.B. Measurement of meso-scale shear deformations for modelling textile composites. *Composites: Part A*. 2006; 37: 303-14.

- [48] Culpin M.F. The shearing of fabric: a novel approach. *Journal of the Textile Institute*. 1979; 70: 81-8.
- [49] Harrison P., Clifford M.J., Long A.C. Shear characterisation of viscous woven textile composites: a comparison between picture frame and bias extension experiments. *Composites Science and Technology*. 2004; 64: 1453-65.
- [50] Cao J., Akkerman R., Boisse P., Chen J., Cheng H.S., et al. Characterization of mechanical behaviour of woven fabrics: Experimental methods and benchmark results. *Composites: Part A*. 2008; 39: 1037-53.
- [51] Harrison P., Abdiwi F., Guo Z., Potluri P., Yu W.R. Characterising the shear-tension coupling and wrinkling behaviour of woven engineering fabrics. *Composites: Part A*. 2012; 43: 903-14.
- [52] de Bilbao E., Soulat D., Hivet G., Gasser A. Experimental study of bending behaviour of reinforcements. *Experimental Mechanics*. 2010; 50: 333-51.
- [53] Syerko E., Comas-Cardona S., Binetruy C. Models of mechanical properties/behaviour of dry fibrous materials at various scales in bending and tension: A review. *Composites: Part A*. 2012; 43: 1365-88.
- [54] Lomov S.V., Dmitry I.S., Verpoest I., Zako M., Kurashiki T., et al. Meso-FE modelling of textile composites: Road map, data flow and algorithms. *Composites Science and Technology*. 2007; 67: 1870-91.
- [55] TexGen. v3.5.3. University of Nottingham; 2013. <http://texgen.sourceforge.net>.
- [56] Verpoest I., Lomov S.V. Virtual textile composites software WiseTex: Integration with micro-mechanical, permeability and structural analysis. *Composites Science and Technology*. 2005; 65: 2563-74.
- [57] Gasser A., Boisse P., Hanklar S. Mechanical behaviour of dry fabric reinforcements. 3D simulations versus biaxial tests. *Computational Materials Science*. 2000; 17: 7-20.
- [58] ASTM D7867-13: Standard test methods for measurement of rotational viscosity of paints, inks and related liquid materials as a function of temperature. ASTM International; 2013.
- [59] Sharma S., Siginer D.A. Permeability measurement methods in porous media of fiber reinforced composites. *Applied Mechanics review*. 2010; 63.
- [60] Arbitter R., Beraud J.M., Binetruy C., Bizet L., Bréard J., et al. Experimental determination of the permeability of textiles: A benchmark exercise. *Composites: Part A*. 2011; 42: 1157-68.
- [61] Park C.H., Lebel A., Saouab A., Bréard J., Lee W.I. Modeling and simulation of voids and saturation in liquid composite molding processes. *Composites: Part A*. 2011; 42: 658-68.
- [62] Hoes K., Dinescu D., Sol H., Parnas R.S., Lomov S.V. Study of nesting induced scatter of permeability values in layered reinforcement fabrics. *Composites: Part A*. 2004; 35: 1407-18.

- [63] Endruweit A., Long A., Robitaille F., Rudd C.D. Influence of stochastic fibre angle variations on the permeability of bi-directional textile fabrics. *Composites: Part A*. 2006; 37: 122-32.
- [64] Loix F., Badel P., Orgéas L., Geindreau C., Boisse P. Woven fabric permeability: From textile deformation to fluid flow mesoscale simulations. *Composites Science and Technology*. 2008; 68: 1624-30.
- [65] Dungan F.D., Senoguz M.T., Sastry A.M., Faillaci D.A. Simulations and experiments on low-pressure permeation of fabrics: Part I - 3D modelling of unbalanced fabric. *Journal of Composite Materials*. 2001; 35(14): 1250-84.
- [66] Takano N., Zako M., Okazaki T., Terada K. Microstructure-based evaluation of the influence of woven architecture on permeability by asymptotic homogenization theory. *Composites Science and Technology*. 2002; 62: 1347-56.
- [67] Lomov S.V., Verpoest I., Peeters T., Roose D., Zako M. Nesting in textile laminates: geometrical modelling of the laminate. *Composites Science and Technology*. 2003; 63: 993-1007.
- [68] Vanaerschot A., Cox B., Lomov S.V., Vandepitte D. Stochastic multi-scale modelling of textile composites based on internal geometry variability. *Computers and Structures*. 2013; 122: 55-64.
- [69] Han K.K., Lee C.W., Rice B.P. Measurements of the permeability of fiber preforms and applications. *Composites Science and Technology*. 2000; 60: 2435-41.
- [70] Adams K.L., Russel W.B., Rebenfeld L. Radial penetration of a viscous liquid into a planar anisotropic porous medium. *International Journal of Multiphase Flow*. 1988; 14(2): 203-15.
- [71] Vernet N., Ruiz E., Advani S.G., Alms J.B., Aubert M., et al. Experimental determination of the permeability of engineering textiles: Benchmark II. *Composites: Part A*. 2014; In Press.
- [72] Lundström T.S., Stenberg R., Bergström R., Partanen H., Birkeland P.A. In-plane permeability measurements: a Nordic round-robin study. *Composites: Part A*. 2000; 31: 29-43.
- [73] Luo Y., Verpoest I., Hoes K., Vanheule M., Sol H., Cardon A. Permeability measurement of textile reinforcements with several test fluids. *Composites: Part A*. 2001; 32: 1497-504.
- [74] Ahn S.H., Lee W.I., Springer G.S. Measurement of the three-dimensional permeability of fiber preforms using embedded fiber optic sensors. *Journal of Composite Materials*. 1995; 29(6): 714-33.
- [75] Weitzenböck J.R., Sheno R.A., Wilson P.A. Measurement of three-dimensional permeability. *Composites: Part A*. 1998; 29: 159-69.
- [76] Endruweit A., McGregor P., Long A.C., Johnson M.S. Influence of the fabric architecture on the variations in experimentally determined in-plane permeability values. *Composites Science and Technology*. 2006; 66: 1778-92.

- [77] Carman P.C. Flow of gases through porous media. London: Butterworths Scientific Publications; 1956.
- [78] Gebart B.R. Permeability of unidirectional reinforcements for RTM. *Journal of Composite Materials*. 1992; 26(8): 1100-34.
- [79] Yu B., Lee L.J. A simplified in-plane permeability model for textile fabrics. *Polymer Composites*. 2000; 21(5): 660-85.
- [80] Belov E.B., Lomov S.V., Verpoest I., Peters T., Roose D., et al. Modelling of permeability of textile reinforcements: lattice Boltzmann method. *Composites Science and Technology*. 2004; 64: 1069-80.
- [81] Dunkers J.P., Phelan F.R., Zimba C.G., Flynn M., Sanders D.P., et al. The prediction of permeability for an epoxy/e-glass composite using optical coherence tomographic images. *Polymer Composites*. 2001; 22(6): 803-14.
- [82] Nedanov P.B., Advani S.G. Numerical computation of the fiber preform permeability tensor by the homogenization method. *Polymer Composites*. 2002; 23(5): 758-70.
- [83] Verleye B., Croce R., Griebel M., Klitz M., Lomov S.V., et al. Permeability of textile reinforcements: simulation, influence of shear and validation. *Composites Science and Technology*. 2008; 68: 2804-10.
- [84] Wong C.C., Long A.C., Sherburn M., Robitaille F., Harrison P., Rudd C.D. Comparisons of novel and efficient approaches for permeability prediction based on the fabric architecture. *Composites: Part A*. 2006; 37: 847-57.
- [85] Hammami A., Trochu F., Gauvin R., Wirth S. Directional permeability measurement of deformed reinforcement. *Journal of Reinforced Plastics and Composites*. 1996; 15: 552-62.
- [86] Slade J., Sozer E.M., Advani S.G. Fluid impregnation of deformed preforms. *Journal of Reinforced Plastics and Composites*. 2000; 19(07): 552-68.
- [87] Smith P., Rudd C.D., Long A.C. The effect of shear deformation on the processing and mechanical properties of aligned reinforcements. *Composites Science and Technology*. 1997; 57: 327-44.
- [88] Lai C.L., Young W.B. Model resin permeation of fiber reinforcements after shear deformation. *Polymer Composites*. 1997; 18(5): 642-8.
- [89] Šimáček P., Advani S.G. Desirable features in mold filling simulations for liquid composite molding processes. *Polymer Composites*. 2004; 25(4): 355-67.
- [90] Correia N.C., Robitaille F., Long A.C., Rudd C.D., Šimáček P., Advani S.G. Analysis of the vacuum infusion moulding process: I. Analytical formulation. *Composites: Part A*. 2005; 36: 1645-56.
- [91] Yenilmez B., Senan M., Sozer E.M. Variation of part thickness and compaction pressure in vacuum infusion process. *Composites Science and Technology*. 2009; 69: 1710-9.

- [92] Joubaud L., Achim V.T., F. Numerical simulation of resin infusion and reinforcement consolidation under flexible cover. *Polymer Composites*. 2005; 26: 417-27.
- [93] Trochu F., Gauvin R. Limitations of a boundary filled finite-difference method for the simulation of the resin transfer molding process. *Journal of Reinforced Plastics and Composites*. 1992; 11(7): 772-86.
- [94] Martinez R.V., Cueto E., Doblare M., Chinesta F. Natural element meshless simulation of flows involving short fiber suspensions. *Journal of Non-Newtonian Fluid Mechanics*. 2003; 115(1): 51-78.
- [95] Trochu F., Ruiz E., Achim V., Soukane S. Advanced numerical simulation of liquid composite molding for process analysis optimization. *Composites: Part A*. 2006; 37: 890-902.
- [96] Soukane S., Trochu F. Application of the level set method to the simulation of resin transfer molding. *Composites Science and Technology*. 2006; 66: 1067-80.
- [97] Brusckhe M.V., Advani S.G. A Finite Element/Control Volume approach to mold filling in anisotropic porous media. *Polymer Composites*. 1990; 11(6): 398-405.
- [98] Kang M.K., Lee W.I., Hahn H.T. Analysis of vacuum bag resin transfer moulding process. *Composites: Part A*. 2001; 32: 1553-60.
- [99] Ngo N.D., Mohan R.V., Chung P.W., Tamma K.K. Recent developments encompassing non-isothermal/isothermal liquid composite molding process modeling/analysis: Physically accurate, computationally effective, and affordable simulations and validations. *Journal of Thermoplastic Composite Materials*. 1998; 11: 493-532.
- [100] Phelan F.R. Simulation of the injection process in resin transfer molding. *Polymer Composites*. 1997; 18(4): 460-76.
- [101] Hirt C.W., Nichols B.D. Volume of Fluid (VOF) method for dynamics of free boundaries. *Journal of Computational Physics*. 1981; 39: 201-25.
- [102] Abaqus 6.11. Dassault Systèmes; 2011. <http://www.3ds.com/products/simulia/portfolio/abaqus/overview>.
- [103] Khan M.A. Numerical and experimental forming analyses of textile composite reinforcements based on a hypoelastic behaviour [Ph.D.]. Lyon, France: Institut National des Sciences Appliquées de Lyon (INSA-Lyon); 2009.
- [104] Mohammed U., Lekakou C., Dong L., Bader M. Shear deformation and micromechanics of woven fabrics. *Composites: Part A*. 2000; 31: 299-308.
- [105] Eberl C. Digital image correlation and tracking - File exchange - MATLAB central. The MathWorks, Inc.; 2006. Accessed: March, 2011. <http://www.mathworks.com.au/matlabcentral/fileexchange/12413-digital-image-correlation-and-tracking>.
- [106] Pierce R.S. Shear strain DIC (for bias extension tests) - File exchange - MATLAB central. The MathWorks, Inc.; 2012. Accessed: June, 2013.

<http://www.mathworks.com.au/matlabcentral/fileexchange/39544-shear-strain-dic-for-bias-extension-tests>.

- [107] Matlab R2012B. MathWorks; 2012. <http://www.mathworks.com.au/products/matlab>.
- [108] Lewis J.P. Fast normalized cross-correlation. *Vision interface*. 1995; 10(1): 120-3.
- [109] Harrison P., Clifford M.J., Long A.C. Shear characterisation of woven textile composites. 10th European Conference on Composite Materials. Brugge, Belgium; 2002.
- [110] Lebrun G., Bureau M.N., Denault J. Evaluation of bias-extension and picture-frame test methods for the measurement of intraply shear properties of PP/glass commingled fabrics. *Composite Structures*. 2003; 61: 341-52.
- [111] Weitzenböck J.R., Shenoï R.A., Wilson P.A. Radial flow permeability measurement. Part B: Application. *Composites: Part A*. 1999; 30: 797-813.
- [112] Weitzenböck J.R., Shenoï R.A., Wilson P.A. Radial flow permeability measurement. Part A: Theory. *Composites: Part A*. 1999; 30: 781-96.
- [113] ASTM D2584-11: Standard Test Method for Ignition Loss of Cured Reinforced Resins. ASTM International; 2011.
- [114] Pierce R.S. Video processing for permeability characterisation - File exchange - MATLAB central. The MathWorks, Inc.; 2014. Accessed: December, 2014. <http://www.mathworks.com/matlabcentral/fileexchange/48002-video-processing-for-permeability-characterisation>.
- [115] Endruweit A., Ermanni P. The in-plane permeability of sheared textiles. Experimental observations and a predictive conversion model. *Composites: Part A*. 2004; 35: 439-51.
- [116] Mesogitis T.S., Skordos A.A., Long A.C. Uncertainty in the manufacturing of fibrous thermosetting composites: A review. *Composites: Part A*. 2014; 57: 67-75.
- [117] Bickerton S., Advani S.G. Characterization and modeling of race-tracking in liquid composite molding processes. *Composites Science and Technology*. 1999; 59: 2215-29.
- [118] Ruiz E., Achim V., Soukane S., Trochu F., Bréard J. Optimisation of injection flow rate to minimize micro/macro-voids formation in resin transfer molded composites. *Composites Science and Technology*. 2006; 66: 475-86.
- [119] Acheson J.A., Simacek P., Advani S.G. The implications of fiber compaction and saturation on fully coupled VARTM simulation. *Composites: Part A*. 2004; 35: 159-69.
- [120] Nguyen Q.T., Vidal-Sallé E., Boisse P., Park C.H., Saouab A., et al. Mesoscopic scale analyses of textile composite reinforcement compaction. *Composites: Part B*. 2013; 44: 231-41.

Appendix A: VUMAT subroutine

Example of the VUMAT subroutine used for the multiple ply simulations in Section 7.7, written in Fortran to support the Abaqus/Explicit draping model. Detailed theory of the method is outlined in Section 3.2.2.

```
      subroutine vumat(
C Read only (unmodifiable)variables -
  1  nblock, ndir, nshr, nstatev, nfieldv, nprops, lanneal,
  2  stepTime, totalTime, dt, cmname, coordMp, charLength,
  3  props, density, strainInc, relSpinInc,
  4  tempOld, stretchOld, defgradOld, fieldOld,
  5  stressOld, stateOld, enerInternOld, enerInelasOld,
  6  tempNew, stretchNew, defgradNew, fieldNew,
C Write only (modifiable) variables -
  7  stressNew, stateNew, enerInternNew, enerInelasNew )

      include 'vaba_param.inc'

      dimension props(nprops), density(nblock), coordMp(nblock,*),
  1  charLength(nblock), strainInc(nblock,ndir+nshr),
  2  relSpinInc(nblock,nshr), tempOld(nblock),
  3  stretchOld(nblock,ndir+nshr), defgradOld(nblock,ndir+nshr+nshr),
  4  fieldOld(nblock,nfieldv), stressOld(nblock,ndir+nshr),
  5  stateOld(nblock,nstatev), enerInternOld(nblock),
  6  enerInelasOld(nblock), tempNew(nblock),
  7  stretchNew(nblock,ndir+nshr), defgradNew(nblock,ndir+nshr+nshr),
  8  fieldNew(nblock,nfieldv), stressNew(nblock,ndir+nshr),
  9  stateNew(nblock,nstatev), enerInternNew(nblock),
  1  enerInelasNew(nblock), R(nblock,ndir+nshr),
  2  gn1(nblock,nshr+nshr), gn2(nblock,nshr+nshr),
  3  f1(nblock,nshr+nshr), f2(nblock,nshr+nshr),
  4  cost1(nblock), cost2(nblock), t1(nblock,ndir+nshr),
  5  t2(nblock,ndir+nshr), sint1(nblock), sint2(nblock),
  6  strainIncf1(nblock,ndir+nshr), shrang(nblock),
  7  strainIncf2(nblock,ndir+nshr), detU(nblock),
  8  stressIncf1(nblock,ndir+nshr), strain(nblock,ndir+nshr),
  9  strainf1(nblock,ndir+nshr), strainf2(nblock,ndir+nshr),
  1  stressIncf2(nblock,ndir+nshr)

      character*80 cmname

      parameter( zero = 0.d0, one = 1.d0, two = 2.d0, half = one/two,
  1  pi = 3.141592653589793238, oneeighty = 180.d0,
  2  a1 = 0.001247, b1 = 4.896, c1 = 0.0000000000000000004336,
  3  d1 = 31.48, e1 = 0, z1 = 0, p1 = 15000, cv = 1000000)

      do k = 1,nblock

C Definition of rotation tensor, R, from polar decomposition
C where R = F*inv(U). Hence need to calculate determinant of U also.
      detU(k) = one / ( stretchNew(k,1) * stretchNew(k,2) -
*                      stretchNew(k,4) * stretchNew(k,4) )
      R(k,1) = detU(k) * ( defgradNew(k,1) * stretchNew(k,2) -
*                          defgradNew(k,4) * stretchNew(k,4) )
      R(k,2) = detU(k) * ( defgradNew(k,4) * stretchNew(k,1) -
*                          defgradNew(k,1) * stretchNew(k,4) )
      R(k,3) = detU(k) * ( defgradNew(k,5) * stretchNew(k,2) -
*                          defgradNew(k,2) * stretchNew(k,4) )
      R(k,4) = detU(k) * ( defgradNew(k,2) * stretchNew(k,1) -
*                          defgradNew(k,5) * stretchNew(k,4) )

C Assuming initial GN axes are: gn01 = [1,0], gn02 = [0,1], gn03 = [0,0,1]
C the updated GN axes can be defined as follows:
      gn1(k,1) = R(k,1)
      gn1(k,2) = R(k,3)
```

```

gn2(k,1) = R(k,2)
gn2(k,2) = R(k,4)

C Updated fibre axes can be defined and normalised as follows, where:
C defgrad1 = F11, defgrad4 = F12, defgrad5 = F21, defgrad2 = F22
f1(k,1) = defgradNew(k,1) /
*   sqrt( defgradNew(k,1)**two + defgradNew(k,5)**two )
f1(k,2) = defgradNew(k,5) /
*   sqrt( defgradNew(k,1)**two + defgradNew(k,5)**two )
f2(k,1) = defgradNew(k,4) /
*   sqrt( defgradNew(k,4)**two + defgradNew(k,2)**two )
f2(k,2) = defgradNew(k,2) /
*   sqrt( defgradNew(k,4)**two + defgradNew(k,2)**two )

C Finding the cos(theta) and sin(theta) values between GN and fibre frames,
C where 'cost1' is 'cos of theta 1'
cost1(k) = ( f1(k,1) * gn1(k,1) + f1(k,2) * gn1(k,2) ) /
*   ( sqrt( f1(k,1)**two + f1(k,2)**two ) *
*   sqrt( gn1(k,1)**two + gn1(k,2)**two ) )

sint1(k) = ( f1(k,2) * gn1(k,1) - f1(k,1) * gn1(k,2) ) /
*   ( sqrt( f1(k,1)**two + f1(k,2)**two ) *
*   sqrt( gn1(k,1)**two + gn1(k,2)**two ) )

cost2(k) = ( f2(k,1) * gn2(k,1) + f2(k,2) * gn2(k,2) ) /
*   ( sqrt( f2(k,1)**two + f2(k,2)**two ) *
*   sqrt( gn2(k,1)**two + gn2(k,2)**two ) )

sint2(k) = ( f2(k,2) * gn2(k,1) - f2(k,1) * gn2(k,2) ) /
*   ( sqrt( f2(k,1)**two + f2(k,2)**two ) *
*   sqrt( gn2(k,1)**two + gn2(k,2)**two ) )

C Defining the shear angle (in radians)
stateNew(k,1) = atan2(sint1(k),cost1(k)) -
*   atan2(sint2(k),cost2(k))

C Transformation matrix T1
t1(k,1) = cost1(k)
t1(k,2) = -sint1(k)
t1(k,3) = sint1(k)
t1(k,4) = cost1(k)

C Transformation matrix T2
t2(k,1) = cost2(k)
t2(k,2) = -sint2(k)
t2(k,3) = sint2(k)
t2(k,4) = cost2(k)

C Strain increments expressed in the first fibre orthogonal frame (f1)
strainIncf1(k,1) =
*   ( t1(k,1) * strainInc(k,1) +
*   t1(k,3) * strainInc(k,4) ) * t1(k,1) +
*   ( t1(k,1) * strainInc(k,4) +
*   t1(k,3) * strainInc(k,2) ) * t1(k,3)
strainIncf1(k,2) =
*   ( t1(k,2) * strainInc(k,1) +
*   t1(k,4) * strainInc(k,4) ) * t1(k,2) +
*   ( t1(k,2) * strainInc(k,4) +
*   t1(k,4) * strainInc(k,2) ) * t1(k,4)
strainIncf1(k,4) =
*   ( t1(k,1) * strainInc(k,1) +
*   t1(k,3) * strainInc(k,4) ) * t1(k,2) +
*   ( t1(k,1) * strainInc(k,4) +
*   t1(k,3) * strainInc(k,2) ) * t1(k,4)

C Strain increments expressed in the second fibre orthogonal frame (f2)
strainIncf2(k,1) =
*   ( t2(k,1) * strainInc(k,1) +
*   t2(k,3) * strainInc(k,4) ) * t2(k,1) +
*   ( t2(k,1) * strainInc(k,4) +

```

```

*      t2(k,3) * strainInc(k,2) ) * t2(k,3)
strainIncf2(k,2) =
*      ( t2(k,2) * strainInc(k,1) +
*      t2(k,4) * strainInc(k,4) ) * t2(k,2) +
*      ( t2(k,2) * strainInc(k,4) +
*      t2(k,4) * strainInc(k,2) ) * t2(k,4)
strainIncf2(k,4) =
*      ( t2(k,2) * strainInc(k,1) +
*      t2(k,4) * strainInc(k,4) ) * t2(k,1) +
*      ( t2(k,2) * strainInc(k,4) +
*      t2(k,4) * strainInc(k,2) ) * t2(k,3)

C Constitutive Tensor definitions -----
D11 = p1 *cv
D22 = p1 *cv
D12 = zero
G12 = ( b1*a1*exp(b1*abs(stateNew(k,1)))
*      + d1*c1*exp(d1*abs(stateNew(k,1))) ) *cv
C -----

C Updating the stress increments in the fibre directions (by applying the
C constitutive tensor to the strain increments)
stressIncf1(k,1) = D11*strainIncf1(k,1) + D12*strainIncf1(k,2)
stressIncf1(k,2) = D12*strainIncf1(k,1) + zero*strainIncf1(k,2)
stressIncf1(k,4) = G12*strainIncf1(k,4)
stressIncf2(k,1) = zero*strainIncf2(k,1) + D12*strainIncf2(k,2)
stressIncf2(k,2) = D22*strainIncf2(k,2) + D12*strainIncf2(k,1)
stressIncf2(k,4) = G12*strainIncf2(k,4)

C Stresses in the fibre directions are tracked as SDVs:
C Sf11, Sf22 and Sf12
stateNew(k,2) = stateOld(k,2) + stressIncf1(k,1)
stateNew(k,3) = stateOld(k,3) + stressIncf2(k,2)
stateNew(k,4) = stateOld(k,4) + half*(
*      stressIncf1(k,4) + stressIncf2(k,4) )

C Converting stresses back to the GN frame for next iteration, using the
C transformation matrices
C S11
stressNew(k,1) =
*      ( t1(k,1) * stateNew(k,2) +
*      t1(k,2) * stateNew(k,4) ) * t1(k,1) +
*      ( t1(k,1) * stateNew(k,4) +
*      t1(k,2) * zero ) * t1(k,2) +
*      ( t2(k,1) * zero +
*      t2(k,2) * stateNew(k,4) ) * t2(k,1) +
*      ( t2(k,1) * stateNew(k,4) +
*      t2(k,2) * stateNew(k,3) ) * t2(k,2)

C S22
stressNew(k,2) =
*      ( t1(k,3) * stateNew(k,2) +
*      t1(k,4) * stateNew(k,4) ) * t1(k,3) +
*      ( t1(k,3) * stateNew(k,4) +
*      t1(k,4) * zero ) * t1(k,4) +
*      ( t2(k,3) * zero +
*      t2(k,4) * stateNew(k,4) ) * t2(k,3) +
*      ( t2(k,3) * stateNew(k,4) +
*      t2(k,4) * stateNew(k,3) ) * t2(k,4)

C S12 / S21
stressNew(k,4) =
*      ( t1(k,1) * stateNew(k,2) +
*      t1(k,2) * stateNew(k,4) ) * t1(k,3) +
*      ( t1(k,1) * stateNew(k,4) +
*      t1(k,2) * zero ) * t1(k,4) +
*      ( t2(k,1) * zero +
*      t2(k,2) * stateNew(k,4) ) * t2(k,3) +
*      ( t2(k,1) * stateNew(k,4) +
*      t2(k,2) * stateNew(k,3) ) * t2(k,4)

```

```
C      stressNew(k,3) = stressOld(k,3)
      end do
      return
      end
```

Appendix B: Python script

Full code for the Python script discussed in Section 7.2, from the multiple ply modelling example in Section 7.7. The code is designed to be run through the Abaqus command interface.

```
import odbAccess

# 1.
# sets up odb object, "REQUIRED USER INPUT (OBJECT FILE NAME)"
odb = odbAccess.openOdb(r"4plyMulti.odb")

odbname = odb.name[:-4] # output database path and name (minus ".odb")

# defining structures related to the last frame of the last step
steplist = odb.steps.keys()
finalframe = odb.steps[steplist[-1]].frames[-1]

# defining field outputs
sdvar1 = finalframe.fieldOutputs["SDV1"].values # ELEMENTAL
stress = finalframe.fieldOutputs["S"].values # ELEMENTAL
displ = finalframe.fieldOutputs["U"].values # NODAL

# determining element type (S4R shell or M3D4R membrane)
eltype = sdvar1[0].instance.elements[0].type

# defining several global variables
instname = [sdvar1[0].instance.name] # deformable body instance name
instels = [len(sdvar1[0].instance.elements)] # elements in body instance
instnds = [len(sdvar1[0].instance.nodes)] # number of nodes in body instance
instindex = [0]

# section points in deformable body instances (x2 for shell bodies)
instpts = len(sdvar1)

# total number of nodes (includes rigid body elements)
totalnds = len(displ)

for i in range(0,instpts):
    tempname = sdvar1[i].instance.name
    for j in range(0,len(instname)):
        if tempname == instname[j]:
            break
        elif (j == len(instname)-1) and (tempname != instname[j]):
            instname.extend([tempname])
            instnds.extend([len(sdvar1[i].instance.nodes)])
            instels.extend([len(sdvar1[i].instance.elements)])
            instindex.extend([i])

for k in range(0,len(instname)):

    # 2.
    # initialising storage of node indices
    ndind = [() for _ in range(instnds[k])]
    # looping through all nodes
    for a in range(0,totalnds):
        # checking that current node is from deformable body instance
        if displ[a].instance.name == instname[k]:
            ndlab = displ[a].nodeLabel # current node label
            ndind[ndlab-1] = a # index storage

    # initialising storage of element indices
    elind = [() for _ in range(instels[k])]
    # looping through all elements as stored under ...instance.elements
    for d in range(0,instels[k]):
        # checking that current node is from deformable body instance
        if sdvar1[instindex[k]].instance.name == instname[k]:
```

```

        ellab = sdvar1[instindex[k]].instance.elements[d].label
        elind[ellab-1] = d # index storage
        # determining the number of rows and columns of nodes
        if ellab == 1:
            rows = \
sdvar1[instindex[k]].instance.elements[d].connectivity[-1] - 1
            columns = instnds[k]/rows

# initialising storage of values
elcoords = [()] for _ in range(instels[k])
locdir1 = [()] for _ in range(instels[k])
locdir2 = [()] for _ in range(instels[k])
locdir3 = [()] for _ in range(instels[k])
shrang1 = [()] for _ in range(instels[k])
shrang5 = [()] for _ in range(instels[k])
defnodecoords = [()] for _ in range(instnds[k])

# 3.
# looping through each instance point 'b'
for b in range(0,instpts):

    if sdvar1[b].instance.name == instname[k]:

        ellabel = sdvar1[b].elementLabel # element number/label

        # ELEMENT COORDINATES
        # connected nodes, as node id tuple (1, 2, 3, 4)
        i = \
sdvar1[b].instance.elements[elind[ellabel-1]].connectivity

        nodesum = 0 # initialising nodesum
        # looping through each connected node
        for c in range(0,len(i)):
            j = int(i[c])-1 # node indices to integers
            nodecoords = \
sdvar1[b].instance.nodes[j].coordinates
            nodedispl = displ[ndind[j]].data
            defnodecoords[j] = nodecoords + nodedispl
            nodesum = nodesum + defnodecoords[j]
        # calculating the effective element centroid
        elcoords[ellabel-1] = nodesum/len(i)

        # LOCAL MATERIAL DIRECTIONS
        # (x1,y1,z1)
        locdir1[ellabel-1] = stress[b].localCoordSystem[0]
        # (x2,y2,z2)
        locdir2[ellabel-1] = stress[b].localCoordSystem[1]
        # (x3,y3,z3)
        locdir3[ellabel-1] = stress[b].localCoordSystem[2]

        # SHEAR ANGLE
        # extracting values (for the 'b'th element) of sdvar1
        if eltype == "S4R":
            pointn = sdvar1[b].sectionPoint.number
            if pointn == 1:
                shrang1[ellabel-1] = sdvar1[b].data
            elif pointn == 5:
                shrang5[ellabel-1] = sdvar1[b].data
        elif eltype == "M3D4R":
            shrang1[ellabel-1] = sdvar1[b].data
            shrang5[ellabel-1] = sdvar1[b].data

# 4.
# opening a new file to report the primary information to
fileobj = open(odbname+instname[k]+".txt", "w")
fileobj.write("%d\n" % (instels[k]))

```

```

    for e1 in range(0,instels[k]):
        fileobj.write("%d, %.8f, %.8f, %.8f, %.8f, %.8f, %.8f, %.8f,
%.8f, %.8f, %.8f, %.8f\n" % (e1+1, elcoords[e1][0], elcoords[e1][1],
elcoords[e1][2], locdir1[e1][0], locdir1[e1][1], locdir1[e1][2],
locdir2[e1][0], locdir2[e1][1], locdir2[e1][2], shrang1[e1], shrang5[e1]))
        fileobj.close()

# opening a new file to report the deformed node coordinates to
ndfileobj = open(odbname+instname[k]+"nd.txt", "w")
column = 1 # initialising current column of node points
for nd in range(0,instnds[k]):
    ndfileobj.write("%d %d %.8f %.8f %.8f\n" % (column, nd+1 -
rows*(column-1), defnodecoords[nd][0], defnodecoords[nd][1],
defnodecoords[nd][2]))
    # checking if end of column is reached
    if nd+1 - rows*(column-1) == rows:
        column += 1
        ndfileobj.write("\n")
ndfileobj.close()

```

Appendix C: UDF subroutine

Example of the complete UDF subroutine with INIT and PROFILE macro functions for the multiple ply simulations in Section 7.7. This interpreted subroutine supports the FLUENT infusion model and relies on ten User Defined Memory locations for property storage.

```
#include "udf.h"

// 1.
// INIT macro function
DEFINE_INIT(init_function,d)
{
    // a.
    // INITIALISATION
    cell_t c;
    Thread *t;
    real centcoords[ND_ND];

    float weightsum, radius, height, delang, D, centSA, centVR1, centVR2,
    centPor, centX1, centY1, centZ1, centX2, centY2, centZ2, centXn, centYn,
    centZn, centXb, centYb, centZb, centXt, centYt, centZt, centXk1, centYk1,
    centZk1, centXk2, centYk2, centZk2, tempX, tempY, tempZ;
    float weight[3], centDIR1[3], currcoords[3], dir1[3], dir2[3],
    closestD[3], closestSA[3], closestX1[3], closestY1[3], closestZ1[3],
    closestX2[3], closestY2[3], closestZ2[3];
    int i, j, k, l, tid, low, high, totel, closestEL[3];

    int elno[8000];
    float currX[8000], currY[8000], currZ[8000], dir1X[8000], dir1Y[8000],
    dir1Z[8000], dir2X[8000], dir2Y[8000], dir2Z[8000], SAngle[8000],
    SAngle2[8000];

    // OPEN FILES
    FILE *fdata1 = fopen("4plyMultiPLY1-0.txt","r");
    FILE *fdata2 = fopen("4plyMultiPLY2-45.txt","r");
    FILE *fdata3 = fopen("4plyMultiPLY3-45.txt","r");
    FILE *fdata4 = fopen("4plyMultiPLY4-0.txt","r");

    // READING FROM DATA FILES, storing values as local variables
    fscanf(fdata1, "%d", &totel); // reading the total number of elements
    for( i = 0; i < totel; i++ ) // reading each line of the data file
    {
        fscanf(fdata1,"%d, %f, %f",
        &elno[i], &currX[i], &currY[i], &currZ[i], &dir1X[i], &dir1Y[i], &dir1Z[i],
        &dir2X[i], &dir2Y[i], &dir2Z[i], &SAngle[i], &SAngle2[i]);
    }

    fscanf(fdata2, "%d", &totel);
    for( i = totel; i < 2*totel; i++ )
    {
        fscanf(fdata2,"%d, %f, %f",
        &elno[i], &currX[i], &currY[i], &currZ[i], &dir1X[i], &dir1Y[i], &dir1Z[i],
        &dir2X[i], &dir2Y[i], &dir2Z[i], &SAngle[i], &SAngle2[i]);
    }

    fscanf(fdata3, "%d", &totel);
    for( i = 2*totel; i < 3*totel; i++ )
    {
        fscanf(fdata3,"%d, %f, %f",
        &elno[i], &currX[i], &currY[i], &currZ[i], &dir1X[i], &dir1Y[i], &dir1Z[i],
        &dir2X[i], &dir2Y[i], &dir2Z[i], &SAngle[i], &SAngle2[i]);
    }

    fscanf(fdata4, "%d", &totel);
    for( i = 3*totel; i < 4*totel; i++ )
    {
```

```

        fscanf(fdata4,"%d, %f, %f, %f, %f, %f, %f, %f, %f, %f, %f",
&elno[i], &currX[i], &currY[i], &currZ[i], &dir1X[i], &dir1Y[i], &dir1Z[i],
&dir2X[i], &dir2Y[i], &dir2Z[i], &SAngle[i], &SAngle2[i]);
    }

    // b.
    // *CENTROID LOOP* through all threads in the domain, and all cells
    thread_loop_c(t,d)
    {

        tid = THREAD_ID(t);
        // printf("\n Thread ID: %d", tid);

        begin_c_loop_all(c,t)
        {
            // extracts centroid information for each cell
            C_CENTROID(centcoords,c,t);

            // init distance to the 3 closest points and weight sum
            // (needs to be re-initialised for every centroid)
            closestD[0] = closestD[1] = closestD[2] = 999;
            weightsum = 0;

            if( tid == 8 ) // set domain id for ply 1
            {
                low = 0;
                high = totel;
            }
            else if( tid == 10 ) // set domain id for ply 2
            {
                low = totel;
                high = 2*totel;
            }
            else if( tid == 9 ) // set domain id for ply 3
            {
                low = 2*totel;
                high = 3*totel;
            }
            else if( tid == 11 ) // set domain id for ply 4
            {
                low = 3*totel;
                high = 4*totel;
            }

            // **COMPARATIVE ELEMENT LOOP**
            // through every stored element centre position
            for( j = low; j < high; j++ )
            {
                // calculating distance from the current centroid
                // to the current element centre
                D = sqrt( pow((currX[j]-centcoords[0]),2) +
pow((currY[j]-centcoords[1]),2) + pow((currZ[j]-centcoords[2]),2) );

                // loop to check if the current centroid is one
                // of the 3 closest points
                for( k = 0; k < 3; k++ )
                {
                    // if the current distance is shorter than
                    // any of the 3 previously stored, then
                    // reassigns the associated values
                    if( D < closestD[k] )
                    {
                        closestD[k] = D;
                        closestSA[k] = SAngle[j];
                        closestEL[k] = elno[j];
                        closestX1[k] = dir1X[j];
                        closestY1[k] = dir1Y[j];
                        closestZ1[k] = dir1Z[j];
                    }
                }
            }
        }
    }

```

```

                                closestX2[k] = dir2X[j];
                                closestY2[k] = dir2Y[j];
                                closestZ2[k] = dir2Z[j];
                                break;
                                }
                                }
                                // **COMPARATIVE ELEMENT LOOP END**

                                // start of the distance weighting approach
                                for( l = 0; l < 3; l++ )
                                {
                                        weight[l] = 1/pow(closestD[l],3);
                                        weightsum += weight[l];
                                }

                                // determining weighted centroid values
                                centSA = (closestSA[0]*weight[0] + closestSA[1]*weight[1]
+ closestSA[2]*weight[2])/weightsum;
                                centX1 = (closestX1[0]*weight[0] + closestX1[1]*weight[1]
+ closestX1[2]*weight[2])/weightsum;
                                centY1 = (closestY1[0]*weight[0] + closestY1[1]*weight[1]
+ closestY1[2]*weight[2])/weightsum;
                                centZ1 = (closestZ1[0]*weight[0] + closestZ1[1]*weight[1]
+ closestZ1[2]*weight[2])/weightsum;
                                centX2 = (closestX2[0]*weight[0] + closestX2[1]*weight[1]
+ closestX2[2]*weight[2])/weightsum;
                                centY2 = (closestY2[0]*weight[0] + closestY2[1]*weight[1]
+ closestY2[2]*weight[2])/weightsum;
                                centZ2 = (closestZ2[0]*weight[0] + closestZ2[1]*weight[1]
+ closestZ2[2]*weight[2])/weightsum;

                                // bias direction vector (dir1 + dir2)/2
                                centXb = ( centX1/(sqrt(centX1*centX1 + centY1*centY1 +
centZ1*centZ1)) + centX2/(sqrt(centX2*centX2 + centY2*centY2 +
centZ2*centZ2)) )/2;
                                centYb = ( centY1/(sqrt(centX1*centX1 + centY1*centY1 +
centZ1*centZ1)) + centY2/(sqrt(centX2*centX2 + centY2*centY2 +
centZ2*centZ2)) )/2;
                                centZb = ( centZ1/(sqrt(centX1*centX1 + centY1*centY1 +
centZ1*centZ1)) + centZ2/(sqrt(centX2*centX2 + centY2*centY2 +
centZ2*centZ2)) )/2;

                                // normal vector (dir1 CROSS dir2)
                                centXn = centY1*centZ2 - centZ1*centY2;
                                centYn = -( centX1*centZ2 - centZ1*centX2);
                                centZn = centX1*centY2 - centY1*centX2;

                                // transverse direction vector (bias CROSS normal)
                                centXt = centYb*centZn - centZb*centYn;
                                centYt = -( centXb*centZn - centZb*centXn);
                                centZt = centXb*centYn - centYb*centXn;

                                // calculating the Viscous Resistances (inverse
                                // permeabilities) and porosity based on shear angle
                                if( centSA < 0 )
                                {
                                        // USER INPUT:
                                        // polynomial factors and initial porosity
                                        centVR1 = 1/ (-6.641E-10*pow((-centSA),4) +
1.328E-9*pow((-centSA),3) - 8.414E-10*pow((-centSA),2) + 2.400E-10*-centSA +
6.028E-11);
                                        centVR2 = 1/ (-7.700E-10*pow((-centSA),4) +
1.466E-9*pow((-centSA),3) - 9.261E-10*pow((-centSA),2) + 1.605E-10*-centSA +
5.313E-11);
                                        centPor = 1 - 0.2757/cos(-centSA);

                                        tempX = centXt;

```

```

tempY = centYt;
tempZ = centZt;
centXt = centXb;
centYt = centYb;
centZt = centZb;
centXb = tempX;
centYb = tempY;
centZb = tempZ;

// PRINCIPAL PERMABILITY DIRECTION function
if( centSA > -0.349066)
{
    delang = -centSA*(-centSA-1.919862)/0.698132
+ 0.78540;
}
else
{
    delang = 0;
}

centXk1 = (delang/0.78540)*centX2 + (1-
delang/0.78540)*centXb;
centYk1 = (delang/0.78540)*centY2 + (1-
delang/0.78540)*centYb;
centZk1 = (delang/0.78540)*centZ2 + (1-
delang/0.78540)*centZb;

centXk2 = centYk1*centZn - centZk1*centYn;
centYk2 = -( centXk1*centZn - centZk1*centXn);
centZk2 = centXk1*centYn - centYk1*centXn;
}
else
{
    // USER INPUT:
    // polynomial factors and initial porosity
    centVR1 = 1/ (-6.641E-10*pow((centSA),4) + 1.328E-
9*pow((centSA),3) - 8.414E-10*pow((centSA),2) + 2.400E-10*centSA + 6.028E-
11);
    centVR2 = 1/ (-7.700E-10*pow((centSA),4) + 1.466E-
9*pow((centSA),3) - 9.261E-10*pow((centSA),2) + 1.605E-10*centSA + 5.313E-
11);
    centPor = 1 - 0.2757/cos(centSA);

    // PRINCIPAL PERMABILITY DIRECTION function
    if( centSA <= 0.349066)
    {
        delang = centSA*(centSA-1.919862)/0.698132 +
0.78540;
    }
    else
    {
        delang = 0;
    }

    centXk1 = (delang/0.78540)*centX2 + (1-
delang/0.78540)*centXb;
    centYk1 = (delang/0.78540)*centY2 + (1-
delang/0.78540)*centYb;
    centZk1 = (delang/0.78540)*centZ2 + (1-
delang/0.78540)*centZb;

    centXk2 = centYk1*centZn - centZk1*centYn;
    centYk2 = -( centXk1*centZn - centZk1*centXn);
    centZk2 = centXk1*centYn - centYk1*centXn;
}

// overall reduction of permeability values
centVR1 = 1.5*centVR1;

```

```

centVR2 = 2*centVR2;
//
/* Calibrations to account for compaction/decompaction can
be included here */
// Storing information in User Defined Memory
C_UDMI(c,t,0) = centSA;
C_UDMI(c,t,1) = centPor;
C_UDMI(c,t,2) = centVR1;
C_UDMI(c,t,3) = centVR2;
C_UDMI(c,t,4) = centXk1;
C_UDMI(c,t,5) = centYk1;
C_UDMI(c,t,6) = centZk1;
C_UDMI(c,t,7) = centXk2;
C_UDMI(c,t,8) = centYk2;
C_UDMI(c,t,9) = centZk2;
}
end_c_loop_all(c,t)
// *CENTROID LOOP END*

}

fclose(fdata1);
fclose(fdata2);
fclose(fdata3);
fclose(fdata4);
}

// 2.
// POROSITY
DEFINE_PROFILE(porosity,t,nv)
{
float phi;
cell_t c;
begin_c_loop(c,t)
{
phi = C_UDMI(c,t,1);
C_PROFILE(c,t,nv) = phi;
}
end_c_loop(c,t)
}

// VISCOUS RESISTANCE (STREAMWISE)
DEFINE_PROFILE(viscresist_s,t,nv)
{
float vr_s;
cell_t c;
begin_c_loop(c,t)
{
vr_s = C_UDMI(c,t,2);
C_PROFILE(c,t,nv) = vr_s;
}
end_c_loop(c,t)
}

// VISCOUS RESISTANCE (TRANSVERSE)
DEFINE_PROFILE(viscresist_t,t,nv)
{
float vr_t;
cell_t c;
begin_c_loop(c,t)
{
vr_t = C_UDMI(c,t,3);
C_PROFILE(c,t,nv) = vr_t;
}
end_c_loop(c,t)
}

// STREAMWISE DIRECTION, X COMPONENT

```

```

DEFINE_PROFILE(streamwise_x, t, nv)
{
    float str_x;
    cell_t c;
    begin_c_loop(c,t)
    {
        str_x = C_UDMI(c,t,4);
        C_PROFILE(c,t,nv) = str_x;
    }
    end_c_loop(c,t)
}

// STREAMWISE DIRECTION, Y COMPONENT
DEFINE_PROFILE(streamwise_y, t, nv)
{
    float str_y;
    cell_t c;
    begin_c_loop(c,t)
    {
        str_y = C_UDMI(c,t,5);
        C_PROFILE(c,t,nv) = str_y;
    }
    end_c_loop(c,t)
}

// STREAMWISE DIRECTION, Z COMPONENT
DEFINE_PROFILE(streamwise_z, t, nv)
{
    float str_z;
    cell_t c;
    begin_c_loop(c,t)
    {
        str_z = C_UDMI(c,t,6);
        C_PROFILE(c,t,nv) = str_z;
    }
    end_c_loop(c,t)
}

// TRANSVERSE DIRECTION, X COMPONENT
DEFINE_PROFILE(transverse_x, t, nv)
{
    float tra_x;
    cell_t c;
    begin_c_loop(c,t)
    {
        tra_x = C_UDMI(c,t,7);
        C_PROFILE(c,t,nv) = tra_x;
    }
    end_c_loop(c,t)
}

// TRANSVERSE DIRECTION, Y COMPONENT
DEFINE_PROFILE(transverse_y, t, nv)
{
    float tra_y;
    cell_t c;
    begin_c_loop(c,t)
    {
        tra_y = C_UDMI(c,t,8);
        C_PROFILE(c,t,nv) = tra_y;
    }
    end_c_loop(c,t)
}

// TRANSVERSE DIRECTION, Z COMPONENT
DEFINE_PROFILE(transverse_z, t, nv)
{
    float tra_z;

```

```
cell_t c;  
begin_c_loop(c,t)  
{  
    tra_z = C_UDMI(c,t,9);  
    C_PROFILE(c,t,nv) = tra_z;  
}  
end_c_loop(c,t)  
}
```